

CHEMICAL SYNTHESIS OF MULTI-CATION OXIDE POWDERS FOR SOLID
OXIDE FUEL (SOFC) COMPONENTS

by
ÇINAR ÖNCEL

Submitted to the Graduate School of Engineering and Natural Sciences
in partial fulfillment of
the requirements for the degree of
Master of Science

Sabancı University
Summer 2003

ACKNOWLEDGEMENTS

First of all, thank Koray, Ülfet and Pınar Öncel for their continuous support, encouragement and trust, not only during my graduate level education, during my whole life.

I would like to thank my advisor, Dr. Mehmet Ali Gülgün, for his generous and non-decreasing support and encouragement during my education at Sabancı University. It was a pleasure to work with his guidance.

I also would like to thank Dr. Alpay Taralp, Dr. Cleva Ow Yang, Dr. A. Cüneyt Taş, Dr. Yusuf Z. Mencilođlu and all my educators for their helps and intensive labors.

Finally, my special thanks go to all my friends. I feel lucky due to your friendship.

ABSTRACT

This study involves the synthesis of LSGM ($\text{La}_{0.9}\text{Sr}_{0.1}\text{Ga}_{0.8}\text{Mg}_{0.2}\text{O}_{3-\delta}$), LSFM ($\text{La}_{0.9}\text{Sr}_{0.1}\text{Fe}_{0.8}\text{Mg}_{0.2}\text{O}_{3-\delta}$), and LSCM ($\text{La}_{0.9}\text{Sr}_{0.1}\text{Cr}_{0.8}\text{Mg}_{0.2}\text{O}_{3-\delta}$) powders via organic precursor method by using different organic carrier materials, investigation on the effects of each organic carrier material on the intended and unwanted phase formations, analyses of formed phases during stages of synthesis, characterization of the synthesized powders, crystallographic studies on the several new crystal phases, the effects of holding time during powder calcination, and further work advices. Citric acid, tartaric acid, Pechini precursors, polyvinyl alcohol, and ethylene diaminetetraacetic acid were used as organic carrier materials. Different organic carrier materials exhibited different behavior on the synthesis of powders. Synthesis of powders without carrier materials was conducted and the effectiveness of organic carrier materials was confirmed. In the LSGM synthesis, the effects of different starting materials (namely lanthanum chloride or gallium sulfate) were also investigated.

X-ray powder diffraction measurements showed that unwanted phases formed, especially below 1000°C . In powders heat treated at low temperatures ($< 1000^{\circ}\text{C}$), maximum LSGM concentration was 88% when citric acid was used as the organic carrier material. Above 1000°C , maximum concentration of LSGM phase in the powders was 95.7% when tartaric acid was utilized as the organic carrier material. For low temperature (below 1000°C) synthesis citric acid, and for above- 1000°C synthesis tartaric acid are the best organic carrier in terms of LSGM percentages in the powders. It was shown that increasing dwell time at calcination temperature could increase the concentration of the desired phases in the powder. The powder synthesized with PVA as the organic carrier material was calcined at 1100°C and LSGM phase in the powder was 33.7%. When same powder held 7 hours at the calcination temperature, LSGM phase in the powder increased

up to 79.8%. Single-phase LSFM was obtained in the powders calcined as low as at 550⁰C. In contrast to LSFM, maximum concentration of LSCM phase in the synthesized powders was 96.9%, when polyvinyl alcohol (PVA) was the organic carrier material.

The factors affecting the purity of the desired phase were stated as the type of the organic carrier material, its cation chelating and/or complexing ability, and the interaction of the functional groups with the constituent cations. The necessity for further studies the organic carrier – cation interaction highlighted.

The structures of La₄Ga₂O₉ and LSCM were discussed in light of the observed shifts in the peak positions in the x-ray spectra.

ÖZET

Bu çalışma, LSGM ($\text{La}_{0.9}\text{Sr}_{0.1}\text{Ga}_{0.8}\text{Mg}_{0.2}\text{O}_{3-\delta}$), LSFM ($\text{La}_{0.9}\text{Sr}_{0.1}\text{Fe}_{0.8}\text{Mg}_{0.2}\text{O}_{3-\delta}$) ve LSCM ($\text{La}_{0.9}\text{Sr}_{0.1}\text{Cr}_{0.8}\text{Mg}_{0.2}\text{O}_{3-\delta}$) tozlarının organik öncül malzeme metodunu ve çeşitli öncül malzemeler kullanarak, her bir öncül malzemenin istenilen ve istenmeyen faz oluşumlarındaki etkilerini, toz sentezinde oluşan fazların analizlerini, sentezlenen tozların karakterizasyon işlemlerini, bazı yeni kristal fazların kristallografik çalışmalarını, tozları sentezlerken kalsinasyon sıcaklığında bekleme süresinin etkilerini ve ileri çalışma konuları hakkında tavsiyeleri içermektedir. Organik taşıyıcı malzeme olarak sitrik asit, tartarik asit, Pechini öncül malzemeleri, polivinil alkol ve etilen diamintetraasetik asit kullanılmıştır. Değişik organik taşıyıcı malzemeleri, toz sentezi sırasında değişik davranışlar sergiledi. Taşıyıcı malzeme kullanılmadan yapılan toz sentezi, taşıyıcı malzemelerin etkinliğini doğruladı. Değişik başlangıç malzemelerinin (lantanium klorat veya galyum sülfat) LSGM toz sentezine etkileri de incelendi.

X-ışını kırınım analizleri, özellikle 1000°C 'nin altında istenmeyen fazların oluştuğunu gösterdi. Düşük sıcaklıklarda ($< 1000^{\circ}\text{C}$) ısıtma işlemi uygulanan tozlarda maksimum LSGM faz konsantrasyonu, %88 ile organik taşıyıcı malzeme olarak sitrik asit kullanıldığında görüldü. 1000°C 'nin üzerinde, maksimum LSGM faz konsantrasyonu, %9.7 ile organik taşıyıcı malzeme olarak tartarik asit kullanıldığında görüldü. Tozlardaki LSGM yüzdelerine göre, düşük sıcaklık (1000°C 'nin altı) sentezi için sitrik asit, 1000°C 'nin üstünde sıcaklıklar için tartarik asit en iyi organik taşıyıcı malzemelerdi. Kalsinasyon sıcaklığında bekleme süresi arttırıldığında, istenilen fazların toz içindeki konsantrasyonlarının arttırılabileceği gösterilmiştir. Organik taşıyıcı malzemesi olarak PVA ile sentezlenen ve 1100°C 'de kalsine edilen tozda LSGM konsantrasyonu %33.7 idi. Aynı toz, aynı kalsinasyon sıcaklığında 7 saat bekletildiğinde tozdaki LSGM konsantrasyonu

79.8%'e yükseldi. 550⁰C kadar düşük sıcaklıkta tek-faz LSCFM tozu elde edildi. Elde edilen maksimum LSCFM faz konsantrasyonu ise organik taşıyıcı malzemesi olarak PVA kullanıldığında ve 850⁰C'de 96.7% idi.

İstenilen fazın saflığına etki eden faktörler; organik taşıyıcı malzemenin cinsi, iyon tutabilme derecesi ve fonksiyonel gruplarının katyonlarla olan etkileşimi olarak gösterilmiştir. Gelecekteki çalışma konularından, organik taşıyıcı – iyon etkileşimi'nin önemi vurgulanmıştır.

La₄Ga₂O₉ ve LSCFM fazlarının yapıları, x-ışını kırınım spektrumlarındaki pik pozisyonlarının kaymaları ışığında incelenmiştir.

LIST of FIGURES

Figure 1.1.	Typical fuel cell configuration.....	2
Figure 1.2.	Alkaline Fuel Cell (AFC) composition.....	4
Figure 1.3.	PEMFC Schematic representation.....	6
Figure 1.4.	Principle of molten carbonate fuel cell.....	8
Figure 1.5.	Solid Oxide Fuel Cell Configuration.....	11
Figure 1.6.	Tubular Solid Oxide Fuel Cell design.....	12
Figure 1.7.	Planar Solid Oxide Fuel Cell design.....	13
Figure 1.8.	The ideal perovskite cubic crystal structure.....	14
Figure 1.9.	Conductivity of Ca-doped LaCrO_3 versus oxygen partial pressure at 1000°C for three different compositions: $x = 0.1, 0.2,$ and 0.3 in $\text{La}_{1-x}\text{Ca}_x\text{CrO}_{3-\delta}$	15
Figure 1.10.	The fluorite crystal structure.....	20
Figure 1.11.	A typical gallium depletion curve from the LSGM surface.....	26
Figure 1.12.	Ester reaction.....	30
Figure 3.1.	XRD Spectra of synthesized $(\text{LaO})_2\text{SO}_4$ powder, calcined at a) 150°C , b) 400°C , and c) 800°C	47
Figure 3.2.	STA plot of the gallium sulfate-lanthanum nitrate-nitric acid solution heated up to 1200°C	48
Figure 4.1.	STA plot of the precursor for LSGM synthesis with Pechini precursor of 60 wt% CA – 40 wt% EG as the organic carrier material.....	64
Figure 4.2.	Visual representation of the phase percentages in LSGM synthesis with Pechini precursor (60 wt% CA – 40 wt% EG mixture) as the organic carrier material.....	65
Figure 4.3.	Visual representation of the phase percentages in LSGM synthesis	

	with Pechini precursor (90 wt% CA – 10 wt% EG mixture) as the organic carrier material.....	66
Figure 4.4.	Powders calcined at 900 ⁰ C and synthesized with a) EDTA, b) PVA, c) TA (2:1), d) Pechini precursor (60 wt% CA – 40 wt% EG), e) TA (1:1), f) TA (1:2), g) CA (1:2), h) Pechini precursor (90 wt% CA – 10 wt% EG), i) CA (2:1), and j) CA (1:1).....	67
Figure 4.5.	Visual representation of the phase percentages in LSGM synthesis with CA (1:1) as the organic carrier material.....	67
Figure 4.6.	Citric acid.....	68
Figure 4.7.	STA plot of the precursor for LSGM synthesis with CA as the organic carrier material.....	69
Figure 4.8.	Tartaric acid.....	69
Figure 4.9.	STA plot of the precursor for LSGM synthesis with TA as the organic carrier material.....	70
Figure 4.10.	Ethylene diaminetetraacetic acid (EDTA).....	71
Figure 4.11.	Possible schematic representation of ammonia attack on EDTA functional groups.....	71
Figure 4.12.	Visual representation of the phase percentages in LSGM synthesis with EDTA as the organic carrier material.....	72
Figure 4.13.	STA plot of the precursor for LSGM synthesis with EDTA as the organic carrier material.....	73
Figure 4.14.	Visual representation of the phase percentages in LSGM synthesis with PVA as the organic carrier material.....	73
Figure 4.15.	STA plot of the precursor for LSGM synthesis with PVA as the organic carrier material.....	74
Figure 4.16.	STA plot of the precursor for LSGM synthesis without any the organic carrier material.....	79
Figure 4.17.	STA plot of the precursor for LSGM synthesis without any organic carrier material, and with sulfate source of gallium.....	82
Figure A1.	X-ray spectra of LSGM powders synthesized with PVA as the organic carrier material.....	106
Figure A2.	X-ray spectra of LSGM powders synthesized with Pechini precursor	

	(60 wt% CA – 40 wt% EG) as the organic carrier material.....	107
Figure A3.	X-ray spectra of LSGM powders synthesized with Pechini precursor (90 wt% CA – 10 wt% EG) as the organic carrier material.....	108
Figure A4.	X-ray spectra of LSGM powders synthesized with CA (1:1 cation to citric acid molecule) as the organic carrier material.....	109
Figure A5.	X-ray spectra of LSGM powders synthesized with CA (2:1 cation to citric acid molecule) as the organic carrier material.....	110
Figure A6.	X-ray spectra of LSGM powders synthesized with CA (1:2 cation to citric acid molecule) as the organic carrier material.....	111
Figure A7.	X-ray spectra of LSGM powders synthesized with TA (1:1 cation to tartaric acid molecule) as the organic carrier material.....	112
Figure A8.	X-ray spectra of LSGM powders synthesized with TA (2:1 cation to tartaric acid molecule) as the organic carrier material.....	113
Figure A9.	X-ray spectra of LSGM powders synthesized with TA (1:2 cation to tartaric acid molecule) as the organic carrier material.....	114
Figure A10.	X-ray spectra of LSGM powders synthesized with EDTA as the organic carrier material.....	115
Figure C1.	X-ray spectra of LSGM powders synthesized without organic carrier material, using nitrate sources of cations.....	123
Figure C2.	X-ray spectra of LSGM powders synthesized with CA as the organic carrier material, and gallium sulfate as the gallium source.....	124
Figure C3.	X-ray spectra of LSGM powders synthesized without organic carrier material, and gallium sulfate as the gallium source.....	125
Figure C4.	X-ray spectra of LSGM powders synthesized without organic carrier material, and lanthanum chloride as the lanthanum source.....	126
Figure E1.	X-ray spectra of LSFM powders synthesized with PVA as the organic carrier material.....	131
Figure E2.	X-ray spectra of LSFM powders synthesized with Pechini precursor (60 wt% CA – 40 wt% EG) as the organic carrier material.....	132
Figure E3.	X-ray spectra of LSFM powders synthesized with CA as the organic carrier material.....	133

Figure E4.	X-ray spectra of LSFM powders synthesized with TA as the organic carrier material.....	134
Figure E5.	X-ray spectra of LSFM powders synthesized with EDTA as the organic carrier material.....	135
Figure E6.	X-ray spectra of LSFM powders synthesized without organic carrier material.....	136
Figure G1.	X-ray spectra of LSCM powders synthesized with PVA as the organic carrier material.....	142
Figure G2.	X-ray spectra of LSCM powders synthesized with Pechini precursor (60 wt% CA – 40 wt% EG) as the organic carrier material.....	143
Figure G3.	X-ray spectra of LSCM powders synthesized with CA as the organic carrier material.....	144
Figure G4.	X-ray spectra of LSCM powders synthesized with TA as the organic carrier material.....	145
Figure G5.	X-ray spectra of LSCM powders synthesized with EDTA as the organic carrier material.....	146
Figure G6.	X-ray spectra of LSCM powders synthesized without organic carrier material.....	147
Figure I 1.	X-ray spectra of LSGM powders synthesized by using CA; a) calcined at 1000 ⁰ C, b) calcined at 1000 ⁰ C and held 11 days at 800 ⁰ C.....	152
Figure I 2.	X-ray spectra of LSGM powders synthesized by Pechini precursor; a) calcined at 1200 ⁰ C, b) calcined at 1200 ⁰ C and held 11 days at 800 ⁰ C...	153
Figure I 3.	X-ray spectra of LSGM powders synthesized by using TA; a) calcined at 1000 ⁰ C, b) calcined at 1000 ⁰ C and held 11 days at 800 ⁰ C.....	154
Figure I 4.	X-ray spectra of LSGM powders synthesized by lanthanum chloride; a) calcined at 1200 ⁰ C, b) same powder held 11 days at 800 ⁰ C.....	155
Figure J 1.	X-ray spectra of LSGM powders synthesized by using PVA; a) calcined at 1100 ⁰ C, b) held 7 hours at 1100 ⁰ C.....	157
Figure J 2.	X-ray spectra of LSGM powders synthesized by using CA; a) calcined at 900 ⁰ C, b) held 7 hours at 900 ⁰ C.....	158
Figure J 3.	X-ray spectra of LSGM powders synthesized by using CA; a) calcined	

	at 1100 ⁰ C, b) held 7 hours at 1100 ⁰ C.....	159
Figure J 4.	X-ray spectra of LSGM powders synthesized by lanthanum chloride; a) calcined at 1100 ⁰ C, b) held 7 hours at 1100 ⁰ C.....	160

LIST of TABLES

Table 1.1.	Typical SOFC air emissions from one year of operation	10
Table 1.2.	Anode-supported CGO film cell performance under moist CO ₂ /H ₂ fuel...	23
Table 1.3.	Comparison of anode supported CGO film cell and self supported cell at 650 ⁰ C under H ₂ /CO ₂ fuel	24
Table 1.4.	Ionic conductivities of YSZ, LSGM, and CGO for 600 ⁰ C, 800 ⁰ C, and 1000 ⁰ C	24
Table 1.5.	Compositional dependence of d _{nor} . The samples are treated at 900 ⁰ C for 10 h in a flowing gas of H ₂ – 1.2%H ₂ O.....	26
Table 2.1.	JCPDS numbers of the discussed compounds	37
Table 3.1.	Table of concentrations and amounts of each phase for the LSGM powders calcined at the original calcination temperature, waited 800 ⁰ C for 11 days	56
Table 3.2.	Table of concentrations and amounts of each phase for the LSGM powders calcined at the original calcination temperature, waited at calcination temperature for 7 hours	56
Table 4.1.	The concentrations and amounts of each phase of the LSGM powders calcined at 900 ⁰ C	75
Table 4.2.	The concentrations and amounts of each phase of the LSGM powders calcined at 1000 ⁰ C	75
Table 4.3.	Crystal ionic radius of the cations for coordination number 6.....	86
Table 4.4.	Lattice parameters of La ₄ Ga ₂ O ₉ and La ₄ Ga _{2-x} Mg _x O _{9-δ} phases	87
Table 4.5.	Diffraction angles and interplanar spacings of LaCrO ₃ and LSCM phases for the selected crystallographic planes	87
Table 4.6.	Lattice parameters of LaCrO ₃ and LSCM phases.....	88

Table B1.	Concentrations and amounts of the phases in LSGM powders synthesized with PVA as the organic carrier material.....	117
Table B2.	Concentrations and amounts of the phases in LSGM powders synthesized with Pechini precursor (60 wt% citric acid – 40 wt% ethylene glycol) as the organic carrier material.....	117
Table B3.	Concentrations and amounts of the phases in LSGM powders synthesized with Pechini precursor (90 wt% citric acid – 10 wt% ethylene glycol) as the organic carrier material.....	118
Table B4.	Concentrations and amounts of the phases in LSGM powders synthesized with CA (1:1 total cation to citric acid molecule) as the organic carrier material.....	118
Table B5.	Concentrations and amounts of the phases in LSGM powders synthesized with CA (2:1 total cation to citric acid molecule) as the organic carrier material.....	119
Table B6.	Concentrations and amounts of the phases in LSGM powders synthesized with CA (1:2 total cation to citric acid molecule) as the organic carrier material.....	119
Table B7.	Concentrations and amounts of the phases in LSGM powders synthesized with TA (1:1 total cation to citric acid molecule) as the organic carrier material.....	120
Table B8.	Concentrations and amounts of the phases in LSGM powders synthesized with TA (2:1 total cation to citric acid molecule) as the organic carrier material.....	120
Table B9.	Concentrations and amounts of the phases in LSGM powders synthesized with TA (1:2 total cation to citric acid molecule) as the organic carrier material.....	121
Table B10.	Concentrations and amounts of the phases in LSGM powders synthesized with EDTA as the organic carrier material.....	121
Table D1.	Concentrations and amounts of the phases in LSGM powders synthesized without organic carrier material, with nitrate sources of the cations.....	128

Table D2.	Concentrations and amounts of the phases in LSGM powders synthesized with CA as the organic carrier material, and with nitrate sources of lanthanum, strontium, magnesium, and sulfate source of gallium.....	128
Table D3.	Concentrations and amounts of the phases in LSGM powders synthesized without organic carrier material; with nitrate sources of lanthanum, strontium, magnesium, and sulfate source of gallium.....	129
Table D4.	Concentrations and amounts of the phases in LSGM powders synthesized without organic carrier material; with nitrate sources of strontium, gallium, magnesium, and chloride source of lanthanum.....	129
Table F1.	Concentrations and amounts of the phases in LSFM powders synthesized with PVA as the organic carrier material.....	138
Table F2.	Concentrations and amounts of the phases in LSFM powders synthesized with Pechini precursor (60 wt% citric acid – 40 wt% ethylene glycol) as the organic carrier material.....	138
Table F3.	Concentrations and amounts of the phases in LSFM powders synthesized with CA as the organic carrier material.....	139
Table F4.	Concentrations and amounts of the phases in LSFM powders synthesized with TA as the organic carrier material.....	139
Table F5.	Concentrations and amounts of the phases in LSFM powders synthesized with EDTA as the organic carrier material.....	140
Table F6.	Concentrations and amounts of the phases in LSFM powders synthesized without any organic carrier material.....	140
Table H1.	Concentrations and amounts of the phases in LSCM powders synthesized with PVA as the organic carrier material.....	148
Table H2.	Concentrations and amounts of the phases in LSCM powders synthesized with Pechini precursor (60 wt% citric acid – 40 wt% ethylene glycol) as the organic carrier material.....	148
Table H3.	Concentrations and amounts of the phases in LSCM powders synthesized with CA as the organic carrier material.....	149
Table H4.	Concentrations and amounts of the phases in LSCM powders synthesized	

	with TA as the organic carrier material.....	149
Table H5.	Concentrations and amounts of the phases in LSCM powders synthesized with EDTA as the organic carrier material.....	150
Table H6.	Concentrations and amounts of the phases in LSCM powders synthesized without any organic carrier material.....	150

© ÇINAR ÖNCEL 2003

All Rights Reserved

ođlu olmakla gurur duyduğum Koray ÖNCEL'e ...

TABLE OF CONTENT

Acknowledgements.....	i
Abstract.....	ii
Özet.....	iv
List of Figures.....	vi
List of Tables.....	xi

CHAPTER 1

1. INTRODUCTION.....	1
1.1. Fuel Cells Overview.....	1
1.1.1. Fuel Cell Types.....	3
1.1.1.1. Alkaline Fuel Cell (AFC).....	3
1.1.1.2. Proton Exchange Membrane Fuel Cell (PEMFC).....	5
1.1.1.3. Phosphoric Acid Fuel Cell (PAFC).....	7
1.1.1.4. Molten Carbonate Fuel Cell (MCFC).....	8
1.1.1.5. Solid Oxide Fuel Cell (SOFC).....	9
1.1.1.5.1. SOFC Working Principle.....	10
1.1.1.5.2. SOFC Construction.....	12
1.1.1.5.3. Important Components.....	13
1.1.1.5.3.1. Interconnect.....	14
1.1.1.5.3.2. Anode.....	15
1.1.1.5.3.3. Cathode.....	17
1.1.1.5.3.4. Electrolyte.....	18

1.1.1.5.3.4.1. YSZ.....	20
1.1.1.5.3.4.2. CGO.....	22
1.1.1.5.3.4.3. LSGM.....	24
1.1.1.5.4. Synthesis of SOFC Components.....	27
1.1.1.5.4.1. Solid-State Reaction Technique.....	27
1.1.1.5.4.2. Co-precipitation Technique.....	28
1.1.1.5.4.3. Organic Precursor Technique.....	29

CHAPTER 2

2. EXPERIMENT.....	32
2.1. Materials.....	32
2.1.1. Cation Sources.....	32
2.1.2. Precursor Materials and Solvents.....	33
2.2. Powder Synthesis.....	34
2.2.1. LSGM Synthesis.....	34
2.2.2. LSFM and LSCM Synthesis.....	35
2.3. Characterization.....	36
2.3.1. Thermal Analyses.....	36
2.3.2. X-Ray Diffraction.....	36

CHAPTER 3

3. RESULTS.....	39
3.1. LSXM (X = Ga, Fe, and Cr) Synthesis.....	39
3.1.1. LSGM Synthesis.....	39
3.1.1.1. Synthesis with Different Organic Carriers.....	40
3.1.1.1.1. PVA.....	40
3.1.1.1.2. Pechini Precursors.....	41
3.1.1.1.3. CA.....	42
3.1.1.1.4. TA.....	43

3.1.1.1.5. EDTA.....	44
3.1.1.2.The Use of Different Starting Materials.....	45
3.1.1.2.1. Nitrate Sources.....	45
3.1.1.2.2. Nitrate and Sulfate Sources with/without CA as Carrier Material.....	46
3.1.1.2.3. Nitrate and Chloride Sources.....	48
3.1.2. LSFM Synthesis.....	49
3.1.2.1.PVA.....	49
3.1.2.2.Pechini Precursor.....	50
3.1.2.3.CA.....	50
3.1.2.4.TA.....	50
3.1.2.5.EDTA.....	51
3.1.2.6.Without Carrier Material.....	51
3.1.3. LSCM Synthesis.....	52
3.1.3.1.PVA.....	52
3.1.3.2.Pechini Precursor.....	53
3.1.3.3.CA.....	53
3.1.3.4.TA.....	54
3.1.3.5.EDTA.....	54
3.1.3.6.Without Carrier Material.....	55
3.2. Holding Time at Calcination Temperature and Durability Test.....	55

CHAPTER 4

4. DISCUSSION.....	58
4.1. Synthesis Method and Material Selection Criteria.....	58
4.2. Relations Between Phases.....	61
4.3. Effect of Carrier Materials.....	63
4.3.1. LSGM Synthesis.....	63
4.3.2. LSFM and LSCM Synthesis.....	77
4.4. Synthesis Without Carrier Materials.....	78

4.4.1. Effect of Gallium Sulfate.....	81
4.4.2. Effect of Lanthanum Chloride.....	82
4.5. Effect of Holding Time and Durability Test.....	84
4.6. Peak Shift.....	85
4.6.1. La ₄ Ga ₂ O ₉ Peaks.....	85
4.6.2. LSCM Peaks.....	87
4.7. Overall Discussion and Future Work.....	88

CHAPTER 5

5. CONCLUSIONS.....	92
REFERENCES.....	94
APPENDIX A.....	105
APPENDIX B.....	117
APPENDIX C.....	122
APPENDIX D.....	128
APPENDIX E.....	130
APPENDIX F.....	138
APPENDIX G.....	141
APPENDIX H.....	148
APPENDIX I.....	151
APPENDIX J.....	156

CHAPTER 1

INTRODUCTION

1.1. Fuel Cell Overview

W. R. Grove first developed the idea of “Fuel Cell” in 1839 [1]. The efforts for developing fuel cells and research to overcome associated problems accelerated in the last decades. The main reasons of this intense effort on the development of fuel cells are the need for cleaner, cheaper, and more efficient energy production systems than the traditional energy plants. To this end, renewable sources such as water, sun, wind, biomass, geothermal, and hydrogen are the most promising fuel candidates. Technological and scientific development until today pushed “Fuel Cells” as the energy transforming devices of the new century.

Fuel cells are energy conversion devices that produce electricity directly from a gaseous fuel by electrochemical combination of the fuel with an oxidant through electrodes and across an ion conductor electrolyte. Fuel cells produce DC electricity from chemical energy, without transforming it first into heat and then into kinetic energy.

Main components of a typical fuel cell are a highly ionic but poorly electronic conductor electrolyte material, highly electronic conductor anode and cathode materials, a catalyst, and an electronic conductor interconnect material. A classic fuel cell configuration is shown in Figure 1.1. Fuel is fed from the anode side of the fuel cell where the ionization of hydrogen occurs. Air is fed from cathode side for the oxidant source (O_2). Electrons released from hydrogen in anode side, follow the path through

interconnect material to the cathode side. The hydrogen ion passes through the electrolyte material and reaches the cathode. Hydrogen ions and electrons meet with the oxygen at the cathode and form water molecule and heat as the exhaust. Power is generated on interconnect material from the current created by the electrons while they are traveling through the interconnect material from anode to cathode.

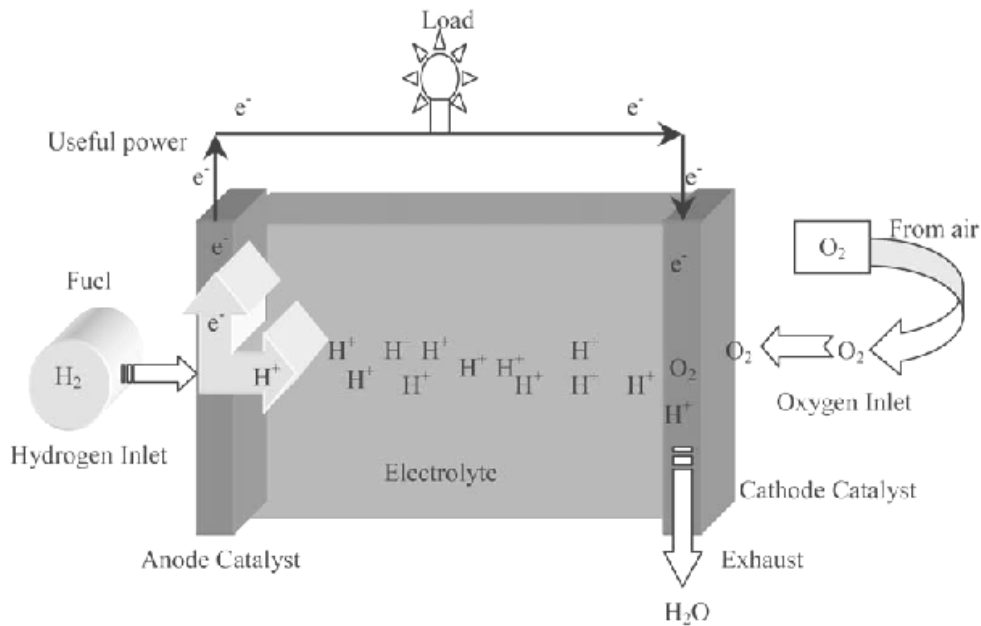


Figure 1.1. Typical fuel cell configuration[2].

The function of the solid or liquid electrolyte material of a fuel cell are: i) to create an environment for ion conductance (oxygen or hydrogen ion conductance), ii) to be an obstacle for electron conductance, iii) to separate electrode materials, and fuel from the oxidant. With its ionic conductance electrolyte material also determines the operating temperature of the fuel cell. For a material to be an effective electrolyte it has to shown high ionic conductance (i.e. ~ 0.1 S/cm for SOFC electrolyte) at the operating temperature. At the anode, ionization of hydrogen coming from the fuel, takes place with the help of the catalyst. According to ionization reaction electron releases from hydrogen and travel to the cathode through the electrical conductor interconnect material. At the anode – electrolyte interface fuel, catalyst, and electrolyte material come into contact. For a hydrogen ion conducting fuel cell system, ionized hydrogen pass through the hydrogen-ion conductor electrolyte material, and meet with electrons and oxygen at the cathode – electrolyte interface and form water with the help of the

catalyst. For an oxygen ion conducting fuel cell system, oxygen ionizes at the cathode side. Formed oxygen ions pass through the oxygen-ion conductor electrolyte material. Oxygen ions and hydrogen ions meet at the anode – electrolyte interface and form water.

Fuel cells can use directly or indirectly a whole variety of fuels, often in a very efficient manner. Hydrogen, most of the hydrocarbons, and alcohols are the current fuel choices of a fuel cell [3]. Despite the fact that hydrogen is the most efficient fuel, storage and transportation problems limit its usage and promote hydrocarbons and alcohols as the alternative fuels [4]. Generally an external reformer is needed to convert hydrocarbon or alcohol fuels into hydrogen [5]. Fuel cells have several advantages over traditional thermo – mechanical energy generation systems, such as high efficiency [6], which is relatively independent of size, modular construction, potential for co-generation, inherently clean, safe, quiet, very reliable and as well as environmentally compatible.

Fuel cells are the most powerful energy production system for areas requiring urgent elimination or degradation of harmful gas emission such as cars, buses, urban areas, industrial facilities, and waste treatment plants. The application areas of fuel cells also include computer, communication facilities, and high technology applications.

1.1.1. Fuel Cell Types

There are basically five different fuel cell types. They are generally classified according to the nature of the electrolyte material. Alkaline fuel cell, proton exchange membrane fuel cell, phosphoric acid fuel cell, and molten carbonate fuel cell are described briefly in the following sections, whereas solid oxide fuel cell described in detail later.

1.1.1.1. Alkaline Fuel Cell (AFC)

The alkaline fuel cell (AFC) is the first fuel cell type used commercially for producing electricity using hydrogen as fuel. The applications of the AFC started with the space exploration, however, in spite of the early success of AFC, the rapid

development of proton exchange membrane (or polymer electrolyte membrane) fuel cells (PEMFC) shadowed AFC, especially in mobile applications.

An AFC uses aqueous potassium hydroxide (KOH) solution (typically 30% concentration) as the electrolyte material. Operation temperature of AFCs is in 50⁰C – 200⁰C range and generally pure hydrogen or hydrazine is used as the fuel [2]. The schematic representation of an AFC fuel cell is shown in the Figure 1.2.

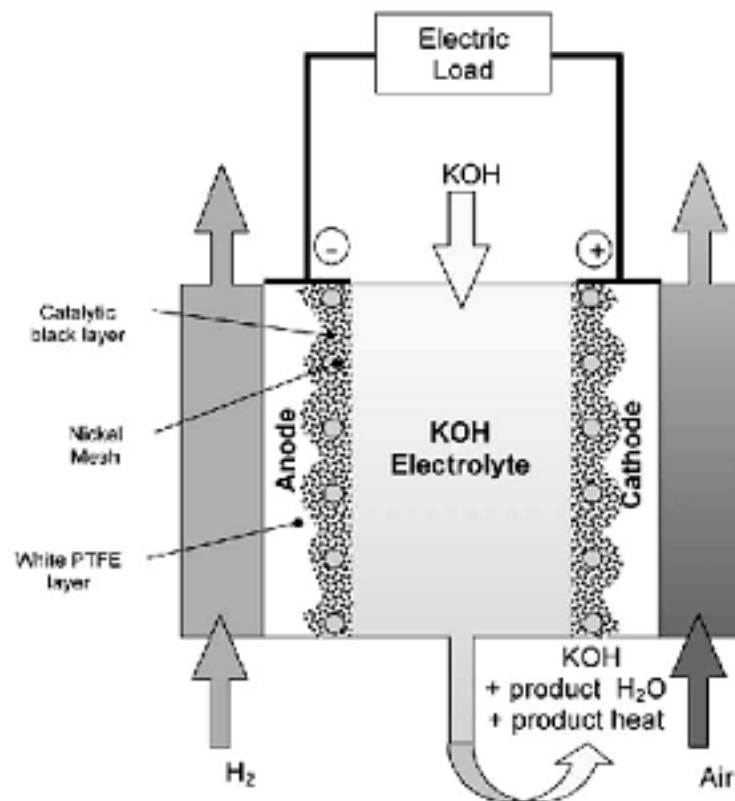


Figure 1.2. Alkaline Fuel Cell (AFC) composition [7].

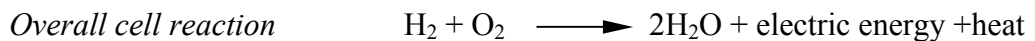
Hydrogen is supplied from the anode side of the fuel cell as the fuel source. The mission of the anode in AFC is to produce electrons according to anode reaction below. The electrodes are consisting of two layers. The active layer is the catalytic dark layer in the Figure 1.2, composed of carbon black, catalyst and PTFE. The function of the hydrophobic white PTFE layer is to prevent the electrolyte from leaking into the reactant gas flow channels and to ensure diffusion of the gases to the reaction site.



The electrons, one of the products of the anode reaction, follow the conducting wire path, rather than the electrolyte path due to the electrical resistance difference between these two materials. Air, the source of the oxidant (oxygen) of the cathode reaction, is fed from the cathode side of the cell. The reactants of the cathode reaction are oxygen from the air, water and electrons from the anode reaction. The product is OH⁻ ion according to the cathode reaction below.



From the overall reaction below, it can be seen that the main product is electric energy, and the by products are water and heat. They have to be removed from the system and this is usually achieved by re-circulating the electrolyte and using it as the coolant liquid, while water is removed by evaporation.



High reliability, and superior kinetics of oxygen reduction in alkaline solution compared to acidic media [8] are the attractive features of AFCs. Low power densities at atmospheric conditions and electrolyte poisoning, effects of carbon dioxide on the anode [9-11] and effects of impurities on the anode [9,12,13], are the reasons of the decrease in interest on AFCs.

1.1.1.2. Proton Exchange Membrane Fuel Cell (PEMFC)

In 1959, Grubb introduced a fuel cell that uses an organic cation exchange membrane as a solid electrolyte, which proved to be one of the most promising fuel cell types [14]. It consists of a solid polymer electrolyte, two porous electrodes and catalytic layers sandwiching the electrolyte material. Operation temperature of PEMFCs is in 50⁰C – 80⁰C range and generally pure hydrogen from hydrocarbons or methanol are used as the fuel. The schematic representation of a PEMFC is shown in Figure 1.3. The humidity of these gases is critically important in terms of the effective operation of the fuel cell. [15,16].

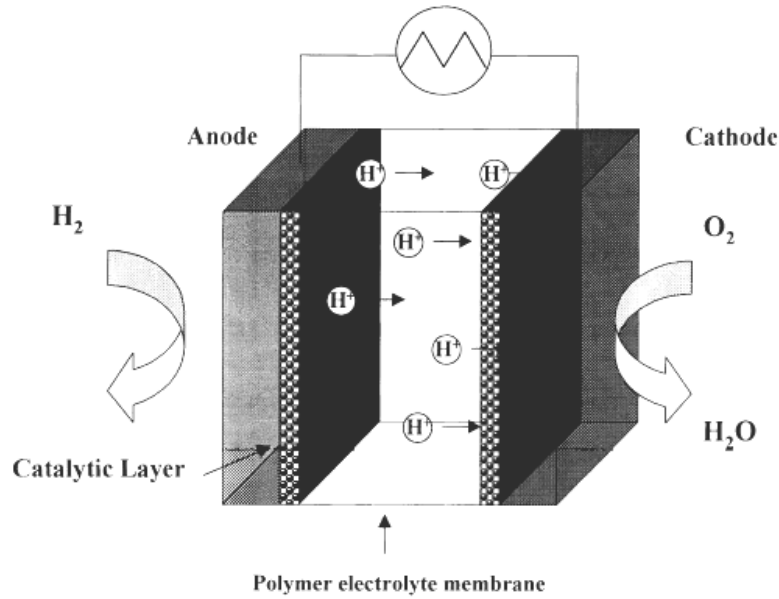
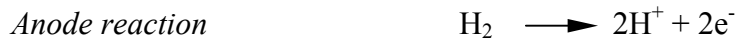
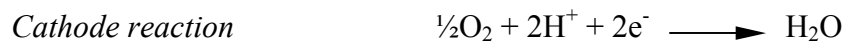


Figure 1.3. PEMFC Schematic representation [14].

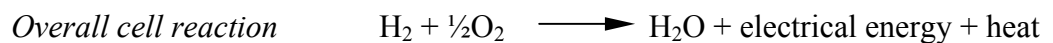
As in the other fuel cell systems, fuel (hydrogen) is fed from the anode side. According to the reaction below, electrons needed to obtain electric energy through the metallic connection between anode and cathode, are obtained from the ionization of the hydrogen gas in the anode.



According to the cathode reaction below, the hydrogen ions traveling through the electrolyte, the required amount of oxygen from the cathode, and electrons passing through the metallic connection, form water as the exhaust gas.



From the overall reaction shown below, the products are water, electrical energy and heat. The electrical energy is obtained while electrons passing through the metallic connection. It is clear that the exhaust gases are free from the environmentally dangerous gases such as NO_x , SO_x and CO .



PEMFCs are one of the promising power sources for mobile applications [17], because of the high power density, low operating temperatures [17], the easy start-up and shut down ability and compact-lightweight feature [18]. Reliability, heat efficiency for co-generation [19], the choice of multiple fuel usage [20] are the attractive features of polymer electrolyte fuel cell systems. The main drawbacks of PEMFCs for commercial use in mobile applications are problems with anodic and cathodic electrocatalyses [21], expensive materials and low performance at high temperatures with low humidity [9,14,15].

1.1.1.3. Phosphoric Acid Fuel Cell (PAFC)

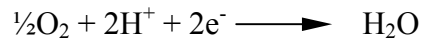
The third type of fuel cells is phosphoric acid fuel cell, which uses phosphoric acid as the electrolyte material. Operation temperature of a PAFC ranges between 150⁰C – 190⁰C. These fuel cell systems generally use platinum (Pt) catalyst for anode and cathode sites. The other components used in PAFC are made of mainly carbon [22]. Basic fuel is used as hydrogen from hydrocarbons and alcohols [2].

The reactions at anode, cathode, and the overall reaction are same with the corresponding reactions of the PEMFC.

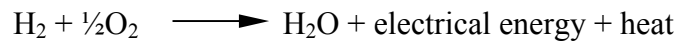
Anode reaction



Cathode reaction



Overall cell reaction



According to the operation experiences, compact design without loop and high value waste heat [23], can be said as the main advantages. Acid absorption in the electrodes [24], the need of pre-heating and significant energy losses due to cell construction, low operational efficiency [23], and carbon monoxide poisoning [25] are the main drawbacks of the PAFCs.

1.1.1.4. Molten Carbonate Fuel Cell (MCFC)

Molten carbonate fuel cell is one of the high temperature (~650⁰C) fuel cell types. The anode material is generally nickel reinforced with chromium or aluminum, or their oxides, and nickel with lithiated nickel oxide agglomerates is used generally as the cathode material [26]. The typical composition of the electrolyte material for MCFC is 62 mol% Li₂CO₃ and 38 mol% K₂CO₃ eutectic [26]. Schematic representation of MCFC is shown in Figure 1.4.

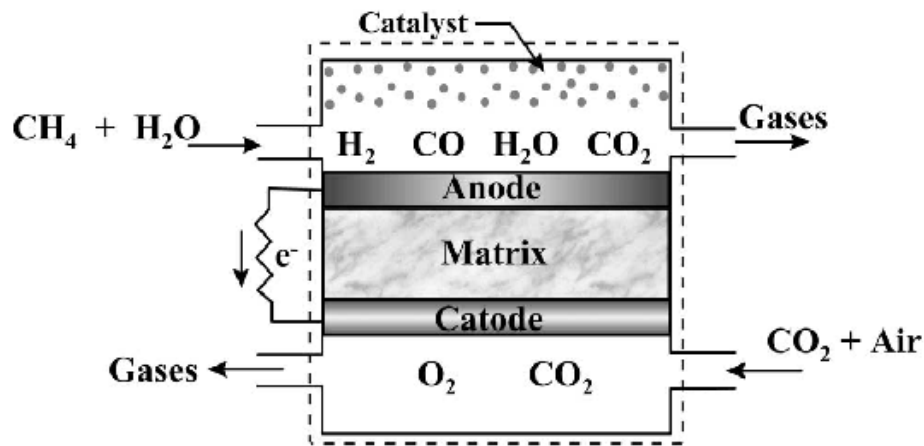
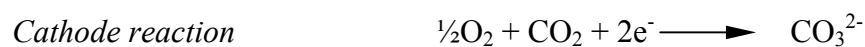


Figure 1.4. Principle of molten carbonate fuel cell [27].

In the anode, carbonate ions travel through the electrolyte material and discharge electrons, which go through the electronically conductor material to the cathode side. Carbon dioxide and oxygen gases are the other products in the anode reaction, which is shown below.



In the cathode, carbon dioxide and oxygen gases combines with the electrons and form carbonate ion. The cathode reaction is shown below.



Very high voltage efficiency [28], flexibility to a variety of fuels [29], fast electrode reaction through the electrolyte material [30] are the main advantages of molten carbonate fuel cells. Corrosion of the separator material, deformation of the electrolyte matrix, and cathode dissolution at high-pressure operation [29] are the most important drawbacks of MCFCs.

1.1.1.5. Solid Oxide Fuel Cell (SOFC)

Solid oxide fuel cells are the most promising energy production systems for 21st century due to their high efficiency, utilization of a variety of the fuel resources, and environmental friendliness.

High efficient-operating among all the other type of fuel cells [6,83,87,99] is one of the major advantages of SOFC. Since working principle of SOFC does not rely on the temperature changes, the efficiency is not limited by the efficiency of the thermodynamic cycle [100]. The theoretical upper limit of the efficiency is 100%. In practice 60%, or for combined heat and power systems 70% or even more [6,83,87] have been already reached.

Variable fuel resources of solid oxide fuel cells include hydrogen, gasoline, diesel, natural gas, and a large range of hydrocarbons. SOFCs generally require also a partial oxidation reformer unit to pre-process the fuel. The emissions of the SOFC system depend on the type of the fuel used. In case of hydrogen as the fuel for the SOFC system, maximum efficiency can be achieved [31], but storage and transportation of hydrogen seem as a drawback. Studies on the elimination of these disadvantages of using pure hydrogen as the fuel for SOFC are on progress [32]. Usage of hydrocarbons as the fuel source eliminates the drawbacks in transport and storage of hydrogen, but results in a decrease in the cell performance [102].

In recent years, more attention has been focused on the atmospheric pollution and greenhouse warming due to increasing global warming rate in the world. CO₂ is considered to be the major responsible emission for the rising global warming rate. Unlike the traditional energy production systems, in a solid oxide fuel cell system NO_x, SO_x, organic compounds and particulate emissions are zero, CO emission is very low, and CO₂ emission is far below when compared to traditional energy production system emissions. In case of hydrogen as the fuel, H₂O is the only exhaust. In case of all other

fuel sources, since SOFC can even convert CO, H₂O and CO₂ are the only exhaust gases. In Table 1.1, the emission values of the two energy production systems are tabulated. The environmental impacts of manufacturing stage of the SOFC components also have been studied [33].

Table 1.1. Typical SOFC air emissions from one year of operation [34]

Air Emissions^a	SO_x	NO_x	CO	Particles	Organic Compounds	CO₂
Fossil Fuelled Plant	12,740	18,850	12,797	228	213	1,840,020
SOFC System	0	0	32	0	0	846,300

^a kgs of emissions per 1650 MWh from one year full operation

SOFC has many advantages over other types of fuel cells. Polymer electrolyte fuel cells (or proton exchange membrane fuel cells) and phosphoric acid fuel cells can use only hydrogen as fuel, but SOFC can directly use many types of fuels other than hydrogen such as carbon monoxide, alcohol, and hydrocarbons. Achievable percentage of efficiency is the highest in SOFC (~70%) [6], compared to other fuel cell types. Moreover, SOFC does not need expensive platinum catalyst because its high operation temperature makes cheaper catalysts highly active. Furthermore, SOFC has advantages such as high stability of electrolyte, flexibility of cell design, and long stack-life because all the components are solid.

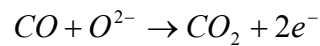
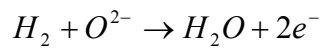
1.1.1.5.1. SOFC Working Principle

Solid oxide fuel cell is mainly composed of solid electrolyte, anode, cathode, and interconnect materials. Oxygen gas (usually air) is supplied to the cathode, and the fuel is supplied to the anode. Porous anode and cathode materials are separated from each other by a dense electrolyte, whereas they are connected by an interconnect material. Schematic illustration of a solid oxide fuel cell is shown in Figure 1.5.

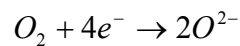


Figure 1.5. Solid Oxide Fuel Cell Configuration

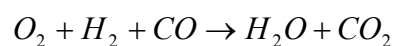
At the anode, oxidation of the fuel takes place. According to the fuel type (H_2 or H_2/CO) possible anode reactions are shown below.



Electrons produced by the anodic reaction(s), travel through the interconnect material reach to the cathode side. At the cathode, electrons meet with oxygen from the air and form oxygen ion (O^{2-}) by the cathode reaction shown below. These oxygen ions travel



through the solid electrolyte material and reach to the anode side by this path. By the reaction of these oxygen ions with the hydrogen ions (H^+) (and CO^{2-}) at the anode side, H_2O (and/or CO_2) are produced as the exhaust gas(es). Possible overall cell reaction is shown below.



Like other fuel cell types, energy production in SOFC system is achieved during travel of electrons through the interconnect material.

1.1.1.5.2. SOFC Construction

The design and fabrication of SOFCs are critical issues for its development and commercialization. Recently, SOFC has two main designs under investigation, namely tubular and planar designs.

The tubular design, which is developed by Siemens-Westinghouse is illustrated schematically in Figure 1.6.

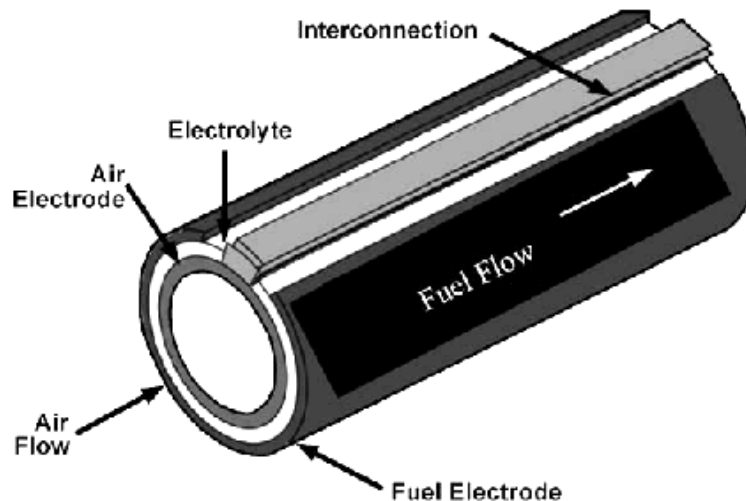


Figure 1.6. Tubular Solid Oxide Fuel Cell design [35]

In this design, oxidant (air) flows through inside of the tubular cathode (air electrode), and the fuel flows on the outside of anode (fuel electrode). A representative example for cell materials and production route can be given as follows. The cell components are deposited on a doped lanthanum manganite cathode tube [35]. The cathode tube is fabricated by extrusion and sintering, and yttrium-stabilized zirconia (YSZ) electrolyte is deposited in the form of about 40 μm thick dense layer by electrochemical vapor deposition [35]. Then the Ni/YSZ cermet anode is deposited by sintering of Ni/YSZ slurry. When these cells are tested for 25,000 h [35], they exhibit

less than 0.1% per 1000 h performance degradation. Such tubular cells have power densities about $0.25 - 0.30 \text{ W/cm}^2$ at 1000°C operation [35]. Due to these low power densities compared to planar cell power densities (about 2 W/cm^2) [35], tubular SOFCs are suitable for stationary power generation, but not for mobile applications.

In planar design, the cell components are designed as flat and thin plates. The configuration of a planar SOFC design is shown in Figure 1.7.

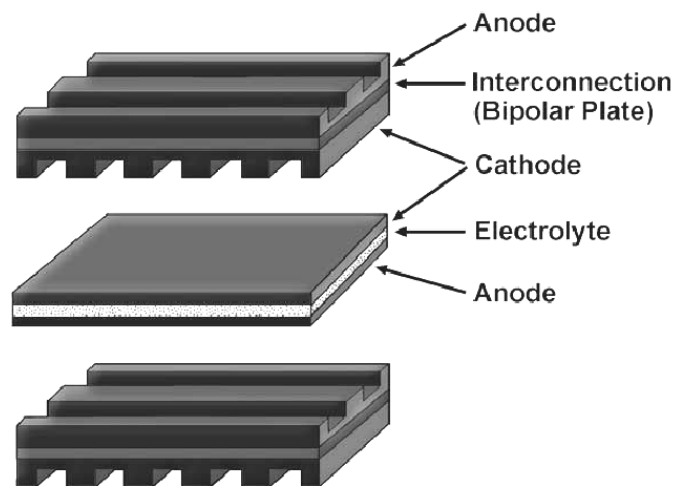


Figure 1.7. Planar Solid Oxide Fuel Cell design [35]

The interconnect connects anode and cathode, and also serves as gas separator between anode and cathode materials. These cells are fabricated by low-cost conventional ceramic processing techniques such as slurry sintering, tape casting, screen printing, or by plasma spraying. There are also different design variations of planar SOFC stacks developed by different organizations [35].

1.1.1.5.3. Important Components

Important components of a solid oxide fuel cell are electrolyte, cathode, anode, and interconnect. The electrolyte needs to be a thin and dense material, good oxygen ion conductor but a poor electronic conductor. The cathode and anode must be porous, good electronic and ionic conductor materials. The interconnect material needs to be good electronic conductor but poor ionic conductor.

1.1.1.5.3.1. Interconnect

The principal function of interconnect material in solid oxide fuel cells is to provide electronic connection between anode and cathode materials. The desired properties of a suitable interconnect material for SOFC system are high electrical conductivity, negligible ionic conductivity, chemical and thermal expansion compatibility with the in-contact materials, chemical stability in oxidizing and reducing atmospheres, and reasonable production and material cost. Gas-tightness is also a critical parameter for planar SOFC systems, where the interconnect material separates the gas compartments (fuel and air). Ceramic and metallic interconnection materials are available as fuel cell components. Mostly, ceramic interconnects are used in SOFC systems.

Practically all the ceramic interconnects of present SOFC systems are based on the perovskite structure of LaCrO_3 type [36]. The ideal perovskite structure is shown in Figure 1.8.

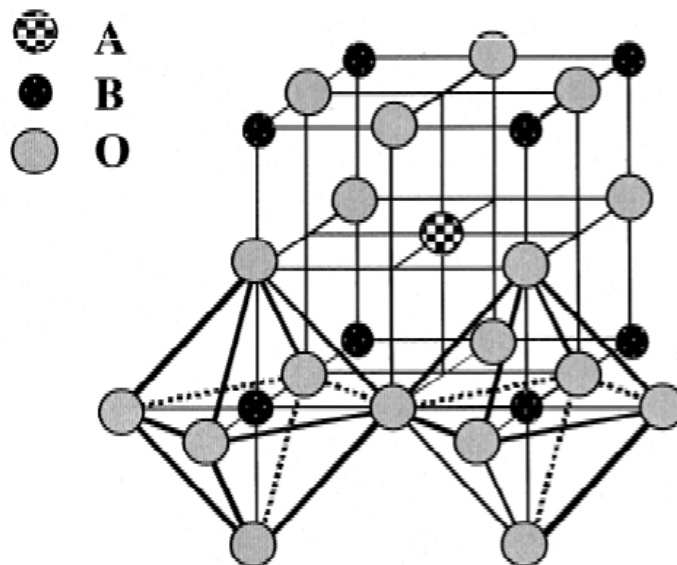


Figure 1.8. The ideal perovskite cubic crystal structure [37]

By modifying the stoichiometry with other elements, it is possible to control the thermal expansion and behavior in oxidizing and reducing atmospheres [36,38]. By doping LaCrO_3 with Sr, Mg, or Ca, the material becomes a highly electronic conductor, depending on the oxygen partial pressure [38]. The electrical conductivity values can

change according to the oxygen partial pressure. The behavior of $\text{La}_{1-x}\text{Ca}_x\text{CrO}_{3-\delta}$ in different oxygen partial pressure is shown in the Figure 1.9. As an example, cathode side conductivity is about 20 – 50 S/cm at 1000°C , but this value can be more than one order of magnitude lower on the anode side [38].

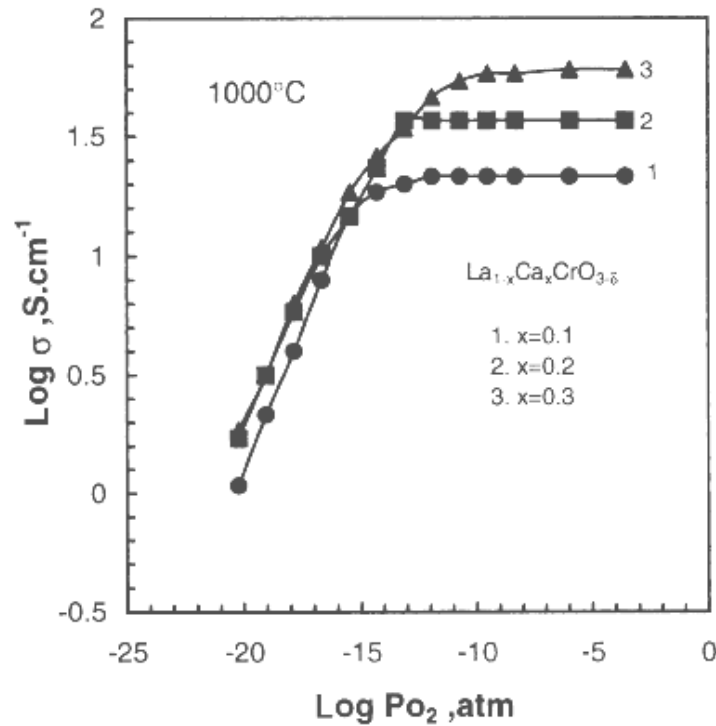


Figure 1.9. Conductivity of Ca-doped LaCrO_3 versus oxygen partial pressure at 1000°C for three different compositions: $x = 0.1, 0.2,$ and 0.3 in $\text{La}_{1-x}\text{Ca}_x\text{CrO}_{3-\delta}$ [39].

The drawbacks of doped LaCrO_3 are their high cost, expensive production processes, such as plasma-spray [36], and being not perfect in terms of electrical, thermal, and chemical requirements. For these reasons, metallic interconnects are employed frequently [36]. There are also investigations to solve the problems associated with the metallic interconnects, such as time-dependent degradation [36], and degradation in catalytic activity [36].

1.1.1.5.3.2. Anode

The function of an anode (sometimes called as *fuel electrode*) material in a solid oxide fuel cell is to provide an interface where fuel, oxygen ions from electrolyte, a

proper catalyst, and electrons from the cathode material meet. A porous anode material is desired to provide high surface area for the anodic reactions to take place at the anode – electrolyte interface, for removal of reaction products, and for temporary storage of fuel gases. High catalytic activity to CO and H₂ oxidation, and good stability are the necessary parameters of a SOFC anode material all under reducing atmospheres.

Triple phase boundaries (TPB) in an anode are the regions where solid electrolyte, catalyst, and gaseous fuel meet in SOFC stack. The TPB area is defined as the product of the TPB length and the active anode thickness. It is assumed that the electrochemical reaction occurs close to the anodic TPB [38]. Development of mixed conducting oxides as electrodes is an attractive approach. In these oxides, both electrons and oxide ions exhibit high mobilities, so that the electrochemical reaction can occur at the electrode/gas interface as opposed to only at the TPBs [40].

The most powerful anode material in terms of catalytic properties with respect to H₂ oxidation is nickel [40]. Sintering and coarsening of Ni – particles at high temperatures leads to a reduction of the porosity and TPB length. Adding YSZ particles and forming Ni/YSZ cermet can eliminate this problem [41]. A porous cermet of nickel and yttria-stabilized zirconia (Ni/YSZ) is generally used as the anode material in solid oxide fuel cells with YSZ electrolyte material [41,42]. NiO and YSZ powders are subjected mixing and sintering to form NiO/YSZ composite ceramic [42]. After this process NiO is reduced to metallic nickel when SOFC is exposed to fuel. By this way, metallic Ni and a porous structure can be obtained. The performance of Ni/YSZ anode depends strongly on its nickel content and its microstructure [42].

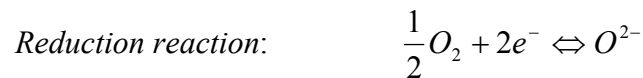
Studies are conducted about the optimal morphology, porosity and thickness of such cermet anodes [38]. The major disadvantage of Ni/YSZ cermet anode arises from the promotion of competitive catalytic cracking of hydrocarbon reactions [40]. High Ni loading to Ni/YSZ cermet results thermal expansion mismatch between the Ni and zirconia electrolyte substrate [40]. In utilization of natural gas as the fuel at Ni cermet anodes, sulphur intolerance occurs which results deposition of nickel sulphide at the anode [40].

There are also studies on the alternative anode materials for YSZ-electrolyte SOFCs. Copper-stabilized zirconia [43], Cu-Ni-YSZ cermet [44], lanthanum-doped strontium titanate [45], doped lanthanum chromites [46,47], and mixed ionic-electronic conducting oxides [48] are some of the anode material candidates for YSZ-electrolyte SOFCs.

Different anode materials have to be used depending on the electrolyte material of SOFC. Ni/CGO cermet [49,50], Ni/YSZ cermet [51-53], and Sr and Fe-doped LaCoO₃ [54] anodes are the main anode candidates for gadolinium-doped ceria electrolytes. Ni-Ce_{1-x}Sm_xO_{2-δ} cermet [37,55,56] seems to be the most suitable anode material for strontium and magnesium-doped lanthanum gallate electrolyte material.

1.1.1.5.3.3. Cathode

Basically, cathode (sometimes called as *air electrode*) material in solid oxide fuel cell should satisfy the requirements of high electronic conductivity to supply electrons, chemical compatibility with the other cell components, similar thermal expansion coefficient with electrolyte material, and high catalytic activity with respect to the reduction reaction shown below.



Similar to anode material, cathode material should have a porous structure to provide high surface area to provide cathodic reaction at the cathode – electrolyte interface, removal of reaction products, and temporary storage of air. Triple phase boundary in cathode is again a necessary region, where the cathode, electrolyte, catalyst, and oxygen meet. The possible reaction paths at TPB are discussed extensively in the literature [38,58]. The bulk of the cathode materials require a certain oxygen ionic conductivity. For an ionic conductivity, there appears the need of high charge carrier concentrations such as vacancies and/or holes. A tool for achieving this is doping of aliovalent cations to the oxide cathode material. Transition metal elements are useful for this purpose due to their easily changeable valences.

The performance of a cathode material depends on the sum of resistances associated with each component, the rates of interfacial reactions such as oxygen dissociation, charge-transfer and gas diffusion.

The polarization resistance of a cathode material is one of the most important factors determining the cell performance in SOFCs [59]. One of the most important properties required for SOFC cathode is the steady-state polarization, which is

characterized mainly by current density [60]. Because of the large cathode polarization at low temperatures the need for considerable improvements in cathode materials and microstructures has resulted. To control the microstructure of the cathode material is also important to obtain good electrode performance [56].

Perovskite-type materials based on LaSrMnO_3 (Lanthanum strontium manganite) (LSM) [61-65], $(\text{LaSr})\text{CoO}_3$ (lanthanum strontium cobaltite) (LSC) [61,66,67] are extensively used as cathode materials for SOFC operating with YSZ electrolyte. Additionally, Ag – YSZ [66] and Pt – YSZ [66] cermet cathodes, mixed ionic-electronic conducting (MIEC) oxides such as SrFeCoO_3 , SrCoFeO_3 , and LaSrFeCoO_3 based oxides [48] are investigated for YSZ – electrolyte SOFCs.

$(\text{LaSr})\text{CoFeO}_3$ [49,51,52,68-70] based cathode material is the most studied air electrode for SOFCs operating with ceria-based electrolytes. $(\text{LaSr})\text{CoO}_3$ [67], strontium-doped gadolinium manganite [72], and some composite cathode materials [73,74] are other cathode materials investigated for the ceria-based electrolytes.

$(\text{LaSr})\text{CoO}_3$ [56,75-77] is the most suitable cathode material SOFCs operating with the strontium and magnesium-doped lanthanum gallate electrolytes. There are also studies on some mixed conducting perovskite-type oxides as the cathode material [78].

The electrolyte types will be explained in detail in the next section.

1.1.1.5.3.4. Electrolyte

Since material selection and design of the SOFCs are conducted according to the electrolyte material, the solid electrolyte can be said to be the most critical component of SOFCs. The requirements on the SOFC electrolyte are plenty:

(i) High ionic conductivity, (ii) chemical stability, (iii) negligible electronic conductivity, (iv) mechanical stability, (v) thermal stability, (vi) thickness, (vii) gas – tightness, (viii) compatibility with other SOFC components, and (ix) processing cost are essential parameters for an electrolyte material in SOFC systems.

The mechanism of ionic conductivity strongly depends on diffusion process [79]. Oxygen ions (O^{2-}) resulting from cathode reaction at the cathode side pass through the electrolyte to the anode side with the help of the oxygen vacancies. At the anode side, anode reaction occurs and depending on the fuel type, H_2O and/or CO_2 forms. For the function of a SOFC, oxygen vacancy concentration is an important parameter in the

electrolyte material. Another aspect is the temperature dependence of the diffusion process. Diffusion rate increases exponentially with increasing temperature. Because of the temperature limitations of SOFC operation in terms of the cost limitations, minimum operation temperatures are desired [80]. Therefore electrolyte material with high oxygen ion conductivity at low temperatures ($< 800^{\circ}\text{C}$) is essential. Present electrolyte material candidates do not fulfill all the requirements listed previously. Worldwide studies on the development of proper electrolyte materials and improving the properties of the present electrolyte candidates are continuing. Adding doping elements to the specified oxide electrolyte materials is the most popular way of increasing the ionic conductivity of the electrolyte material, by creating additional oxygen vacancies according to their valance state.

The thickness of the electrolyte material is an important parameter in terms of ionic conductivity and SOFC operation temperature. In thinner electrolytes, oxygen ion travel through electrolyte occurs easily and at lower temperatures, same (or more) amount of ionic conductance can be obtained, compared to thicker electrolytes [81].

Electronic conductance of the electrolyte material should be as low as possible in order to minimize ohmic resistance (loss) during operation. Ionic conductivity is a function of diffusion process, and diffusion is a function of temperature. Anode side of electrolyte is subjected to oxidizing, and cathode is subjected side reducing atmospheres. In case of hydrocarbon fuel usage, CO_2 atmosphere is also present. The electrolyte material must be stable at these atmospheres.

The effects of grain boundaries on ionic conductivity of solid electrolyte materials are also investigated [38]. It is known that grain boundaries can increase the resistance of electrolyte material [38]. Highly resistive grain boundaries lead to an additional semicircle in the complex impedance plane and impedance spectroscopy can be used to separate grain boundary and bulk resistances. Different models are discussed to explain grain boundary resistances, such as i) complete wetting, highly resistive grain boundary phase, ii) space charge depletion layers, or iii) current restriction due to partially wetting, ionically blocking grain boundary phase.

Most of the efforts in the scientific community are focused on three types of electrolyte materials; yttrium-stabilized zirconia (YSZ), gadolinium-doped ceria (GDC or CGO), and strontium and magnesium-doped lanthanum gallate (LSGM).

1.1.1.5.3.4.1. YSZ

Yttria-stabilized zirconia (YSZ) is the most common electrolyte material in SOFCs. Pure ZrO_2 has low ionic conductivity; therefore it is a poor electrolyte material for SOFC. However, the crystal structure of ZrO_2 plays an important role for its ionic conductivity. It has three different crystal structures at different temperatures. From room temperature to $1170^{\circ}C$, ZrO_2 has monoclinic structure. Between $1170^{\circ}C$ and $2370^{\circ}C$ tetragonal, and from $2370^{\circ}C$ to melting point ($2680^{\circ}C$) cubic fluorite structure is present (see Figure 1.10).

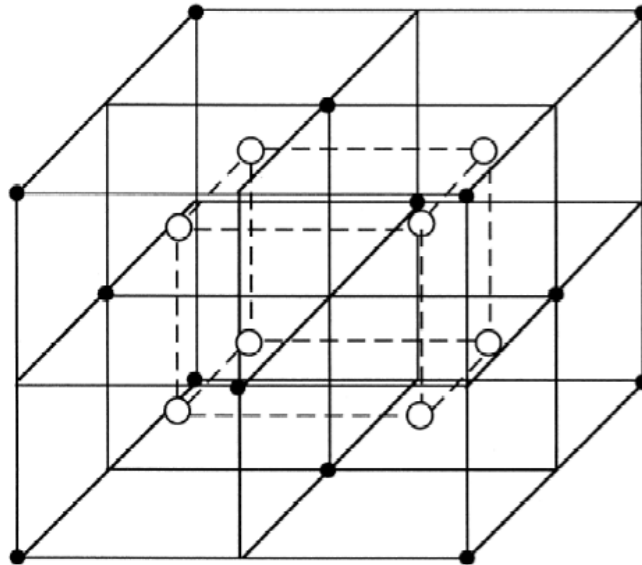
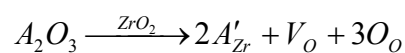


Figure 1.10. The fluorite crystal structure [37]. (Black dots represent cations, open circles represent oxygens)

Addition of certain oxides (e.g. CaO , MgO , Y_2O_3 , Sc_2O_3) stabilizes the cubic fluorite structure of ZrO_2 from room temperature up to melting point. Stabilization of ZrO_2 is attempted by direct substitution of divalent or trivalent cations of suitable size for the host lattice Zr^{4+} cation. This substitution also creates oxygen vacancies according to the following equation using Kröger – Vink Notation :



where A is a trivalent cation, dissolution of A_2O_3 in ZrO_2 creates an oxygen vacancy, V_o , A^{3+} substitution on Zr^{4+} site by leaving an excess electron, A'_{Zr} , and substitution of 3 oxygen ions from A_2O_3 to the 3 oxygen sites of ZrO_2 lattice.

The origin of ionic conduction is oxygen ion mobility, and it is proportional with oxygen ion vacancy concentration in the solid electrolyte material. The ionic conductivity of stabilized- ZrO_2 is independent of oxygen partial pressures for SOFC operation temperatures [82]. Under these conditions, the electronic conductivity of YSZ is negligible.

The ionic conductivity of YSZ varies with the dopant concentration [82]. The maximum conductivity for YSZ electrolyte material is obtained near minimum concentration of dopant required to fully stabilize the cubic fluorite crystal structure. By increasing the dopant concentration, the ionic conductivity decreases, which is believed due to vacancy clustering, defect ordering, or electrostatic interaction [82].

For a polycrystalline material, there are basically two regions, which may resist to ionic diffusion resulting in a decrease in the ionic conductivity. They are the grain boundary and the bulk itself. Impedance measurements of polycrystalline stabilized- ZrO_2 are conducted to determine bulk and grain boundary resistivities [82]. Generally, the effect of grain boundaries on the ionic conductivity is seen below $700^{\circ}C$. It is found that grain boundary effects are negligible at $1000^{\circ}C$ -operation of SOFC [82].

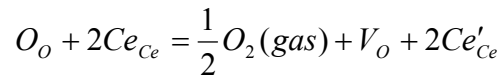
Mechanical properties of the electrolyte material are also important for SOFC operation. The electrolyte material must withstand the conditions of production and operation without being damaged. Fracture in the electrolyte material allows fuel and oxidant come into contact and this reduces the cell performance. For this reason, several approaches were applied to improve the mechanical properties of YSZ. These approaches are basically based on fracture resistance of the electrolyte by toughening [82]. These approaches are based on introducing inclusions of monoclinic- ZrO_2 [82], fine particles of Al_2O_3 [82], and MgO [82]. There are also studies on tetragonal- ZrO_2 as the electrolyte material itself, because of its high toughness, high strength, and high bulk ionic conductivity at low temperatures compared to YSZ [82]. Aging effect [82] is reported as the disadvantage of tetragonal- ZrO_2 for SOFC electrolyte application.

Generally 8-mol% yttria is doped to ZrO_2 and the conductivity of this YSZ at $1000^{\circ}C$ is about 0.1 S/cm [38]. There are also reports that 10-mol% yttria doping resulted in an ionic conductivity value of 0.1 S/cm [83]. The main drawback of YSZ-

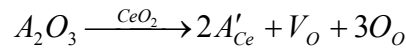
electrolyte SOFC is the relatively high operation temperature (1000⁰C). Materials problems associated with high operating temperature are electrode sintering, interfacial diffusion between electrolyte and electrode, and mechanical stresses due to different thermal expansion coefficients of the components. High operating temperature is also great obstacle for SOFCs in terms of cost of operation and limited choice of other components and insulation materials.

1.1.1.5.3.4.2. CGO

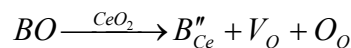
Because of high operation temperature of YSZ-electrolyte SOFCs (1000⁰C), new candidates for electrolyte materials for intermediate temperatures are investigated. One of the most popular electrolyte materials for intermediate temperature solid oxide fuel cell (IT-SOFC) application is ceria-based electrolytes [70]. Pure cerium oxide (CeO₂) has fluorite type structure over the whole temperature range from room temperature to the melting point. When CeO₂ reduced to CeO_{2-x}, defects are formed in the form of Ce³⁺. Ce³⁺ has one negative charge compared to the normal lattice site (Ce⁴⁺). It is agreed that these substitutional negative defects are balanced by oxygen vacancies [84]. The process of ceria reduction may be written as:



Oxygen vacancies may also be introduced by doping with metal oxides with lower valencies such as:



or



where A is a trivalent, and B is divalent cations. The effects of oxides as dopants such as CaO, MgO, SrO, and BaO [85], and Sm₂O₃, Gd₂O₃, and Y₂O₃ were studied [85]. Among these doping agents, Gd₂O₃ and Sm₂O₃ seem to be most promising. There are

some inconsistencies in the literature regarding to the best doping agent for ceria based electrolyte material. There are publications reporting that the best ionic conductor was found as CeO₂ – Gd₂O₃ system [6,86], and also others claim that, CeO₂ – Sm₂O₃ system would be the proper one [84,86]. Among them, CeO₂ – Gd₂O₃ system (CGO) is the most-studied system. The conclusion is that the most promising composition of CeO₂ – Gd₂O₃ system is Ce_{0.9}Gd_{0.1}O_{1.95} [6,51].

Because CGO-type electrolyte material is developed for IT-SOFC applications, the properties for temperatures below 800⁰C are essential. CGO's high ionic conductivity (0.1 S/cm) at 800⁰C and stability in fuel environments [86] are the attractive features.

At the anode side (fuel rich region), because of reduction of Ce⁴⁺ to Ce³⁺, electronic conduction is introduced, which causes internal short-circuiting in the cell and due to lattice expansion mechanical stresses are generated. Only at temperatures as low as 500⁰C, the electronic contribution is low and does not affect the cell performance [81]. Steady-state open circuit voltage, OCV (the voltage of a fuel cell circuit when it has no load is attached), area specific resistance, and maximum obtained power values for 550⁰C, 600⁰C, and 650⁰C under the moist CO₂/H₂ fuel are shown in Table 1.2.

Table 1.2. Anode-supported CGO film cell performance under moist CO₂/H₂ fuel [51].

Temperature (°C)	Open Circuit Voltage(V)	Area Specific Resistance (Ω.cm ²)	Maximum Power (mW/cm ²)
650 ⁰ C	0.68	0.8	120
600 ⁰ C	0.73	1.8	70
550 ⁰ C	0.76	4.3	30

These OCV values are lower than the predicted values calculated via Nernst equation (equation 1.1), which is approx. 1V for 650⁰C.

$$E = -(RT / 4F) \ln(P'_{O_2} / P''_{O_2}) \quad (1.1)$$

where E is the cell EMF or OCV, F is the Faraday's constant, P'_{O₂} the partial pressure of oxygen at the cathode, and P''_{O₂} is the partial pressure of oxygen at the anode. As the temperature increases, OCV value decreases. The reason of this is believed to be a

possible leakage of minor amount of gas through micropores in the CGO film, some fuel leakage to the air side may have taken place, which would lower the oxygen partial pressure and lead to a decrease in OCV. Because CGO electrolyte has some electronic conductivity at low oxygen partial pressures [38], under open circuit conditions there may be some short-circuiting.

The decreasing trend in the area specific resistance (ASR) and the increase in the maximum obtained power with increasing temperature can be seen from Table 1.2. The thickness of the electrolyte material also plays important role in the cell performance. The changes of ASR and maximum obtained power according to the electrolyte thickness are shown in Table 1.3.

Table 1.3. Comparison of anode supported CGO film cell and self supported cell at 650⁰C under H₂/CO₂ fuel [52].

SOFC Electrolyte Thickness	Area Specific Resistance ($\Omega\cdot\text{cm}^2$)	Maximum Power (mW/cm^2)
Dense Film (5 –10 μm)	0.9	146
Self Supported ($\sim 300\mu\text{m}$)	4.1	45

1.1.1.5.3.4.3. LSGM

Strontium and magnesium-doped lanthanum gallate (LSGM, e.g. La_{1-x}Sr_xGa_{1-y}Mg_yO_{3-(x+y)/2}) is a perovskite-type oxide and one of the most promising electrolyte materials for IT-SOFC applications. Its ionic conductivity values are much higher than the one of YSZ electrolyte, and comparable to that of ceria-based electrolytes for high and intermediate temperatures. Ionic conductivities of YSZ, LSGM, and CGO electrolytes for temperatures 600⁰C, 800⁰C, and 1000⁰C are tabulated in Table 1.4.

Table 1.4. Ionic conductivities of YSZ, LSGM, and CGO for 600⁰C, 800⁰C, and 1000⁰C.

Electrolyte	600 ⁰ C	800 ⁰ C	1000 ⁰ C
YSZ	0.003 S/cm [38]	0.03 S/cm [38]	0.1 S/cm [38]
LSGM	0.02 S/cm [101]	0.12 - 0.17 S/cm [38]	0.25 S/cm [101]
CGO	0.025 S/cm [38]	0.1 S/cm [101]	0.25 S/cm [38]

Moreover, wide ionic domain of LSGM suppresses the electrical conductivity problem associated with ceria under reducing conditions. Due to these excellent conductivity properties, phase purity, chemical stability with other cell components, and mechanical stability are under investigation.

Perovskites, based on lanthanum gallate are very sensitive to small changes in the stoichiometry and may lead to the formation of undesired phases [87]. The highest conductivity of LSGM at 800⁰C (0.17 S/cm) has been reported for the composition $\text{La}_{0.8}\text{Sr}_{0.2}\text{Ga}_{0.83}\text{Mg}_{0.17}\text{O}_{3-\delta}$ [87]. Because stoichiometry of the LSGM should be maintained, vaporization of gallium in the form of Ga_2O from LSGM in reducing atmospheres [88] is an important issue, which causes a change in the LSGM composition over time during service. The main factors affecting gallium vaporization from a LSGM electrolyte are temperature, oxygen partial pressure, and the amount of strontium in the composition of LSGM electrolyte. With increasing annealing (or operation) temperature, the amount of gallium depletion increases. At temperatures lower than 800⁰C, gallium loss was not observed. Gallium depletion increases with decreasing partial oxygen pressure [88]. The compositional dependence of gallium loss is mainly due to strontium content in the composition. An increase in the strontium content results in an increase in the amount of gallium loss [88]. In Figure 1.11, a typical depletion curve of a Ga component from a LSGM surface. The area over the depletion curve is converted into a rectangle, which gives the same area. In the figure, C_{Ga} and $C_{\text{Ga_bulk}}$ mean the concentration of gallium at each depth and the concentration of gallium in the bulk, respectively.

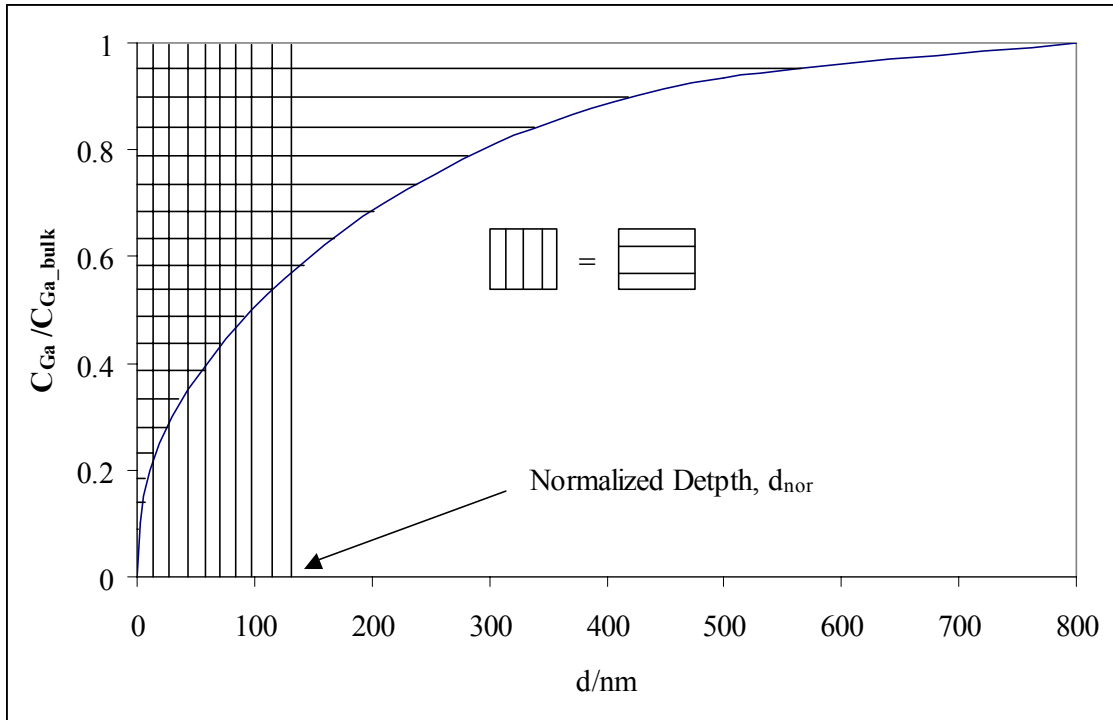


Figure 1.11. A typical gallium depletion curve from the LSGM surface (Horizontal and vertical shaded areas are supposed to be equal).

The normalized depth (d_{nor}) values for gallium for different strontium and magnesium additions are shown in Table 1.5.

Table 1.5. Compositional dependence of d_{nor} . The samples are treated at 900^oC for 10 h in a flowing gas of H₂ – 1.2%H₂O [88].

Composition	d_{nor} (nm)
La _{0.8} Sr _{0.2} Ga _{0.8} Mg _{0.2} O _{2.80}	87.6
La _{0.9} Sr _{0.1} Ga _{0.8} Mg _{0.2} O _{2.85}	56.3
La _{0.9} Sr _{0.1} GaO _{2.95}	330.5
La _{0.8} Ga _{0.9} Mg _{0.1} O _{2.95}	27.7
La _{0.8} Ga _{0.8} Mg _{0.2} O _{2.90}	19.7
LaGaO ₃	19.4

Electronic conductivity of lanthanum gallate electrolyte strongly depends on the type of dopant ion and LSGM has negligible electronic in SOFC operating conditions. Co-doping with transition metals can increase electronic conductivity of LSGM [38]. Only a limited number and range metal concentrations (e.g. La_{0.8}Sr_{0.2}Ga_{0.8}Mg_{0.115}Co_{0.085}O_{3-δ}) do not affect the electronic conductivity, as well as

activation energy, at lower temperatures [38]. Neodymium, samarium, gadolinium, yttrium, and ytterbium dopings on La-site of LSGM are investigated in terms of ionic and electronic conductivity. $(\text{La}_{0.9}\text{Nd}_{0.1})_{0.8}\text{Sr}_{0.2}\text{Ga}_{0.8}\text{Mg}_{0.2}\text{O}_{3-\delta}$ exhibited almost pure oxide ionic conductivity over the oxygen partial pressure from 1 to 10^{-21} atm, and the electrical conductivity was negligibly small [89].

Second phases forming during synthesis and/or sintering processes are La_2O_3 , $\text{La}(\text{OH})_3$, LaSrGaO_4 , $\text{LaSrGa}_3\text{O}_7$, SrGaO_3 , $\text{Sr}_3\text{Ga}_2\text{O}_6$, La_4SrO_7 [87,88,90]. It is reported that LaSrGaO_4 is the responsible phase for gallium evaporation [88,90]. Yamaji et al. connected the formation of LaSrGaO_4 phase to excess gallium evaporation [91].

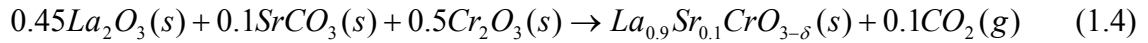
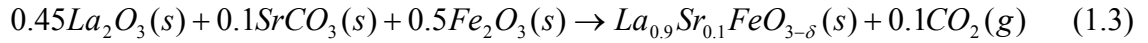
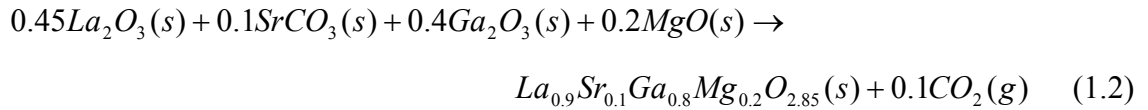
1.1.1.5.4. Synthesis of SOFC Components

As indicated in the previous sections, all the important SOFC components are multi-cation oxide materials. Synthesis of these materials is one of the most important step in the realization of SOFC production and service. Any decrease in the cost of the oxide synthesis will result in a decrease of the overall SOFC production cost.

Each oxide material in SOFC construction is chemically designed to exhibit the best performance in SOFC operating conditions. Every small discrepancy in the material composition results in a poorer performance of SOFC. For example, the best ionic conductivity values can be achieved with $\text{La}_{0.9}\text{Sr}_{0.1}\text{Ga}_{0.83}\text{Mg}_{0.17}\text{O}_{3-\delta}$ composition of Sr and Mg-doped LaGaO_3 electrolyte material [37]. Small deviations from that composition mostly result in decrease in the ionic conductivity. Therefore, to be able to operate SOFC at desired efficiency, pure and single-phase synthesis of SOFC components in desired compositions is extremely important. Several techniques for multi-cation oxide material synthesis are described in the following sections.

1.1.1.5.4.1. Solid-State Reaction Technique

Solid-state reaction technique is the most common synthesis method in synthesizing SOFC materials [37,91,101]. Some examples of reactions for desired compositions of SOFC components are shown below.



In this powder synthesis method, constituent oxides and/or carbonates, i.e. reactants in the reactions 1.2, 1.3, and 1.4, are mixed in the desired stoichiometry. After a long grinding operation, which results in a homogeneously mixed powder, calcination of the powder is conducted. Since desired phase formation in this technique is based on solid-state diffusion of atoms, high calcination temperatures and long holding times at that temperature are required to obtain single-phase oxide material. Thus, laborious and time consuming pre-calcination powder preparation, high calcination temperatures and long holding times at that temperatures increase the cost of the powder synthesis. Moreover, in case of improper powder preparation, formation of undesired phases may appear in the final powder.

1.1.1.5.4.2. Co-precipitation Technique

Co-precipitation method is another technique that is used to synthesize SOFC components. This method involves “co-precipitation” of a precursor salt, and then thermal decomposition (or called calcination) to desired oxide composition. The advantage of co-precipitation technique in synthesis of powders is mixing at a molecular level, unlike the solid-state reaction technique.

A solution of metal salts, i.e. nitrates, sulfates, are mixed with a precipitation agent such as oxalic, citric, or other organic acid or ammonium hydroxide. The reason of using these precipitation agents is the low solubility of metal oxalates, citrates, or hydroxides. During precipitation, there are generally two possibilities; i) precipitation of a mixed metal precursor crystal with a specific stoichiometric ratio of the metals, or ii) segregative precipitation of individual particles, such as precipitation of different metal

oxalates that are colloiddally unstable and hetero-coagulate into a mixed aggregate particle.

In order to achieve precipitation, decrease in the solubility limit of the desired phase has to be satisfied. Generally, temperature, pressure, pH of the solution, and chemical precipitant are the factors affecting the solubility of the phase to be precipitate.

During precipitation, the pH of the solution may vary markedly and the powder composition and homogeneity may be affected. Also the powders must be separated from their supernatants, dried, and calcined to the desired composition. This drying and calcination often lead to aggregates. Special precautions such as calcination in very dry atmospheres must be used to prevent formation of aggregates [92]. Moreover, extremely rapid precipitation may result in trapping of foreign ions in the particles.

Considering all the problems associated with solid-state reaction and co-precipitation techniques, new powder synthesis techniques are required to be able to synthesize homogeneous, pure, and single-phase mixed oxides in the desired composition.

1.1.1.5.4.3. Organic Precursor Technique

Organic precursor technique is the method that more recently started to be widely used in mixed oxide powder synthesis in the literature [77,93,98,103]. In this method synthesis stages are i) dissolution of stoichiometric amounts of cation salts in a proper solvent, ii) dissolution of desired amount of organic carrier material(s), where molecular ratio of cation to organic carrier material is important, iii) proper mixing the constituents in the solution and solvent evaporation, and iv) calcination of the formed pre-ceramic powder to obtain the oxide powder in desired composition.

The predicted mechanism in organic precursor method for achieving a stable precursor is chelating/complexing the metal cations by the functional groups of the organic carrier materials in the solution [94]. This chelating/complexing action is believed to be due to columbic attraction forces between the carboxylic and/or hydroxyl groups of the carrier materials and metal cations. The molecular geometry of the functional groups is also believed to play an important role in the chelating/complexing action. As a result of this action, metal cations are believed to have a perfect-homogeneous distribution in the solution and in the pre-ceramic precursor after solvent

removal. This cation distribution results in an amorphous powder at room temperature. In the calcination stage, crystallization of the desired composition takes place. Due to the homogeneity in molecular level, lower diffusion distances for the solid-state reaction process is required to obtain desired crystal phase. This in turn may result in much lower calcination temperatures compared to the solid-state reaction technique. Moreover, combustion of the organic materials results local temperature increments, which helps diffusion process and final crystallization.

Different types of the organic carrier materials can be used in oxide synthesis, but one of the most successful techniques for single phase mixed oxide powders is Pechini process [95]. Pechini process operates through polyesterification between hydrocarboxylic acids such as citric acid, and polyhydroxy alcohols such as ethylene glycol [95]. According to the ester reaction shown below, carboxyl end of citric acid and hydroxyl end of ethylene glycol binds and a water molecule is released. The acid acts as a chelating agent which chemically binds the cations that are dissolved in the solution.

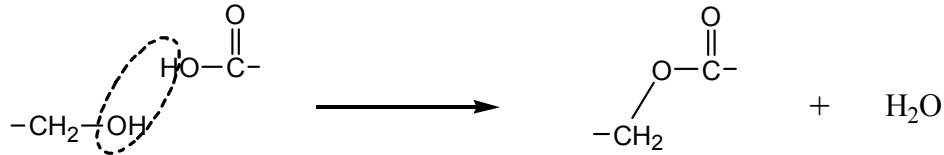


Figure 1.12. Ester reaction.

The polymerization is based on the polyesterification between the metal-chelate complexes and polyhydroxyl alcohols. By polyesterification process, randomly coiled macromolecular chains are obtained. These chains may chelate cations uniformly and form very stable complexes. Moreover, due to chelating action and high viscosity polymeric network, cation segregation is hindered. The resultant ceramic powders possess better chemical homogeneity and smaller particle size. There are also organic precursor methods with different organic carrier materials, such as citrate synthesis, polymeric precursor synthesis, and urea method however there are few studies on the chemical synthesis of SOFC components via different carrier materials [96,104].

It is believed that organic precursor synthesis method can eliminate the problems associated with other synthesis techniques, such as high calcination temperatures,

undesired phase formation in the final powders, and laborious powder preparation stages. Elimination of these hurdles will result in a considerable decrease in the cost of material synthesis, and therefore SOFC production, as well as in an increase in the performance of SOFCs. Obviously, these problems are not SOFC-specific problems. This method can solve similar problems associated with other types of mixed oxides.

It is believed that synthesis of SOFC components can be performed by using different organic carrier materials at relatively low calcination temperatures. As mentioned before, LSGM is one of the rare electrolyte candidate materials for SOFCs. Pure and single-phase synthesis of LSGM powders is extremely important for the performance of SOFCs. For this reason, in this study LSGM synthesis was conducted via the organic precursor method. Also the effects of different carrier materials on phase purity and calcination temperature were investigated.

Additionally, $\text{La}_{0.9}\text{Sr}_{0.1}\text{Fe}_{0.8}\text{Mg}_{0.2}\text{O}_{2.85}$ (LSFM) and $\text{La}_{0.9}\text{Sr}_{0.1}\text{Cr}_{0.8}\text{Mg}_{0.2}\text{O}_{2.85}$ (LSCM) powders were synthesized with same synthesis route and organic carrier materials. In synthesis of LSFM and LSCM powders, the stoichiometry used in LSGM synthesis was kept to investigate the effects of different cations (Fe^{3+} or Cr^{3+} in place of Ga^{3+}), simultaneously. Selection criteria of iron and chromium as the cations replacing gallium cations are to synthesize mixed oxides, which are similar to candidates of SOFC interconnect material ($\text{La}_{0.9}\text{Sr}_{0.1}\text{CrO}_{3-\delta}$) [97] and cathode material ($\text{La}_{0.8}\text{Sr}_{0.2}\text{Fe}_{0.8}\text{Co}_{0.2}\text{O}_{3-\delta}$) [98].

CHAPTER 2

EXPERIMENT

The aim of this study is to chemically synthesize multi-cation oxide powders for solid oxide fuel cell electrolytes, with a desired stoichiometry at relatively low temperatures ($< 1200^{\circ}\text{C}$) compared to traditional solid-state reaction technique. Determined by the desired stoichiometry of the final powder, the required amounts of constituents are dissolved in aqueous solution. The functional groups of the organic carrier materials were believed to chelate/complex the cations in the solution, and circumvent the formation of undesired oxide phases. A calcination removed solvents and organic carrier materials, and the formation of the final oxide powders in desired stoichiometry. Starting materials, synthesis procedure and technique, and characterization procedure are described in the following sections.

2.1. Materials

2.1.1. Cation Sources

Cation sources were nitrate and chloride salts selected for their high solubility in cold water. Therefore, lanthanum nitrate hexahydrate ($\text{La}(\text{NO}_3)_3 \cdot 6\text{H}_2\text{O}$, $>99\%$, Sigma Aldrich Chemie GmbH, Taufkirchen, Germany) and lanthanum chloride heptahydrate ($\text{LaCl}_3 \cdot 7\text{H}_2\text{O}$, $>99\%$, Sigma Aldrich Chemie GmbH, Taufkirchen, Germany) were used as the lanthanum sources. Gallium sulfate ($\text{Ga}_2(\text{SO}_4)_3$, 99.999% , Sigma Aldrich Chemie GmbH, Taufkirchen, Germany) and gallium nitrate nanohydrate ($\text{Ga}(\text{NO}_3)_3 \cdot 9\text{H}_2\text{O}$,

99.9%, ChemPur Feinchemikalien und Forschungsbedarf GmbH, Karlsruhe, Germany) served as gallium sources. Strontium nitrate ($\text{Sr}(\text{NO}_3)_2$, >99%, Sigma Aldrich Chemie GmbH, Taufkirchen, Germany), magnesium nitrate hexahydrate ($\text{Mg}(\text{NO}_3)_2 \cdot 6\text{H}_2\text{O}$, >99%, Merck KgaA, Darmstadt, Germany), iron nitrate nanohydrate ($\text{Fe}(\text{NO}_3)_3 \cdot 9\text{H}_2\text{O}$, >99%, Merck KgaA, Darmstadt, Germany), chromium nitrate nanohydrate ($\text{Cr}(\text{NO}_3)_3 \cdot 9\text{H}_2\text{O}$, >99%, Merck KgaA, Darmstadt, Germany) were the sources for strontium, magnesium, iron, and chromium, respectively. Gallium sulfate is reported in the CRC handbook [105] as easily soluble in hot and cold water. However, these gallium sulfate powders dissolved in neither cold, nor in hot water (the phase purity was examined and confirmed by x-ray diffraction).

2.1.2. Precursor Materials and Solvents

Polyvinyl alcohol, PVA ($n \cdot \text{C}_2\text{H}_4\text{O}$, MW = 72000, >98%, Merck KgaA, Darmstadt, Germany), citric acid ($\text{C}_6\text{H}_8\text{O}_7$, >99.5%, Sigma Aldrich Chemie GmbH, Taufkirchen, Germany), ethylenediaminetetraacetic acid, EDTA ($\text{C}_{10}\text{H}_{16}\text{N}_2\text{O}_8$, 98%, Sigma Aldrich Chemie GmbH, Taufkirchen, Germany), tartaric acid ($\text{C}_4\text{H}_6\text{O}_2$, 99.7%, Sigma Aldrich Chemie GmbH, Taufkirchen, Germany) and ethylene glycol, EG ($\text{C}_2\text{H}_6\text{O}_2$, 99.5%, Carlo Erba Reagenti, Mendetison Group) were the organic/polymeric materials used as “carriers” for the cations.

Distilled water, citric acid, ammonia (NH_3 , 25% solution, Merck KgaA, Darmstadt, Germany), and nitric acid (HNO_3 , 65% solution, Sigma Aldrich Chemie GmbH, Taufkirchen, Germany) were utilized as solvents in the experiments where indicated.

Various organic molecules were selected for their chelating/complexing ability to serve as organic/polymeric carriers in the synthesis of mixed cation powders. These organic carriers are polyvinyl alcohol (PVA), citric acid (CA), ethylene glycol (EG), tartaric acid (TA), and ethylene diaminetetraacetic acid (EDTA).

2.2. Powder Synthesis

Chemical synthesis was investigated for three different four-cation oxide materials, $\text{La}_{0.9}\text{Sr}_{0.1}\text{Ga}_{0.8}\text{Mg}_{0.2}\text{O}_{2.85}$ (LSGM), $\text{La}_{0.9}\text{Sr}_{0.1}\text{Cr}_{0.8}\text{Mg}_{0.2}\text{O}_{2.85}$ (LSCM), and $\text{La}_{0.9}\text{Sr}_{0.1}\text{Fe}_{0.8}\text{Mg}_{0.2}\text{O}_{2.85}$ (LSFM). The aim was to produce these mixed-oxides as fine powders of a single phase.

For the synthesis of LSGM, LSFM, and LSCM powders, desired amounts of cation salts were measured and dissolved in distilled water to obtain exact stoichiometry in the solutions. In the organic precursor route with organic/polymeric carrier materials, the amounts of carrier materials were determined to obtain 1:1, 1:2, or 2:1 cation to organic molecule ratio in the solution. Thus, for example, in 1:2 cation to citric acid case for one mole of total cation, two moles citric acid molecules were added to the solution.

2.2.1. LSGM Synthesis

For the synthesis of LSGM, two different synthesis concepts were applied. The first uses organic carriers to contain the cations mixed on the molecular level in the desired proportions. Nitrate salts of each constituent cation were selected as the cation source. Polyvinyl alcohol (PVA, Steric entrapment method [106]), citric acid (CA), tartaric acid (TA), ethylene diaminetetraacetic acid (EDTA), Pechini precursors (with 60% citric acid – 40% and ethylene glycol, or 90% citric acid – 10% ethylene glycol mixtures) were selected as the organic carrier materials in solution.

For each experiment, the calculated amounts of nitrates of the cations and the required amount of organic carrier material for the selected cation to organic carrier molecule ratio were dissolved in distilled water. In the synthesis of LSGM with EDTA as the carrier material, 25% ammonia was added to the solution to dissolve EDTA, since EDTA does not dissolve in distilled water. The amount of ammonia was adjusted to approx. 25 wt% of the amount of the distilled water.

The second production route consisted of three sets of experiments. In this route the main difference was the absence of organic carrier materials in the solutions and/or usage of different starting materials. Also, selected cation sources were substituted for nitrate salts. In the first set, nitrate salts of each constituent cation were chosen as the cation source and dissolved in distilled water. Second set of synthesis efforts is composed of two parts. In the first part, gallium sulfate was used as the gallium source.

Nitrates of lanthanum, strontium, magnesium, and sulfate of gallium were added into distilled water. Citric acid had to be added to the solution to dissolve gallium sulfate, also served as a complexing agent for cations. The amount of citric acid was adjusted such that there will be one citric acid molecule for each cation in the solution. In the second part, nitrates of lanthanum, strontium, magnesium, and sulfate of gallium were added into distilled water. To dissolve gallium sulfate, again citric acid was added to the solution. However, this time the amount of citric acid was selected such that there will be one citric acid molecule for four cations in the solution. In the third set, lanthanum chloride was used as the lanthanum source. Nitrates of strontium, gallium, and magnesium were dissolved in distilled water.

Solutions were mixed with a magnetic stirrer and heated up to 300⁰C to evaporate the solvents and to obtain a crisp powder. When lanthanum chloride was used, it was mixed with the crisp precursor powder (containing desired proportions of strontium, gallium, and magnesium), and the mixture was ground to obtain homogeneous distribution.

Organo-metallic precursors were calcined in pure alumina crucibles up to 700⁰C, 800⁰C, 900⁰C, 1000⁰C, 1050⁰C, 1100⁰C, 1150⁰C, and 1200⁰C in a box furnace with 10⁰C/min heating rate. After reaching the final temperature the furnace was turned off immediately and the powders were allowed to cool down in the furnace.

2.2.2. LSFM and LSCM Synthesis

In synthesis of LSFM and LSCM with carrier materials, PVA, CA, TA, EDTA, and Pechini precursor (with 60% citric acid – 40% and ethylene glycol mixture) were selected as the polymeric/organic carrier materials. For each experiment, calculated amounts of nitrates of the cations, and required amount of organic carrier material for the selected cation to organic carrier molecule ratio were dissolved in distilled water. In synthesis of LSFM and LSCM without a carrier material, nitrate salts of each constituent cation were selected as the cation source and dissolved in distilled water.

Organo-metallic precursors were again calcined in pure alumina crucibles up to 500⁰C, 550⁰C, 600⁰C, 650⁰C, 700⁰C, 750⁰C, 800⁰C, and 850⁰C in a box furnace with 10⁰C/min heating rate.

2.3. Characterization

2.3.1. Thermal Analyses

The thermal decomposition profiles of the pre-ceramic precursor and the conversion to the multi-cation ceramics, as well as the thermal behavior of bare precursor materials were investigated using a simultaneous differential thermal and thermo gravimetric analysis set-up (Netzsch STA 449C Jupiter, Selb, Germany) up to 1200⁰C in air and nitrogen atmosphere in pure alumina crucibles. The analyses were run with the same heating rates (10⁰C/min) as the calcination of pre-ceramic precursors.

2.3.2. X-Ray Diffraction

Crystal structure and phase distribution of the powders at room temperature were studied with an x-ray powder diffractometer (Bruker AXS-D8, Karlsruhe, Germany). The measurements were performed in the 2 θ range of 10^o - 90^o at 40 kV and 40 mA, using Cu-K α radiation. In all measurements, the step size was 0.03^o, and data collection period was 2 seconds in each step. K α ₂ peaks are suppressed in the x-ray diffraction measurements.

In x-ray diffraction plots, the percentages of each phase are calculated by taking the ratio of the height in the intensity axis of the main peak (100% peak) of each phase, to the sum of the height of the main peaks of all phases. The amount of each phase at each temperature is approximated as the height of the main peak at the intensity axis and given in terms of x-ray photon counts. Prior to the peak-height measurements, background subtraction is performed.

For phase identification, the experimental spectra were compared to the characteristic x-ray card file in the JCPDS database. For phases that are synthesized in this work for the first time, the experimental spectra were compared to the JCPDS file for the compound from which the new mixed cation oxide is derived, i.e. the LSFM x-

ray spectrum was compared to the JCPDS file for LaFeO₃ and La_{0.9}Sr_{0.1}FeO_{2.95}, while the LSCM x-ray spectrum was compared to the JCPDS file for LaCrO₃. The compounds and corresponding JCPDS numbers of the compounds that are used for phase identification in this work, are tabulated in Table 2.1.

Table 2.1. JCPDS numbers of the discussed compounds.

Compound Chemical Formula	JCPDS Number
La _{0.9} Sr _{0.1} Ga _{0.8} Mg _{0.2} O _{2.85}	98-0080
La ₂ O ₃	05-0602
LaSrGa ₃ O ₇	45-0637
LaSrGaO ₄	80-1806
La ₄ Ga ₂ O ₉	37-1433
(LaO) ₂ SO ₄	85-1534
MgGa ₂ O ₄	72-1520
LaOCl	08-0477
LaFeO ₃	37-1493
La _{0.9} Sr _{0.1} FeO ₃	82-1959
La ₂ SrO _x	42-0343
LaCrO ₃	24-1016
LaCrO ₄	89-0448
La ₂ CrO ₆	26-0817
SrCrO ₄	15-0356
SrFeLaO ₄	29-1305

For calculating the lattice parameters of magnesium-substituted La₄Ga₂O₉ phase (or La₄Ga_{2-x}Mg_xO_{9-δ}), 2θ values of the peaks with corresponding plane Miller indices (013), (22 $\bar{1}$), and (023) are used. From Bragg's condition (see equation 4.11 in chapter 4.6.1), 2θ values are converted to interplanar spacings (d) for each peak. In this conversion, wavelength of the x-rays (λ) is taken as 1.5406 Angstrom. Equation 4.10 in section 4.6.1 gives the relation between interplanar spacing (d), Miller indices (hkl), the only non-right angle of the monoclinic unit cell (β), and lattice parameters (a,b,c) for the monoclinic unit cell. It is assumed that the new La₄Ga_{2-x}O_{9-δ} phase has a monoclinic unit cell like La₄Ga₂O₉ phase. In the calculations, β is taken as 108.3⁰, referring to

JCPDS card of $\text{La}_4\text{Ga}_2\text{O}_9$ phase. For each plane, d , h , k , and l values are put into equation and a , b , c values of supposed $\text{La}_4\text{Ga}_{2-x}\text{O}_{9-\delta}$ phase are calculated iteratively. Iteration was done by assuming that the substitution of magnesium addition in gallium sites will result in equal increment in each dimensions of the unit cell. Unit cell volume calculations are conducted by simple volume calculation of monoclinic unit cell with $\beta = 108.3^\circ$.

For calculating the lattice parameters of synthesized LSCM phase, 2θ values of the x-ray diffraction peaks of LaCrO_3 planes [(110), (002), and (112)] are used. Same calculation procedure as in the calculation of so called “Mg-doped $\text{La}_4\text{Ga}_2\text{O}_9$ ” phase is used. Synthesized LSCM phase is assumed to have orthorhombic unit cell, as LaCrO_3 . Thus, orthorhombic unit cell equation (equation 4.12) is used to calculate lattice parameters of LSCM phase. When calculating the lattice parameters, iterations were done by assuming that strontium substitution into lanthanum site, and magnesium substitution into chromium site will result in an equal increment in each unit cell direction.

CHAPTER 3

RESULTS

3.1. LSXM (X = Ga, Fe, and Cr) Synthesis

Three different multi-cation oxide materials $\text{La}_{0.9}\text{Sr}_{0.1}\text{Ga}_{0.8}\text{Mg}_{0.2}\text{O}_{2.85}$ (LSGM), $\text{La}_{0.9}\text{Sr}_{0.1}\text{Fe}_{0.8}\text{Mg}_{0.2}\text{O}_{2.85}$ (LSFM) and $\text{La}_{0.9}\text{Sr}_{0.1}\text{Cr}_{0.8}\text{Mg}_{0.2}\text{O}_{2.85}$ (LSCM) were synthesized by the organic carrier precursor method, which is also sometimes referred to as polymerized complex method [107], depending on the carrier material. Necessary x-ray diffraction and thermal analysis plots are shown. Measured x-ray intensities of the main peak for the phases, and corresponding percentages of the phases for each powder and temperature are tabulated. Since the crystalline phases are forming within an amorphous matrix, it is also informative to consider the “amounts” of each crystal phase when comparing the phases for different temperatures. Thus, the amount of each crystal phase at each temperature is shown in brackets in the same table.

3.1.1. LSGM Synthesis

Synthesis of LSGM ($\text{La}_{0.9}\text{Sr}_{0.1}\text{Ga}_{0.8}\text{Mg}_{0.2}\text{O}_{2.85}$) was attempted through two different routes. In the first synthesis route, different organic carrier materials such as polyvinyl alcohol (PVA), citric acid (CA), tartaric acid (TA), ethylene diaminetetraacetic acid (EDTA), and citric acid – ethylene glycol mixtures (Pechini precursor) were used as the chelating/complexing agents in the solution. In the second route, synthesis of LSGM was performed without precursor materials, and using different starting materials such as nitrate, sulfate, and chloride salts of the necessary cations.

Phase evolution and phase composition of powders synthesized using different routes and under different conditions are investigated by the use of x-ray powder diffraction and thermal analysis techniques.

XRD plots of all powders synthesized using different organic carrier material and the ones synthesized without any organic carrier material for the temperatures 700⁰C, 800⁰C, 900⁰C, 1000⁰C, 1050⁰C, 1100⁰C, 1150⁰C, and 1200⁰C are illustrated in Appendix A, and the percentages and amounts of the x-ray detectable crystalline phases in the system for temperatures 800⁰C, 900⁰C, 1000⁰C, 1050⁰C, 1100⁰C, 1150⁰C, and 1200⁰C are tabulated in Appendix B. Out of this comprehensive list, some x-ray diagrams will be presented throughout the results section where necessary.

3.1.1.1. Synthesis with Different Organic Carriers

In the synthesis of LSGM powders, five different organic carrier molecules as the chelating and/or complexing agents, and nitrate salts of each cation (lanthanum, strontium, gallium, and magnesium) were used. First the results of experiments with different organic carrier materials will be presented.

3.1.1.1.1. PVA

In synthesis of LSGM powders by PVA as the organic carrier material, 1:2 total cation to PVA molecule ratio was used. X-ray diffraction (XRD) spectra of the calcined powders with PVA are illustrated in App. A1. In App. B1, the percentages and amounts of the calcined powders for each temperature were tabulated. LSGM phase first appears in significant amounts around 1050⁰C, and the amount increases with increasing temperature. Below 1050⁰C, the dominant phases are LaSrGa₃O₇, and La₄Ga₂O₉. At each temperature, small concentrations (between 2.2% and 10.1%) of an unknown phase were observed (unknown A), by an x-ray diffraction peak at $2\theta = 33.4^\circ$. Above 1050⁰C, formation of a small amount (2.4%, 73 counts) LaSrGaO₄ was observed. LaSrGaO₄ concentration increased from 2.4% up to 4.1% at 1200⁰C, with increasing temperature. Below 1150⁰C, LaSrGa₃O₇, La₄Ga₂O₉, and the unknown A phases coexisted in the powders. The amount of LaSrGa₃O₇ phase increased up to 1000⁰C.

Above 1000⁰C the amount of LaSrGa₃O₇ decreased and disappeared all together at 1200⁰C. The amounts of La₄Ga₂O₉, and the unknown A phases exhibited a decreasing behavior with minor discrepancies, with increasing temperature from 800⁰C to 1200⁰C. Maximum concentration of LSGM phase (93.7%) in the powder was obtained at 1200⁰C.

3.1.1.1.2. Pechini Precursors

LSGM powder was synthesized by using nitrates of the cations and citric acid – ethylene glycol mixture as the organic carrier material (Pechini process). Two different citric acid – ethylene glycol mixtures were used as the carrier material, 60 wt% citric acid – 40 wt% ethylene glycol, and 90 wt% citric acid – 10 wt% ethylene glycol. Total cation to Pechini precursor molar ratio was 1:1. XRD plots of the calcined powders with 60 wt% CA – 40 wt% ethylene glycol mixture at selected temperatures are shown in App. A2. The percentages and amounts of the phases for each temperature were tabulated in App. B2.

Pechini process is applied to investigate its effect on the synthesis of LSGM powders. Citric acid – ethylene glycol ratio in the mixture is essential for the chain length formed. By changing citric acid - ethylene glycol ratio in the mixture, the effect of chain length on the chelating action for the La³⁺, Sr²⁺, Ga³⁺, and Mg²⁺ ions in the solution is also investigated.

In the LSGM synthesis with 60 wt% citric acid – 40 wt% ethylene glycol as the carrier material, a sharp increase in the amount and percentage of LSGM phase was observed between 900⁰C and 1000⁰C, from 12.8% to 48.7%. A continued increase in temperature produced further increase in the amount of LSGM phase. Maximum concentration of LSGM phase was obtained at 1150⁰C (92.8%), and maximum “amount” of LSGM phase was observed at 1200⁰C (3563 counts). As in the case with PVA based precursors, LaSrGa₃O₇, La₄Ga₂O₉, and the unknown A phases decrease in amount with increasing temperature, and LaSrGaO₄ phase increased in its concentration and amount with increasing temperature. Above 1100⁰C, LaSrGa₃O₇ and La₄Ga₂O₉ phases were absent from x-ray plots.

XRD plots of the calcined powders with 90 wt% CA – 10 wt% ethylene glycol mixture at selected temperatures are shown in App. A3. The percentages and amounts of

the phases for each temperature were tabulated in App. B3. When the LSGM was synthesized with 90 wt% citric acid – 10 wt% ethylene glycol as the carrier material, a sharp increase in the amount of LSGM phase was observed at a lower temperatures, i.e. between 800⁰C and 900⁰C, from 7% to 71.2% (from 84 to 2029 counts). Similar to the behavior in the synthesis of the powders with 60 wt% citric acid – 40 wt% ethylene glycol as the carrier material, a further increase in temperature resulted in a further increase in the LSGM phase amount in the system with an exception between 1150⁰C and 1200⁰C, where the LSGM concentration and amount decreased slightly from 91% (3467 counts) to 87.4% (3323 counts), at 1200⁰C. At 1150⁰C the La₄Ga₂O₉ phase was not detectable by x-ray diffraction.

3.1.1.1.3. CA

In the synthesis of LSGM powders with citric acid, three batches were prepared. In these batches 1:2, 1:1, and 2:1 total cation to CA molecule ratio was used. XRD spectra of the calcined powders for 1:1 case are shown in App. A4, for 2:1 case are shown in App. A5, and for 1:2 case are shown in App. A6. Corresponding percentages and amounts of the phases for each temperature were tabulated in App. B4, B5, and B6, respectively.

At 800⁰C LSGM, LaSrGa₃O₇, LaSrGaO₄, La₄Ga₂O₉, and the unknown A phases were the x-ray detectable phases (similar to the PVA case). LaSrGa₃O₇ and La₄Ga₂O₉ phases were the major phases at this temperature. At 900⁰C, a sharp decrease in the amount of these phases (LaSrGa₃O₇ and La₄Ga₂O₉) was observed. This sharp decrease coincided with a very sharp increase in the concentration of LSGM phase (from 11.1% to 88%). With further increasing temperature, the LSGM phase amount continued to increase with a decrease in the amounts of other phases, except for the LaSrGaO₄ phase. Maximum concentration of LSGM phase achieved was 92.1% at both 1050⁰C (3381 counts) and 1150⁰C (3610 counts). Above 1000⁰C no x-ray detectable LaSrGa₃O₇, or La₄Ga₂O₉ phases were present in the powders.

In order to maximize the amount and concentration of LSGM in the final powder, precursors with different citric acid to cation ratios were prepared. When a precursor with 2:1 cation to citric acid molecule was calcined, x-ray plots are similar to 1:1 ratio case, but the concentrations of the unwanted phases are larger at each

temperature. All of the undesired phases were persistent at all temperatures up to 1200⁰C. Comparison of the 1:1 ratio case for precursors with 2:1 cation/CA, only 85.6% LSGM phase was observed at 900⁰C. Maximum concentration of LSGM phase was obtained at 1200⁰C with 86.4%, which is less than the percentage of LSGM phase at 900⁰C when 1:1 cation/CA was used.

In the 1:2 ratio case, the formation of the LSGM phase was first seen at 800⁰C with 22%, and much larger amounts of undesired phases were observed up to 1100⁰C, compared to 1:1 ratio case. The maximum LSGM phase concentration was observed at 1150⁰C with 93.9%. Again no LaSrGa₃O₇ phase was detected above 1050⁰C, and the La₄Ga₂O₉ phase disappeared above 1100⁰C.

3.1.1.1.4. TA

XRD plots of the calcined powders with TA are illustrated in App. A7, A8, and A9 for the total cation to TA molecule ratios of 1:1, 2:1, and 1:2, respectively. Corresponding percentages and amounts of the phases for each temperature were tabulated in App. B7, B8, and B9, respectively.

The amount of LSGM phase in the system increased with a large step between 1000⁰C and 1050⁰C, from 863 counts (56.6%) to 2097 counts (90.3%). The maximum concentration of LSGM phase was observed at 1150⁰C with 95.7%. Below 1050⁰C, the LaSrGaO₄ phase was not detected by XRD, although it was observed above 1050⁰C. The amount of LaSrGa₃O₇ phase decreased with increasing temperature from 800⁰C to 1100⁰C, and disappeared above 1100⁰C. The amount of La₄Ga₂O₉ phase exhibited first an increase between 800⁰C and 1000⁰C, then a monotonic decrease with increasing temperature. Above 1100⁰C, LaSrGa₃O₇ and La₄Ga₂O₉ phases could not be detected by XRD in this powder. The amount of the unknown A varied randomly with temperature. Its concentration ranged between 2.3% and 7%.

Similar to LSGM powder synthesis with citric acid as the carrier material, the cation to tartaric acid molecule ratio was varied as 2:1 and 1:2. In 2:1 cation to TA ratio case, the variation of the phases and the phase composition in the powders for each temperature were similar to powder calcined from 1:1 ratio case. The amount of LSGM phase in the system increased with a large step between 900⁰C and 1000⁰C from 197 counts (14.7%) to 1873 counts (68.3%). Below 1000⁰C, there were no x-ray detectable

LaSrGaO₄ phase in the system, and the amount of LaSrGaO₄ phase increased with increasing temperature above 1000⁰C. The amount and concentration LaSrGa₃O₇ phase decreased with increasing temperature between 800⁰C and 1050⁰C. The amount of La₄Ga₂O₉ phase showed first an increase between 800⁰C and 900⁰C, then a decrease with increasing temperature. After 1050⁰C, LaSrGa₃O₇ and La₄Ga₂O₉ phases were absent from x-ray spectrum. The amount of the unknown A phase again fluctuated with temperature and the concentration of it ranged between 2.5% and 6.6%.

In the 1:2 cation to TA case, an increase was observed in the concentration of LSGM phase with increasing temperature. A sharp increase in the LSGM phase amount was between 900⁰C and 1000⁰C, from 590 counts (34.8%) to 2082 counts (78.9%). The maximum amount and concentration of LSGM phase was obtained again at 1150⁰C with 3227 counts (95.5%). Below 1050⁰C, there was no x-ray detectable LaSrGaO₄ phase in the powders. Above 1100⁰C, LaSrGa₃O₇ and La₄Ga₂O₉ phases were not detected by x-ray analysis of the powders.

3.1.1.1.5. EDTA

Synthesis of LSGM powder was conducted by using nitrates of the cations and ethylene diaminetetraacetic acid (EDTA) as the organic carrier material. XRD spectra of the powders are shown in App. A10. The concentrations and amounts of each phase are tabulated in App. B10.

The concentration and amount of the LSGM phase increased regularly from 7.7% (103 counts) at 800⁰C, to 68.4% (2275 counts) at 1200⁰C. All of the other phases previously mentioned were present at all temperatures. The amount of LaSrGa₃O₇ and La₄Ga₂O₉ phases exhibited a diminishing behavior with increasing temperature up to 1200⁰C. The concentrations of LaSrGaO₄ and unknown A phases in the final powder varied sporadically with temperature. The ranges were 5% - 6.7% for LaSrGaO₄ and 3.6% - 6.4% for the unknown A phases.

3.1.1.2. The Use of Different Starting Materials

In this set of experiments, it was attempted to produce LSGM powders with different starting materials and without complexing or chelating agents to assess the effectiveness of the organic carrier materials. Three different sets of experiment were conducted. In the first set, nitrate sources of the cations as the starting materials were used and carrier material was omitted. In the second one, sulfate source of gallium, and nitrate sources of lanthanum, strontium, and magnesium were the starting materials. This experiment set was composed of two parts. In the first part, besides cation sources, citric acid was used as the carrier material in 1:1 total cation to citric acid molecule ratio. In the second part, 4:1 total cation to citric acid molecule ratio was applied. In the third set, the chloride source of lanthanum, nitrate sources of strontium, gallium, and magnesium were used as cation sources, without any organic “carrier” material.

3.1.1.2.1. Nitrate Sources

LSGM powders were synthesized by using nitrate sources of all cations without using any complexing or chelating agent to compare the powders with the results of experiments utilizing organic carrier materials. XRD plots and percentage-amount table of the powders are shown in App. C1 and App. D1, respectively. The formation of LSGM phase started at 1000⁰C with 9.3%. Maximum concentration of the LSGM phase was as low as 54.6% at 1200⁰C. Previously mentioned unwanted phases, i.e. LaSrGaO₄, LaSrGa₃O₇, La₄Ga₂O₉, and the unknown A phases were detected in the powders. Generally, at each temperature, the total concentration of these undesired phases was larger than in the LSGM powder synthesized by using an organic carrier material. As a consequence, the amount and concentration of LSGM phase were much smaller in comparison to the LSGM powders synthesized with an organic or polymeric carrier material.

3.1.1.2.2. Nitrate and Sulfate Sources with/without CA as Carrier Material

LSGM was synthesized by using gallium sulfate for the gallium source, and nitrate sources as the lanthanum, strontium, and magnesium sources. Citric acid was used as the carrier material, which acted as the most efficient chelating agent in experiments done with all nitrate sources. XRD spectra are shown in App. C2, and percentages and amounts of the phases are tabulated in App. D2. Gallium sulfate did not dissolve in cold or in hot water despite the claims in materials handbooks [105] for its high solubility in cold and hot water. However, it is easily dissolved in citric acid solution.

The phases formed after calcination were LSGM, $(\text{LaO})_2\text{SO}_4$, $\text{LaSrGa}_3\text{O}_7$, MgGa_2O_4 , unknown A, and yet another unknown phase with an x-ray peak at $2\theta = 34^\circ$ (unknown phase B). At 800°C , two phases were present in the powders; 91.7% $(\text{LaO})_2\text{SO}_4$ phase and 8.3% MgGa_2O_4 phase. At 1050°C , the formation of $\text{LaSrGa}_3\text{O}_7$, LSGM phase, and the unknown B were observed. Their respective concentrations were: 23.4% $\text{LaSrGa}_3\text{O}_7$, 3.6% LSGM, and 2% unknown B phases. With increasing temperature, the concentrations of $(\text{LaO})_2\text{SO}_4$ and MgGa_2O_4 phases decreased simultaneously. Above 1100°C , the percentages of $(\text{LaO})_2\text{SO}_4$ and MgGa_2O_4 phases decreased further, where the amounts of LSGM, $\text{LaSrGa}_3\text{O}_7$, and the unknown B phases increased. Between 1100°C and 1150°C , a sharp increase in the concentration LSGM from 4.8% to 85.1%, formation of an unknown A phase, and a simultaneous decrease in the amounts of $(\text{LaO})_2\text{SO}_4$, $\text{LaSrGa}_3\text{O}_7$, MgGa_2O_4 , and unknown B phases were observed.

LSGM synthesis was attempted by using sulfate salt of gallium, and nitrate salts of lanthanum, strontium, and magnesium. This time, amount of citric acid used was selected as $\frac{1}{4}$ of the amount of citric acid used in the previous experiment. The reason of using deficient CA amount is to eliminate chelating action of CA as much as possible. The desired property of CA in this experiment is only to dissolve gallium sulfate in the solution. XRD plots and corresponding phase concentration-amount table are shown in App. C3 and App. D3, respectively. At 800°C two phases were present in the system; 89.2% $(\text{LaO})_2\text{SO}_4$ phase, and 10.8% MgGa_2O_4 phase. Continuous increase in the amount of LSGM phase, and decrease in the amount of $(\text{LaO})_2\text{SO}_4$ phase were observed above 1100°C . Initial formation of $\text{LaSrGa}_3\text{O}_7$ phase was observed at 1100°C with a

percentage of 31.4%. Amount of MgGa_2O_4 phase increased up to 1100°C , and then decreased up to 1200°C .

To prove the stability of $(\text{LaO})_2\text{SO}_4$ phase over LSGM phase up to 1150°C , synthesis of $(\text{LaO})_2\text{SO}_4$ was attempted by an additional experiment on the reaction of gallium sulfate and lanthanum nitrate. XRD plots of the resulting powders for 150°C , 400°C , and 800°C are shown in Figure 3.1. An STA plot of the sample previously heated up to 800°C is shown in Figure 3.2

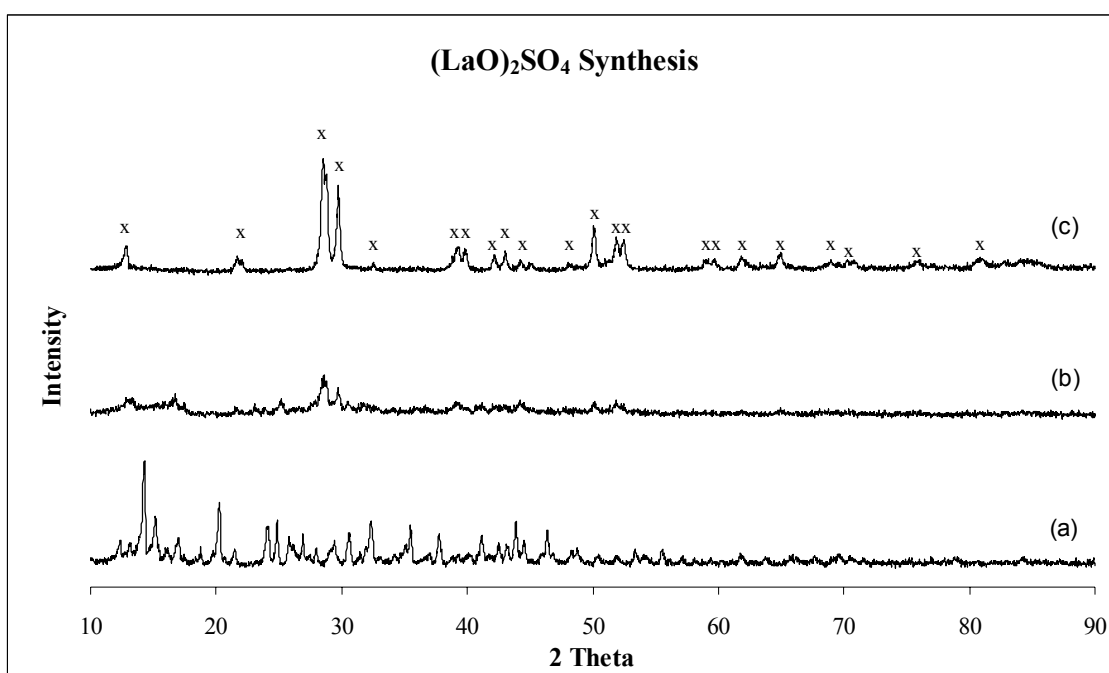


Figure 3.1. XRD Spectra of synthesized $(\text{LaO})_2\text{SO}_4$ powder, calcined at a) 150°C , b) 400°C , and c) 800°C . X-ray diffraction peaks of $(\text{LaO})_2\text{SO}_4$ phase are shown as “x”.

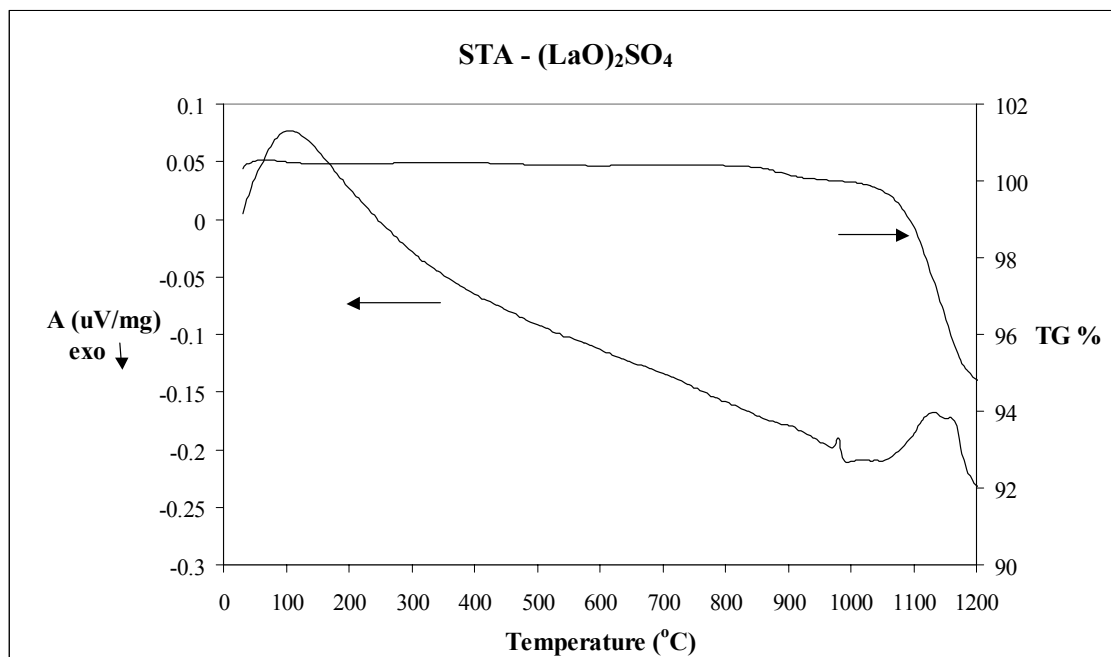


Figure 3.2. STA plot of the gallium sulfate-lanthanum nitrate-nitric acid solution heated up to 1200⁰C (Previously heated up to 800⁰C).

3.1.1.2.3. Nitrate and Chloride Sources

In this set of experiments, lanthanum chloride was substituted for lanthanum nitrate as the starting material. Nitrate salts of strontium, gallium, and magnesium were still used, without the addition of any organic carrier material. XRD plots of the calcined powders are shown in App. C4. The percentages and amounts of the phases for each calcination temperature are tabulated in App. D4.

The LSGM phase started to form at 1000⁰C with 3.7%, and the concentration in the powder increased with temperature. A sharp increase in LSGM phase content was observed between 1050⁰C and 1100⁰C (from 12.4% to 71.8%). A maximum amount and concentration of LSGM phase was obtained at 1150⁰C with 3148 counts and 82.2%.

The concentration of LaSrGa₃O₇ phase increased up to 1050⁰C, and above 1050⁰C it started to decrease. Sharp drop in the concentration of LaSrGa₃O₇ phase was observed between 1050⁰C and 1100⁰C from 33.9% down to 5%. At 800⁰C, 100% LaOCl phase appeared and further on decreased monotonously with increasing temperature. Above 1150⁰C, LaOCl phase was not detected by x-ray analysis. There are two unknown phases in the system (unknown A and C, unknown C with peak at 2θ =

27.43⁰). These unknown phases were not present in the system up to 1150⁰C, and they increased in quantity with increasing temperature.

3.1.2. LSFM Synthesis

Synthesis of LSFM ($\text{La}_{0.9}\text{Sr}_{0.1}\text{Fe}_{0.8}\text{Mg}_{0.2}\text{O}_{2.85}$) was attempted by six different experiments. In the first five experiments, different organic/polymeric carrier materials, i.e. polyvinyl alcohol (PVA), citric acid (CA), tartaric acid (TA), ethylene diaminetetraacetic acid (EDTA), and Pechini precursor (60 wt% citric acid – 40 wt% ethylene glycol mixture), were used as the chelating/complexing agents. Nitrate salts were used as the cation sources. Sixth experiment was conducted with nitrate salts as cation sources, without using any organic/polymeric carrier material. Selection criteria of these carrier materials are due to same reasons as in the synthesis of LSGM powders.

Phase evolution and phase composition of powders synthesized under different conditions are followed by x-ray powder diffraction and thermal analysis techniques. XRD plots of all synthesized powders for the temperatures 500⁰C, 550⁰C, 600⁰C, 650⁰C, 700⁰C, 750⁰C, 800⁰C, and 850⁰C are illustrated in Appendix E, and the concentrations and amounts of the x-ray detectable crystalline phases in the system for temperatures 500⁰C, 550⁰C, 600⁰C, 650⁰C, 700⁰C, 750⁰C, 800⁰C, and 850⁰C are tabulated in Appendix F.

3.1.2.1. PVA

XRD plots of synthesized LSFM powders with PVA at temperatures between 500⁰C and 850⁰C are illustrated in App. E1. The concentrations and amounts of the x-ray detectable crystalline phases in the system at temperatures between 500⁰C and 850⁰C are tabulated in App. F1. Between 500⁰C and 700⁰C, the phases present were LSFM and an unknown phase with a peak at around $2\theta = 29.4^{\circ}$ (unknown D). At 700⁰C, formation of crystalline La_2SrO_x phase was observed. After 750⁰C, the powders did not contain any unknown D phase. The percentage of LSFM decreased (from 81.9% to 75.2%), and unknown D increased (from 18.1% to 24.8%) between 500⁰C and 550⁰C. Between 550⁰C and 850⁰, the concentration of LSFM phase increased up to 96.2%, and

the amount of unknown D decreased, until fully consumed at 750⁰C. At 700⁰C, formation of La₂SrO_x phase was observed with 6.5%, and its lowest concentration was 3.8% at 850⁰C.

3.1.2.2. Pechini Precursor

XRD plots of synthesized LSFM powders with Pechini precursor at temperatures between 500⁰C and 850⁰C are illustrated in App. E2. The concentrations and amounts of the x-ray detectable crystalline phases in the system at temperatures between 500⁰C and 850⁰C are tabulated in App. F2. It can be seen from XRD plot that there were no x-ray crystal phases in the powder at 500⁰C. Starting from 550⁰C, crystallization of single-phase LSFM was observed. There were no undesired crystalline phases observed. Maximum amount of LSFM was observed at 850⁰C with 1820 counts.

3.1.2.3. CA

XRD plots of synthesized LSFM powders with CA at temperatures between 500⁰C and 850⁰C are illustrated in App. E3. The concentrations and amounts of the x-ray detectable crystalline phases in the system at temperatures between 500⁰C and 850⁰C are tabulated in App. F3. From the XRD plots, at 500⁰C there was no x-ray crystalline phase in the powders. From 550⁰C to 850⁰C, the only crystalline phase observed was LSFM, with maximum amount of 1901 counts, at 800⁰C. In experiments with CA, no La₂SrO_x, or any other unknown phases were observed.

3.1.2.4. TA

XRD plots of synthesized LSFM powders with TA at temperatures between 500⁰C and 850⁰C are presented in App. E4. The concentrations and amounts of the x-ray detectable crystalline phases in the system at temperatures between 500⁰C and 850⁰C are tabulated in App. F4. There were no x-ray crystal phases in synthesized powders at 500⁰C and 550⁰C. Between 600⁰C and 800⁰C, single-phase LSFM was

observed in the powder. Above 800⁰C, formation of an unknown phase (unknown E) was observed with x-ray diffraction peak at $2\theta = 33.24^{\circ}$. The maximum amount of LSFM phase in the powder was observed at 850⁰C (1283 counts), and maximum concentration was observed at 800⁰C (94.7%).

3.1.2.5. EDTA

XRD plots of synthesized LSFM powders with EDTA at temperatures between 500⁰C and 850⁰C are shown in App. E5. The concentrations and amounts of the x-ray detectable crystalline phases in the system at temperatures between 500⁰C and 850⁰C are tabulated in App. F5. According to the XRD plot, there were no x-ray crystal phases in the powder at 500⁰C. Formation of LSFM phase was observed at 550⁰C without any other x-ray crystalline phase. At 700⁰C formation of La₂SrO_x phase (3%) was observed and this phase was present in the powders until 850⁰C with 5%.

3.1.2.6. Without Carrier Material

XRD plots of synthesized LSFM powders without any organic precursor at temperatures between 500⁰C and 850⁰C are illustrated in App. E6. The amounts of the x-ray detectable crystalline phases in the system at temperatures between 500⁰C and 850⁰C are tabulated in App. F6. In the synthesis of LSFM without precursor, undesired La₂SrO_x and La₂O₃ phases were observed. The amount of LSFM phase increased from 500⁰C to 850⁰C. At 500⁰C the present phases were LSFM (17.8%), and La₂SrO_x (82.2%). Between 550⁰C and 600⁰C, the percentage of La₂SrO_x phase decreased from 77.2% to 14.5%, and formation of La₂O₃ phase (from 0% to 66.5%) were observed. The amount of LSFM phase remained almost constant. Between 600⁰C and 700⁰C, increase in the percentages of LSGM (from 19% to 32%) and La₂SrO_x (from 14.5% to 57.6%) phases, and decrease in La₂O₃ (from 66.5% to 10.4%) phase were observed. Between 700⁰C and 800⁰C, decrease in the percentages of La₂SrO_x phase (from 57.6% to 11.2%), and increase in La₂O₃ phase (from 10.4% to 59.2%) were observed. After 800⁰C, increase in the percentage of LSFM (from 29.6% to 61.2%) and La₂SrO_x (from 11.2% to 34.4%) phases, and decrease in the percentage of La₂O₃ phase were observed.

3.1.3. LSCM Synthesis

Synthesis of LSCM ($\text{La}_{0.9}\text{Sr}_{0.1}\text{Cr}_{0.8}\text{Mg}_{0.2}\text{O}_{2.85}$) was attempted by six different experiments. In the first five experiments, different organic carrier materials, i.e. polyvinyl alcohol (PVA), citric acid (CA), tartaric acid (TA), ethylene diaminetetraacetic acid (EDTA), and Pechini precursor (60 wt% citric acid – 40 wt% ethylene glycol mixture), were used as the chelating/complexing agents. Nitrate salts were used as the cation sources. The sixth experiment was conducted with nitrate salts as cation sources, without using any organic carrier material. Selection criteria of these carrier materials followed those used in synthesis of LSGM powders.

Phase evolution and phase composition of powders synthesized under different conditions are followed by x-ray powder diffraction and thermal analysis techniques. XRD plots of all synthesized powders for the temperatures 500°C , 550°C , 600°C , 650°C , 700°C , 750°C , 800°C , and 850°C are illustrated in Appendix G, and the percentages and amounts of the x-ray detectable crystalline phases in the powder at temperatures 500°C , 550°C , 600°C , 650°C , 700°C , 750°C , 800°C , and 850°C are tabulated in Appendix H. In these tables, the percentages of the phases were calculated for each temperature separately.

3.1.3.1. PVA

XRD plots of synthesized LSCM powders with PVA at temperatures between 500°C and 850°C are illustrated in App. G1. The percentages and amounts of the x-ray detectable crystalline phases for each temperature, in the powders calcined at temperatures between 500°C and 850°C are tabulated in App. H1. In calcined powders, La_2CrO_6 phase was the only undesired phase. In the synthesized powders between 500°C and 850°C , LSCM and La_2CrO_6 phases were present. According to table in App. H1, the amounts of LSCM and La_2CrO_6 phases between 500°C and 750°C were almost constant. Between 750°C and 850°C , increase in the amount of LSCM, and decrease in the amount of La_2CrO_6 phase were observed. Maximum LSCM concentration was obtained at 850°C (96.9%).

3.1.3.2. Pechini Precursor

XRD plots of synthesized LSCM powders with Pechini precursor at temperatures between 500⁰C and 850⁰C are illustrated in App. G2. The percentages and amounts of the x-ray detectable crystalline phases for each temperature, in the powders calcined at temperatures between 500⁰C and 850⁰C are tabulated in App. H2. In calcined powders, LaCrO₄, La₂CrO₆, SrCrO₄, and unknown A phases were undesired phases. XRD plots show that, no x-ray crystalline phases exist in the powder at 500⁰C and 550⁰C. The only x-ray crystalline phase at 600⁰C was LaCrO₄. At 650⁰, formation of La₂CrO₆ phase, and increase in the amount of LaCrO₄ phase was observed. The increase in the amounts of these phases continued until 750⁰C, at which point the LSCM phase forms and the amounts of LaCrO₄ and La₂CrO₆ phases decrease. Between 750⁰C and 850⁰C, the amount of LSCM increased and the amounts of LaCrO₄ and La₂CrO₆ phases continuously decreased. Formation of unknown A and SrCrO₄ phases at 800⁰C and a slight decrease between 800⁰C and 850⁰C of these phases were observed.

3.1.3.3. CA

XRD plots of synthesized LSCM powders with CA at temperatures between 500⁰C and 850⁰C are illustrated in App. G3. The percentages and amounts of the x-ray detectable crystalline phases for each temperature, in the powders calcined at temperatures between 500⁰C and 850⁰C are tabulated in App. H3. In calcined powders, LaCrO₄, La₂CrO₆, SrCrO₄, and unknown A phases were undesired phases. From the XRD plots, it can be seen that at 500⁰C there was no x-ray crystalline phase in the powder. From 550⁰C to 700⁰C, the crystalline phase in the powders was LaCrO₄ phase. Between 650⁰C and 700⁰C, formation of LSCM phase was observed (57.4%). Between 700⁰C and 750⁰C, decrease in the amount of LaCrO₄, the formation of La₂CrO₆ and an unknown A, and an increase in the amount of LSCM phase were observed (see App. H3). Between 750⁰C and 800⁰C, the amount of LSCM phase increased, and the amount of La₂CrO₆ decreased. Formation of SrCrO₄ phase was observed at 850⁰C with 3%. Maximum concentration (90.1%) and amount (2337 counts) of LSCM phase was observed at 800⁰C.

3.1.3.4. TA

XRD plots of synthesized LSCM powders with TA at temperatures between 500⁰C and 850⁰C are illustrated in App. G4. The percentages and amounts of the x-ray detectable crystalline phases for each temperature, in the powders calcined at temperatures between 500⁰C and 850⁰C are tabulated in App. H4. From XRD plots it can be seen that there was no x-ray crystalline phases in synthesized powders at 500⁰C. In calcined powders, LaCrO₄, La₂CrO₆, and unknown A phases were the undesired phases. At 550⁰C, the crystalline phase in the powders was LaCrO₄ phase. Between 550⁰C and 600⁰C, formation of LaCrO₄ phase, formation of La₂CrO₆ phase, and further increase in the amounts of these phases between 600⁰C and 650⁰C were observed. Above 700⁰C, the amounts of La₂CrO₆ and LaCrO₄ phases decreased, and the formation of LSCM phase was observed. Between 800⁰C and 850⁰C an increase in the amounts of LaCrO₄, La₂CrO₆ and LSCM phases were observed. Other than these phases, an unknown A phase was formed at 750⁰C (2.9%). The amount of this phase did not change significantly with increasing temperature.

3.1.3.5. EDTA

XRD plots of synthesized LSCM powders with EDTA at temperatures between 500⁰C and 850⁰C are illustrated in App. G5. The percentages and amounts of the x-ray detectable crystalline phases in the powders calcined at temperatures between 500⁰C and 850⁰C are tabulated in App. H5. In calcined powders, LaCrO₄, La₂CrO₆, SrCrO₄, and an unknown A phases were the undesired phases. According to the XRD plots, the only x-ray crystalline phases in the powders at 500⁰C and 550⁰C were LaCrO₄ phase. The amount of LaCrO₄ phase increased up to 650⁰C. Formation of La₂CrO₆ phase at 600⁰C, and increase in the amount between 600⁰C and 650⁰C were observed. Between 650⁰C and 700⁰C, decrease in the amount of LaCrO₄ and La₂CrO₆ phases, and formation of LSCM phase were observed. Above 750⁰C, increase in the amount of LSCM, and decrease in the amounts of LaCrO₄ and La₂CrO₆ phases were observed. At 700⁰C formation of an unknown A phase, and later at 800⁰C formation of SrCrO₄ phase were observed. The concentration of unknown A phase did not change considerably

above 700⁰C. The amount and concentration of SrCrO₄ phase increased between 800⁰C and 850⁰C.

3.1.3.6. Without Carrier Material

XRD plots of synthesized LSCM powders without any organic precursor at temperatures between 500⁰C and 850⁰C are illustrated in App. G6. The percentages and amounts of the x-ray detectable crystalline phases in the powders calcined at temperatures between 500⁰C and 850⁰C are tabulated App. H6. In synthesis of LSCM without precursor, LaCrO₄, La₂CrO₆, and SrCrO₄ phases were observed as the undesired phases. At 500⁰C, the powder was consisted of LaCrO₄ and La₂CrO₆ phases. The amounts of these phases did not changed considerably until 700⁰C. Above 700⁰, formation of LSCM and SrCrO₄ phases, consumption of LaCrO₄ phase, and decrease in the amount of La₂CrO₆ phase were observed.

3.2. Holding Time at Calcination Temperature and Durability Test

Previously synthesized powders were held at 800⁰C for 11 days for durability test. Tested LSGM powders are i) synthesized with CA as the organic carrier material, and calcined at 1000⁰C, ii) synthesized with Pechini precursor (90 wt% citric acid – 10 wt% ethylene glycol mixture) as the organic carrier material, and calcined at 1200⁰C, iii) synthesized with TA as the organic carrier material, and calcined at 1100⁰C, and iv) synthesized without organic carrier material, with nitrate (for strontium, gallium, and magnesium) and chloride (for lanthanum) sources, and calcined at 1200⁰C. X-ray spectra of the tested powders are compared to the x-ray spectra of the original powders in Figures I1-I4 (see Appendix I). The concentrations and amounts of each phase are tabulated in Table 3.1.

Table 3.1. Table of concentrations and amounts of each phase for the LSGM powders calcined at the original calcination temperature, waited 800⁰C for 11 days.

<i>Wait 11 Days(*)</i>	<i>LSGM</i>	<i>LaSrGaO₄</i>	<i>SrLaGa₃O₇</i>	<i>La₄Ga₂O₉</i>	<i>Unknown A</i>	<i>Unknown C</i>
CA-1000	90.4% (3235)	2.3% (82)	1.2% (45)	2.3% (81)	3.8% (135)	Not Detected
CA-1000*	89.3% (2658)	6.4%(189)	Not Detected	Not Detected	4.3% (130)	Not Detected
Pechini(90:10)-1200	87.4% (3323)	7% (265)	1.9% (73)	Not Detected	3.7% (140)	Not Detected
Pechini(90:10)-1200*	88.4% (2894)	6.3% (208)	2.1% (70)	Not Detected	3.2% (104)	Not Detected
TA-1100	94.4% (2306)	2.4% (60)	Not Detected	Not Detected	3.2% (79)	Not Detected
TA-1100*	94% (2370)	2.5% (62)	Not Detected	Not Detected	3.5% (90)	Not Detected
Nitrates-Chlorides-1200	80% (2368)	4.7% (139)	6.4% (189)	Not Detected	3.3% (97)	5.6% (166)
Nitrates-Chllorides-1200*	81.9% (2626)	4.2% (135)	5.8% (185)	Not Detected	3% (96)	5.1% (163)

Several LSGM powders synthesized at different temperatures are held 7 hours at their calcination temperatures. They are LSGM powders, i) with PVA as the organic carrier material and calcined at 1100⁰C, ii) with CA as the organic carrier material and calcined at 900⁰C, iii) with CA as the organic carrier material and calcined at 1000⁰C, and iv) without organic carrier material, with lanthanum chloride as the lanthanum source, and nitrates of the strontium, gallium, and magnesium with calcined at 1100⁰C. X-ray spectra of the 7-hours-calcined powders and x-ray spectra of the original powders are shown in Figures J1-J4 (see Appendix J). The concentrations and amounts of each phase are tabulated in Table 3.2.

Table 3.2. Table of concentrations and amounts of each phase for the LSGM powders calcined at the original calcination temperature, waited at calcination temperature for 7 hours.

<i>Wait 7 Hours(*)</i>	<i>LSGM</i>	<i>LaSrGaO₄</i>	<i>SrLaGa₃O₇</i>	<i>La₄Ga₂O₉</i>	<i>Unknown A</i>	<i>LaOCl</i>
PVA-1100	33.7% (1014)	1.4% (46)	23.8% (717)	34.1% (1027)	7% (209)	-
PVA-1100*	79.8% (2893)	3.5% (126)	5.5% (198)	7.1% (258)	4.1% (150)	-
CA-900	88% (2829)	1.6% (53)	3.1% (98)	3.5% (112)	3.8% (122)	-
CA-900*	89.8% (2713)	5.9% (177)	Not Detected	Not Detected	4.3% (130)	-
CA-1100	88.8% (3261)	8.1% (279)	Not Detected	Not Detected	3.1% (113)	-
CA-1100*	88.8% (3170)	7.3% (261)	Not Detected	Not Detected	3.9% (140)	-
Nitrates-Chloride-1100	71.8% (2962)	Not Detected	5% (207)	Not Detected	Not Detected	23.2% (958)
Nitrates-Chlloride1100*	70.1% (2269)	12.4% (400)	2.4% (78)	Not Detected	Not Detected	15.1% (489)

From Table 3.1 it can be seen that the concentrations of the phases in the powders was not changed considerably, when they hold 11 days at 800⁰C. When the powders synthesized with PVA, are held 7 hours at their calcination temperature (1100⁰C) (see Table 3.2), increase in the concentration of LSGM phase (from 33.7% to 79.8%) was observed. The LSGM concentrations in the other powders were not changed considerably. During holding time at calcination temperature, increase in the LaSrGaO₄ phase was also observed.

CHAPTER 4

DISCUSSION

4.1.Synthesis Method and Material Selection Criteria

In the synthesis of mixed cation oxides, the most common technique is the conventional solid-state reaction method [37,56,75,78,90,93,101,108]. It involves heating stoichiometric mixtures of two or more oxides and/or carbonates of the desired cations to form a mixed-oxide phase product. Unlike gas phase and solution reactions, the limiting factor in solid-state reactions is the sluggishness of the diffusion process. For such a system Fick's first law states that the quantity of diffusing material, which passes per unit time through a unit area normal to the direction of diffusion, is proportional to its concentration gradient. This is given by

$$J = -D \frac{\partial c}{\partial x} , \quad (4.1)$$

where J is the flux of diffusing species ($\#/cm^2\cdot s$), D is diffusion coefficient (cm^2/s), c is the concentration per unit volume, and x is the direction of diffusion. The average distance that a diffusing species will travel, $\langle x \rangle$, is given by

$$\langle x \rangle \approx (2Dt)^{1/2} , \quad (4.2)$$

where t is the time. Rates of reaction are controlled by (i) the contact area between reacting solids, (ii) the rate of diffusion, and (iii) the rate of nucleation of the product phase.

To maximize the contact between reactants, usually starting reagents with a large specific surface area are needed. Thus, stoichiometric amounts of oxides and/or carbonates need to be ground for a long grinding period to obtain a homogeneously mixed and fine powder. Generally organic additives (solvents such as toluene, acetone, or ethanol) are used to enhance the mixing and grinding actions. Pelletization after grinding encourages an intimate contact between crystallites.

According to the equation 4.3, diffusion coefficient (D) has an exponential, Arrhenius type temperature dependence.

$$D = D_0 \exp(-Q/RT) \quad , \quad (4.3)$$

where D_0 is the pre-exponential term, Q is the experimental activation energy, and R is the gas constant. After a thorough mixing step, the powder is calcined generally at high temperatures ($> 1200^\circ\text{C}$) for a long time (several hours to overnight). Since the desired phase formation is based on solid-state diffusion, high calcination temperature is required to increase the diffusion rate (see equation 4.3). A long holding time at the calcination temperature is desired to increase the average diffusion distance of diffusing species (see equation 4.2).

The rate of nucleation of the product phase is a characteristic material property. It may be maximized by using reactants with crystal structures similar to that of the product.

In summary, solid-state reaction technique requires costly and long grinding operation to obtain fine and homogeneous powders. High calcination temperatures and long holding times at calcination temperature are required to promote diffusion process between the reactant species. The high calcination temperature and holding times result in an increase in cost of powder production. Moreover, control of powder characteristics is important in the synthesis of multi-component mixed oxide powders. Solid-state reaction synthesis often leads to a coarse final product with multiple, undesired phases.

The disadvantages of the solid-state reaction technique such as high temperature and long holding period in order to form the desired phase may be reduced or eliminated

by the use of a polymeric precursor method. Since mixing of the constituent cations in aqueous solution occurs at a molecular level, perfect homogenization is expected in solution preparation stage. Homogenization of the constituents for the final powder is also important in terms of the holding time at calcination temperatures. A decrease in the required travel distance of the diffusing species will result in a decrease in the holding time at calcination temperature [109] (see equation 4.2). The high temperature requirement for high diffusion rates (see equation 4.1 and 4.3) in solid-state reaction synthesis is relaxed by short diffusion distances of the species and this may result in a decrease in the calcination temperature for the desired final powder composition.

In this study, syntheses of mixed oxide powders with the use of simpler molecules and less expensive organic carriers (e.g. PVA) than Pechini precursor (citric acid – ethylene glycol mixture) have been investigated [94,110,111]. The hydroxyl groups (OH) of PVA and cations form complexes homogeneously via hydrogen bonding and due to columbic attraction force in the aqueous solution. Gulgun et al. showed that non-chelating functional groups could also be used as the carrier in the system [111]. Also, the weight ratio of the ceramic powders to the organics that are used in the preparation (ceramic-to-polymer yield) is close to or above 2.0, compared to 0.15 for the Pechini process [94]. In addition, combustion of PVA produces heat, so that fine and single-phase powders can be formed at relatively low external heat input, similar to the Pechini process.

In this study, the chelating/complexing ability of the Pechini precursor/PVA were used i) to obtain perfect homogenization at molecular level, ii) to prevent the disproportionation of cations and the consecutive formation of phases other than desired phase, and iii) to promote the formation of the desired phase at temperatures as low as possible, iv) to decrease the cost of synthesis. The ease of the powder preparation step may account for an advantage over the solid-state reaction synthesis.

In the synthesis of LSGM powders via Pechini process, two different citric acid – ethylene glycol ratios were applied; 60 wt% CA – 40 wt% EG and 90 wt% CA – 10 wt% EG. A decrease in the formation temperature of crystalline LSGM phase was observed with increasing citric acid percentage in the precursor mixture. To this end, in synthesis of all oxide powders (i.e. LSGM, LSFM, and LSCM) citric acid alone was also considered as an effective chelating agent. It is known that chelating ability in Pechini process is due to active carboxylic ends (COOH) of citric acid, which has three of them. In addition to CA, other organic acids with different number of carboxylic ends

were investigated as chelating agents. Tartaric acid (two carboxylic ends), and ethylene diaminetetraacetic acid (four carboxylic ends) are the other two chelating agents used for this purpose.

In synthesis of powders, nitrate salts were chosen as the cation sources, due to their high solubility in cold water [94], and due to their commercial availability. Less soluble salts result in inhomogeneities in the final product, due to early precipitation of certain cations during precursor forming. One further complication in the synthesis of mixed-cation oxides is the formation of carbonates. Nitrates are strong oxidizing agents and help reduce or eliminate the formation of carbonates.

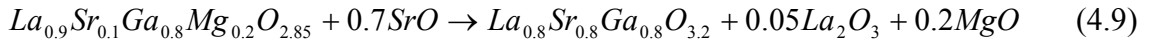
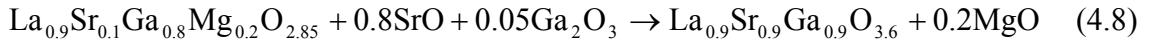
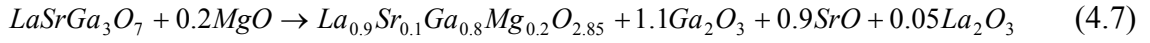
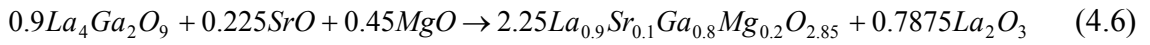
4.2. Relations Between Phases

In this section, the possible interactions of the formed phases are investigated during LSGM synthesis at each temperature. In powders calcined at temperatures between 800⁰C and 1200⁰C, six “unwanted” phases were observed besides LSGM phase. These phases are LaSrGaO₄, LaSrGa₃O₇, La₄Ga₂O₉, and unknown phases A, B, and C.

For all different routes used to synthesize the powders, LaSrGaO₄ phase was always present in the system at temperatures between 1050⁰C and 1200⁰C. The amount of this phase was between 1.1% and 9.3% for this temperature range. Below 1050⁰C, LaSrGaO₄ phase was either not present in the powders, or present with amounts that are not easily detected by x-rays (i.e. ≤ 1%). It is believed that the formation of LaSrGaO₄ phase around 1050⁰C is due to decomposition of LaSrGa₃O₇ phase into LaSrGaO₄ and Ga₂O₃ phases (see reaction 4.4). The increase in the amount of LaSrGaO₄ phase between 1150⁰C and 1200⁰C is believed to be due to reaction of a small amount of LSGM phase with SrO phase (and/or with Ga₂O₃ phase) to form LaSrGaO₄ (see reactions 4.8 and 4.9). Also, when LaSrGaO₄ formation was observed as a consequence of the decomposition of LaSrGa₃O₇ phase, a simultaneous increase was always observed in the percentage of LSGM phase. This may confirm the occurrence of reaction 4.7.

An increase in the amount of LaSrGaO₄ phase is always followed by a simultaneous decrease in LaSrGa₃O₇. If there is no LaSrGa₃O₇ phase in the powder

(generally between 1150⁰C and 1200⁰C), a decrease in the amount of LSGM phase was observed while LaSrGaO₄ phase is increasing. An additional observation is a decrease in the amount of La₄Ga₂O₉ phase simultaneously with a decrease in the amount of the LaSrGa₃O₇ phase. Possible corresponding reactions are shown below.



Unlike the LaSrGaO₄ phase, the concentration of LaSrGa₃O₇ and La₄Ga₂O₉ phases decreased with increasing temperature. These phases generally exhibited a sharp drop above 900⁰C or 1000⁰C, disappearing with a further increase in temperature. During the decrease in the amounts of LaSrGa₃O₇ and La₄Ga₂O₉ phases, sharp increases were observed in the amounts and percentages of LSGM phase. The sharp increases in the amount of LSGM phases is most likely connected with the decomposition and further reactions of La₄Ga₂O₉ and LaSrGa₃O₇ phases with the x-ray amorphous portions of the powders to form LSGM. Possible reactions are 4.4, 4.5, 4.6, and 4.7.

In reaction 4.6, large amounts of La₂O₃ phase should be present in the powders. However, according to the x-ray spectra, the crystalline La₂O₃ phase was not observed in x-ray diffraction measurements. Thus, it can be claimed that reaction 4.6 is not likely to occur in the syntheses.

In reaction 4.4, during possible formation of LaSrGaO₄ phase, Ga₂O₃ phase is required to occur and should have been perhaps detected in the x-ray analysis of the powders. However, because the decomposition of LaSrGa₃O₇ phase and La₄Ga₂O₉ phase occur simultaneously, the Ga₂O₃ phase formed in reaction 4.4, may be consumed

in the reaction 4.5. In reactions 4.8 and 4.9, the amounts of remaining and/or formed MgO, SrO, or Ga₂O₃ phases were believed to be under the detection limit of the XRD equipment (1%). Therefore, they were not observed in x-ray analysis.

From the reactions it can be seen that from 1 mole LaSrGa₃O₇, 1 mole LSGM is formed (see reaction 4.7), but from 0.9 moles La₄Ga₂O₉, 4 moles LSGM can be formed (see reaction 4.5). To this end, it is believed that formation of LSGM phase is mostly due to the decomposition of La₄Ga₂O₉ phase and further reactions of its decomposition products.

According to the reactions above, the amounts of formed or pre-existing SrO and Ga₂O₃ phases should be detected by XRD equipment. But it is believed that the reactions 4.4, 4.5 and 4.7, which produce or consume these phases, occur simultaneously. Therefore the absence of the x-ray peaks of SrO and Ga₂O₃ phases in x-ray plots is possible. In section 4.6.1, a possible Mg²⁺ ion substitution into La₄Ga₂O₉ phase will be described. The substitution of Mg²⁺ ions into the La₄Ga₂O₉ lattice may explain the absence of MgO phase in the x-ray plots. Existence of x-ray amorphous MgO phase in the powders may also be a reason for the absence of crystalline MgO in x-ray plots.

In order to explain the behavior of the unknown phases, their identities must be determined.

4.3.Effect of Carrier Materials

4.3.1. LSGM Synthesis

Pechini Precursors : In order to ascertain the effectiveness of the Pechini process, a 60 wt% citric acid – 40 wt% ethylene glycol mixture was used as the carrier material. According to the esterification reactions, it is believed that by using this citric acid – ethylene glycol mixture, the number of long chains may be increased. In LSGM synthesis, at 800⁰C major phases were LaSrGa₃O₇ and La₄Ga₂O₉. A sharp increase in the amount of LSGM phase and corresponding sharp decreases in the amounts of LaSrGa₃O₇ and La₄Ga₂O₉ phases were seen between 900⁰C and 1000⁰C (from 237 to

1318 counts). This sharp increase in the amount of LSGM phase resulted in 48.7% of LSGM in the powder at 1000°C.

From STA plot in Figure 4.1, the endothermic DTA peak at 125°C is due to evaporation of water. The small mass increase in the beginning of the TG curve is due to the “buoyancy” effect. The exothermic DTA peak at 380°C is believed to be due to the breakdown of the polymer, as stated by Kakihana et al. [112]. The mass loss between 380°C and 510°C with a corresponding exothermic peak at 438°C may be due to pyrolysis of the organics. The exothermic peak at 648°C with a corresponding mass loss is believed to be due to the char burnout.

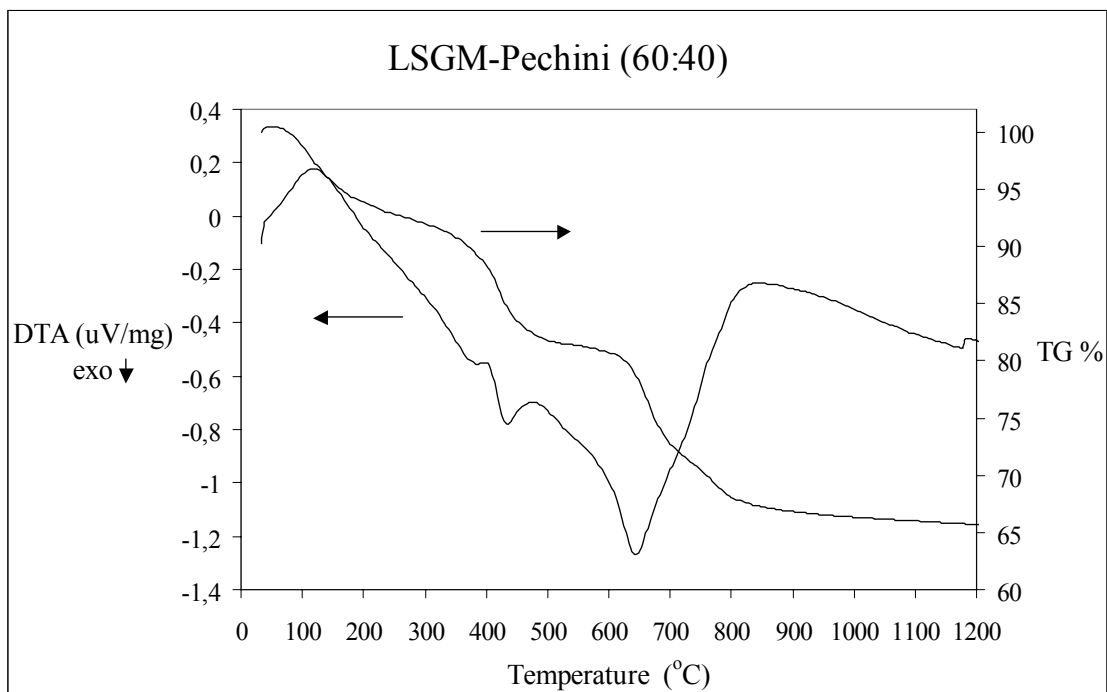


Figure 4.1. STA plot of the precursor for LSGM synthesis with Pechini precursor of 60 wt% CA – 40 wt% EG as the organic carrier material.

In a separate experiment, the amount of ethylene glycol in the mixture was decreased down to 10 wt%, to obtain shorter chains compared to 60:40 citric acid to ethylene glycol mixture. Changes in the percentages of the phases for each calcination temperature are shown in Figures 4.2 and 4.3 to visualize phase behaviors. Similar to 60:40 ratio case, at 800°C major phases were $\text{LaSrGa}_3\text{O}_7$ and $\text{La}_4\text{Ga}_2\text{O}_9$. However, the sharp increase in the amount of LSGM phase was observed between 800°C and 900°C (from 84 to 2029 counts). This sharp increase in LSGM phase resulted in a 71.2% LSGM in the powder at 900°C.

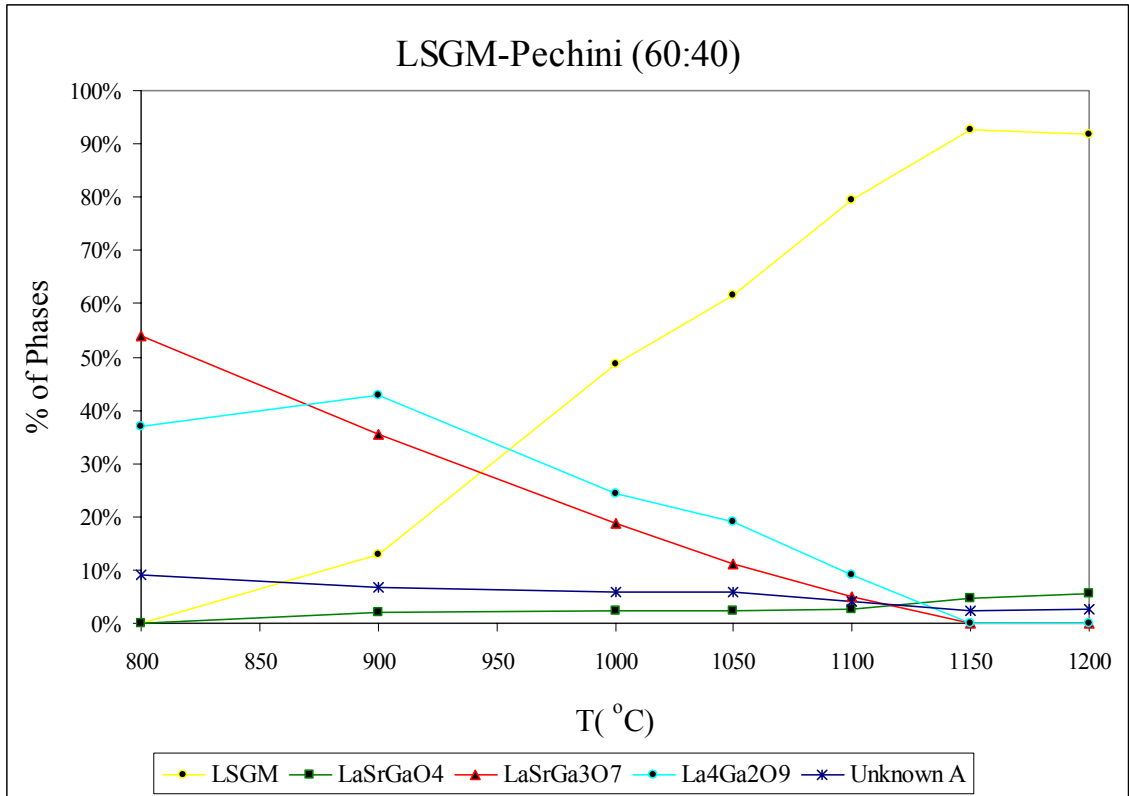


Figure 4.2. Visual representation of the phase percentages in LSGM synthesis with Pechini precursor (60 wt% CA – 40 wt% EG mixture) as the organic carrier material.

The rise in the amount of LSGM phase was stronger, and the calcination temperature decreased when ethylene glycol amount in citric acid – ethylene glycol mixture decreased (from 40 wt% to 10 wt%). This may be due to a decrease in the chain length. Short chains move more easily in the gel-like solution than long chains. Therefore, the chelated cations may blend more easily to form desired oxide composition. Moreover, in the 90:10 CA:EG ratio case, active carboxylic ends of citric acid are in larger amount compared to the 60:40 CA:EG ratio case. In the mixture, ethylene glycol molecules attach themselves also to active carboxylic groups of citric acid molecules. Visual representation of the percentages of each phase for each temperature is shown in Figure 4.3. Thus, it was expected that the complete removal of ethylene glycol might result in a higher increase in the amount of LSGM phase and/or decrease in calcination temperature. To this end, the use of citric acid alone was supposed to give better phase distribution due to a more effective chelating action.

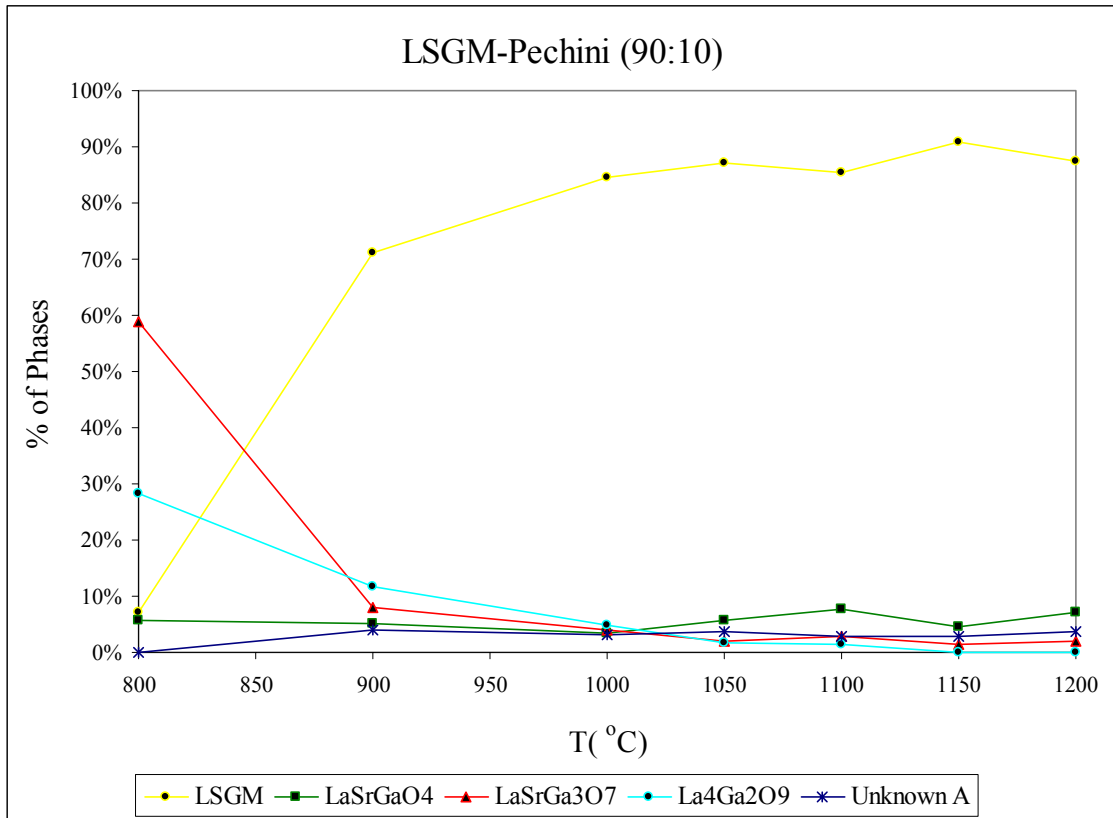


Figure 4.3. Visual representation of the phase percentages in LSGM synthesis with Pechini precursor (90 wt% CA – 10 wt% EG mixture) as the organic carrier material.

When citric acid alone was used as the organic carrier, and when a 1:1 cation to citric acid molecule ratio was applied, a sudden increase in the amount of LSGM phase was observed between 800⁰C and 900⁰C (from 138 to 2829 counts). Moreover, 88% LSGM phase was obtained at temperatures as low as 900⁰C. XRD plots of powders synthesized at 900⁰C with all carrier materials are shown in App. A4, and the phases present, their percentages and amounts are tabulated in App. B4. In Figure 4.4, the x-ray spectra of synthesized powders that are calcined at 900⁰C with different organic carrier materials, are shown on the same graph. Visual phase distribution is shown in Figure 4.5.

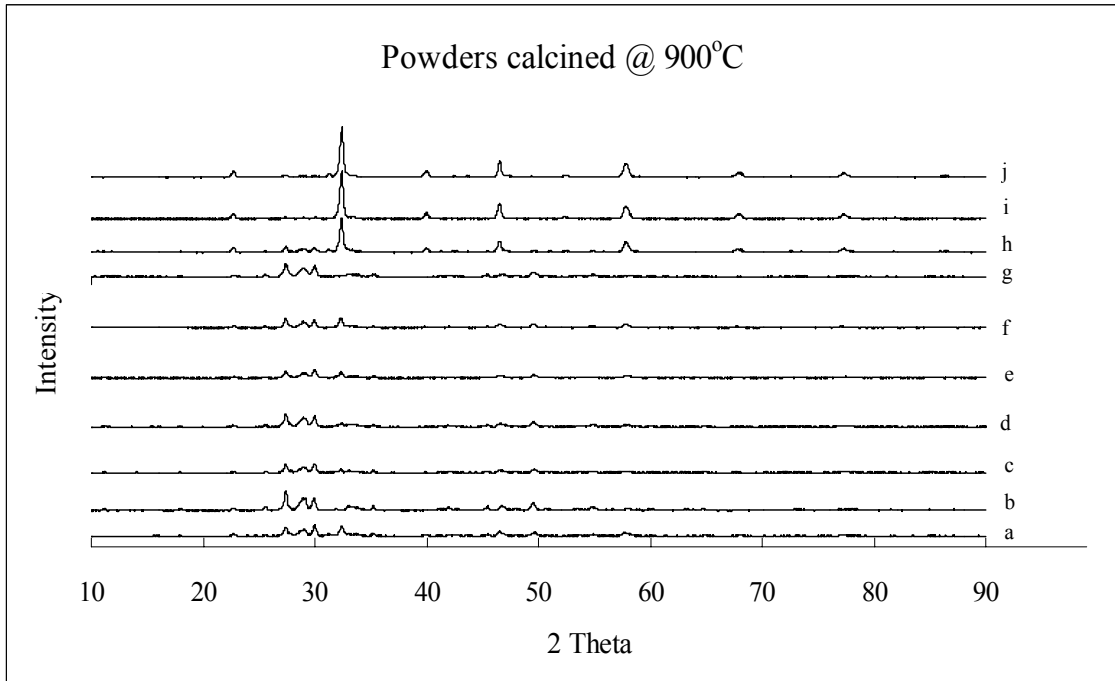


Figure 4.4. Powders calcined at 900°C and synthesized with a) EDTA, b) PVA, c) TA (2:1), d) Pechini precursor (60 wt% CA – 40 wt% EG), e) TA (1:1), f) TA (1:2), g) CA (1:2), h) Pechini precursor (90 wt% CA – 10 wt% EG), i) CA (2:1), and j) CA (1:1).

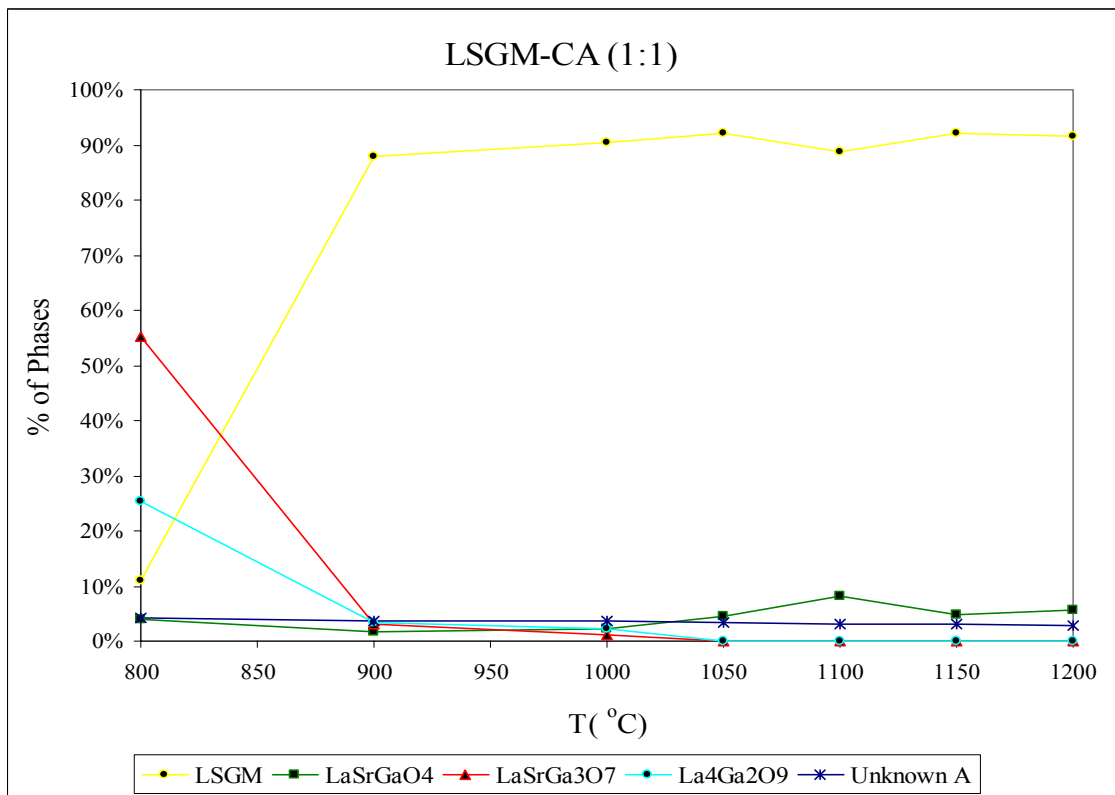


Figure 4.5. Visual representation of the phase percentages in LSGM synthesis with CA (1:1) as the organic carrier material.

The better LSGM yield of the citric acid as the carrier material, compared to Pechini process may be explained by the large number of the active carboxylic ends of the citric acid, when it is used alone as the organic carrier material. The effectiveness of the citric acid stems from the “claw” shape arrangement of carboxylic groups of the citric acid, which is suitable to chelate cations (see Figure 4.6).

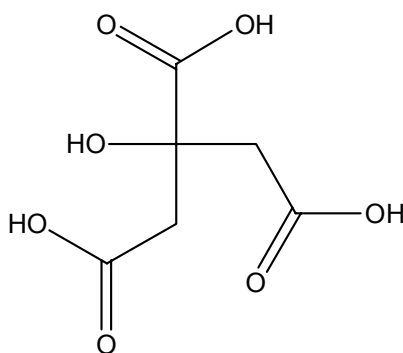


Figure 4.6. Citric acid

In Pechini process, ethylene glycol molecules may attach to the two carboxylic ends of citric acid molecules and may decrease the number of active carboxylic ends. This behavior is believed to have decreased the activity of carboxylic ends of citric acid molecules in terms of chelating ability for La^{+3} , Sr^{+2} , Ga^{+3} , and Mg^{+2} ions in the solution. Presence of all the unwanted phases in the system until 1150°C , and 12.8% LSGM phase amount at 900°C in contrast to 88% of LSGM for the citric acid case (1:1 cation to CA ratio), may be indicative of a decreased chelating ability of citric acid molecules in Pechini precursors. It is also believed that the mobility of citric acid molecules is larger than the chain-like structure in the Pechini precursor. When the percentage of ethylene glycol in the mixture decreased from 40 wt% to 10 wt%, concentration of LSGM phase in the powder increased for synthesized powders calcined at 900°C (from 12.8% to 71.2%), consistent with the expectations for decreasing chain length.

The STA plot of the precursor prepared with citric acid as the carrier material is shown in Figure 4.7. Similar to previous experiment, an endothermic peak was seen around 127°C with a corresponding mass loss due to evaporation of water. At 437°C , the exothermic peak was associated with the nitrate removal and oxidation of the

organic precursor with the corresponding mass loss in the TG plot. The exothermic peaks at 392^oC, 572^oC, and 657^oC are attributed to the stepwise combustion of citric acid molecules.

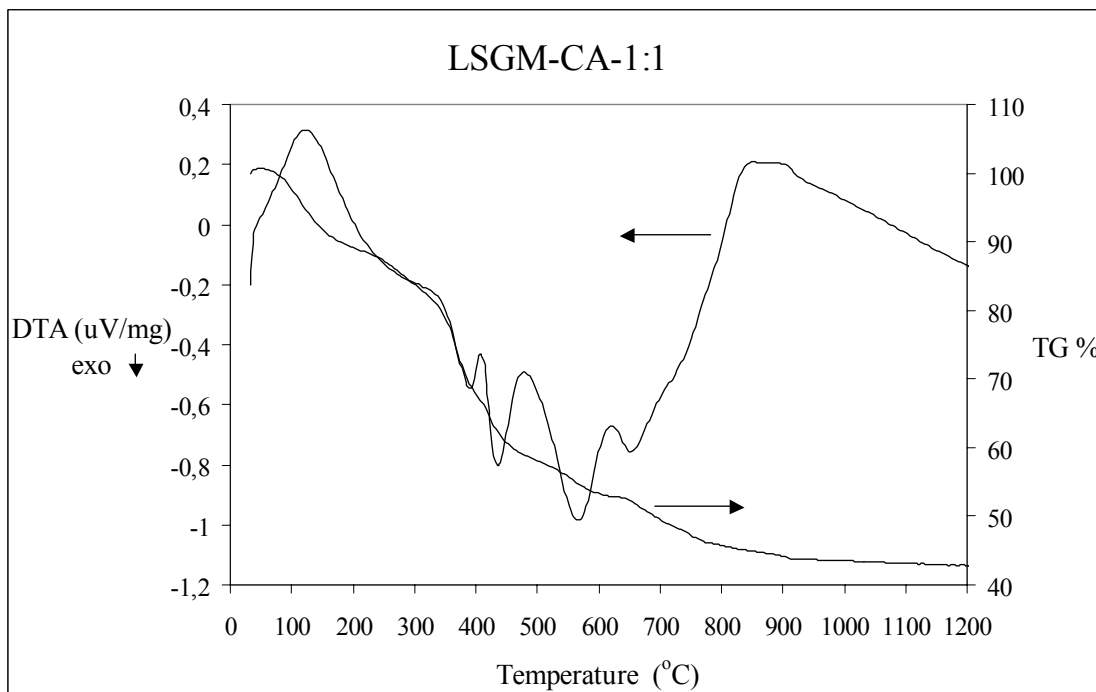


Figure 4.7. STA plot of the precursor for LSGM synthesis with CA as the organic carrier material.

To see the effect of the number of carboxylic ends in the chelating action, different acids with two and four carboxylic ends (tartaric acid and EDTA) were used as the carrier material.

Tartaric acid has two carboxylic ends in its molecular structure (see Figure 4.8).

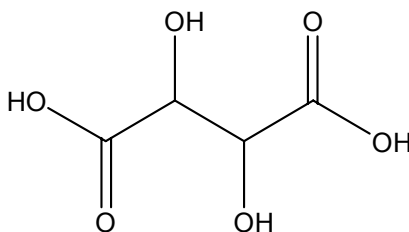


Figure 4. 8. Tartaric acid.

As mentioned before, the chelating ability of citric acid may be due to its three carboxylic ends. Therefore tartaric acid with two carboxylic ends may have lower chelating ability, resulting in a lower LSGM phase amount for the same temperatures. Also the geometry of these molecules may play an important role in the chelating action. By comparing the shapes of these molecules, the claw-shape structure of citric acid may attract and hold the cations better than the tartaric acid molecule (see Figures 4.6 and 4.8). Experiments with tartaric acid confirmed the expected relationship between the number of carboxylic ends, geometry of the carrier molecule and the chelating ability. In LSGM powder synthesis with tartaric acid as the carrier material, lower amounts of LSGM phase were obtained in comparison to the LSGM powder synthesized with citric acid as the carrier material (see App. A4 and A7) at the same temperatures. However, the amount of LSGM phase at temperatures above 1100⁰C was larger than those prepared with citric acid based precursors.

In the STA plot of the precursor material (see Figure 4.9), as in the previous experiments, an endothermic peak appeared at 130⁰C with a corresponding mass loss due to water evaporation. At 446⁰C, again the exothermic peak of nitrate removal was seen with corresponding mass loss. The exothermic peaks at 581⁰C and 666⁰C are believed to belong to the combustion of tartaric acid based organic precursor in two steps.

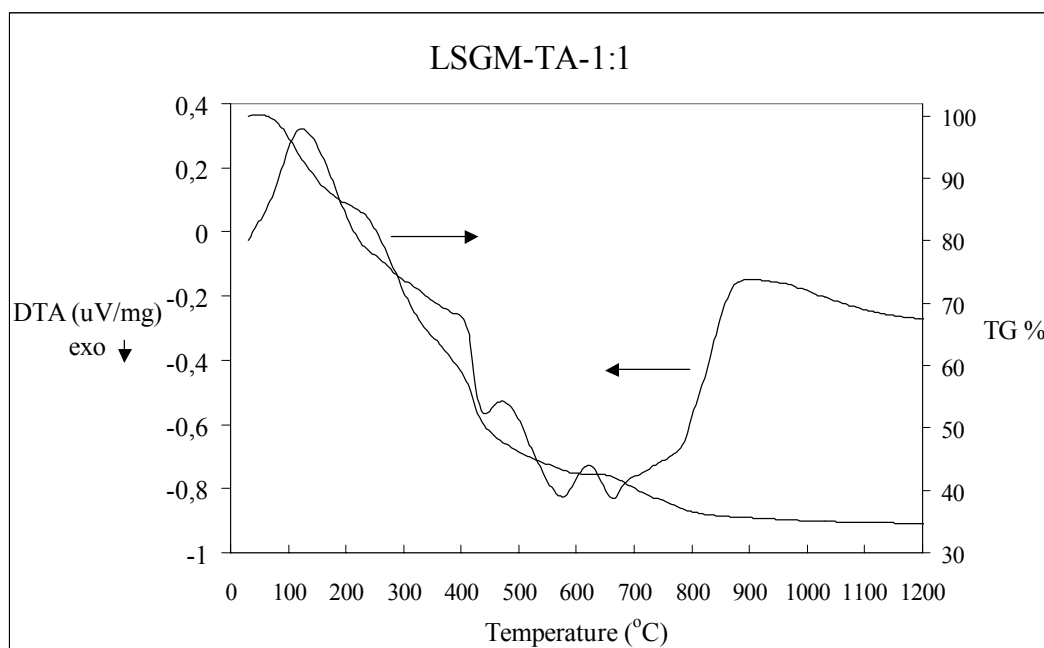


Figure 4.9. STA plot of the precursor for LSGM synthesis with TA as the organic carrier material.

To see the effect of four carboxylic ends, and a different molecular geometry (see Figure 4.10), EDTA was used as the carrier material in the LSGM synthesis.

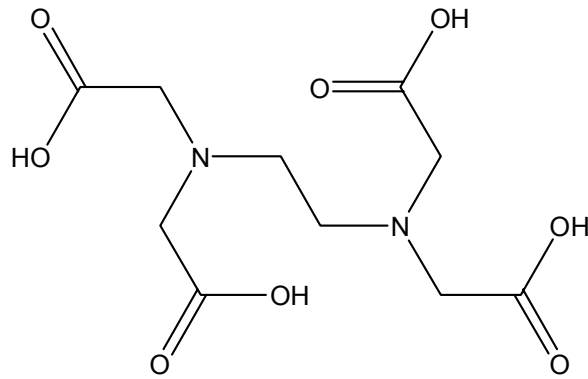


Figure 4.10. Ethylene diaminetetraacetic acid (EDTA).

The maximum amount of LSGM phase obtained was 68.4%, which is far less than in powders synthesized with other organic carrier materials. In the solution preparation step, 25% ammonia had to be added to the solution to dissolve EDTA. This may cause ammonia ions to attack the active carboxylic ends of EDTA, thereby decreasing its chelating ability (see Figure 4.11). Visual phase distribution of LSGM powder with EDTA is shown in Figure 4.12.

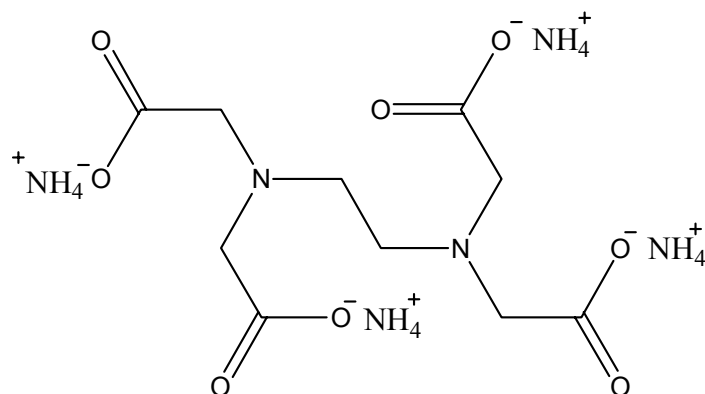


Figure 4.11. Possible schematic representation of ammonia attack on EDTA functional groups.

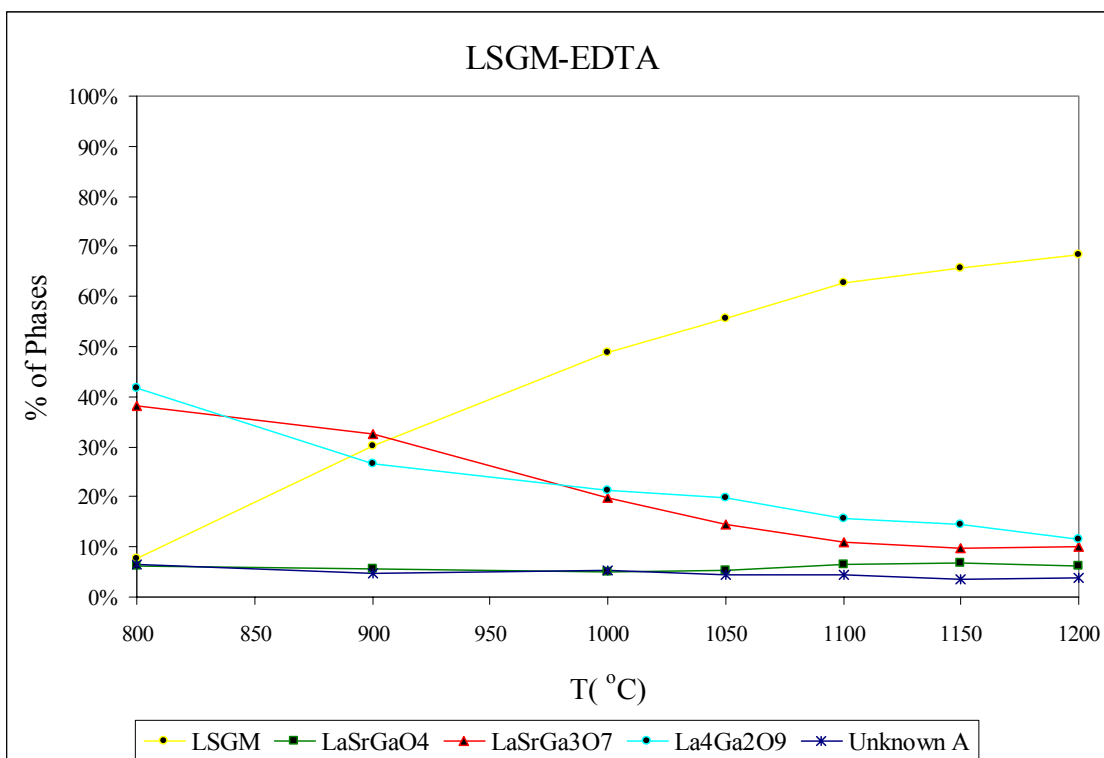


Figure 4.12. Visual representation of the phase percentages in LSGM synthesis with EDTA as the organic carrier material.

The STA plot of the precursor with EDTA in Figure 4.13 shows similar features to plots of other precursors with different carrier materials. The endothermic DTA peak at 115⁰C corresponds to weight loss due to water removal, while the exothermic DTA peak at around 450⁰C suggests nitrate removal and oxidation reactions. The strong exothermic DTA peak at 493⁰C indicates a single step combustion of EDTA, which may be due to the explosive nature of ammonia in the precursor.

The cation complexing ability of hydroxyl groups (OH) of polyvinyl alcohol was investigated in the synthesis of LSGM powders. Changes in the percentages of the phases for each calcination temperature are shown in Figure 4.14, to visualize phase behaviors. The amounts of LaSrGa₃O₇ and La₄Ga₂O₉ phases were almost constant between 800⁰C and 1000⁰C. Formation of LaSrGaO₄ phase is mainly due to the decomposition of LaSrGa₃O₇ (see reaction 4.4), or due to the decomposition of LSGM phase in the absence of LaSrGa₃O₇ phase (generally above 1150⁰C, see reactions 4.8 and 4.9). The decrease in the amount of LaSrGa₃O₇ phase between 1000⁰C and 1050⁰C resulted in formation of LaSrGaO₄ phase at 1050⁰C, which may account for the absence of LaSrGaO₄ phase between 800⁰C and 1000⁰C, due to the delayed decomposition of

LaSrGa₃O₇ phase in this temperature range. The sharp decrease in the concentrations of LaSrGa₃O₇ and La₄Ga₂O₉ phases between 1100°C and 1150°C may account for the increase in LSGM phase amount from 33.7% to 81.1% between these temperatures (see reactions 4.5 and 4.7).

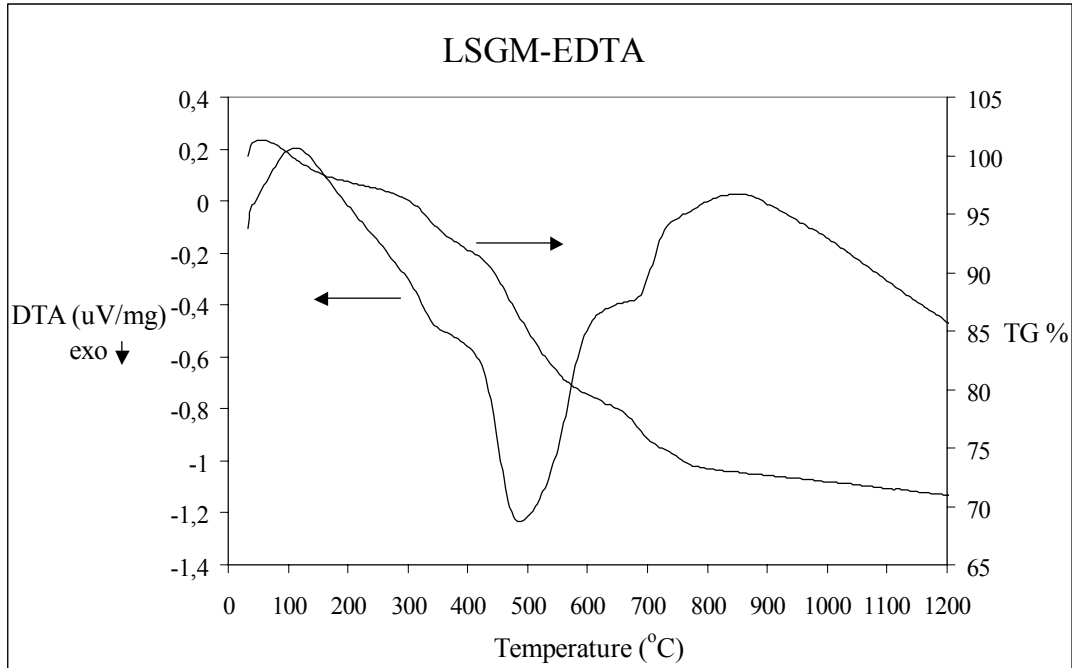


Figure 4.13. STA plot of the precursor for LSGM synthesis with EDTA as the organic carrier material.

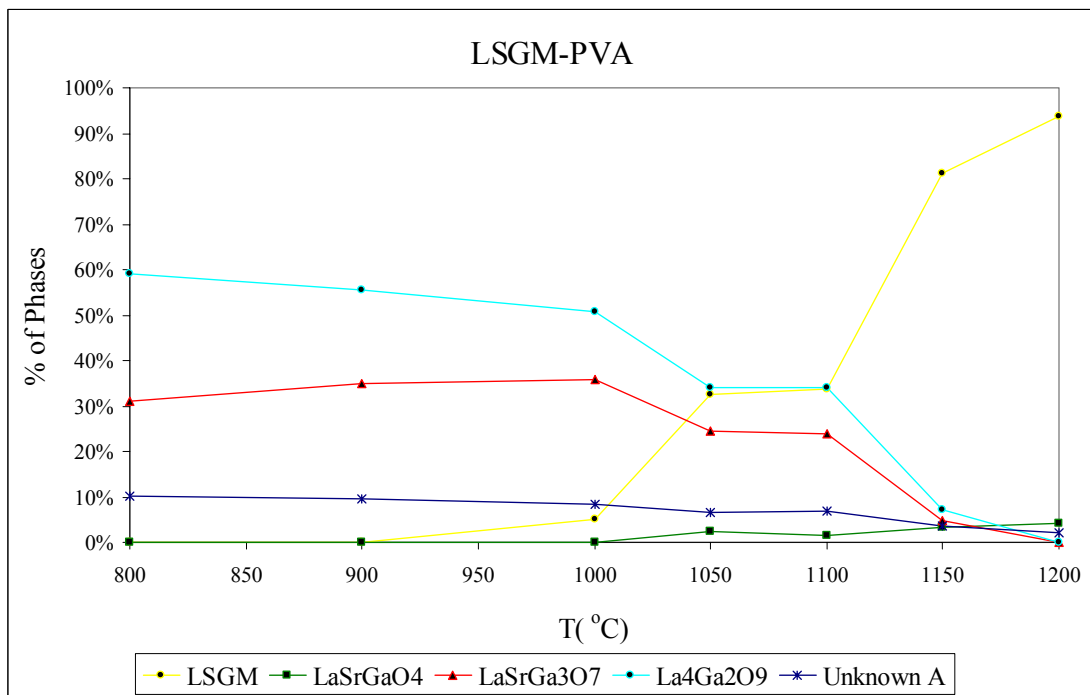


Figure 4.14. Visual representation of the phase percentages in LSGM synthesis with PVA as the organic carrier material.

In the LSGM synthesis with PVA, lower amounts and percentages of LSGM phase formation were observed below 1150⁰C. The reason of this is believed to be presence of high amount and percentage La₄Ga₂O₉ phase at low temperatures (below 1150⁰C). It should be noted that the amount and concentration of La₄Ga₂O₉ phase were always less than the amount of LaSrGa₃O₇ phase in all other experiments, which resulted in a high amount of LSGM formation at low temperatures. Understandably this phase is a lanthanum-rich one, compared to LaSrGa₃O₇ and LSGM phases. Therefore, it appears that an interaction (complexing) of PVA with lanthanum ions may be less favored compared to gallium ions in a system composed of these four cations. Thus, an early crystallization of La₄Ga₂O₉ phase is more favorable than the other phases because of the loosely bound or held of La³⁺ ions in PVA-cation polymeric network at low temperatures (< 800⁰C).

The STA plot of the precursor is shown in Figure 4.15. There is an endothermic DTA peak at 115⁰C due to water evaporation and an exothermic DTA peak at 430⁰C due to removal of nitrates and oxidation of the organic precursor with the corresponding weight losses. The exothermic DTA peak at 615⁰C can be due to combustion of charred PVA with the corresponding weight loss.

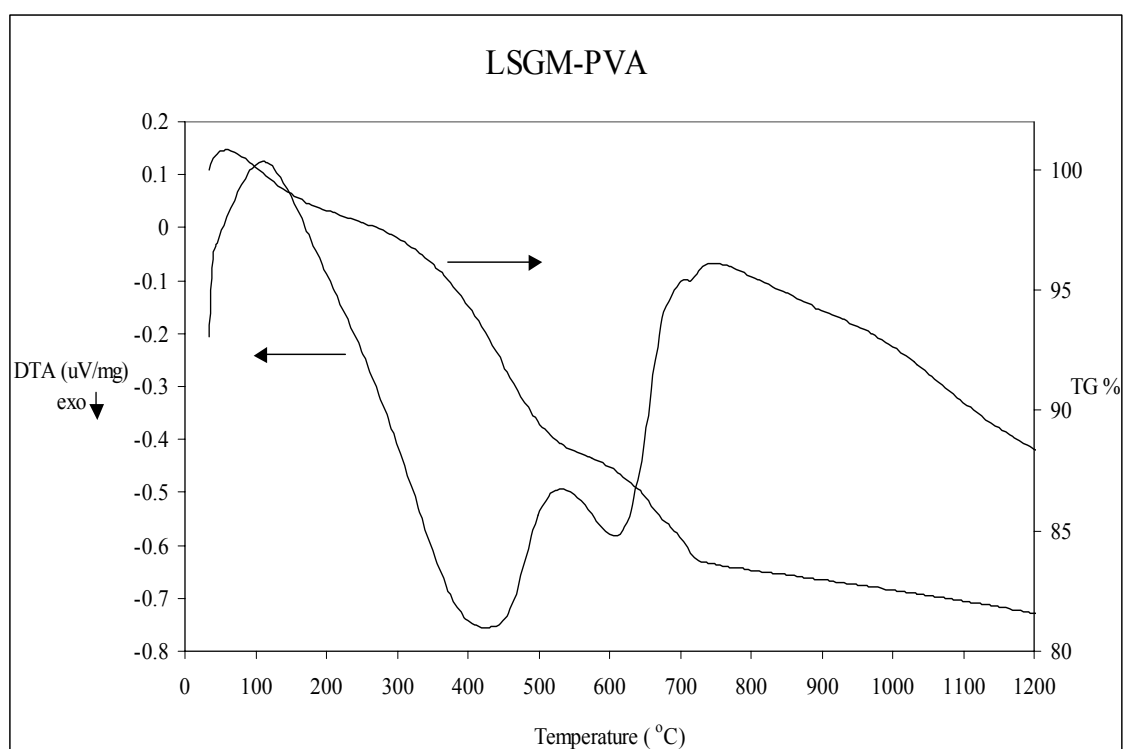


Figure 4.15. STA plot of the precursor for LSGM synthesis with PVA as the organic carrier material.

Among the powder syntheses without citric acid-containing carrier materials at 900°C, the largest LSGM amount is 34.8% with tartaric acid (1:2 cation:TA case), which is much less than 88% in the 1:1 cation to citric acid molecule ratio case (see Table 4.1).

Table 4.1. The concentrations and amounts of each phase of the LSGM powders calcined at 900°C.

<i>900°C</i>	<i>LSGM</i>	<i>LaSrGaO₄</i>	<i>SrLaGa₃O₇</i>	<i>La₄Ga₂O₉</i>	<i>Unknown A</i>
CA	88% (2829)	1.6% (53)	3.1% (98)	3.5% (112)	3.8% (122)
CA-2:1	85.6% (2965)	5.4% (188)	2% (70)	3.7% (127)	3.3% (116)
CA-1:2	41.5% (793)	0.00%	24% (459)	27.8% (530)	6.7% (127)
EDTA	30.3% (606)	5.6% (111)	32.6% (652)	26.7% (534)	4.8% (97)
NoPrec-All Nitrates	0.00%	4.5% (83)	52.6% (971)	36.5% (673)	6.4% (119)
Pechini (60-40)	12.8% (237)	2.1% (40)	35.6% (664)	42.8% (798)	6.7% (125)
Pechini (90-10)	71.2% (2029)	5.2% (148)	7.9% (226)	11.6% (331)	4.1% (117)
PVA	0.00%	0.00%	34.9% (730)	55.5% (1163)	9.6% (202)
TA	27.5% (340)	0.00%	36.6% (453)	30.1% (372)	5.8% (72)
TA-2:1	14.7% (197)	0.00%	40% (536)	38.9% (523)	6.6% (88)
TA-1:2	34.8% (590)	0.00%	26.3% (445)	31.8% (539)	7.1% (120)

Table 4.2. The concentrations and amounts of each phase of the LSGM powders calcined at 1000°C.

<i>1000°C</i>	<i>LSGM</i>	<i>LaSrGaO₄</i>	<i>SrLaGa₃O₇</i>	<i>La₄Ga₂O₉</i>	<i>Unknown A</i>
CA	90.4% (3235)	2.3% (82)	1.2% (45)	2.3% (81)	3.8% (135)
CA-2:1	84.2% (2867)	6.7% (228)	3.1% (105)	3.1% (105)	2.9% (100)
CA-1:2	63.8% (1975)	1.5% (45)	11.9% (367)	17.1% (531)	5.7% (177)
EDTA	48.7% (1206)	5% (125)	19.8% (492)	21.3% (527)	5.2% (128)
NoPrec-All Nitrates	9.3% (227)	4.1% (100)	41% (1002)	38.7% (946)	6.8% (167)
Pechini (60-40)	48.7% (1318)	2.2% (59)	18.8% (509)	24.4% (662)	5.9% (160)
Pechini (90-10)	84.5% (2987)	3.5% (123)	4% (142)	4.9% (175)	3.1% (109)
PVA	5% (119)	0.00%	35.9% (855)	50.6% (1205)	8.5% (203)
TA	56.6% (863)	0.00%	16.3% (249)	20.1% (306)	7% (107)
TA-2:1	68.3% (1873)	1.2% (33)	10.5% (289)	15.3% (420)	4.7% (130)
TA-1:2	78.9% (2082)	0.00%	7.6% (200)	10.1% (269)	3.4% (89)

Comparing Table 4.1 and Table 4.2, two extreme cases were observed: 88% LSGM phase formation at 900⁰C with citric acid, and 5% LSGM formation at 1000⁰C with polyvinyl alcohol. This striking difference may be due to the formation of large amount of La₄Ga₂O₉ phase in PVA case, as mentioned before. The interaction of PVA with these cations may be promoted the formation of La₄Ga₂O₉ phase at low temperatures (≤ 800⁰C). The large differences between LSGM phase formation in CA cases and the others, may be due to the ability of citric acid to bind all these cations together to form an amorphous LSGM-like phase in its precursor. Also the chelating ability of carboxylic ends of citric acid is believed to be stronger than the complexing ability of hydroxyl groups of PVA. Also the mobility of small molecules of citric acid may be larger than the long polymer chains of PVA. Thus, the shorter cation – functional group complexes may come together easily to form the desired LSGM composition. Therefore citric acid appears to be one of the best organic carriers for LSGM formation at relatively low temperatures among the other organic carrier materials. The power of citric acid may come from the three, well-oriented carboxylic ends of it in chelating La³⁺, Sr²⁺, Ga³⁺, and Mg²⁺ ions.

In all powder syntheses, removal of a large portion of the water and some fraction of nitrates occurs in the system during heat treatment on a hot plate up to 300⁰C. Other exothermic peaks below 800⁰C may be due to combustion of different charred organic carrier materials of the precursors.

In all DTA plots, above 800⁰C, there is a “hump” in endothermic direction, but no sharp exothermic or endothermic peaks. Many phases decompose (i.e. La₄Ga₂O₉ and LaSrGa₃O₇) simultaneously with crystallization of LSGM phase. The hump in DTA plots after 800⁰C may be due to the overlap of many endothermic decomposition processes and the sluggish and exothermic LSGM phase crystallization. The absence of “sharp” exothermic or endothermic peaks associated with these processes may be connected to the nature of decomposition and crystallization processes, which are continuous and slow, compared to processes (i.e. melting, phase transition) giving rise to sharp peaks in DTA curve. Heating the precursors extremely rapidly (i.e. 100⁰C/min) may help sharpen the decomposition and crystallization peaks in the DTA plot.

Precursors with different citric acid to cation, and tartaric acid to cation ratios were used in order to determine the optimum carrier material amount in LSGM synthesis. Neither in the CA case, nor in the TA case did experiments conducted with cation to organic molecule ratios of 2:1 and 1:2 show a better performance in terms of

the amount of LSGM synthesized. The 1:1 organic carrier – cation ratio was the best combination, but further investigations are necessary.

4.3.2. LSFM and LSCM Synthesis

In synthesis of LSFM and LSCM powders, PVA exhibited similar behavior to the synthesis of LSGM. In both powder syntheses, high percentages (> 80%) of powders were obtained even at 500⁰C, due to similar interaction (or complexing affinity) of PVA with the relevant ions for both compositions.

The behavior of both the Pechini precursor (60 wt% citric acid – 40 wt% ethylene glycol mixture) and the citric acid were similar in all powder syntheses. In the LSFM powder synthesis, both synthesis methods resulted in 100% LSFM phase in the powders above 550⁰C. In terms of the amount of LSFM phase produced, the performance of CA was better than that of the Pechini precursor, similar to the LSGM synthesis. In the synthesis of LSCM powders, the first LSCM phase was observed at 700⁰C in the CA case, and at 750⁰C in the Pechini precursor case. Moreover, the amounts of LSCM phase produced in powders were higher in CA case. Therefore, the performance of CA was better compared to Pechini precursor in both LSFM and LSCM syntheses, which confirms the claims made for LSGM synthesis (see section 4.3.1).

In the use of tartaric acid and EDTA as the organic carrier materials, below 700⁰C, LSFM was the only x-ray crystalline phase. In both cases, undesired phases were observed above 700⁰C. The performances of these organic carrier materials were poor compared to other organic carrier materials, in terms of amounts of LSFM phases produced in the powders. In LSCM synthesis, similar behaviors of TA and EDTA were again observed. Below 700⁰C no crystalline LSCM phase were present using both LSCM precursors. Unlike in LSGM synthesis of both carrier materials, performance of EDTA was better in terms of amounts of LSFM and LSCM phase produced than the performance of TA.

As a summary, synthesis of LSFM powders by using citric acid, Pechini precursor, EDTA, and tartaric acid resulted in single-phase LSFM powders. In EDTA and TA cases, undesired phases were observed above 700⁰C. In Pechini precursor and CA cases, the powders were composed of single-phase LSFM powders above 550⁰C. Citric acid exhibited the best performance among the other organic carrier materials, in

terms of the amount of LSCM phases produced and the LSCM percentages for each powder. It may be said that, the strong interaction of La^{3+} , Sr^{2+} , Fe^{3+} , and Mg^{2+} ions with the organic carrier materials resulted in single-phase powder synthesis at low temperatures. Also the chelating ability and suitable geometry for chelating action of carboxylic ends of citric acid may be effective for its high performance.

In synthesis of LSCM powders, PVA exhibited best performance in terms of produced LSCM percentage in the powders among other organic carrier materials. 88.8% LSCM phase was obtained at 500°C , and 96.9% LSCM phase was obtained at 850°C by using PVA. In all other LSCM syntheses, the x-ray crystalline LSCM phase was not observed below 700°C , and the behavior of the phases were effectively the same. Relatively poor performances of the organic carrier materials in synthesis of LSCM powders compared to synthesis of LSCM and LSGM powders may be the indication of the strong effect of organic carrier – constituent ion interaction in the crystalline phase formation in the organic precursor method.

The presence of the same unknown in LSGM synthesis (unknown A) and in the synthesized LSCM powders proves that this phase does not contain gallium and chromium. This information may be helpful in the identification of the unknown A phase.

4.4.Synthesis Without Carrier Materials

In the LSGM powder synthesis with carrier materials, the effects of different carrier materials were discussed in section 4.3. In order to understand the importance of carrier materials, it is imperative to see the distribution of phases in the synthesis routes without the carrier materials. The only difference in these two kinds of experiment sets was the presence or the absence of the organic carrier materials. In the synthesis LSGM powder without organic carriers, again a perfect homogenization in the solution has been achieved. When the salts were dissolved in water, precipitation was not observed. However, the formation of large quantities of LaSrGaO_4 , $\text{LaSrGa}_3\text{O}_7$, $\text{La}_4\text{Ga}_2\text{O}_9$, or the unknown A phases could not be prevented, since there were no complexing or chelating agents to suppress the disproportionation of the cations as the water of solution evaporates. This caused the formation and presence of each of these phases at examined

temperatures. The maximum amount of LSGM phase was obtained at 1200°C with 54.6%. This amount is much lower compared to the concentrations of LSGM phase, synthesized with any of the organic carrier materials. Unlike experiments conducted with carrier materials, the unwanted phases do not exhibit a behavior that can be described as a “sharp decrease” in their concentration in the powder. Accordingly, the LSGM phase does not exhibit a “sharp increase” in its concentration in the powders (see App. D1). In the absence of an organic carrier for chelating or complexing action, the cations with different solubilities are free to precipitate out, forming the undesired phases. In contrast to powder preparation with an organic carrier material, the hump in DTA curve above 800°C was not observed in the STA plot of this experiment (Figure 4.16). This hump may be due to overlap of endothermic decomposition peaks of the unwanted phases and the crystallization peak of the LSGM phase (see section 4.3.1). The absence of the hump after 800°C may give clue about the lower degrees of decomposition and crystallization events.

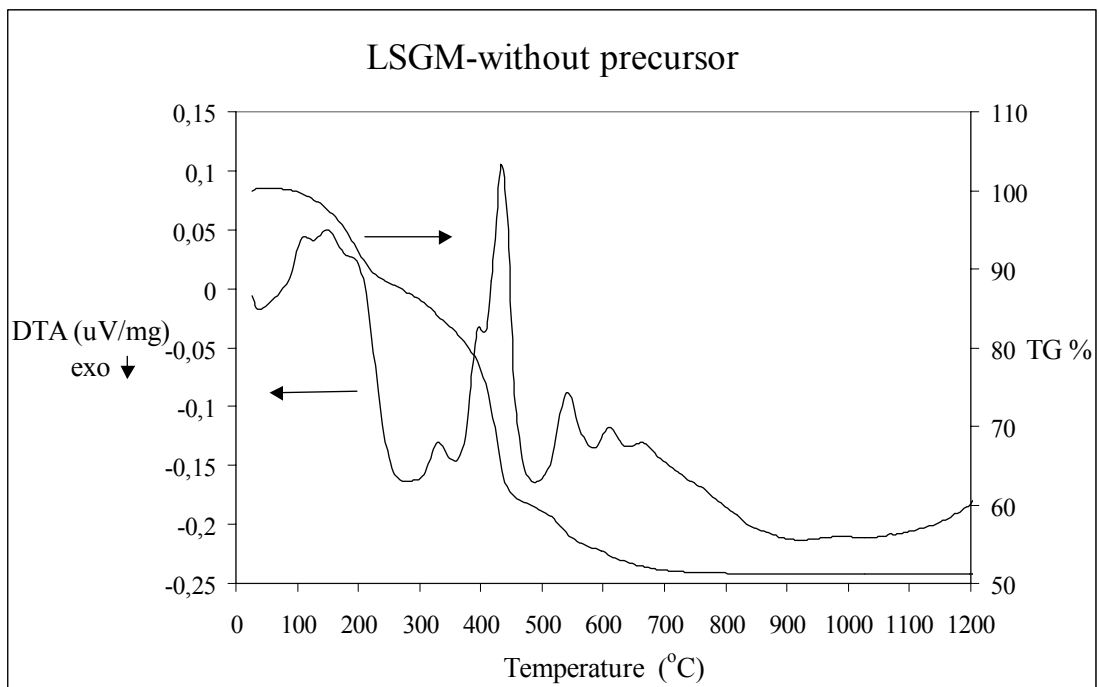


Figure 4.16. STA plot of the precursor for LSGM synthesis without any the organic carrier material.

The endothermic DTA peaks at 115°C, 157°C, and 197°C may be the indication of stepwise evaporations of mostly crystalline water of different nitrate sources. The

endothermic reactions at temperatures between 250⁰C and 700⁰C may be due to decomposition of nitrates with the corresponding mass losses.

Table in App. D1 may not give exact information about the amounts of each phase due to experimental errors and error due to peak-height measurements; but it gives an idea about stability and behavior for each phase in such a system according to temperatures of the heat treatments between 800⁰C and 1200⁰C. In general, the quantities of LaSrGa₃O₇, La₄Ga₂O₉, and the unknown A phases decrease with increasing temperature. On the other hand, the amount of LSGM and LaSrGaO₄ phases increase with increasing temperature. Slight inconsistencies in this behavior could be well within the experimental errors.

4.4.1. Effect of Gallium Sulfate

The effect of gallium sulfate as the gallium source in LSGM synthesis was investigated through two sets of experiments. In both sets of experiments, a negative influence of gallium sulfate on the LSGM formation at low temperatures was seen.

In LSGM synthesis by using gallium sulfate as the gallium source, we suspected that the main obstacle in the formation of single-phase, crystalline LSGM phase was the early formation of (LaO)₂SO₄ phase. In both sets of experiment, a high amount of crystalline (LaO)₂SO₄ phase formation around 800⁰C was observed (see App. D2 and D3). With increasing temperature up to 1050⁰C, the amount of (LaO)₂SO₄ phase increased. Above 1100⁰C the amount and percentage of (LaO)₂SO₄ phase decreased sharply. Around 1100⁰C, formation of the x-ray crystalline LaSrGa₃O₇ phase may be due to crystallization of the x-ray amorphous LaSrGa₃O₇ phase, because the (LaO)₂SO₄ phase did not decompose during formation of the LaSrGa₃O₇ phase.

On the other hand, the high amount of crystal LSGM phase formation above 1100⁰C is due to decomposition of (LaO)₂SO₄ and LaSrGa₃O₇ phases between 1100⁰C and 1150⁰C. The sharp drop in the amounts of these two phases can be seen in x-ray intensities listed in tables in App. D2 and D3.

It should be noted that the percentage of maximum LSGM phase in the synthesis with CA as carrier material (high CA to cation ratio) was 85.1% at 1150⁰C. In synthesis of LSGM using CA only as the solvent for gallium sulfate (low CA to cation ratio), maximum amount of LSGM phase obtained was 73.6% at 1200⁰C. Thus, the increased

percentage of LSGM phase for the experiment with a high amount of CA may be connected with the positive performance of citric acid as the carrier material.

The unknown B phase was not observed in any other experiment sets in this study, therefore this phase may be a sulphur-containing phase, stemming from the use of gallium sulfate as the starting material.

In order to prove our speculation that above 1100⁰C, the (LaO)₂SO₄ decomposition leads to the formation of LSGM, it is essential to prove the stability of (LaO)₂SO₄ phase over LSGM phase up to 1100⁰C. For this reason, synthesis of (LaO)₂SO₄ phase was undertaken as described in section 3.1.1.2.2. The XRD plots in Figure 3.1, show that the (LaO)₂SO₄ phase formed before 800⁰C, and is the only x-ray detectable phase in the system at this temperature. Referring to the STA plot of the sample previously heated to 800⁰C in Figure 3.2, decomposition of (LaO)₂SO₄ phase started at about 1050⁰C. This is consistent with the strong x-ray diffraction peaks of LSGM at 1150⁰C and 1200⁰C (see App. C3). Mass loss in the STA plot between 1050⁰C and 1200⁰C can be explained by removal of the sulfate group of the (LaO)₂SO₄ compound. Around 10 wt% mass loss is consistent with the amount of the sulfate group in the system at 1050⁰C.

As it can be seen in the x-ray plot of the synthesized (LaO)₂SO₄ in Figure 3.1, the formation of crystal (LaO)₂SO₄ phase starts around 400⁰C. Thus, formation of amorphous (LaO)₂SO₄ phase at 236⁰C is likely.

In Figure 4.17, the exothermic peaks between 600⁰C and 750⁰C may be attributed to the stepwise removal of sulfates and charred citric acid. The almost constant DTA curve between 800⁰C and 1200⁰C is due to “slow” simultaneous decomposition-crystallization reactions. Additionally, between 800⁰C and 1000⁰C, there is no change in the DTA plot, which is consistent with the almost constant amount of crystalline phases in this temperature range, as shown in the in App. D2 and D3 tables.

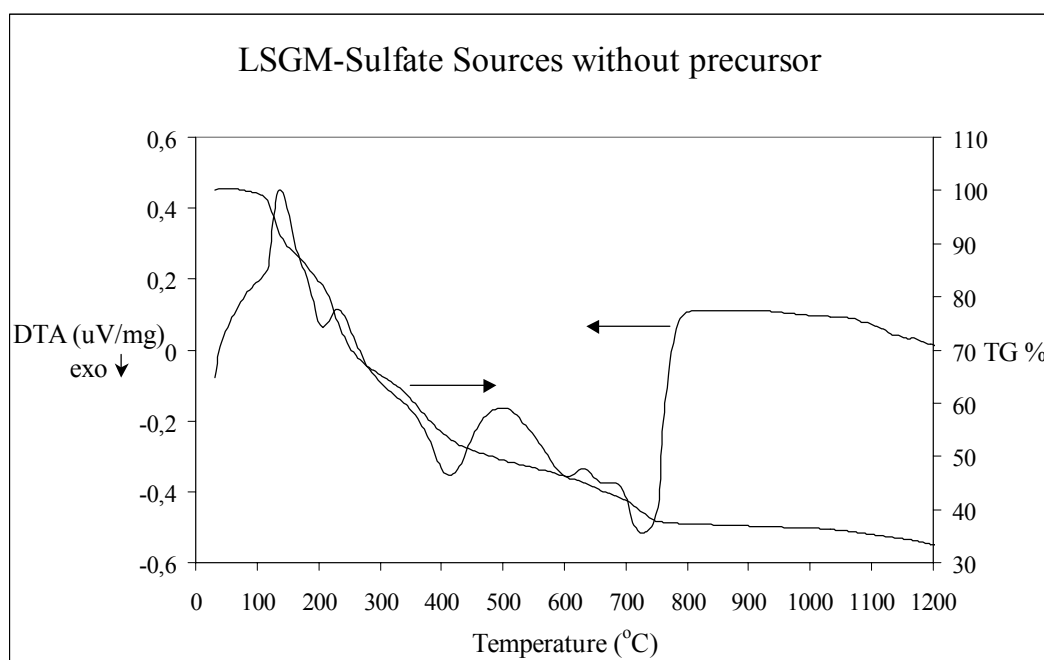


Figure 4.17. STA plot of the precursor for LSGM synthesis without any organic carrier material, and with sulfate source of gallium.

The largest mass loss between 1100⁰C and 1200⁰C is most probably due to decomposition of the (LaO)₂SO₄ phase (from 948 to 172 counts) and consequent sulfate-group removal. Also the endothermic peaks around 1150⁰C may be due to decomposition of (LaO)₂SO₄ and LaSrGa₃O₇ phases. The relatively small exothermic peak at approximately same temperature may be due to SO₃ removal with the corresponding mass loss, or due to crystallization of LSGM phase (see Figure 4.17).

It should be noted that the presence of (LaO)₂SO₄ phase in the system prevents the formation of LaSrGaO₄ and La₄Ga₂O₉ phases, which were present in all other experiments conducted with/without carrier materials and complicated LSGM formation.

4.4.2. Effect of Lanthanum Chloride

As an alternative route in synthesis of LSGM powders, lanthanum chloride (as lanthanum source) and nitrate salts of strontium, gallium, and magnesium were used. The melting point of LaCl₃ is 860⁰C according to CRC Handbook [105]. By using the

stability of LaCl_3 up to 860°C , prevention of the formation of unwanted phases such as $\text{La}_2\text{Ga}_4\text{O}_9$, $\text{LaSrGa}_3\text{O}_7$, LaSrGaO_4 , and unknown phases was aimed.

At 800°C the system was completely composed of the LaOCl crystalline phase. With increasing temperature, decomposition of the LaOCl phase and simultaneous formation of the $\text{LaSrGa}_3\text{O}_7$ phase were observed. Between 900°C and 1050°C , the decomposition of the LaOCl phase resulted in the La_2O_3 phase formation. Reaction of this La_2O_3 phase with the gallium and strontium cations of the x-ray amorphous powder, may have produced the $\text{LaSrGa}_3\text{O}_7$ phase. As shown earlier, the $\text{LaSrGa}_3\text{O}_7$ phase is more stable than LSGM phase in this temperature range and in the absence of carrier materials. A similar behavior was observed in the powders prepared without any organic carrier material. The sharp increase in the amount of the LSGM phase was seen again between 1050°C and 1100°C from 12.4% to 71.8%. The reason of this sharp increase may be the decomposition of both $\text{LaSrGa}_3\text{O}_7$ (from 33.9% to 5%) and LaOCl phases (from 53.7% to 23.2%).

Above 1150°C , formation of LaSrGaO_4 phase was again observed. Formation of the LaSrGaO_4 phase between 1100°C and 1150°C may be due to continued decomposition of the LaOCl phase between these temperatures. Moreover, formation of unknown phases A and C were observed between 1100°C and 1150°C , which may also be due to decomposition of the LaOCl phase. These two arguments may be strengthened by the fact that only LaOCl decomposed between these temperatures. On the other hand, between 1150°C and 1200°C slight increase in the LaSrGaO_4 phase (from 4.4% to 4.7%), as well as the increase in the amounts of unknown phases (A and C) may be due to consumption of some LSGM phase (from 82.2% to 80.0%) and/or decomposition of the $\text{LaSrGa}_3\text{O}_7$ phase (from 7% to 6.4%). The LaSrGaO_4 phase tends to increase in the synthesis of LSGM powder with or without carrier materials between 1150°C and 1200°C , due to the stability of LaSrGaO_4 over LSGM. In Table 3.2, it can be seen that formation of LaSrGaO_4 phase occurs (from 0% to 12.4%), which leads to a decrease in the concentrations of the other phases, when the powder was held 7 hours at the calcination temperature. This may indicate that the formation LaSrGaO_4 is due to decomposition of other phases, but not due to crystallization of x-ray amorphous LaSrGaO_4 phase.

To discuss the behavior of the unknown phases, the identification of these phases should be done. It may be worthwhile studying the characterization of these phases. Unknown C phase may contain chlorine atoms, because unknown C was not

observed in any other experiments and this was the only experiment in which chloride source was used.

4.5.Effect of Holding Time and Durability Test

To determine the effect of holding time at calcination temperatures on LSGM phase formation, selected powders are calcined for 7 hours at their calcination temperature, at which the maximum LSGM percentage was obtained.

The most prominent effect was seen in LSGM synthesized with PVA as the organic carrier material and calcined at 1100⁰C. The concentration of LSGM phase in the powder increased from 33.7% to 79.8% by holding for 7 hours (see Table 3.2). Large decreases in the amounts and concentrations of LaSrGa₃O₇ and La₄Ga₂O₉ phases indicate decomposition of these phases and formation of LSGM phase. In addition to formation of large amounts LSGM phase, an increase in the amount and concentration of the LaSrGaO₄ phase was also observed. This confirms simultaneous occurrence of reactions 4.4 and 4.7, which are described in section 4.2.

In the other powders, approximately the same LSGM concentrations in the powders were observed. In each powder, an increase in the amount and concentration of LaSrGaO₄ was observed. This is believed to be mostly due to decomposition of the LaSrGa₃O₇ phase into LaSrGaO₄ phase (see reaction 4.4 in section 4.2.). In the absence of LaSrGa₃O₇ phase, (LSGM synthesized with CA and calcined at 1100⁰C) a decrease in the amount and concentration of LaSrGaO₄ phase was observed, consistent with the proposed behavior of the LaSrGaO₄ phase behavior described in section 4.2.

A previous study reported that, even the single-phase LSGM powders that are initially synthesized at or above 1400⁰C may not be thermally stable at the SOFC service temperatures ($\leq 800^0$ C) and undesired phases such as LaSrGa₃O₇ and LaSrGaO₄ may reappear in the powders [93]. Therefore, to examine chemical stability of the synthesized LSGM phase, previously synthesized powders were tested by holding for 11 days at 800⁰C, which is considered as the maximum service temperature of intermediate temperature SOFCs (IT-SOFC). As seen from the x-ray plots of the powders and associated tables containing concentrations and amounts of each phase, there was no considerable change in the phase amounts and concentrations in the

powders (see App. I and Table 3.1). Thus, once formed, LSGM may be stable at the operating temperature in the absence of any catalyst for its decomposition.

4.6. Peak Shift

In synthesis of LSGM powders, the x-ray diffraction peaks of the product $\text{La}_4\text{Ga}_2\text{O}_9$, and LSCM phases exhibited a shift to the left in 2θ axis of the x-ray diffraction plots. The possible reasons of these peak-shifts are investigated.

4.6.1. $\text{La}_4\text{Ga}_2\text{O}_9$ Peaks

In all of the LSGM synthesis other than the experiment conducted by gallium sulfate, $\text{La}_4\text{Ga}_2\text{O}_9$ phase was observed and the peaks were shifted to the left of the peaks of the reference $\text{La}_4\text{Ga}_2\text{O}_9$ phase (JCPDS no: 37-1433). Magnesium and strontium have solubility limit of %16 in the LSGM phase, and the remaining magnesium and/or strontium atoms precipitate in the matrix [113]. According to the composition used in this study ($\text{La}_{0.9}\text{Sr}_{0.1}\text{Ga}_{0.8}\text{Mg}_{0.2}\text{O}_{2.85}$) magnesium addition is approximately 20%. Thus, the amount of magnesium, which did not dissolve in LSGM (~4%), should be detected by x-ray diffractometer. A possible explanation for the lack of magnesium related peaks may be that magnesium substitutes gallium in the $\text{La}_4\text{Ga}_2\text{O}_9$ phase. The reason of the peak shift in the $\text{La}_4\text{Ga}_2\text{O}_9$ phase may be explained by the Mg^{2+} ion substitution to the Ga^{3+} sites. The crystal ionic radius of Mg^{2+} ion (0.072 nm) is larger than Ga^{3+} ion (0.062 nm), if coordinated by 6 oxygens (see Table 4.3). Thus, a substitution of Mg^{2+} ions to the Ga^{3+} site may result in a larger unit cell.

Table 4.3. Crystal ionic radius of the cations for coordination number 6 [114].

	<i>Crystal Ionic Radius(nm)</i> <i>Coordination No: 6</i>
<i>La</i>³⁺	0,106
<i>Sr</i>²⁺	0,116
<i>Ga</i>³⁺	0,062
<i>Mg</i>⁺²	0,072
<i>Fe</i>³⁺	0,065
<i>Cr</i>³⁺	0,062

Therefore, the resultant dimensions of the unit cell can slightly be larger than the dimensions of the unit cell of La₄Ga₂O₉. According to the relation between lattice parameters “*a, b, c*” and interplanar spacing, “*d*” for the monoclinic unit cell of La₄Ga₂O₉ (see Equation 4.10), unit cell dimensions are proportional to the interplanar spacing.

$$\frac{1}{d^2} = \frac{1}{\sin^2 \beta} \left(\frac{h^2}{a^2} + \frac{k^2 \sin^2 \beta}{b^2} + \frac{l^2}{c^2} - \frac{2hl \cos \beta}{ac} \right) \quad (4.10)$$

where: *d* is the interplanar spacing, *a, b, c* are lattice parameters, *h, k, l* are Miller indices of a plane in a unit cell, and β is the only angle of monoclinic unit cell, which is not equal to 90⁰. According to Bragg’s condition (see Equation 4.11), an increase in the interplanar spacing generates decrease in diffraction angle θ .

$$n\lambda = 2d \sin \theta \quad (4.11)$$

where: *n* is an integer number, λ is the wavelength of the x-ray, *d* is the interplanar spacing of a specific plane in a unit cell, and θ is the diffraction angle in x-ray diffraction. This result confirms our hypothesis in explaining the peak shifts of the La₄Ga₂O₉ phase.

The lattice parameters *a, b, and c* of the supposed La₄Ga₂O₉ phase with supposed Mg²⁺ substitution into Ga³⁺ sites, are calculated according to equation 4.10. Also the approximate monoclinic unit cell volume is calculated (see Table 4.4). As suggested

before, an increase in the unit cell dimensions can be seen from Table 4.4. The increase in the unit cell by substitution of Mg^{2+} ions to Ga^{3+} sites, is approximately 0.39%.

Table 4.4. Lattice parameters of $La_4Ga_2O_9$ and $La_4Ga_{2-x}Mg_xO_{9-\delta}$ phases.

	a*	b*	c*	Volume of Unit Cell[#]
$La_4Ga_2O_9$	7.974	10.968	11.569	~960.64
$La_4Ga_{2-x}Mg_xO_{9-\delta}$	7.987	10.981	11.682	~964.43

*: unit of Angstrom , #: unit of cubic Angstrom

4.6.2. LSCM Peaks

In the synthesized LSCM powders, x-ray diffraction peaks of the LSCM phase shifted to the left compared to $LaCrO_3$ peaks. The 2θ and d values for synthesized LSCM and $LaCrO_3$ phase for the selected planes are tabulated in Table 4.5.

Table 4.5. Diffraction angles and interplanar spacings of $LaCrO_3$ and LSCM phases for the selected crystallographic planes.

Plane	$LaCrO_3$			LSCM		
	(110)	(002)	(112)	(110)	(002)	(112)
2θ	22.902 ⁰	22.962 ⁰	32.594 ⁰	22.81 ⁰	22.9 ⁰	32.5 ⁰
d^*	3.88	3.87	2.745	3.8954	3.8804	2.75275

*: units in Angstrom

It may be possible that Sr^{2+} ions substitute into La^{3+} sites, and Mg^{2+} ions substitute into Cr^{3+} sites. From Table 4.3, it can be seen that ionic radius of strontium is larger than lanthanum ions, and magnesium ions are larger than gallium ions. Therefore substitution of these ions to the lanthanum and chromium sites may increase the unit cell dimensions of the LSCM phase. Thus, lattice parameters of LSCM phase may be larger than $LaCrO_3$ lattice parameters. According to the relation between lattice parameters “ a, b, c ” and interplanar spacing, “ d ” for the orthorhombic unit cell of $LaCrO_3$ (see equation 4.12), unit cell dimensions are proportional to the interplanar spacing.

$$\frac{1}{d^2} = \frac{h^2}{a^2} + \frac{k^2}{b^2} + \frac{l^2}{c^2} \quad (4.12)$$

where: d is the interplanar spacing, a, b, c are lattice parameters, h, k, l are Miller indices of a plane in a unit cell. According to the Bragg condition (see Equation 4.11), an increase in the plane spacing decreases the diffraction angle θ , consistent with the peak shifts of LSCM phase relative to the LaCrO_3 phase.

The lattice parameters a , b , and c of the supposed LSCM phase with supposed Mg^{2+} substitution into Cr^{3+} sites, are calculated according to equation 4.12. Also the orthorhombic unit cell volume is calculated (see Table 4.6). As demonstrated before, the increase in the unit cell dimensions can be seen from Table 4.6. The increase in the unit cell by substitution of Mg^{2+} ions into Cr^{3+} sites, and Sr^{2+} ions into La^{3+} sites is approximately 0.89%.

Table 4.6. Lattice parameters of LaCrO_3 and LSCM phases.

	a*	b*	c*	Volume of Unit Cell[#]
LaCrO₃	5.479	5.513	7.756	~234.28
LSCM	5.497	5.531	7.774	~236.36

*: unit of Angstrom, #: unit of cube of Angstrom

4.7. Overall Discussion and Future Work

LSGM is one of the rare candidate electrolyte materials for IT-SOFCs. The problems associated with this material are mainly: undesired phase formations during synthesis, sintering, and/or service [37,77,88,90], and gallium depletion in the form of $\text{Ga}_2\text{O}(\text{g})$ or $\text{Ga}(\text{g})$ at high operation temperatures ($> 800^\circ\text{C}$) and in reducing atmospheres [88,91]. In our study, gallium loss was not observed. However, it must be mentioned that the synthesis atmosphere was not reducing.

Single-phase LSGM synthesis temperatures are reported as above 1300°C in the literature [78,101,108]. Synthesis of powders with different organic carrier materials via organic precursor method below 1200°C with near or more than 90% LSGM phase (i.e.

95.7% at 1150⁰C with TA, 88% at 900⁰C with CA, 93.7% at 1150⁰C with PVA, 92.8% at 1150⁰C with Pechini precursor) may be regarded as a success in decreasing the synthesis temperature of single-phase LSGM powder. Moreover, it was showed that increasing holding time at calcination temperature increases the concentration of the LSGM phase in the powders even further.

The formation of LSFM powders is likely to occur with a structure similar to that of strontium-doped lanthanum ferrite material, which was reported to be a good candidate for cathode material in SOFCs [115,116]. A previous work reports that the two-cation oxide (LaFeO₃) was synthesized at 550⁰C (with 6 hours holding time) by the Pechini process [117], but single-phase Sr-doped lanthanum ferrite could not be synthesized even after a 1200⁰C calcination [115]. Thus, single-phase synthesis of four-cation oxide, LSFM, at 550⁰C without holding time is an important achievement. Similarly, synthesized LSCM powders are believed to be a similar in structure to strontium-doped lanthanum chromite material, which was reported as an interconnect [118,119] and anode [47,120] material for SOFCs. Previous work reported that synthesis of Sr-doped LaCrO₃ was possible at or above 1000⁰C [47,118]. In comparison to these reports, 96.9% four-cation oxide (LSCM) synthesis at 850⁰C without holding time is also believed to be an achievement. After determination of most proper organic carrier material, the optimum catio-to-organic carrier material ratio and different holding times at calcination temperatures, single-phase LSGM and LSCM powders may be obtained at lower synthesis temperatures than those reported in the literature.

We conclude that the high amount of La₄Ga₂O₉ phase formation at low temperatures ($\leq 800^0\text{C}$) compared to LaSrGa₃O₇ and LSGM phases, and formation of LaSrGaO₄ and unknown A phases at high temperatures ($> 1000^0\text{C}$) are the main obstacles of single-phase LSGM synthesis. It may be essential to work on identification of unknown A phase and elimination of these phases during LSGM powder synthesis.

Cation – functional group interaction may play an important role in mixed oxide powder synthesis via organic precursor method. The functional group of the organic carrier may exhibit a different affinity to different ions and/or ion groups. According to the degree of this interaction for each ion, functional groups of the organic carrier material may release one or more chelated/complexed cation(s). This may result in the formation of phases with undesired composition. It may be essential to work on the interactions of functional groups of different organic carrier material with different cations. The usage of nuclear magnetic resonance spectrometry (NMR) can be helpful in

identification of the chemical nature of the powders, which are calcined at different temperatures. Changes in the molecular level environments of the ions can be determined after each calcination step. Infrared spectrometry (IR) can also be a useful technique to identify the chemical functional group compositions, and relative amount of such groups.

In the synthesis of powders (LSGM, LSFM, and LSCM) with ethylene diaminetetraacetic acid (EDTA), inconsistent results were obtained in terms of phase purity of synthesized powders. More studies with EDTA as the organic carrier material in mixed oxide powder synthesis must be conducted. It may be essential to dissolve EDTA in solutions with different additives. Ammonia most likely decreases chelating ability of EDTA considerably.

Formation of lanthanum oxysulfate phase ($\text{La}_2\text{O}_2\text{SO}_4$) was observed in LSGM synthesis with gallium sulfate as the gallium source, and nitrates of lanthanum, strontium, and magnesium as the corresponding cation sources. Lanthanum oxysulfate was reported to increase the Na^+ conductivity of the Na_2SO_4 phase forming $\text{La}_2\text{O}_2\text{SO}_4 - \text{Na}_2\text{SO}_4$ solid solution [121]. It may be essential to determine the effects of lanthanum oxysulfate on the oxygen ion conductivity of LSGM electrolyte material.

In LSGM synthesis with lanthanum chloride as the lanthanum sources and nitrates of strontium, gallium, and magnesium as the corresponding cation sources, present phases were 71.8% LSGM, 23.2% LaOCl , and 5% $\text{LaSrGa}_3\text{O}_7$ at 1100°C . Except 5% $\text{LaSrGa}_3\text{O}_7$ phase, the powder calcined at 1100°C may be thought as a two-phase LSGM – LaOCl system. LaOCl is known as a chlorine ion conductor material [122], and this material possesses chlorine ion vacancies. With its chlorine ion vacancies, the existence of LaOCl phase may be not as detrimental to the ionic conductivity of LSGM, as was the case with the other impurity phases such as LaSrGaO_4 , $\text{La}_4\text{Ga}_2\text{O}_9$, and $\text{LaSrGa}_3\text{O}_7$.

Doping of 20% Ca^{2+} ions to the La^{3+} site creates additional chlorine vacancies, and the ionic conductivity of LaOCl increases considerably [123]. Therefore, it may be essential to investigate the effects of cations in LSGM (namely La^{3+} , Sr^{2+} , Ga^{3+} , and Mg^{2+}) on the ionic conductivity of the overall LSGM – LaOCl system. The absence of LaSrGaO_4 phase in the final powder may be a promising achievement in terms of gallium loss in the form of Ga_2O at operating temperatures of solid oxide fuel cells [90]. Synthesis temperature of 1100°C is another promising feature compared to single-phase synthesis temperature above 1300°C [124,125].

This is the first report of the LSGM – LaOCl system. To be leveraged as the electrolyte material in an SOFC, we will need to characterize the ionic and electronic conductivity, thermal expansion, and electrode compatibility.

CHAPTER 5

CONCLUSIONS

In this study, synthesis of LSGM, LSFM, and LSCM powders were performed via organic precursor method by using different organic carrier materials.

When calcined at a low temperature ($< 1000^{\circ}\text{C}$), precursors synthesized using citric acid (CA) as the organic carrier material yielded 88% LSGM phase in the powders. Maximum LSGM concentration (95.7%) in the synthesized powders was obtained at 1150°C using tartaric acid (TA) as the organic carrier material. In contrast to LSGM, single-phase LSFM was obtained with relative ease in the powder calcined at 550°C . CA appeared to be most effective precursor for low temperature synthesis of LSFM. The best concentration of LSCM phase in the synthesized powders was 96.9%, when polyvinyl alcohol (PVA) was used as the organic carrier material.

Every organic carrier material has exhibited a different performance for the synthesis of different powders. When CA was used as the organic carrier material in LSGM synthesis, LSGM concentration in the powders was 88% when calcined at 900°C . The powders synthesized with PVA as the organic carrier material, there was no x-ray crystalline LSGM phase at 900°C .

Moreover, the performance of one organic carrier material varied for each type of mixed oxide powder synthesis. TA was the best organic carrier material for LSGM synthesis at calcination temperatures larger than 1000°C , but it performed poorly in LSCM synthesis when compared to PVA at all calcination temperatures. Maximum LSCM concentration in the powders was 85.7% when TA was used as the organic carrier material at 800°C , whereas even the minimum LSCM concentration in the powders was 88.8% at as low as 550°C , when PVA was used as the organic carrier material.

Other than the cation chelating and/or complexing ability of the functional groups of the organic carrier materials, the interaction with cations may play an important role in synthesis of mixed oxide powders at relatively low temperatures.

In LSGM synthesis, when gallium sulfate was used as the gallium source, lanthanum oxysulfate was formed below 400⁰C and was more stable over the LSGM phase up to 1150⁰C. Thus lanthanum oxysulfate formation suppressed formation of LSGM phase in the powders below 1150⁰C. Besides preventing formation of LSGM phase, lanthanum oxysulfate suppressed formation of La₄Ga₂O₉ and LaSrGaO₄ phases, which were always present in the powders when nitrate sources of cations were used. When lanthanum chloride was used as the lanthanum source, lanthanum oxychloride formed in the powders and this phase was more stable than LSGM phase up to 1100⁰C. Again formation of La₄Ga₂O₉ was prevented. However, LaSrGaO₄ phase was present in the powders. Therefore we conclude that using different starting materials as the cation sources can eliminate some of the undesired phases during powder synthesis, but may also be the source of new phases other than the target phase.

Calcination of the LSGM powders at 1100⁰C produced 33.7% LSGM phase when PVA was used as the organic carrier material. When the same powder was held at 1100⁰C for 7 hours, 79.8% LSGM phase was observed in the powders. Thus, increasing the holding time at the calcination temperatures increases the LSGM phase concentration in the powders. However, holding powders at their calcination temperature also increased the concentrations of LaSrGaO₄ phase. Formation of LaSrGaO₄ is due to i) decomposition of LSGM phase at or above 1150⁰C in the absence of LaSrGa₃O₇ phase, and ii) decomposition of LaSrGa₃O₇ phase when present.

To determine stability of LSGM phase at SOFC operation temperature, synthesized LSGM powders were held for 11 days at 800⁰C. The changes in the concentrations of phases were within the experimental error limit.

REFERENCES

1. W.R. Grove, "On voltaic series and the combination of gases by platinum", *Phil. Mag.* 14, 127-130 (1839)
2. A. Boudghene Stambouli, E. Traversa, "Fuel Cells, an alternative to standard sources of energy", *Renewable and Sustainable Energy Reviews* 6, 297-306 (2002)
3. J.H. Hirschenhofer, D.B. Stauffer, R.R. Engleman, M.G. Klett, "Fuel Cell Handbook", 4th Edition, Orinda, USA, 1997
4. Seungdoo Park, Raymond J. Gorte, John M. Vohs, "Application of heterogeneous catalysis in the direct oxidation of hydrocarbons in a solid-oxide fuel cell", *Applied Catalysis A: General* 200, 55-61 (2000)
5. S. Katikaneni, C. Yuh, S. Abens, M. Farooque, "The direct carbonate fuel cell technology: advances in multi-fuel processing and internal reforming", *Catalysis Today* 77, 99-106 (2002)
6. B.C.H. Steele, *Solid State Ionics* 129, "Appraisal of $Ce_{1-y}Gd_yO_{2-y/2}$ electrolytes for IT-SOFC operation at 500⁰C", 95-110 (2000)
7. G.F.McLean, T.Niet, S.Prince-Richard, N.Djilali, "An assessment of alkaline fuel cell technology", *International Journal of Hydrogen Energy* 27, 507-526 (2002)
8. Vogel W, Lundquist JT, *J. Electrochem. Soc.* 117, 1512 (1970)
9. Al-Saleh MA, Gultekin S, Al-Zakri AS, Celiker H, "Effect of carbon dioxide on the performance of Ni =PTFE and Ag =PTFE electrodes in an alkaline fuel cell", *J. Appl. Electrochem.* 24, 575 –80 (1994)
10. Al-Saleh MA, Gultekin S, Al-Zakri AS, Celiker H, "Performance of porous nickel electrode for alkaline H₂\O₂ fuel cell", *Int. J. Hydrogen Energy* 19, 713 –8 (1994)
11. Kordesch K, Gunter S, "Fuel cells and their applications" Berlin, Germany: Wiley-VCH, 1996.

12. Gultekin S, Al-Saleh MA, Al-Zakri AS, "Effect of CO impurity in H₂ on the performance of Ni =PTFE diffusion electrodes in alkaline fuel cells", *Int. J. Hydrogen Energy* 19, 181 –5 (1994)
13. Kiros Y, "Tolerance of gases by the anode for the alkaline fuel cell", 1994 Fuel Cell Seminar, San Diego, CA, 1994
14. M. Rikukawa, K. Sanui, "Proton-conducting polymer electrolyte membranes based on hydrocarbon polymers, *Prog. Polym. Sci.* 25, 1463-1502 (2000)
15. S. Ahmed, J. Kopasz, R. Kumar, M. Krumpelt, "Water balance in a polymer electrolyte fuel cell system", *Journal of Power Sources* 112, 519-530 (2002)
16. M.H. Fronk, D.L. Wetter, D.A. Masten, A. Bosco, "PEM Fuel Cell System Solutions for Transportation", SAE Technical Paper Series, No. 2000-01-0373.
17. Viral Metha, Joyce Smith Cooper, "Review and analysis of PEM fuel cell design and manufacturing", *Journal of Power Sources* 114, 32-53 (2003)
18. T. Susai, A. Kawakami, A. Hamada, Y. Miyake, Y. Azegami, "Development of a 1 kW polymer electrolyte fuel cell power source", *Journal of Power Sources* 92, 131-138 (2001)
19. Cecilia Wallmark, Per Alvfors, "Design of stationary PEFC system configurations to meet heat and power demands", *Journal of Power Sources* 106, 83-92 (2002)
20. E. Danial Doss, R. Kumar, R.K. Ahluwalia, M. Krumpelt, "Fuel processors for automotive fuel cell systems: a parametric analysis", *Journal of Power Sources* 102, 1-15 (2001)
21. Paola Costamagna, Supramaniam Srinivasan, "Quantum jumps in the PEMFC science and technology from the 1960s to the year 2000 Part I. Fundamental scientific aspects", *Journal of Power Sources* 102, 242-252 (2001)
22. Suman Roy Choudhury, M.B. Deshmukh, R. Rengaswamy, "A two-dimensional steady-state model for phosphoric acid fuel cells (PAFC)", *Journal of Power Sources* 112, 137-152 (2002)
23. J.P. Vanhanen, P.S. Kauranen, P.D. Lund, "Operation experiences of a phosphoric acid fuel cell in a solar hydrogen energy system", *Int. J. Hydrogen Energy*, vol.22, no.7, 707-713 (1997)
24. M. Ghouse, H. Abaoud, A. Al-Boeiz, "Operational experience of a 1 kW PAFC stack", *Applied Energy* 65, 303-314 (2000)

25. B. Zhu, "Advantages of intermediate temperature solid oxide fuel cells for tractionary applications", *Journal of Power Sources* 93, 82-86 (2001)
26. Vidya S. Batra, Sanjay Bali, S. Venkatesh, "Fabrication of porous components for molten carbonate fuel cells", *Ceramics International*, Volume 29, Issue 5, 547-553 (2003)
27. José Luz Silveira, Elisangela Martins Leal, Luis F. Ragonha Jr., "Analysis of molten carbonate fuel cell: cogeneration to produce electricity and cold water", *Energy* 26, 891-904 (2001)
28. Shigenori Mitsushima, Koichi Matsuzawa, Nobuyuki Kamiya, Ken-ichiro Ota, "Improvement of MCFC cathode stability by additives", *Electrochimica Acta* 47, 3823-3830 (2002)
29. Prabhu Ganesan, Hector Colon, Bala Haran, Ralph White, Branko N. Popov, "Study of cobalt-doped lithium–nickel oxides as cathodes for MCFC", *Journal of Power Sources* 111, 109-120 (2002)
30. Choong-Gon Lee, Byoung-Sam Kang, Hai-Kyung Seo, Hee-Chun Lim, "Effect of gas-phase transport in molten carbonate fuel cell", *Journal of Electroanalytical Chemistry* 540, 169-188 (2003)
31. Changrong Xia, Meilin Liu, "Microstructures, conductivities, and electrochemical properties of $Ce_{0.9}Gd_{0.1}O_2$ and GDC – Ni anodes for low-temperature SOFCs", *Solid State Ionics* 152-153, 423-430 (2002)
32. D.V. Schur, B.P. Tasarov, S. Yu. Zaginaichenko, V.K. Pishuk, T.N. Veziroglu, Yu.M. Shul'ga, A.G. Dubovoi, N.S. Anikina, A.P. Pomytkin, A.D. Zolotareno, "The prospects for using carbon nanomaterials as hydrogen storage systems", *International Journal of Hydrogen Energy* 27, 1063-1069 (2002)
33. V. Karakoussis, N.P. Brandon, M. Leach, R. van der Vorst, "The environmental impact of manufacturing planar and tubular solid oxide fuel cells", *Journal of Power Sources* 101, 10-26 (2001)
34. A. Boudghene Stambouli, E. Traversa, "Solid oxide fuel cells (SOFCs): a review of an environmentally clean and efficient source of energy", *Renewable and Sustainable Energy Reviews* 6, 433-455 (2002)
35. S.C. Singhal, "Solid oxide fuel cells for stationary, mobile, and military applications", *Solid State Ionics* 152-153, 405-410 (2002)
36. F. Tietz, H.-P. Buchkremer, D. Stöver, "Components manufacturing for solid oxide fuel cells", *Solid State Ionics* 152-153, 373-381 (2002)

37. Keqin Huang, John B. Goodenough, "A solid oxide fuel cell based on Sr- and Mg-doped LaGaO₃ electrolyte: the role of a rare-earth oxide buffer", *Journal of Alloys and Compounds* 303-304, 454-464 (2000)
38. J. Fleig, K.D. Kreuer, J. Maier, "Handbook of Advanced Ceramics", *Materials, Applications, and Processing*, Academic Press, 1-60 (2001)
39. W.Z. Zhu, S.C. Deevi, "Development of interconnect materials for solid oxide fuel cells", *Materials Science and Engineering A*, Volume 348, Issues 1-2, 227-243 (2003)
40. J.T.S. Irvine, D.P. Fagg, J. Labrincha, F.M.B. Marques, "Development of novel anodes for solid oxide fuel cells", *Catalysis Today* 38, 467-472 (1997)
41. B. de Boer, M. Gonzales, H.J.M. Bouwmeester, H. Verweij, "The effect of the presence of fine YSZ particles on the performance of porous nickel electrodes", *Solid State Ionics* 127, 269-276 (2000)
42. Ying Li, Yusheng Xie, Jianghong Gong, Yunfa Chen, Zhongtai Zhang, "Preparation of Ni/YSZ materials for SOFC anodes by buffer-solution method", *Material Science and Engineering B86*, 119-122 (2001)
43. Mohan K. Dongare, Avinash M. Dongare, V.B. Tare, Erhard Kemnitz, "Synthesis and characterization of copper-stabilized zirconia as an anode material for SOFC", *Solid State Ionics* 152-153, 455-462 (2002)
44. Zhe Lü, Li Pei, Tian-min He, Xi-qiang Huang, Zhi-guo Liu, Yuan Ji, Xing-hai Zhao, Wen-hui Su, "Study on new copper-containing SOFC anode materials", *Journal of Alloys and Compounds* 334, 299-303 (2002)
45. Olga A. Marina, Nathan L. Canfield, Jeff W. Stevenson, "Thermal, electrical, and electrocatalytical properties of lanthanum-doped strontium titanate", *Solid State Ionics* 149, 21-28 (2002)
46. A.-L. Sauvet, J. Fouletier, "Electrochemical properties of a new type anode material La_{1-x}Sr_xCr_{1-y}Ru_yO_{3-δ} for SOFC under hydrogen and methane at intermediate temperatures", *Electrochimica Acta* 47, 987-995 (2001)
47. A.-L. Sauvet, J. Fouletier, F. Gaillard, M. Primet, "Doped lanthanum chromites as SOFC anode materials", *J. of Catalysis* 209 (1), 25-34 (2002)
48. Shizhong Wang, Yi Jiang, Yahong Zhang, Wenzhao Li, Jingwang Yan, Zigui Lu, "Electrochemical performance of mixed ionic-electronic conducting oxides as anodes for solid oxide fuel cell", *Solid State Ionics* 120, 75-84 (1999)

49. Stephanie J.A. Livermore, John W. Cotton, R. Mark Ormerod, "Fuel reforming and electrical performance studies in intermediate temperature ceria-gadolinia based SOFCs", *Journal of Power Sources* 86, 411-416 (2000)
50. B.C.H. Steele, "Materials for IT-SOFC stacks 35 years R&D: the inevitability of gradualness?", *Solid State Ionics* 134, 3-20 (2000)
51. M. Sahibzada, B.C.H. Steele, K. Zheng, R.A. Rudkin, I.S. Metcalfe, "Development of solid oxide fuel cells based on a Ce(Gd)O_{2-x} electrolyte film for intermediate temperature operation", *Catalysis Today* 38, 459-466 (1997)
52. M. Sahibzada, B.C.H. Steele, D. Barth, R.A. Rudkin, I.S. Metcalfe, "Operation of solid oxide fuel cells at reduced temperatures", *Fuel* 78, 639-643 (1999)
53. Mortaza Sahibzada, Brian C.H. Steele, Klaus Hellgardt, Dieter Barth, Astrid Effendi, Dionissos Mantzavinos, Ian S. Metcalfe, "Intermediate temperature solid oxide fuel cells operated with methanol fuels", *Chemical Engineering Science* 55, 3077-3083 (2000)
54. A. Hartley, M. Sahibzada, M. Weston, I.S. Metcalfe, D. Mantzavinos, "La_{0.6}Sr_{0.4}Co_{0.2}Fe_{0.8}O₃ as the anode and cathode for intermediate temperature solid oxide fuel cells", *Catalysis Today* 55, 197-204 (2000)
55. Kiyoshi Kuroda, Ikiko Hashimoto, Kazunori Adachi, Jun Akikusa, Yoshitaka Tamou, Norikazu Komada, Tatsumi Ishihara, Yusaku Takita, "Characterization of solid oxide fuel cell using doped lanthanum gallate", *Solid State Ionics* 132, 199-208 (2000)
56. Toru Inagaki, Kazuhiro Miura, Hiroyuki Yoshida, Radenka Maric, Satoshi Ohara, Xinge Zhang, Kazuo Mukai, Takehisa Fukui, "High-performance electrodes for reduced temperature solid oxide fuel cells with doped lanthanum gallate electrolyte II. La(Sr)CoO₃ cathode", *Journal of Power Sources* 86, 347-351 (2000)
57. Keqin Huang, John B. Goodenough, "A solid oxide fuel cell based on Sr- and Mg-doped LaGaO₃ electrolyte: the role of a rare-earth oxide buffer", *Journal of Alloys and Compounds* 303-304, 454-464 (2000)
58. J. Fleig, "On the width of the electrochemically active region in mixed conducting solid oxide fuel cell cathodes", *Journal of Power Sources* 105, 228-238 (2002)
59. T. Kenjo, Y. Kanehira, "Influence of the local variation of the polarization resistance on SOFC cathodes", *Solid State Ionics* 148, 1-14 (2002)

60. Yoshio Matsuzaki, Isamu Yasuda, "Electrochemical properties of a SOFC cathode in contact a chromium-containing alloy separator", *Solid State Ionics* 132, 271-278 (2000)
61. S. Charojrochkul, K.-L. Choy, B.C.H. Steele, "Cathode/electrolyte systems for solid oxide fuel cells fabricated using flame assisted vapour deposition technique", *Solid State Ionics* 121, 107-113 (1999)
62. E. Boehm, J.-M. Bassat, M.C. Steil, P. Dordor, F. Mauvy, J.-C. Greiner, "Oxygen transport properties of $\text{La}_2\text{Ni}_{1-x}\text{Cu}_x\text{O}_{4+\delta}$ mixed conducting oxides", *Solid State Sciences* 5, 973-981 (2003)
63. J. Van herle, R. Ihringer, R. Vasquez Cavieres, L. Constantin, O. Bucheli, "Anode supported solid oxide fuel cells with screen-printed cathodes", *Journal of the European Ceramic Society* 21, 1855-1859 (2001)
64. Selmar de Souza, Steven J. Visco, Lutgard C. De Jonghe, "Thin-film solid oxide fuel cell with high performance at low-temperature", *Solid State Ionics* 98, 57-61 (1997)
65. Tsepin Tsai, Scott A. Barnett, "Increased solid-oxide fuel cell power density using interfacial ceria layers", *Solid State Ionics* 98, 191-196 (1997)
66. L.S. Wang, S.A. Barnett, "Ag-perovskite cermets for thin film solid oxide fuel cell air-electrode applications", *Solid State Ionics* 76, 103-113 (1995)
67. H. Uchida, S. Arisaka, M. Watanabe, "High performance electrodes for medium-temperature solid oxide fuel cells: Activation of $\text{La}(\text{Sr})\text{CoO}_3$ cathode with highly dispersed Pt metal electrocatalysts", *Solid State Ionics* 135, 347-351 (2000)
68. M. Sahibzada, S.J. Benson, R.A. Rudkin, J.A. Kilner, "Pd-promoted $\text{La}_{0.6}\text{Sr}_{0.4}\text{Co}_{0.2}\text{Fe}_{0.8}\text{O}_3$ cathodes", *Solid State Ionics* 113-115, 285-290 (1998)
69. Joong-Myeon Bae, B.C.H. Steele, "Properties of $\text{La}_{0.6}\text{Sr}_{0.4}\text{Co}_{0.2}\text{Fe}_{0.8}\text{O}_{3-\delta}$ (LSCF) double layer cathodes on gadolinium-doped ceria oxide (CGO) electrolytes I. Role of SiO_2 ", *Solid State Ionics* 106, 247-253 (1998)
70. E. Maguire, B. Gharbage, F.M.B. Marques, J.A. Labrincha, "Cathode materials for intermediate temperature SOFCs", *Solid State Ionics* 127, 329-335 (2000)
71. Dionissos Mantzavinos, Anne Hartley, Ian S. Metcalfe, Mortaza Sahibzada, "Oxygen stoichiometries in $\text{La}_{1-x}\text{Sr}_x\text{Co}_{1-y}\text{Fe}_y\text{O}_{3-\delta}$ perovskites at reduced oxygen partial pressures", *Solid State Ionics* 134, 103-109 (2000)

72. Hee Sung Yoon, Seung Woo Choi, Dokyol Lee, Byong Ho Kim, "Synthesis and characterization of $Gd_{1-x}Sr_xMnO_3$ cathode for solid oxide fuel cells", *Journal of Power Sources* 93, 1-7 (2001)
73. F.M. Figueiredo, J.R. Frade, F.M.B. Marques, "Performance of composite $LaCoO_3 - La_2(Zr,Y)_2O_7$ cathodes", *Solid State Ionics* 135, 463-467 (2000)
74. N.T. Hart, N.P. Brandon, M.J. Day, N.Lapena-Rey, "Functionally graded composite cathodes for solid oxide fuel cells", *Journal of Power Sources* 106, 42-50 (2002)
75. Keqin Huang, Robin Tichy, John B. Goodenough, "Superior perovskite Oxide-ion conductor; strontium- and magnesium-doped $LaGaO_3$: III, performance tests of single ceramic fuel cells", *J. Am. Ceram. Soc.* 81 [10], 2581-2585 (1998)
76. Teruhisa Horita, Katsuhiko Yamaji, Natsuko Sakai, Harumi Yokokawa, André Weber, Ellen Ivers-Tiffée, "Oxygen reduction mechanism at porous $La_{1-x}Sr_xCoO_{3-\delta}$ cathodes/ $La_{0.8}Sr_{0.2}Ga_{0.8}Mg_{0.2}O_{2.8}$ electrolyte interface for solid oxide fuel cells", *Electrochimica Acta* 46, 1837-1845 (2001)
77. G.Ch. Kostogloudis, Ch. Ftikos, A. Ahmad-Khanlou, A. Naoumidis, D. Stöver, "Chemical compatibility of alternative perovskite oxide SOFC cathodes with doped lanthanum gallate solid electrolyte", *Solid State Ionics* 134, 127-138 (2000)
78. H. Ullmann, N. Trofimenko, F. Tietz, D. Stöver, A. Ahmad-Khanlou, "Correlation between thermal expansion and oxide ion transport in mixed conducting perovskite-type oxides for SOFC cathodes", *Solid State Ionics* 138, 79-90 (2000)
79. J.A. Kilner, "Fast oxygen transport in acceptor doped oxides", *Solid State Ionics* 129, 13-23 (2000)
80. Rajiv Doshi, Von L. Richards, J.D. Carter, Xianoping Wang, Michael Krumpelt, "Development of solid-oxide fuel cells that operate at $500^{\circ}C$ ", *Journal of The Electrochemical Society* 146(4), 1273-1278 (1999)
81. J.P.P. Huijsmans, "Ceramics in solid oxide fuel cells", *Current Opinion in Solid State and Materials Sciences* 5, 317-323 (2001)
82. Nguyen Q. Minh, "Ceramic fuel cells", *J. Am. Ceram. Soc.* 76[3], 563-588 (1993)
83. S.C. Singhal, "Advances in solid oxide fuel cell technology", *Solid State Ionics* 135, 305-313 (2000)

84. Mogens Mogensen, Nigel M. Sammes, Geoff A. Tompsett, "Physical, chemical and electrochemical properties of pure and doped ceria", *Solid State Ionics* 129, 63-94 (2000)
85. Hideaki Inaba, Hiroaki Tagawa, "Ceria-based solid electrolytes", *Solid State Ionics* 83, 1-16 (1996)
86. S.P.S. Badwal, F.T. Ciacchi, J. Drennan, "Investigation of the stability of ceria-gadolinia electrolytes in solid oxide fuel cell environments", *Solid State Ionics* 121, 253-262 (1999)
87. S.P.S. Badwal, "Stability of solid oxide fuel cell components", *Solid State Ionics* 143, 39-46 (2001)
88. Katsuhiko Yamaji, Hideyuki Negishi, Teruhisa Horita, Natsuko Sakai, Harumi Yokokawa, "Vaporization process of Ga from doped LaGaO₃ electrolytes in reducing atmospheres" *Solid State Ionics* 135, 389-396 (2000)
89. Tatsumi Ishihara, Hideaki Matsuda, Yusaku Takita, "Effects of rare earth cations doped for La site on the oxide ionic conductivity of LaGaO₃-based perovskite type oxide", *Solid State Ionics* 79, 147-151 (1995)
90. A. Ahmad-Khanlou, F. Tietz, D. Stöver, "Material properties of La_{0.8}Sr_{0.2}Ga_{0.9+x}Mg_{0.1}O_{3-δ} as a function of Ga content", *Solid State Ionics* 135, 543-547 (2000)
91. Katsuhiko Yamaji, Teruhisa Horita, Masahiko Ishikawa, Natsuko Sakai, Harumi Yokokawa, "Chemical stability of the La_{0.9}Sr_{0.1}Ga_{0.8}Mg_{0.2}O_{2.85} electrolyte in a reducing atmosphere", *Solid State Ionics* 121, 217-224 (1999)
92. Terry A. Ring, "Fundamentals of Ceramic Powder Processing and Synthesis", Academic Press, 1996
93. A. Cüneyt Taş, Peter J. Majewski, Fritz Aldinger, "Chemical preparation of pure and strontium- and/or magnesium-doped lanthanum gallate powders", *J. Am. Ceram. Soc.* 83[12], 2954-2960 (2000)
94. Mehmet A. Gülgün, My H. Nguyen, Waltraud M. Kriven, "Polymerized organic-inorganic synthesis of mixed oxides", *J. Am. Ceram. Soc.* 82[3], 556-560 (1999)
95. M.P. Pechini, U.S. Patent No.3, 330, 697, July (1967)
96. M. Marinsek, K. Zupan, J. Maeek, "Ni-YSZ cermet anodes prepared by citrate/nitrate combustion synthesis", *J. Power Sources* 106, 178-188 (2002)

97. S. Tanasescu, D. Berger, D. Neiner, N.D. Totir, "Thermodynamic characterization of some doped lanthanum chromites used as interconnects in SOFC", *Solid State Ionics*, Volume 157, Issues 1-4, 365-370 (2003)
98. F. Riza, Ch. Ftikos, F. Tietz, W. Fischer, "Preparation and characterization of $\text{Ln}_{0.8}\text{Sr}_{0.2}\text{Fe}_{0.8}\text{Co}_{0.2}\text{O}_{3-\delta}$ (Ln=La, Pr, Nd, Sm, Eu, Gd)", *Journal of the European Ceramic Society* 21, 1769-1773 (2001)
99. V. Dusastre, J.A. Kilner, "Optimisation of composite cathodes for intermediate temperature SOFC applications", *Solid State Ionics* 126, 163-174 (1999)
100. Supplement of *Journal of Bilim Teknik*, January 2002, p.22
101. Helmut Ullmann, Nikolai Trofimenko, "Composition, structure and transport properties of perovskite-type oxides", *Solid State Ionics* 119, 1-8 (1999)
102. G.J. Saunders, K. Kendall, "Reactions of hydrocarbons in small tubular SOFCs", *Journal of Power Sources* 106, 258-263 (2002)
103. Marko Hrovat, Ariane Ahmad-Khanlou, Zoran Samadzija, Janez Holc, "Interactions between lanthanum gallate based solid electrolyte and ceria", *Materials Research Bulletin*, Vol. 34, Nos. 12/13, 2027-2034 (1999)
104. K. Zupan, S. Pejovnik, J. Maeek, "Synthesis of nanometer crystalline lanthanum chromite powders by the citrate-nitrate autoignition reaction", *Acta Chim. Slov.* 48(1), 137-145 (2001)
105. *CRC Handbook of Chemistry and Physics*, 1981-1982 62nd Edition, CRC Press, Inc.
106. "Polymerized Organic-Inorganic Complex Route for Mixed-Oxide Synthesis", M.A. Gülgün, W.M. Kriven, US patent# 6,482,387
107. O. Uchiyama, M. Kakihana, M. Arima, M. Yashima, Y. Suzuki, M. Yoshimura, "Polymerized complex precursors for the synthesis of pure PbTiO_3 powders at 400-600 °C", *Advanced Materials'93, I / A: Ceramics, Powders, Corrosion and Advanced Processing*, edited by N: Mizutani et al. *Trans. Mat. Res. Soc. Jpn.*, Volume 14A
108. Xinge Zhang, Satoshi Ohara, Hajime Okawa, Radenka Maric, Takehisa Fukui, "Interactions of a $\text{La}_{0.9}\text{Sr}_{0.1}\text{Ga}_{0.8}\text{Mg}_{0.2}\text{O}_{3-\delta}$ electrolyte with Fe_2O_3 , Co_2O_3 and NiO anode materials", *Solid State Ionics* 139, 145-152 (2001)
109. Mehmet A. Gülgün, Oludele O. Popoola, Waltraud M. Kriven, "Chemical synthesis and characterization of calcium aluminate powders", *J. Am. Ceram. Soc.* 77[2], 531-539 (1994)

110. W.M. Kriven, S.J. Lee, M.A. Gülgün, M.H. Nguyen, D.K. Kim, "Synthesis of oxide powders via polymeric steric entrapment", invited paper, in Innovative Processing/Synthesis: Ceramics, Glass, Composites III, Ceramic Transactions, Vol 108, 99-110 (2000)
111. M.A. Gülgün, W.M. Kriven, "A simple solution-polymerization route for oxide powder synthesis", Technology and Commercialization of Powder Synthesis and Shape Forming Processes, in Ceramic Transactions Vol. 62. (Cincinnati, OH, April, 1995). Edited by J.J. Kingsley, C.H. Schilling, and J.H. Adair. American Ceramic Society, Westerville, Ohio, 1996
112. M. Kakihana, M. Arima, M. Yashima, M. Yoshimura, Y. Nakamura, H. Makazi, H. Yasuoka, "Polymerized complex route to the synthesis of multi-component oxides", An invited paper for "The International Symposium on Sol-Gel Science and Technology" (19-22 October, 1994. Los Angeles, USA)
113. V.P. Gorelov, D.I. Bronin, Ju. V. Sokolava, H. Nafe, F. Aldinger, "The effect of doping and processing conditions on properties of $\text{La}_{1-x}\text{Sr}_x\text{Ga}_{1-y}\text{Mg}_y\text{O}_{3-\alpha}$ ", Journal of the European Ceramic Society 21, 2311-2317 (2001)
114. W.D. Kingery, H.K. Bowen, D.R. Uhlmann, "Introduction to Ceramics", John Wiley & Sons, Inc., 1997
115. S.P. Simner, J.R. Bonnett, N.L. Canfield, K.D. Meinhardt, J.P. Shelton, V.L. Sprenkle, J.W. Stevenson, "Development of lanthanum ferrite SOFC cathodes", Journal of Power Sources 113(1), 1-10 (2003)
116. S.P. Simner, J.R. Bonnett, N.L. Canfield, K.D. Meinhardt, V.L. Sprenkle, J.W. Stevenson, "Optimized lanthanum ferrite-based cathodes for anode-supported SOFCs", Electrochemical and Solid State Letters 5(7), A173-A175 (2002)
117. Monica Popa, Johannes Frantti, Masato Kakihana, "Lanthanum ferrite LaFeO_{3+d} anopowders obtained by the polymerizable complex method", Solid State Ionics 154-155, 437-445 (2002)
118. S. Tanasescu, D. Berger, D. Neiner and N. D. Totir, "Thermodynamic characterisation of some doped lanthanum chromites used as interconnects in SOFC", Solid State Ionics 157, Issues 1-4, 365-370 (2003)
119. Hideko Hayashi, Mieko Watanabe, Miwako Ohuchida, Hideaki Inaba, Yoshiko Hiei, Tohru Yamamoto and Masashi Mori, "Thermal expansion of $\text{La}_{1-x}\text{Sr}_x\text{CrO}_{3-\delta}$ ", Solid State Ionics 144, 301-313 (2001)

120. Joseph Sfeir, "LaCrO₃-based anodes: stability considerations", *Journal of Power Sources* 118, 276-285 (2003)
121. N. Imanaka, K. Okamoto, G. Adachi, "New type of sodium ion conducting solid electrolyte based on lanthanum oxysulfate", *Electrochemical and Solid State Letters* 5(9), E51-E53 (2002)
122. N. Imanaka, K. Okamoto, G. Adachi, "Chloride ion conducting characteristics in rare earth oxychlorides", *Chemistry Letters* 2, 130-131 (2001)
123. K. Okamoto, N. Imanaka, G. Adachi, "Chloride ion conduction in rare earth oxychlorides", *Solid State Ionics* 154-155, 577-580 (2002)
124. Jae Yeon Yi, Gyeong Man Choi, "Phase characterization and electrical conductivity of LaSr(GaMg)_{1-x}Mn_xO₃ system", *Solid State Ionics* 148, 557-565 (2002)
125. V.V. Kharton, A.L. Shaula, N.P. Vyshatko, F.M.B. Marques, "Electron-hole transport in (La_{0.9}Sr_{0.1})_{0.98}Ga_{0.8}Mg_{0.2}O_{3-δ} electrolyte: effects of ceramic microstructure", *Electrochimica Acta* 48, 1817-1828 (2003)

Appendix A.

X-ray diffraction spectra of the powders in LSGM synthesis with different organic carrier materials are illustrated. Calcination temperatures are 700⁰C, 800⁰C, 900⁰C, 1000⁰C, 1050⁰C, 1100⁰C, 1150⁰C, and 1200⁰C. Present phases are shown on the XRD plots.

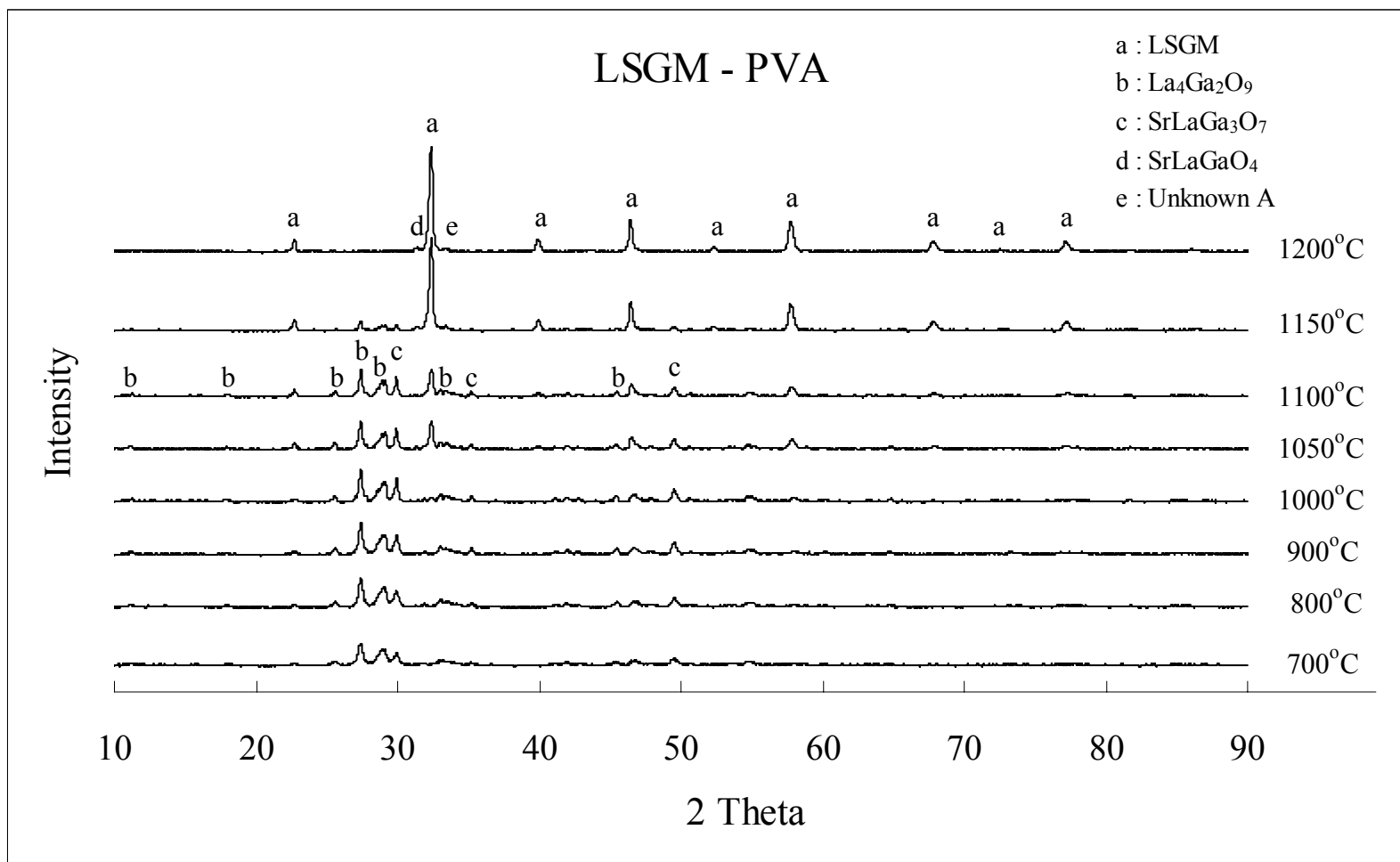


Figure A1. X-ray spectra of LSGM powders synthesized with PVA as the organic carrier material.

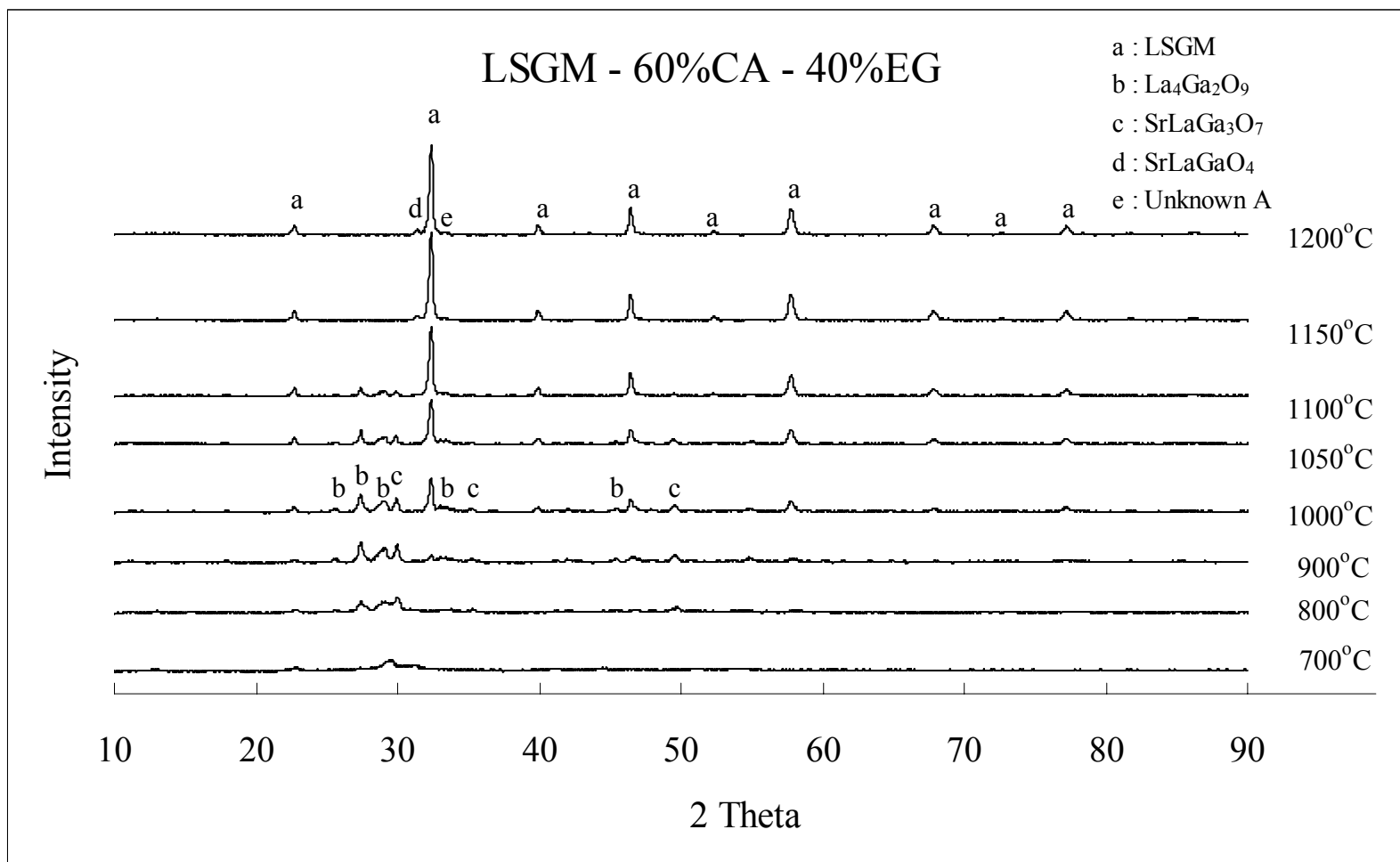


Figure A2. X-ray spectra of synthesized LSGM powders with Pechini precursor as the organic carrier material.

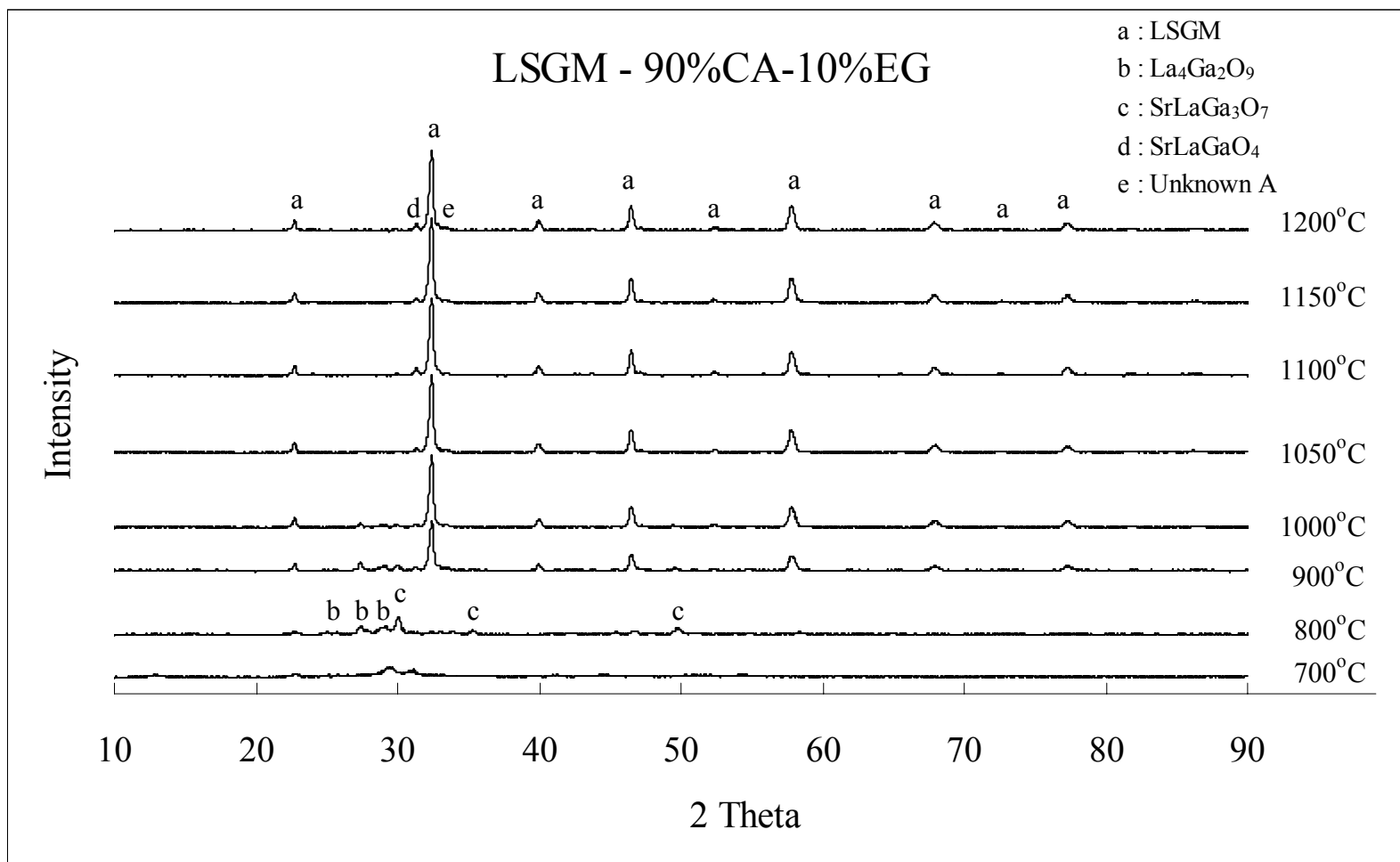


Figure A3. X-ray spectra of LSGM powders synthesized with Pechini precursor (90 wt% CA - 10 wt% EG) as the organic carrier material.

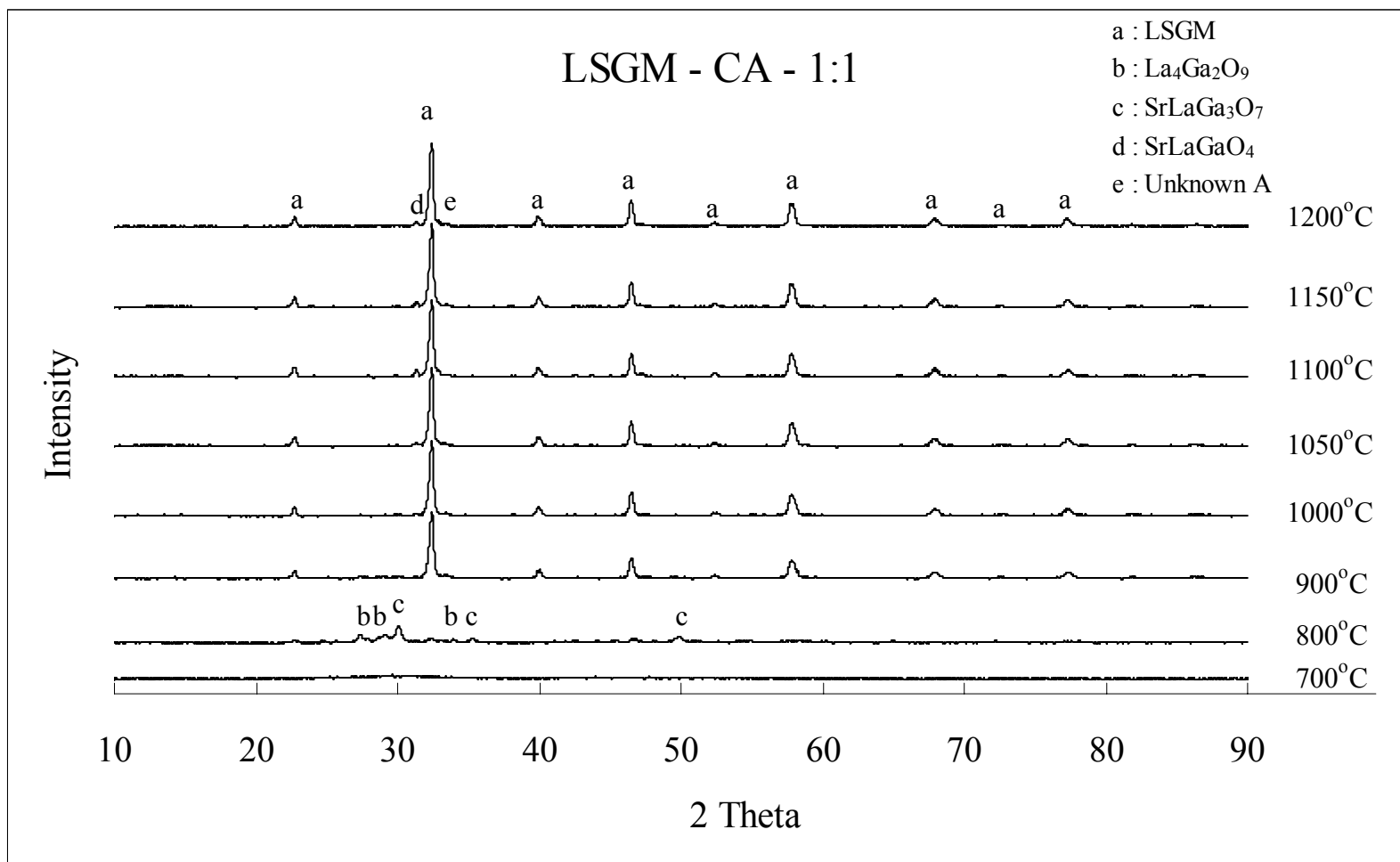


Figure A4. X- ray spectra of LSGM powders synthesized with CA (1:1 cation to citric acid molecule) as the organic carrier material.

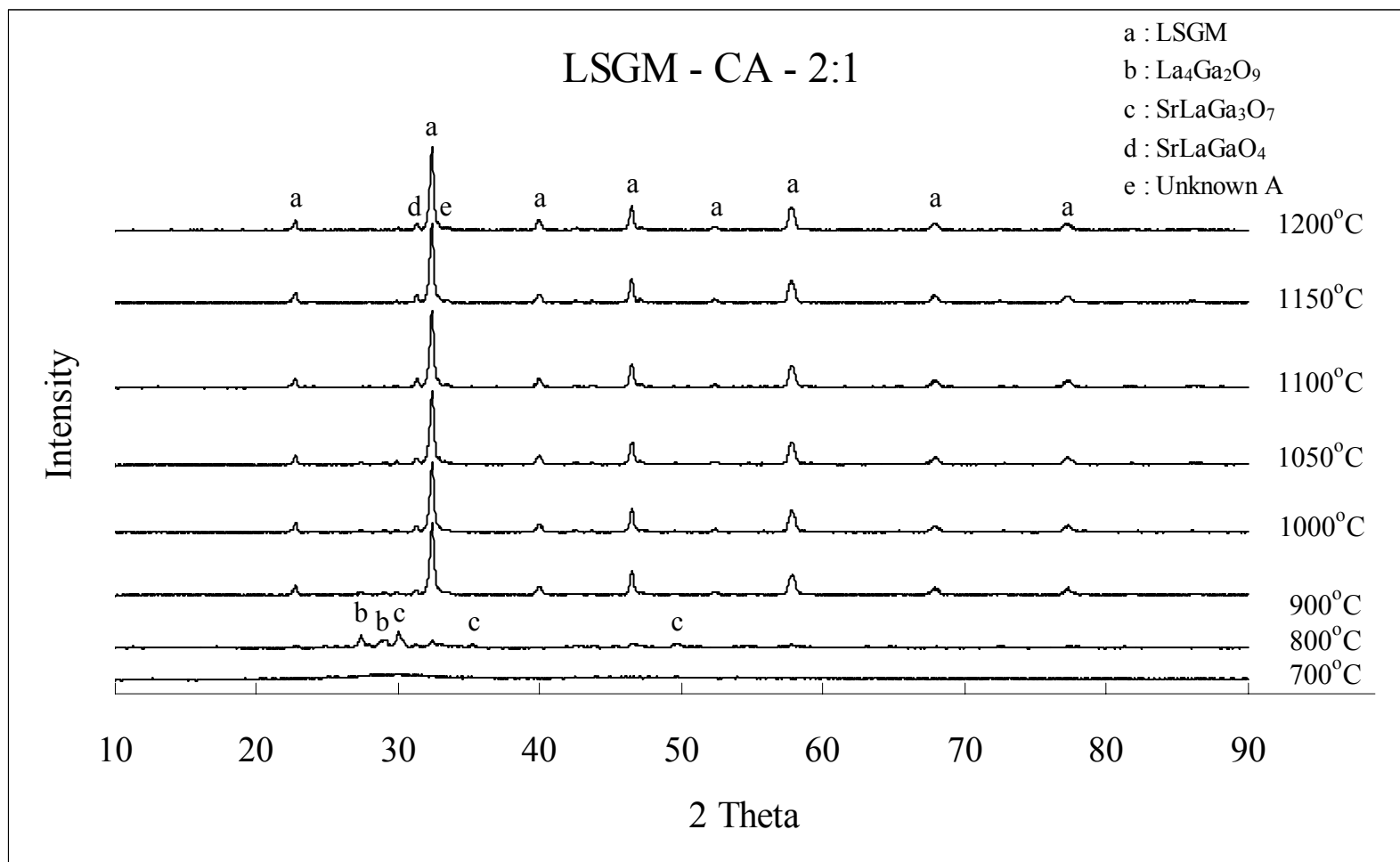


Figure A5. X-ray spectra of LSGM powders synthesized with CA (2:1 cation to citric acid molecule) as the organic carrier material.

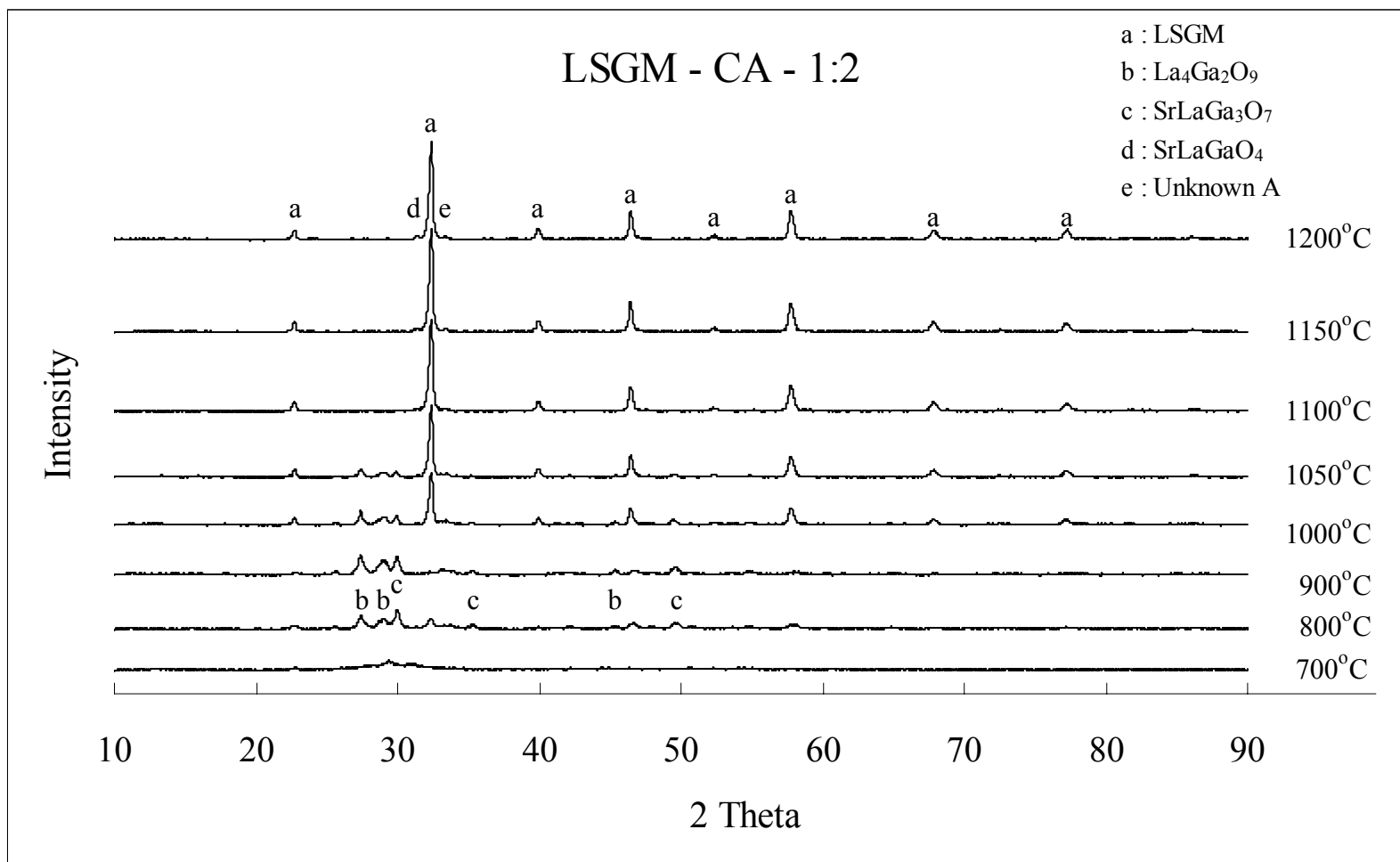


Figure A6. X-ray spectra of LSGM powders synthesized with CA (1:2 cation to citric acid molecule) as the organic carrier material.

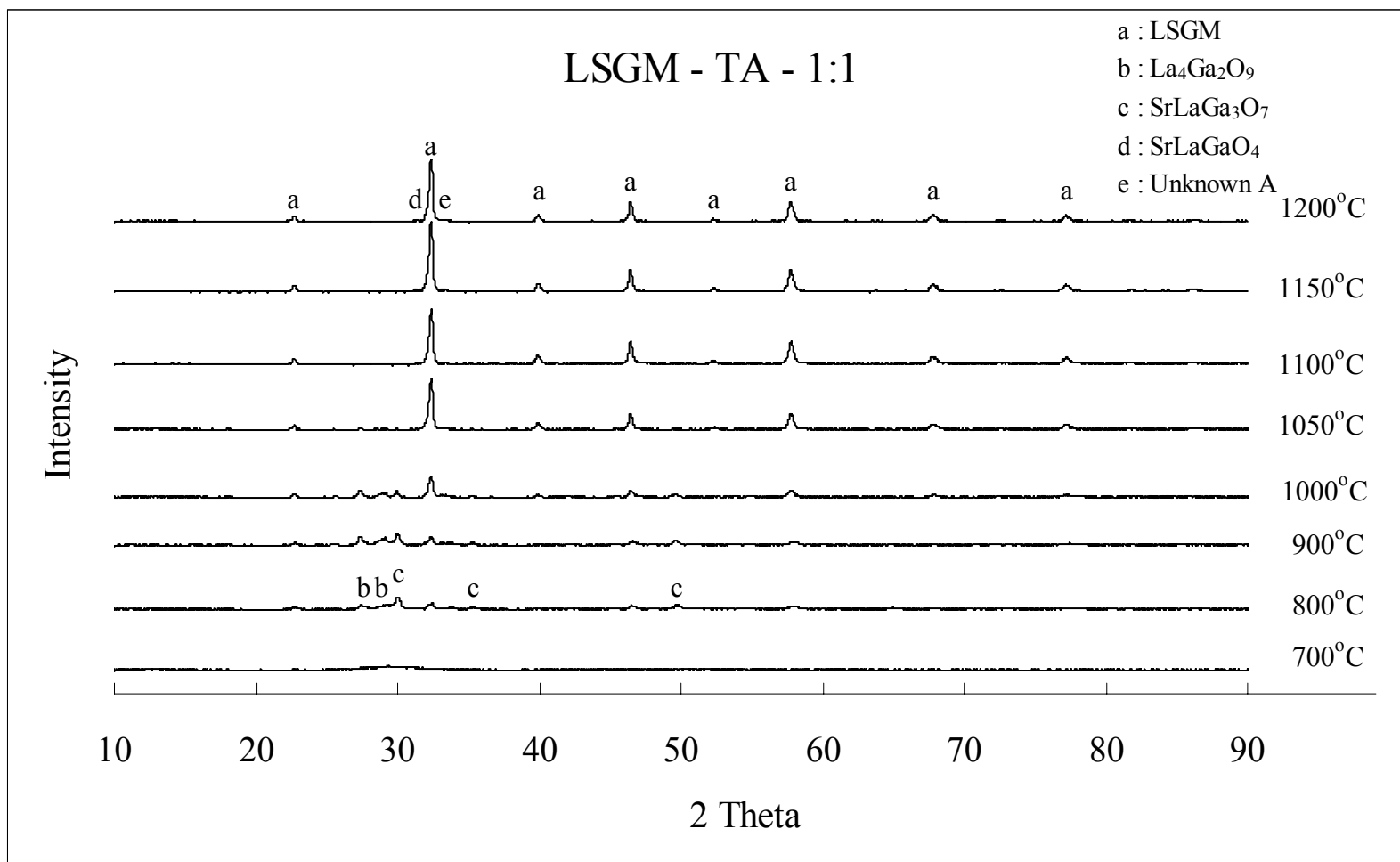


Figure A7. X-ray spectra of LSGM powders synthesized with TA (1:1 cation to tartaric acid molecule) as the carrier material.

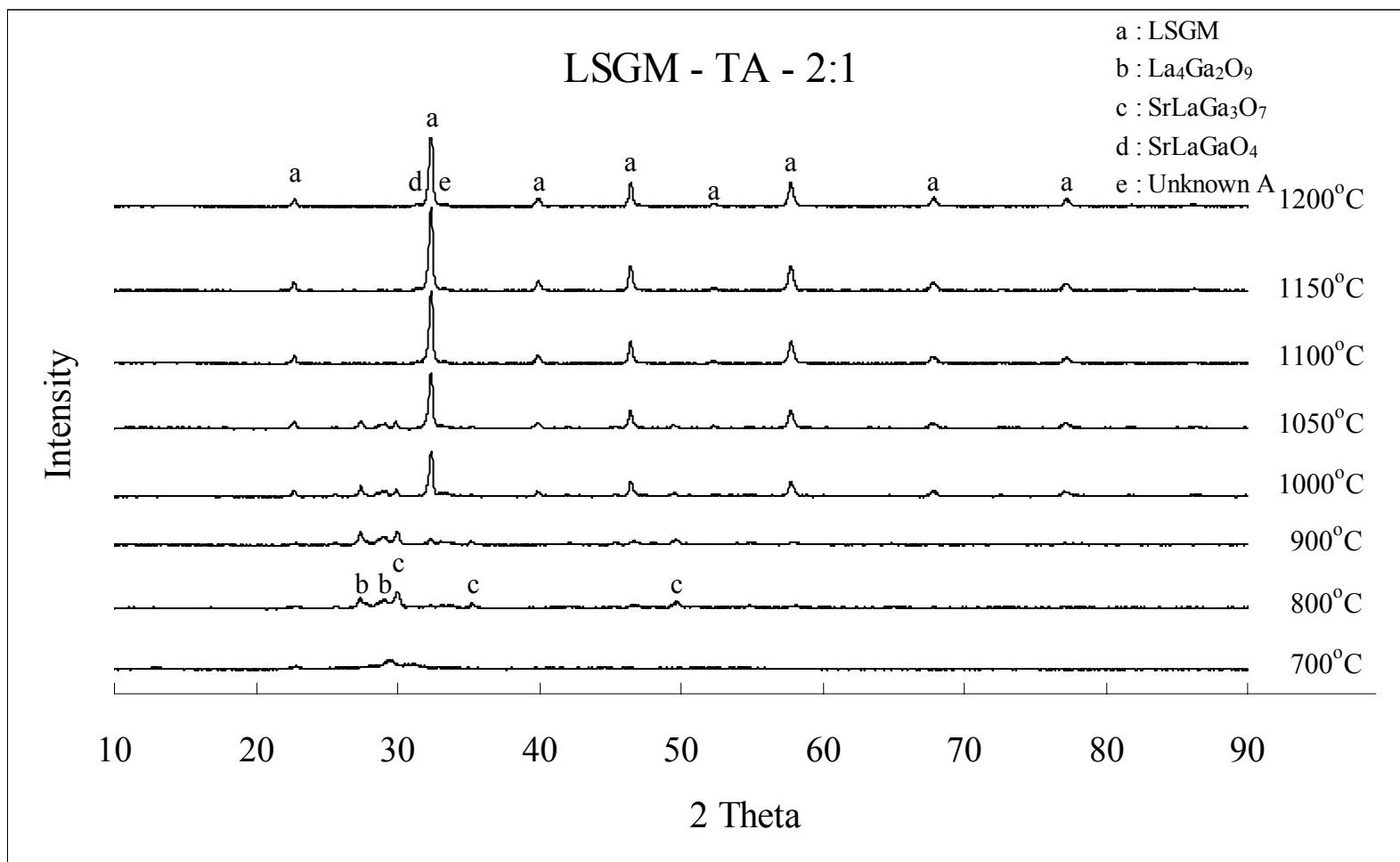


Figure A8. X-ray spectra of LSGM powders synthesized with TA (2:1 cation to tartaric acid molecule) as the organic carrier material.

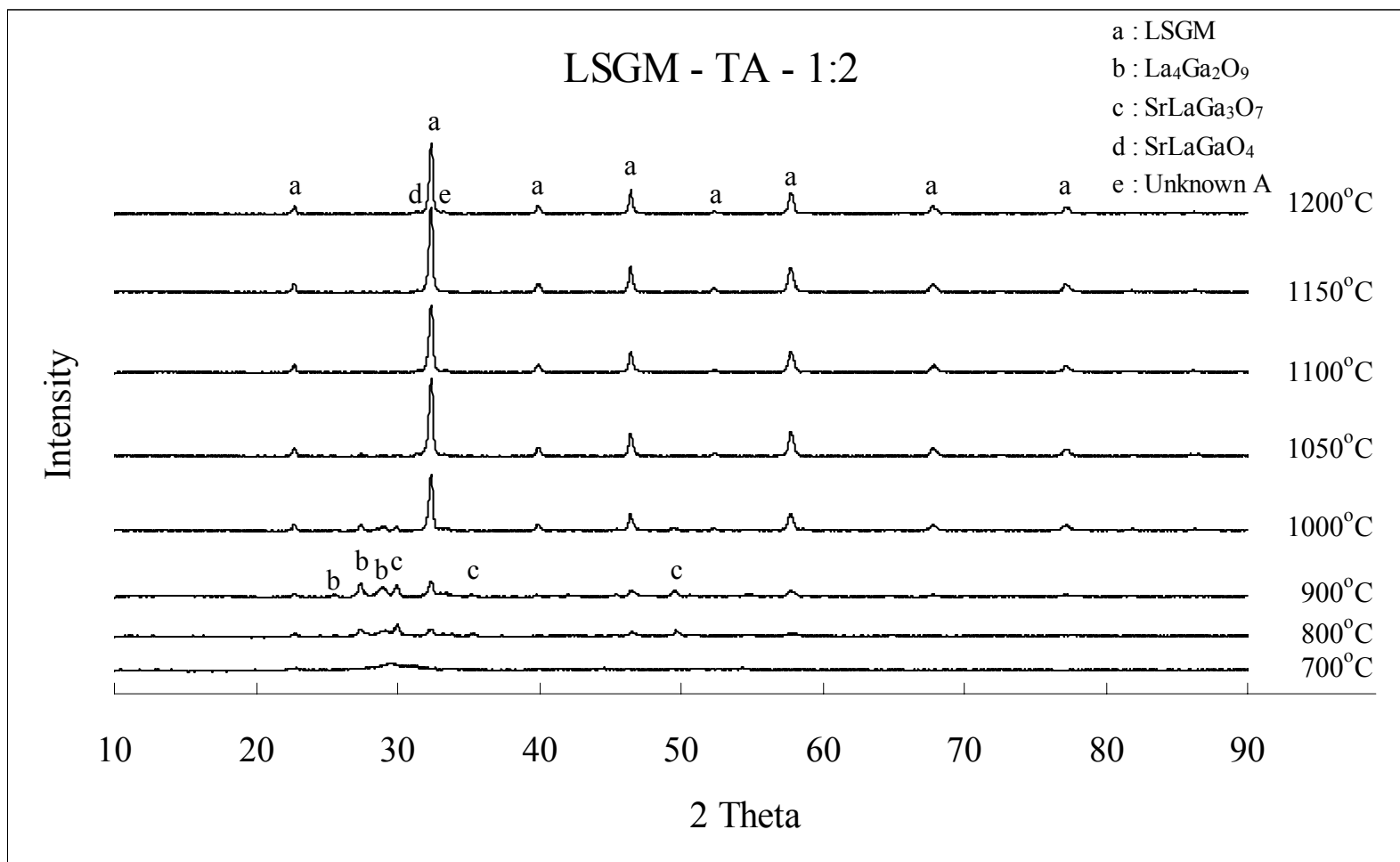


Figure A9. X-ray spectra of LSGM powders synthesized with TA (1:2 cation to citric acid molecule) as the organic carrier material.

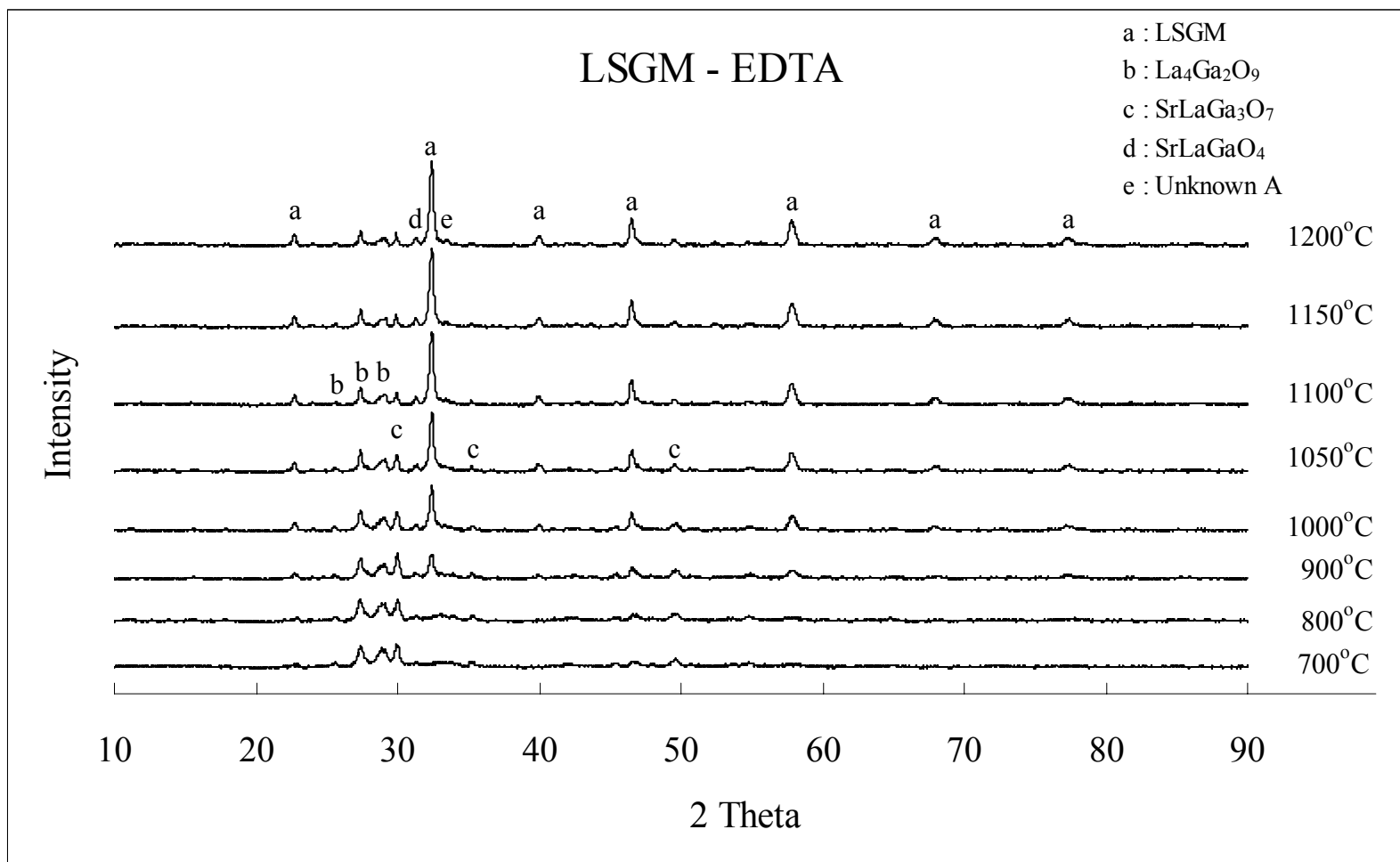


Figure A10. X-ray spectra of LSGM powders synthesized with EDTA as the organic carrier material.

Appendix B.

The concentrations and amounts of each phase in the LSGM powders synthesized at different calcination temperatures and with organic carrier materials are tabulated. Amounts of each phase are shown in the parentheses.

Table B1. Concentrations and amounts of the phases in LSGM powders synthesized with PVA as the organic carrier material.

<i>PVA</i>	<i>LSGM</i>	<i>LaSrGaO₄</i>	<i>SrLaGa₃O₇</i>	<i>La₄Ga₂O₉</i>	<i>Unknown A</i>
800°C	Not Detected	Not Detected	30.9% (581)	59% (1108)	10.1% (190)
900°C	Not Detected	Not Detected	34.9% (730)	55.5% (1163)	9.6% (202)
1000°C	5% (119)	Not Detected	35.9% (855)	50.6% (1205)	8.5% (203)
1050°C	32.4% (1008)	2.4% (73)	24.6% (764)	34% (1057)	6.6% (204)
1100°C	33.7% (1014)	1.4% (46)	23.8% (717)	34.1% (1027)	7% (209)
1150°C	81.1% (3506)	3.2% (138)	4.8% (210)	7.3% (315)	3.6% (156)
1200°C	93.7% (3961)	4.1% (174)	Not Detected	Not Detected	2.2% (91)

Table B2. Concentrations and amounts of the phases in LSGM powders synthesized with Pechini precursor (60 wt% citric acid – 40 wt% ethylene glycol) as the organic carrier material.

<i>Pechini (60-40)</i>	<i>LSGM</i>	<i>LaSrGaO₄</i>	<i>SrLaGa₃O₇</i>	<i>La₄Ga₂O₉</i>	<i>Unknown A</i>
800°C	Not Detected	Not Detected	53.9% (551)	37% (378)	9.1% (93)
900°C	12.8% (237)	2.1% (40)	35.6% (664)	42.8% (798)	6.7% (125)
1000°C	48.7% (1318)	2.2% (59)	18.8% (509)	24.4% (662)	5.9% (160)
1050°C	61.6% (1746)	2.2% (63)	11.1% (315)	19.1% (542)	6% (170)
1100°C	79.5% (2751)	2.5% (88)	5% (172)	9% (310)	4% (138)
1150°C	92.8% (3473)	4.8% (180)	Not Detected	Not Detected	2.4% (89)
1200°C	91.7% (3563)	5.7% (221)	Not Detected	Not Detected	2.6% (103)

Appendix B. Continued

Table B3. Concentrations and amounts of the phases in LSGM powders synthesized with Pechini precursor (90 wt% citric acid – 10 wt% ethylene glycol) as the organic carrier material.

<i>Pechini (90-10)</i>	<i>LSGM</i>	<i>LaSrGaO₄</i>	<i>SrLaGa₃O₇</i>	<i>La₄Ga₂O₉</i>	<i>Unknown A</i>
800°C	7% (84)	5.6% (67)	59% (707)	28.4% (340)	Not Detected
900°C	71.2% (2029)	5.2% (148)	7.9% (226)	11.6% (331)	4.1% (117)
1000°C	84.5% (2987)	3.5% (123)	4% (142)	4.9% (175)	3.1% (109)
1050°C	87.1% (3199)	5.6% (206)	1.9% (69)	1.6% (60)	3.8% (138)
1100°C	85.3% (3163)	7.8% (289)	2.8% (105)	1.3% (48)	2.8% (103)
1150°C	91% (3467)	4.7% (179)	1.4% (55)	Not Detected	2.9% (112)
1200°C	87.4% (3323)	7% (265)	1.9% (73)	Not Detected	3.7% (140)

Table B4. Concentrations and amounts of the phases in LSGM powders synthesized with CA (1:1 total cation to citric acid molecule ratio) as the organic carrier material.

<i>CA (1:1)</i>	<i>LSGM</i>	<i>LaSrGaO₄</i>	<i>SrLaGa₃O₇</i>	<i>La₄Ga₂O₉</i>	<i>Unknown A</i>
800°C	11.1% (138)	4% (50)	55.3% (689)	25.3% (316)	4.3% (54)
900°C	88% (2829)	1.6% (53)	3.1% (98)	3.5% (112)	3.8% (122)
1000°C	90.4% (3235)	2.3% (82)	1.2% (45)	2.3% (81)	3.8% (135)
1050°C	92.1% (3381)	4.6% (170)	Not Detected	Not Detected	3.3% (122)
1100°C	88.8% (3261)	8.1% (279)	Not Detected	Not Detected	3.1% (113)
1150°C	92.1% (3610)	4.9% (192)	Not Detected	Not Detected	3% (119)
1200°C	91.6% (3557)	5.6% (217)	Not Detected	Not Detected	2.8% (111)

Appendix B. Continued

Table B5. Concentrations and amounts of the phases in LSGM powders synthesized with CA (2:1 total cation to citric acid molecule ratio) as the organic carrier material.

<i>CA (2:1)</i>	<i>LSGM</i>	<i>LaSrGaO₄</i>	<i>SrLaGa₃O₇</i>	<i>La₄Ga₂O₉</i>	<i>Unknown A</i>
800°C	16.4% (253)	7.4% (115)	40% (618)	31% (480)	5.2% (80)
900°C	85.6% (2965)	5.4% (188)	2% (70)	3.7% (127)	3.3% (116)
1000°C	84.2% (2867)	6.7% (228)	3.1% (105)	3.1% (105)	2.9% (100)
1050°C	83.7% (2992)	7.4% (263)	3.4% (123)	2.7% (99)	2.8% (100)
1100°C	83.9% (3145)	9.3% (350)	2.6% (96)	1.3% (50)	2.9% (107)
1150°C	85.2% (3236)	7.9% (302)	1.7% (65)	1.9% (71)	3.3% (126)
1200°C	86.4% (3433)	6.9% (273)	2.7% (108)	1.3% (51)	2.7% (108)

Table B6. Concentrations and amounts of the phases in LSGM powders synthesized with CA (1:2 total cation to citric acid molecule ratio) as the organic carrier material.

<i>CA (1:2)</i>	<i>LSGM</i>	<i>LaSrGaO₄</i>	<i>SrLaGa₃O₇</i>	<i>La₄Ga₂O₉</i>	<i>Unknown A</i>
800°C	22% (351)	Not Detected	42.7% (679)	28.8% (459)	6.5% (103)
900°C	41.5% (793)	Not Detected	24% (459)	27.8% (530)	6.7% (127)
1000°C	63.8% (1975)	1.5% (45)	11.9% (367)	17.1% (531)	5.7% (177)
1050°C	79.1% (2696)	1.8% (61)	6.4% (220)	9.3% (316)	3.4% (115)
1100°C	92.7% (3414)	3% (112)	Not Detected	1.3% (48)	3% (111)
1150°C	93.9% (3858)	3.4% (138)	Not Detected	Not Detected	2.7% (104)
1200°C	93.5% (3650)	3.3% (130)	Not Detected	Not Detected	3.2% (124)

Appendix B. Continued

Table B7. Concentrations and amounts of the phases in LSGM powders synthesized with TA (1:1 total cation to tartaric acid molecule ratio) as the organic carrier material.

<i>TA (1:1)</i>	<i>LSGM</i>	<i>LaSrGaO₄</i>	<i>SrLaGa₃O₇</i>	<i>La₄Ga₂O₉</i>	<i>Unknown A</i>
800°C	26.7% (253)	Not Detected	51.3% (487)	18.3% (174)	3.7% (35)
900°C	27.5% (340)	Not Detected	36.6% (453)	30.1% (372)	5.8% (72)
1000°C	56.6% (863)	Not Detected	16.3% (249)	20.1% (306)	7% (107)
1050°C	90.3% (2097)	1.7% (40)	2.7% (65)	2.7% (63)	2.6% (61)
1100°C	94.4% (2306)	2.4% (60)	Not Detected	Not Detected	3.2% (79)
1150°C	95.7% (2906)	2% (60)	Not Detected	Not Detected	2.3% (70)
1200°C	94% (2556)	3% (84)	Not Detected	Not Detected	3% (84)

Table B8. Concentrations and amounts of the phases in LSGM powders synthesized with TA (2:1 total cation to tartaric acid molecule ratio) as the organic carrier material.

<i>TA (2:1)</i>	<i>LSGM</i>	<i>LaSrGaO₄</i>	<i>SrLaGa₃O₇</i>	<i>La₄Ga₂O₉</i>	<i>Unknown A</i>
800°C	8.6% (103)	Not Detected	51.1% (614)	34.5% (414)	5.8% (70)
900°C	14.7% (197)	Not Detected	40% (536)	38.9% (523)	6.6% (88)
1000°C	68.3% (1873)	1.2% (33)	10.5% (289)	15.3% (420)	4.7% (130)
1050°C	76.1% (2254)	1.2% (36)	8.9% (265)	10.5% (312)	3.3% (98)
1100°C	94.7% (2969)	2.8% (87)	Not Detected	Not Detected	2.5% (80)
1150°C	94.8% (3453)	2.6% (97)	Not Detected	Not Detected	2.6% (97)
1200°C	93.8% (3171)	3.1% (105)	Not Detected	Not Detected	3.1% (104)

Appendix B. Continued

Table B9. Concentrations and amounts of the phases in LSGM powders synthesized with TA (1:2 total cation to tartaric acid molecule ratio) as the organic carrier material.

<i>TA (1:2)</i>	<i>LSGM</i>	<i>LaSrGaO₄</i>	<i>SrLaGa₃O₇</i>	<i>La₄Ga₂O₉</i>	<i>Unknown A</i>
800°C	24.5% (240)	Not Detected	43.4% (426)	25.5% (250)	6.6% (65)
900°C	34.8% (590)	Not Detected	26.3% (445)	31.8% (539)	7.1% (120)
1000°C	78.9% (2082)	Not Detected	7.6% (200)	10.1% (269)	3.4% (89)
1050°C	89.9% (2916)	3.6% (116)	1.5% (49)	2.8% (92)	2.2% (73)
1100°C	90.7% (2504)	2.8% (78)	1.5% (43)	1.5% (43)	3.5% (98)
1150°C	95.5% (3227)	2.6% (90)	Not Detected	Not Detected	1.9% (66)
1200°C	93.9% (2644)	3.4% (95)	Not Detected	Not Detected	2.7% (78)

Table B10. Concentrations and amounts of the phases in LSGM powders synthesized with EDTA as the organic carrier material.

<i>EDTA</i>	<i>LSGM</i>	<i>LaSrGaO₄</i>	<i>SrLaGa₃O₇</i>	<i>La₄Ga₂O₉</i>	<i>Unknown A</i>
800°C	7.7% (103)	6.1% (81)	38.2% (509)	41.6% (554)	6.4% (85)
900°C	30.3% (606)	5.6% (111)	32.6% (652)	26.7% (534)	4.8% (97)
1000°C	48.7% (1206)	5% (125)	19.8% (492)	21.3% (527)	5.2% (128)
1050°C	55.7% (1544)	5.4% (150)	14.5% (401)	19.9% (551)	4.5% (124)
1100°C	62.7% (1918)	6.5% (200)	10.8% (331)	15.7% (480)	4.3% (130)
1150°C	65.6% (2104)	6.7% (215)	9.7% (310)	14.4% (462)	3.6% (114)
1200°C	68.4% (2275)	6.2% (206)	10% (332)	11.5% (383)	3.9% (130)

Appendix C.

X-ray diffraction spectra of the powders in LSGM synthesis with different starting materials are illustrated. Calcination temperatures are 700⁰C, 800⁰C, 900⁰C, 1000⁰C, 1050⁰C, 1100⁰C, 1150⁰C, and 1200⁰C. Present phases are shown on the XRD plots.

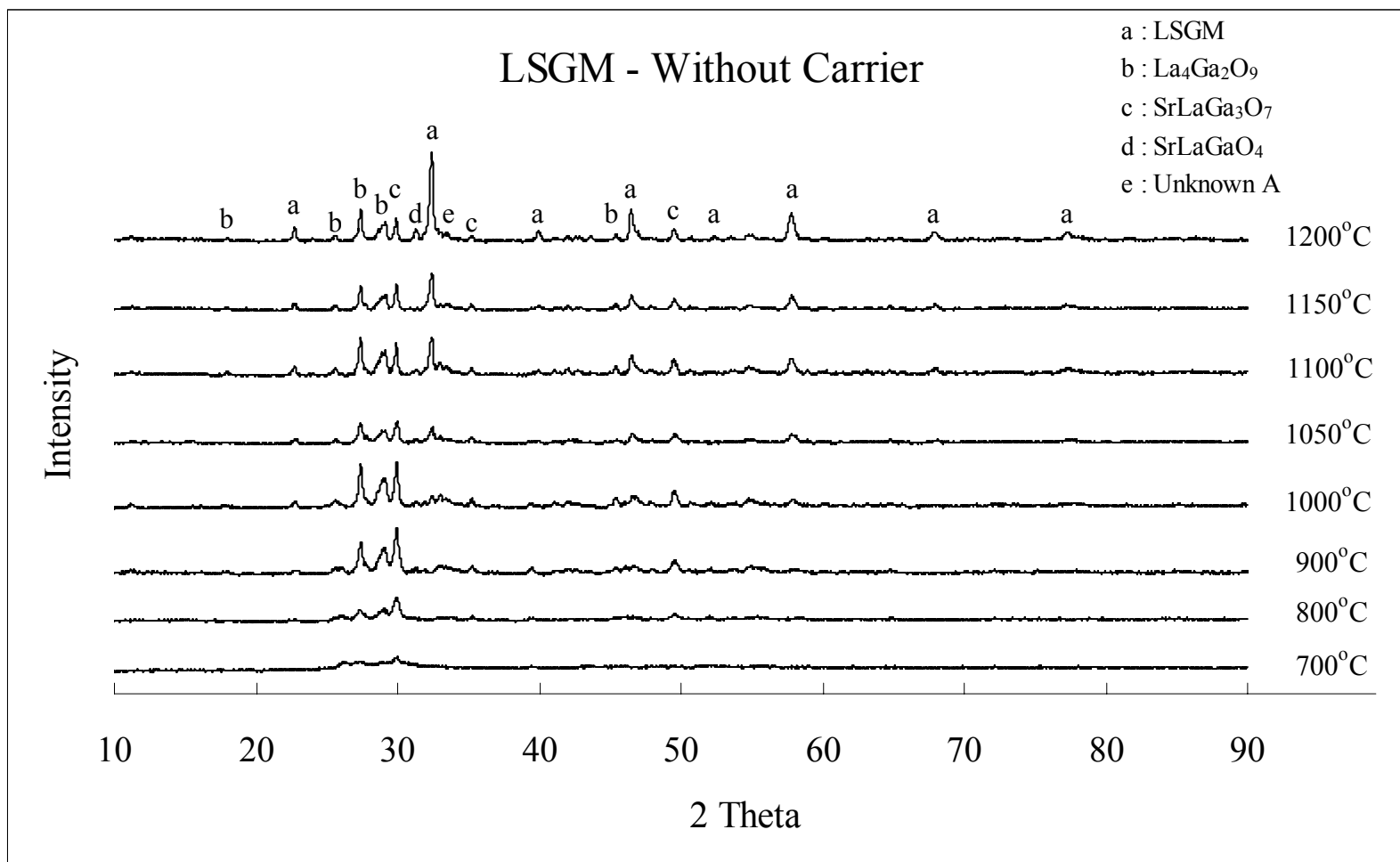


Figure C1. X-ray spectra of LSGM powders synthesized without organic carrier material, using nitrate sources of cations.

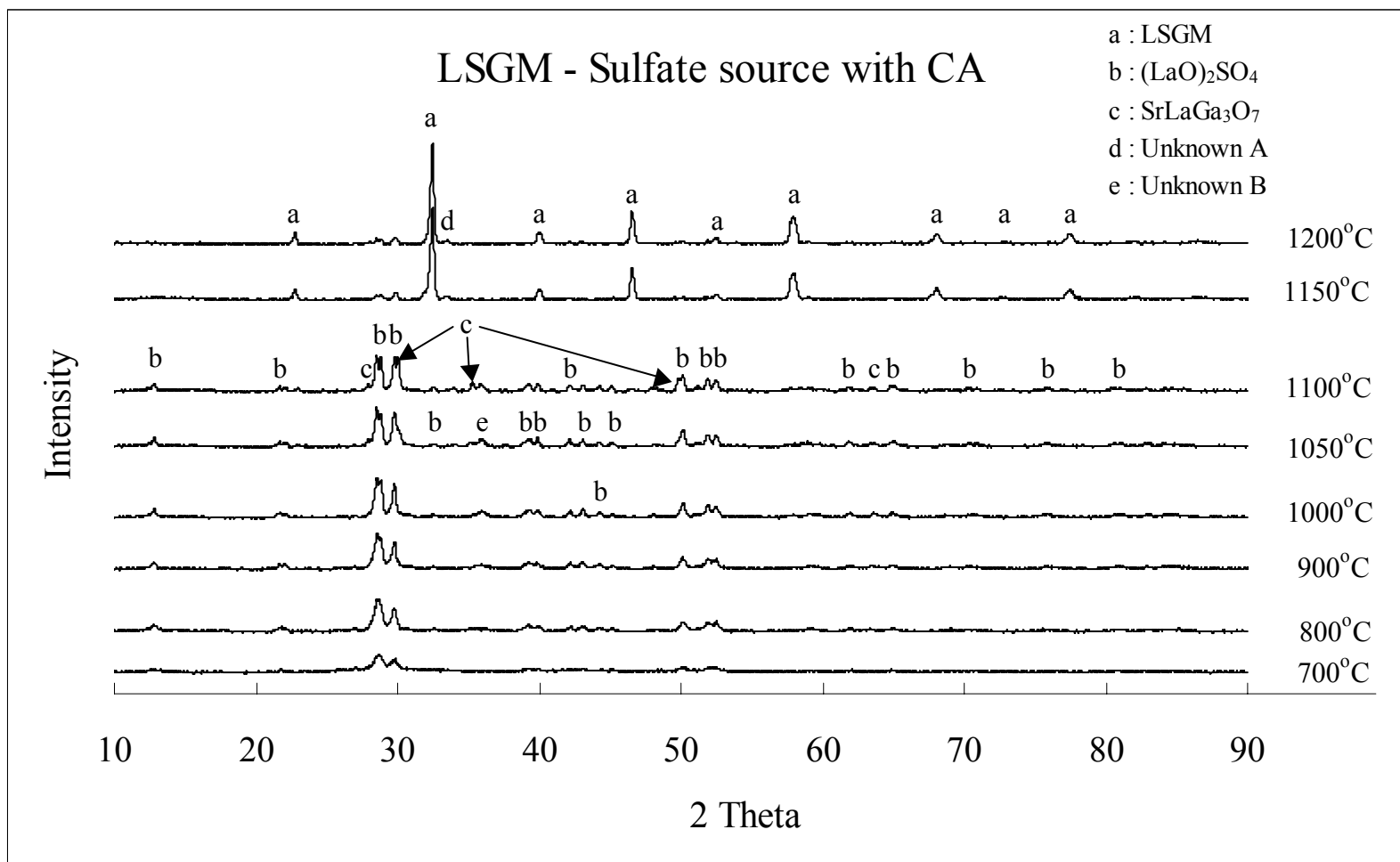


Figure C2. X-ray spectra of LSGM powders synthesized with CA as the organic carrier material, and gallium sulfate as the gallium source

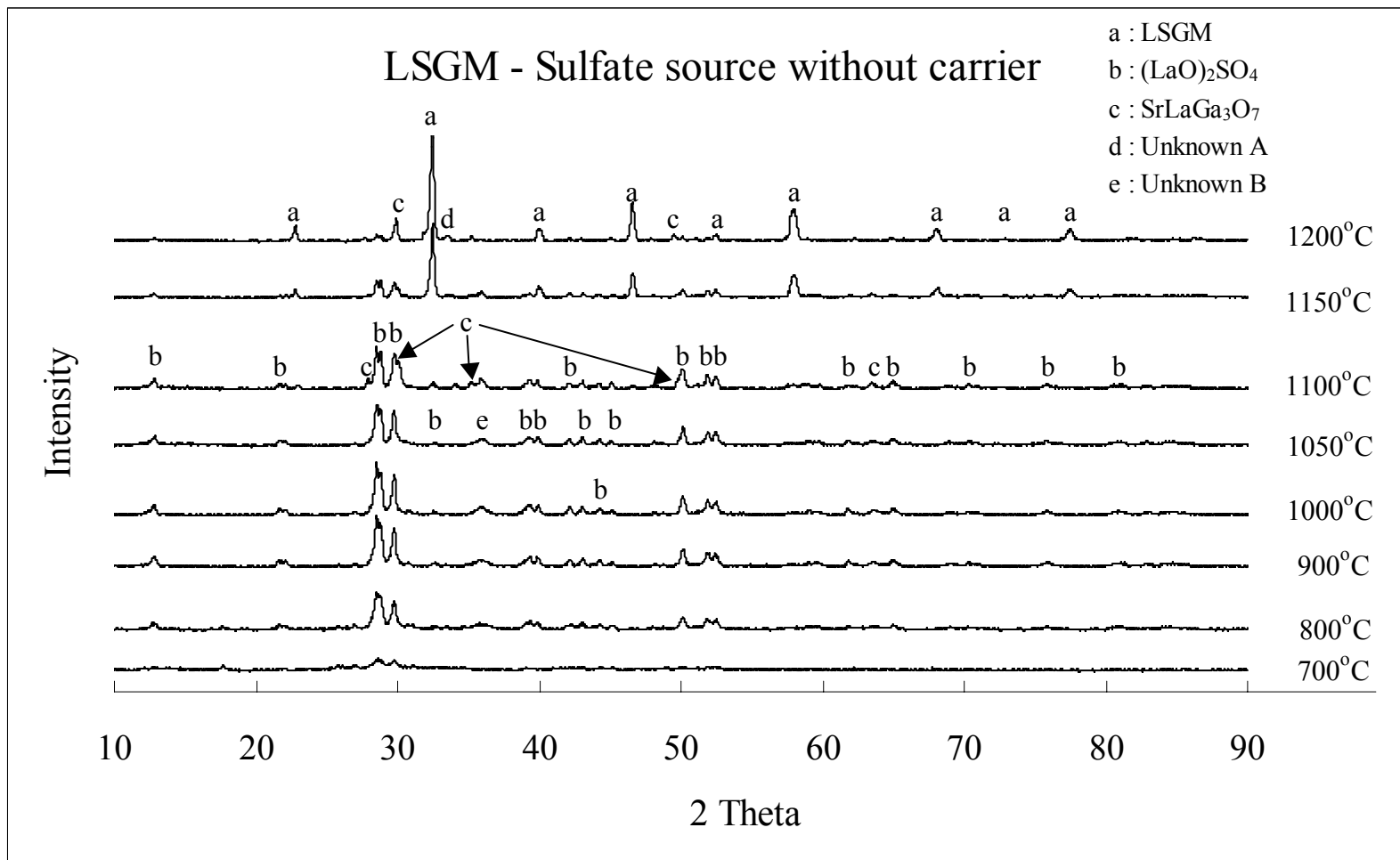


Figure C3. X-ray spectra of LSGM powders synthesized without carrier material, and gallium sulfate as the gallium source.

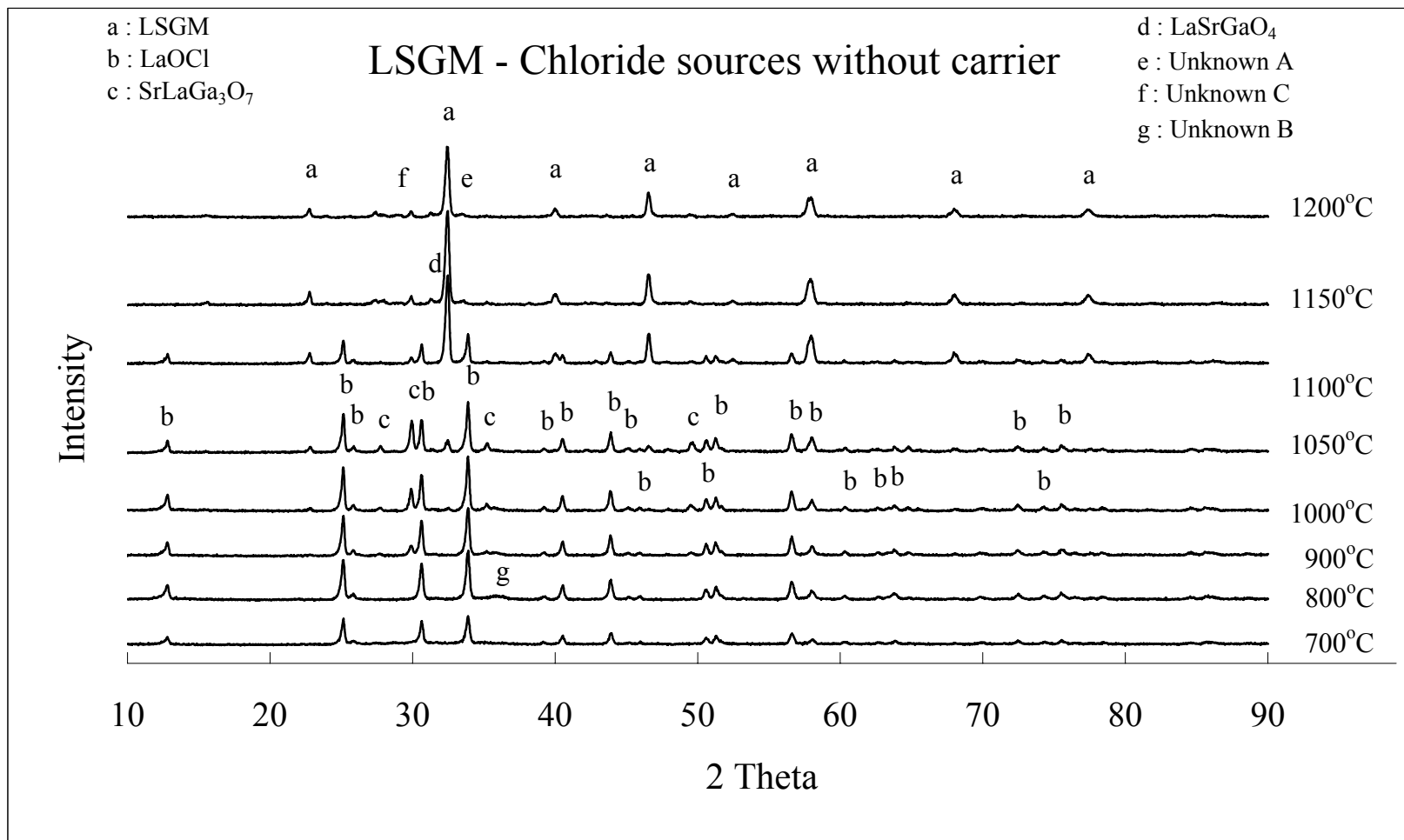


Figure C4. X-ray spectra of LSGM powders synthesized without organic carrier material and lanthanum chloride for lanthanum source.

Appendix D.

The concentrations and amounts of each phase in the LSGM powders synthesized at different calcination temperatures and with different starting materials are tabulated. Amounts of each phase are shown in the parentheses.

Table D1. Concentrations and amounts of the phases in LSGM powders synthesized without organic carrier material, with nitrate sources of the cations.

<i>Nitrate Sources</i>	<i>LSGM</i>	<i>LaSrGaO₄</i>	<i>SrLaGa₃O₇</i>	<i>La₄Ga₂O₉</i>	<i>Unknown A</i>
800°C	Not Detected	Not Detected	64.1% (470)	29.6% (217)	6.3% (46)
900°C	Not Detected	4.5% (83)	52.6% (971)	36.5% (673)	6.4% (119)
1000°C	9.3% (227)	4.1% (100)	41% (1002)	38.7% (946)	6.8% (167)
1050°C	24.3% (343)	5% (71)	32.5% (460)	32.2% (456)	6% (84)
1100°C	30.7% (805)	4.2% (110)	27.4% (720)	31.5% (827)	6.2% (162)
1150°C	39.4% (826)	1.9% (41)	27.7% (581)	25.8% (541)	5.2% (108)
1200°C	54.6% (1947)	6.7% (239)	13.9% (495)	20% (713)	4.8% (169)

Table D2. Concentrations and amounts of the phases in LSGM powders synthesized with CA as the organic carrier material, and with nitrate sources of lanthanum, strontium, magnesium, and sulfate source of gallium.

<i>Nitrate And Sulfate Sources with CA</i>	<i>LSGM</i>	<i>(LaO)₂SO₄</i>	<i>SrLaGa₃O₇</i>	<i>MgGa₂O₄</i>	<i>Unknown A</i>	<i>Unknown B</i>
800°C	Not Detected	91.7% (834)	Not Detected	8.3% (75)	Not Detected	Not Detected
900°C	Not Detected	89.5% (938)	Not Detected	10.5% (110)	Not Detected	Not Detected
1000°C	Not Detected	86.1% (1032)	Not Detected	13.9% (167)	Not Detected	Not Detected
1050°C	3.6% (64)	60% (1032)	23.4% (416)	11% (194)	Not Detected	2% (35)
1100°C	4.8% (110)	41.5% (948)	39.1% (893)	9.2% (210)	Not Detected	5.4% (123)
1150°C	85.1% (2493)	4.3% (125)	6.2% (183)	1.2% (35)	3.2% (93)	Not Detected
1200°C	84.4% (2690)	5.4% (172)	5.8% (184)	1.3% (40)	3.1% (95)	Not Detected

Appendix D. Continued

Table D3. Concentrations and amounts of the phases in LSGM powders synthesized without organic carrier material; with nitrate sources of lanthanum, strontium, magnesium, and sulfate source of gallium.

<i>Nitrate and Sulfate Sources</i>	<i>LSGM</i>	<i>(LaO)₂SO₄</i>	<i>SrLaGa₃O₇</i>	<i>MgGa₂O₄</i>	<i>Unknown A</i>
800°C	Not Detected	89.2% (953)	Not Detected	10.8% (145)	Not Detected
900°C	5.4% (88)	83.6% (1355)	Not Detected	11% (178)	Not Detected
1000°C	5.6% (92)	83% (1385)	Not Detected	11.4% (191)	Not Detected
1050°C	6.1% (82)	81% (1089)	Not Detected	12.9% (174)	Not Detected
1100°C	7.8% (179)	48.7% (1127)	31.4% (727)	12.1% (281)	Not Detected
1150°C	66.5% (1977)	15.7% (466)	8.7% (260)	6.6% (196)	2.5% (75)
1200°C	73.6% (2953)	4.6% (187)	14.6% (586)	3.6% (144)	3.6% (146)

Table D4. Concentrations and amounts of the phases in LSGM powders synthesized without organic carrier material; with nitrate sources of strontium, gallium, magnesium, and chloride source of lanthanum.

<i>Nitrate and Chloride Sources</i>	<i>LSGM</i>	<i>LaSrGaO₄</i>	<i>SrLaGa₃O₇</i>	<i>LaOCl</i>	<i>Unknown A</i>	<i>Unknown C</i>
800°C	Not Detected	Not Detected	Not Detected	100% (1627)	Not Detected	Not Detected
900°C	Not Detected	Not Detected	16.7% (319)	83.3% (1589)	Not Detected	Not Detected
1000°C	3.7% (96)	Not Detected	27.6% (733)	68.7% (1829)	Not Detected	Not Detected
1050°C	12.4% (378)	Not Detected	33.9% (1050)	53.7% (1659)	Not Detected	Not Detected
1100°C	71.8% (2962)	Not Detected	5% (207)	23.2% (958)	Not Detected	Not Detected
1150°C	82.2% (3148)	4.4% (173)	7% (270)	Not Detected	2.8% (130)	3.6% (149)
1200°C	80% (2368)	4.7% (139)	6.4% (189)	Not Detected	3.3% (97)	5.6% (166)

Appendix E.

X-ray diffraction spectra of the powders in LSMF synthesis with different organic carrier materials are illustrated. Calcination temperatures are 500⁰C, 550⁰C, 600⁰C, 650⁰C, 700⁰C, 750⁰C, 800⁰C, and 850⁰C. Present phases are shown on the XRD plots.

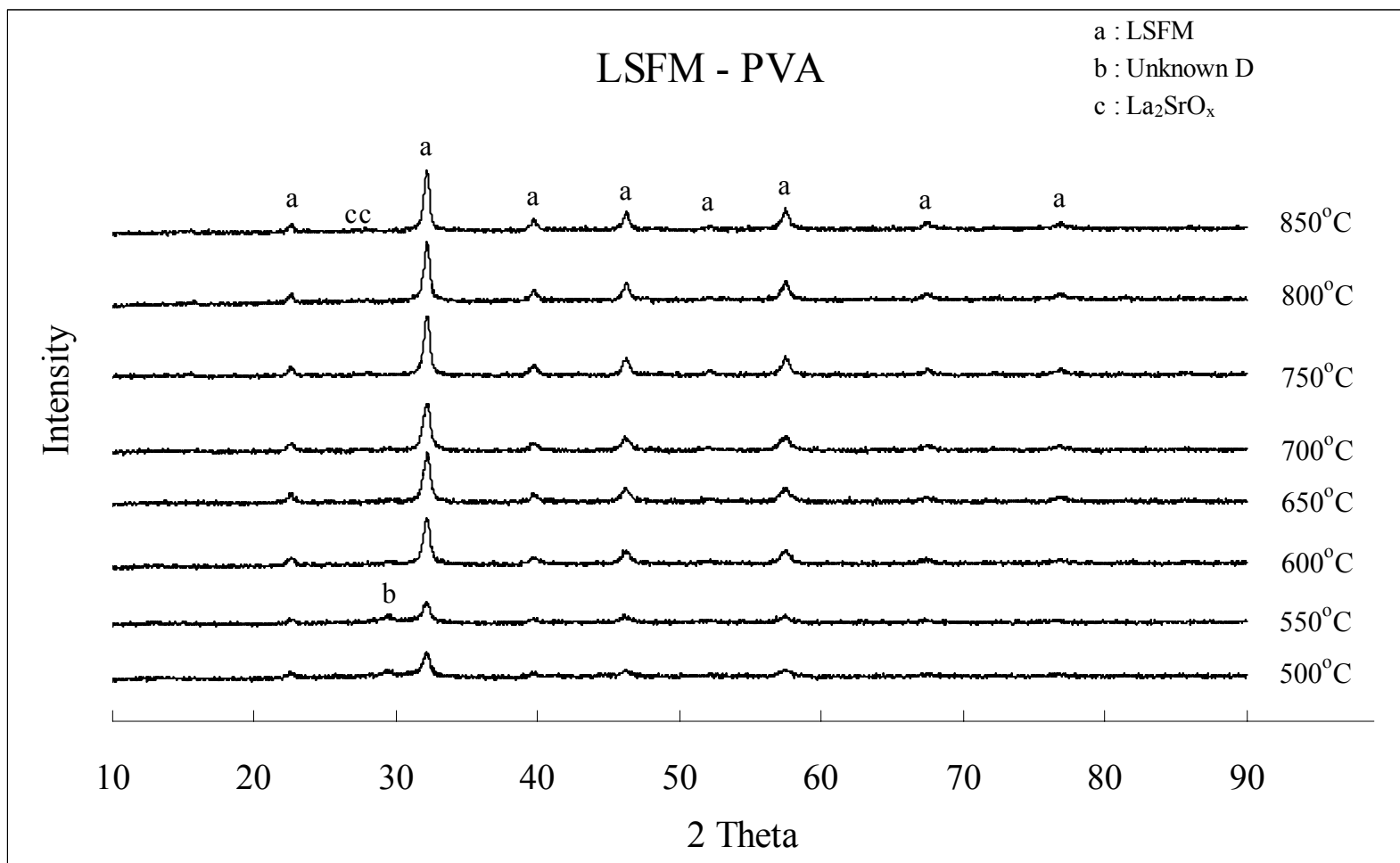


Figure E1. X-ray spectra of LSMF powders synthesized with PVA as the organic carrier material.

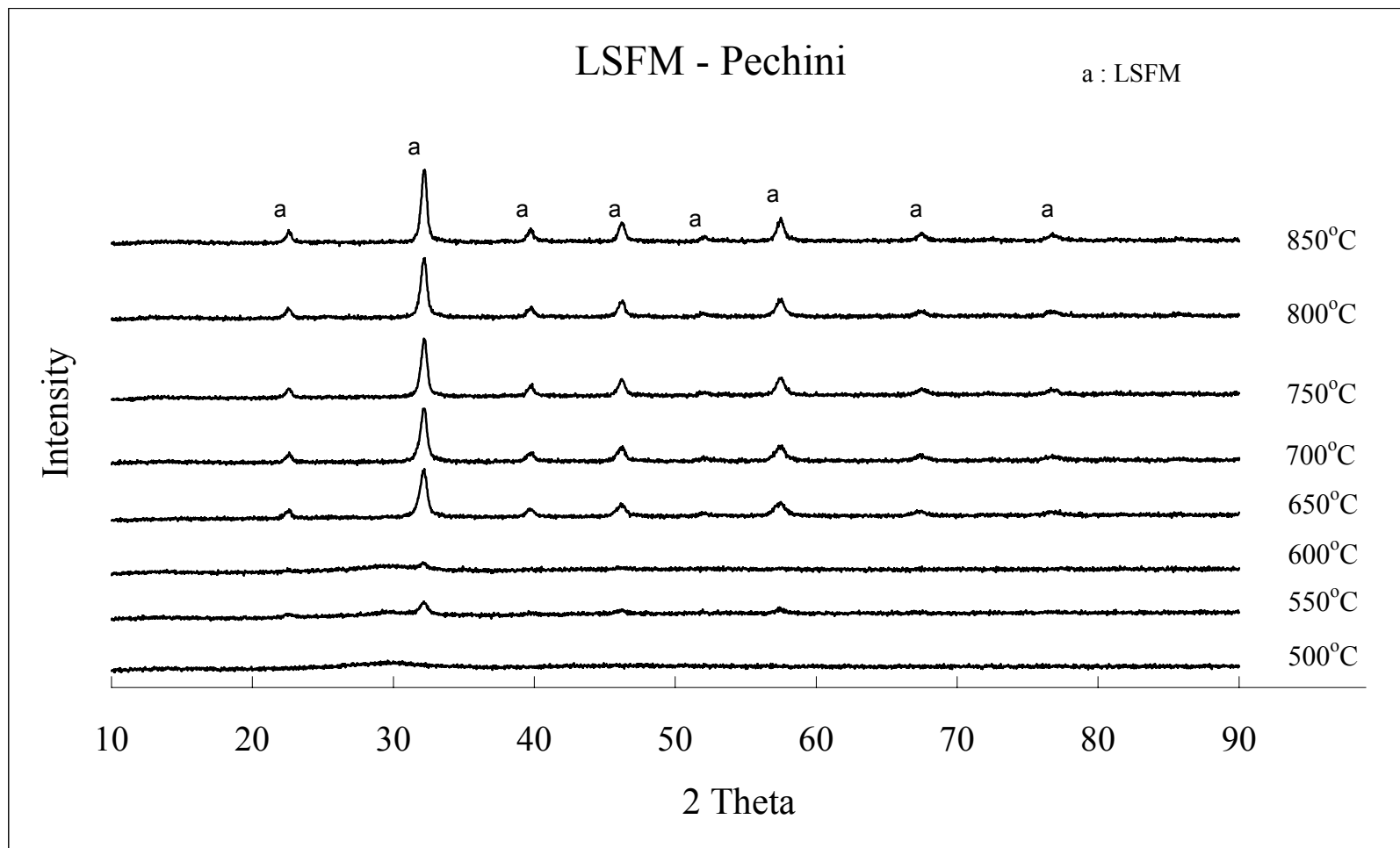


Figure E2. X-ray spectra of LSFM powders synthesized with Pechini precursor (60 wt% CA - 40 wt% EG) as the organic carrier material.

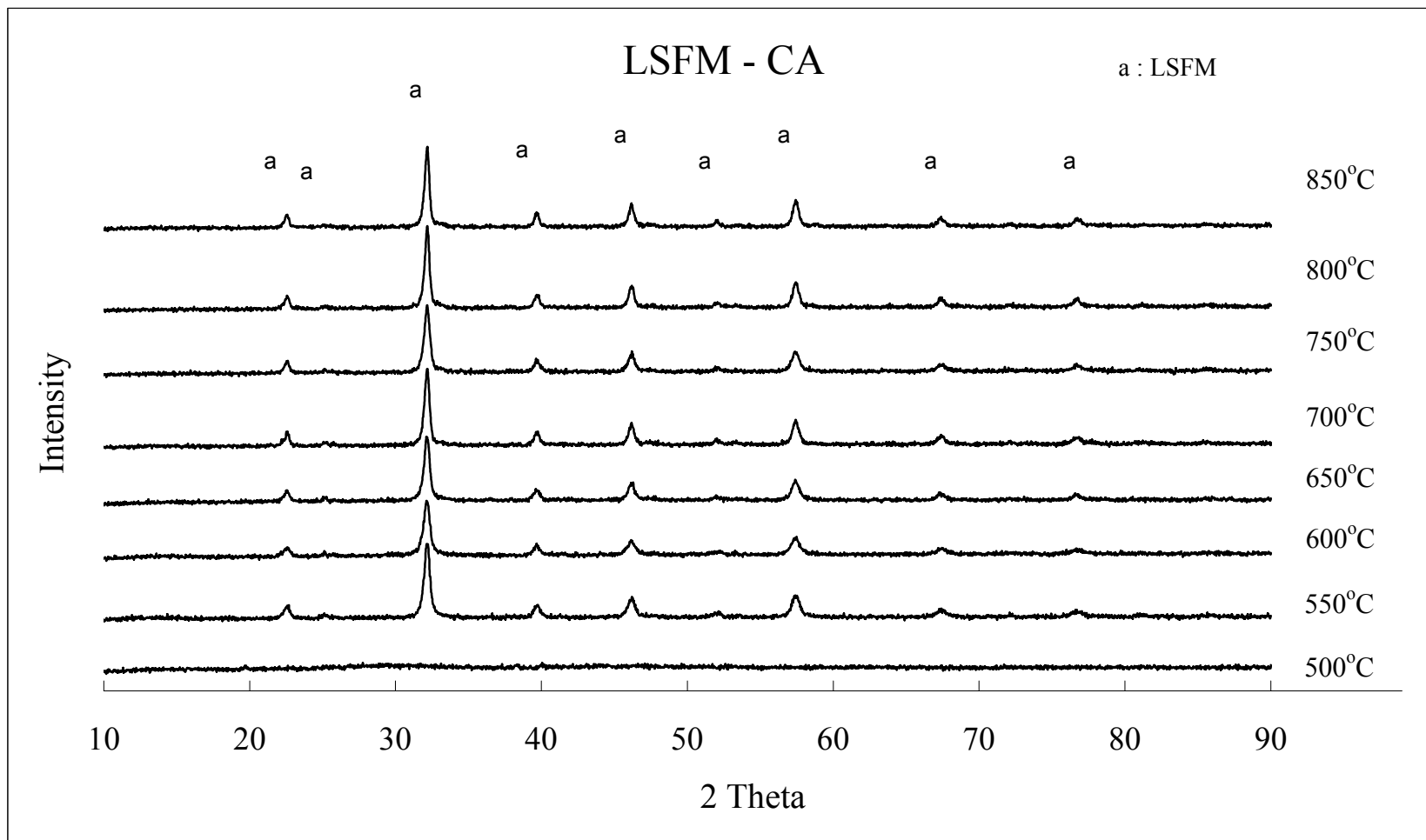


Figure E3. X-ray spectra of LSFM powders synthesized with CA as the organic carrier material.

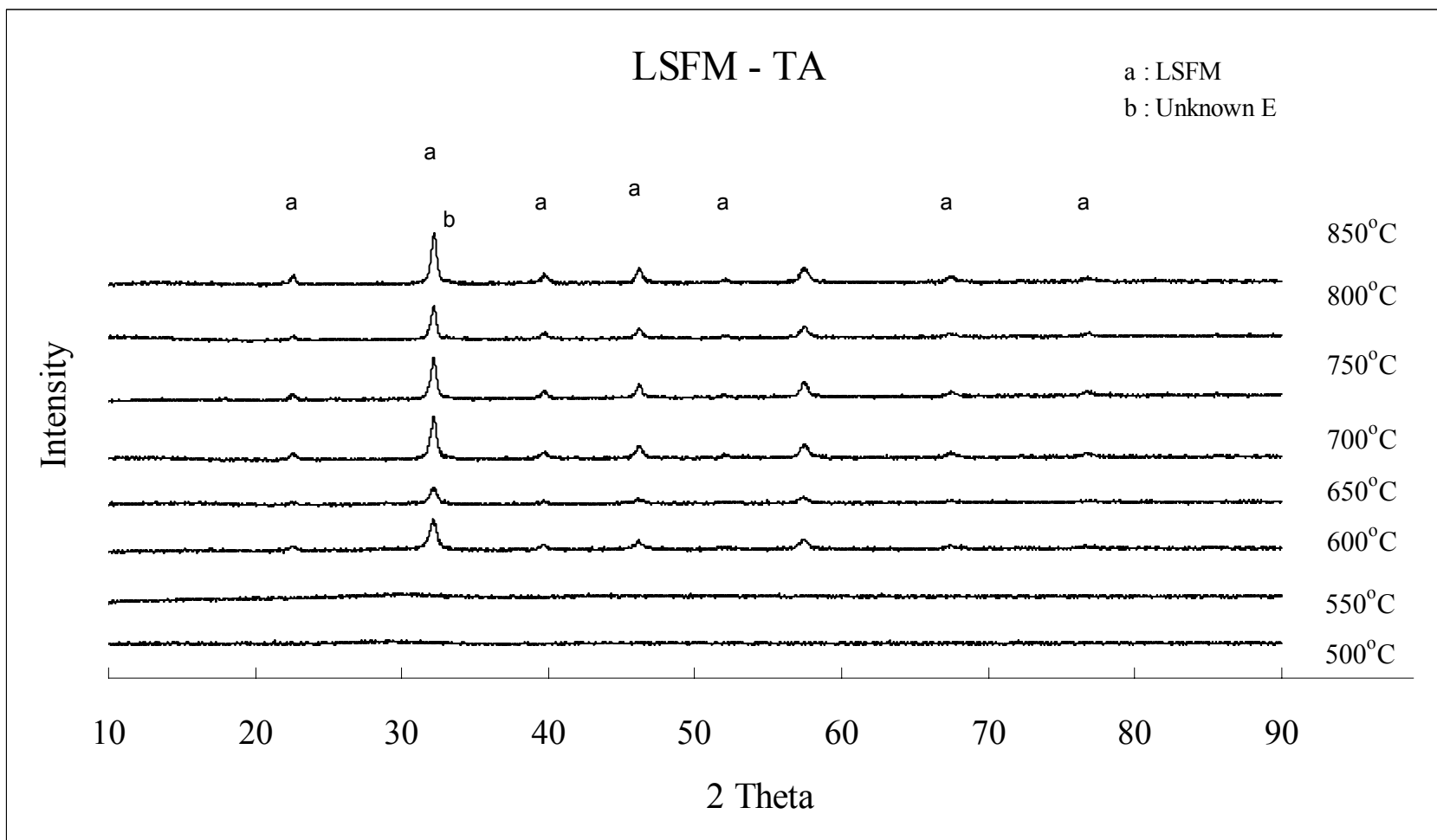


Figure E4. X-ray spectra of LSFM powders synthesized with TA as the organic carrier material.

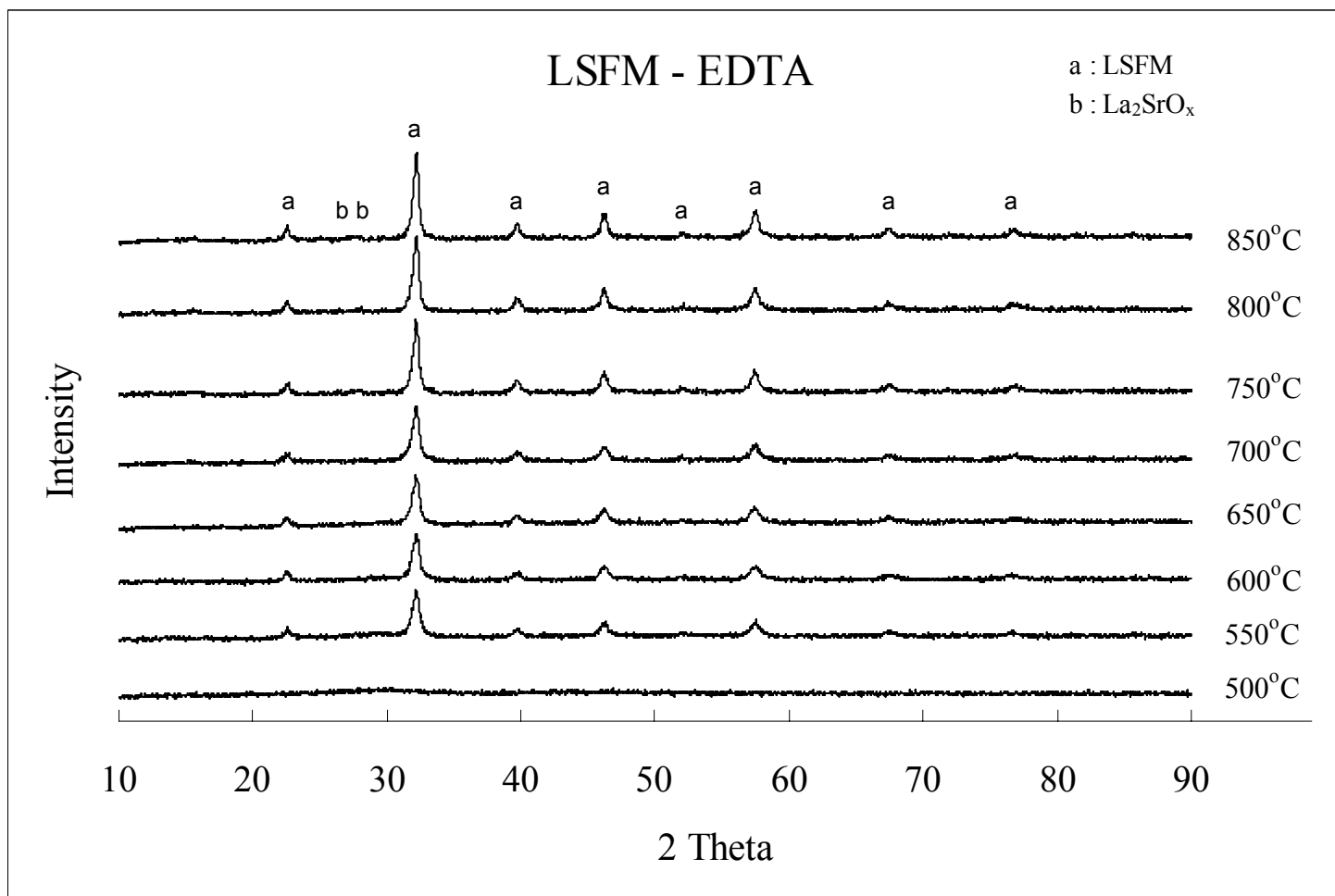


Figure E5. X-ray spectra of LSFM powders synthesized with EDTA as the organic carrier material.

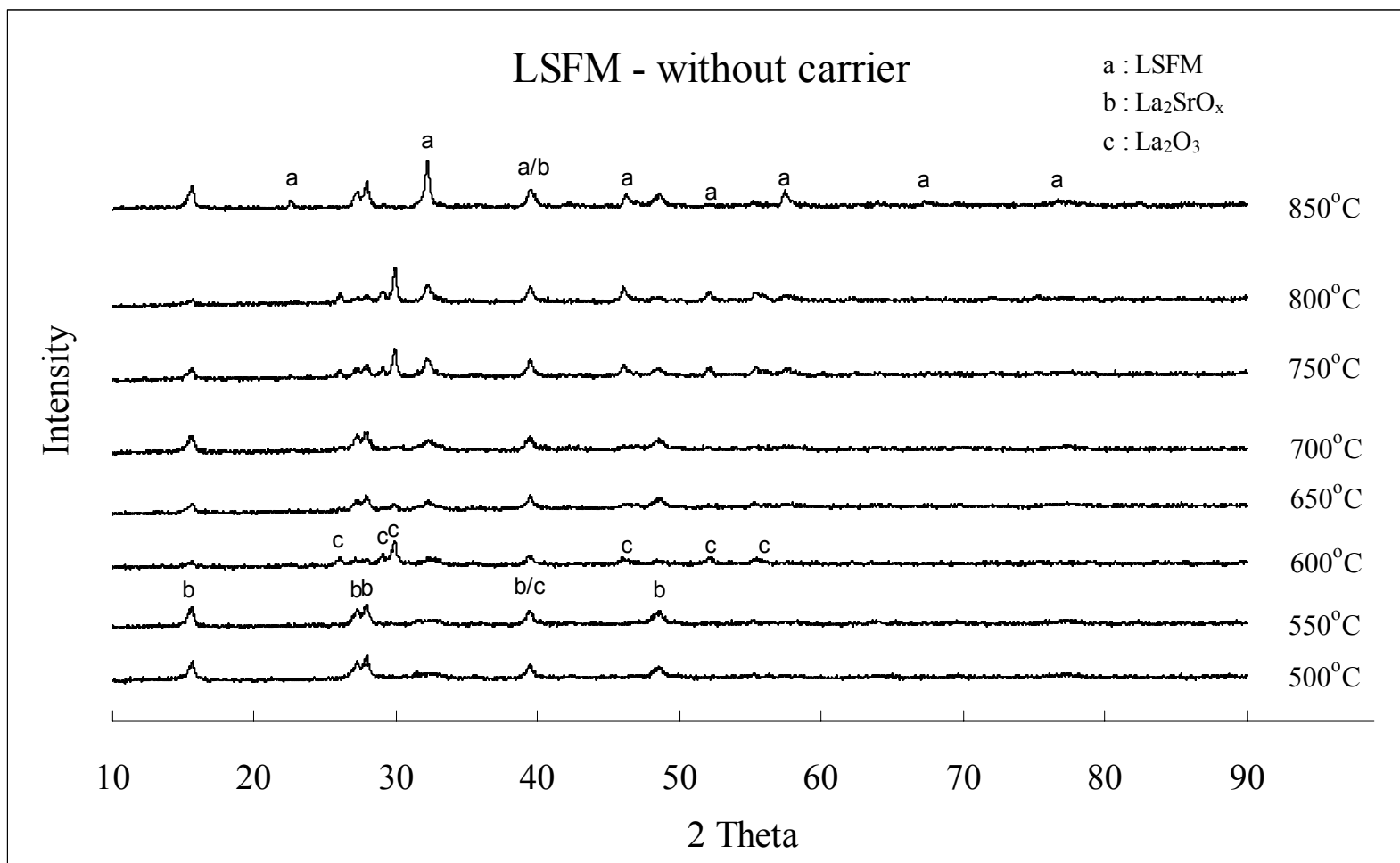


Figure E6. X-ray spectra of LSFM powders synthesized without using organic carrier material.

Appendix F.

The concentrations and amounts of each phase in the LSFM powders synthesized at different calcination temperatures and with different starting materials are tabulated. Amounts of each phase are shown in the parentheses.

Table F1. Concentrations and amounts of the phases in LSFM powders synthesized with PVA as the organic carrier material.

<i>PVA</i>	<i>LSFM</i>	<i>La₂SrO_x</i>	<i>Unknown D</i>
500°C	81.9% (501)	Not Detected	18.1% (111)
550°C	75.2% (421)	Not Detected	24.8% (139)
600°C	92.6% (939)	Not Detected	7.4% (75)
650°C	92.9% (1072)	Not Detected	7.1% (82)
700°C	87.5% (978)	6.5% (73)	6% (67)
750°C	94.4% (1237)	5.6% (74)	Not Detected
800°C	93.9% (1258)	6.1% (82)	Not Detected
850°C	96.2% (1248)	3.8% (50)	Not Detected

Table F2. Concentrations and amounts of phases in LSFM powders synthesized with Pechini precursor (60 wt% citric acid – 40 wt% ethylene glycol) as the organic carrier material.

<i>Pechini</i>	<i>LSFM</i>
550°C	100% (320)
600°C	100% (180)
650°C	100% (1207)
700°C	100% (1341)
750°C	100% (1466)
800°C	100% (1496)
850°C	100% (1820)

Appendix F. Continued

Table F3. Concentrations and amounts of the phases in LSFM powders synthesized with CA as the organic carrier material.

<i>CA</i>	<i>LSFM</i>
550°C	100% (1702)
600°C	100% (1260)
650°C	100% (1465)
700°C	100% (1772)
750°C	100% (1566)
800°C	100% (1901)
850°C	100% (1861)

Table F4. Concentrations and amounts of the phases in LSFM powders synthesized with TA as the organic carrier material.

<i>TA</i>	<i>LSFM</i>	<i>Unknown E</i>
600°C	100% (768)	Not Detected
650°C	100% (415)	Not Detected
700°C	100% (1068)	Not Detected
750°C	100% (1056)	Not Detected
800°C	94.7% (842)	5.3% (47)
850°C	93.7% (1283)	6.3% (86)

Appendix F. Continued

Table F5. Concentrations and amounts of the phases in LSFM powders synthesized with EDTA as the organic carrier material.

<i>EDTA</i>	<i>LSFM</i>	<i>La₂SrO_x</i>
550°C	100% (930)	Not Detected
600°C	100% (933)	Not Detected
650°C	100% (988)	Not Detected
700°C	97% (1110)	3% (35)
750°C	95% (1510)	5% (80)
800°C	95% (1560)	5% (83)
850°C	95% (1785)	5% (95)

Table F6. Concentrations and amounts of the phases in LSFM powders synthesized without any organic carrier material; and with nitrate sources of the cations.

<i>Nitrate Sources</i>	<i>LSFM</i>	<i>La₂SrO_x</i>	<i>La₂O₃</i>
500°C	17.8% (104)	82.2% (481)	Not Detected
550°C	22.8% (127)	77.2% (431)	Not Detected
600°C	19% (141)	14.5% (108)	66.5% (494)
650°C	29.5% (182)	49% (303)	21.5% (133)
700°C	32% (192)	57.6% (345)	10.4% (62)
750°C	31.6% (379)	19.9% (238)	48.5% (581)
800°C	29.6% (356)	11.2% (135)	59.2% (712)
850°C	61.2% (979)	34.4% (550)	4.4% (70)

Appendix G.

X-ray diffraction spectra of the powders in LSCM synthesis with different organic carrier materials are illustrated. Calcination temperatures are 500⁰C, 550⁰C, 600⁰C, 650⁰C, 700⁰C, 750⁰C, 800⁰C, and 850⁰C. Present phases are shown on the XRD plots.

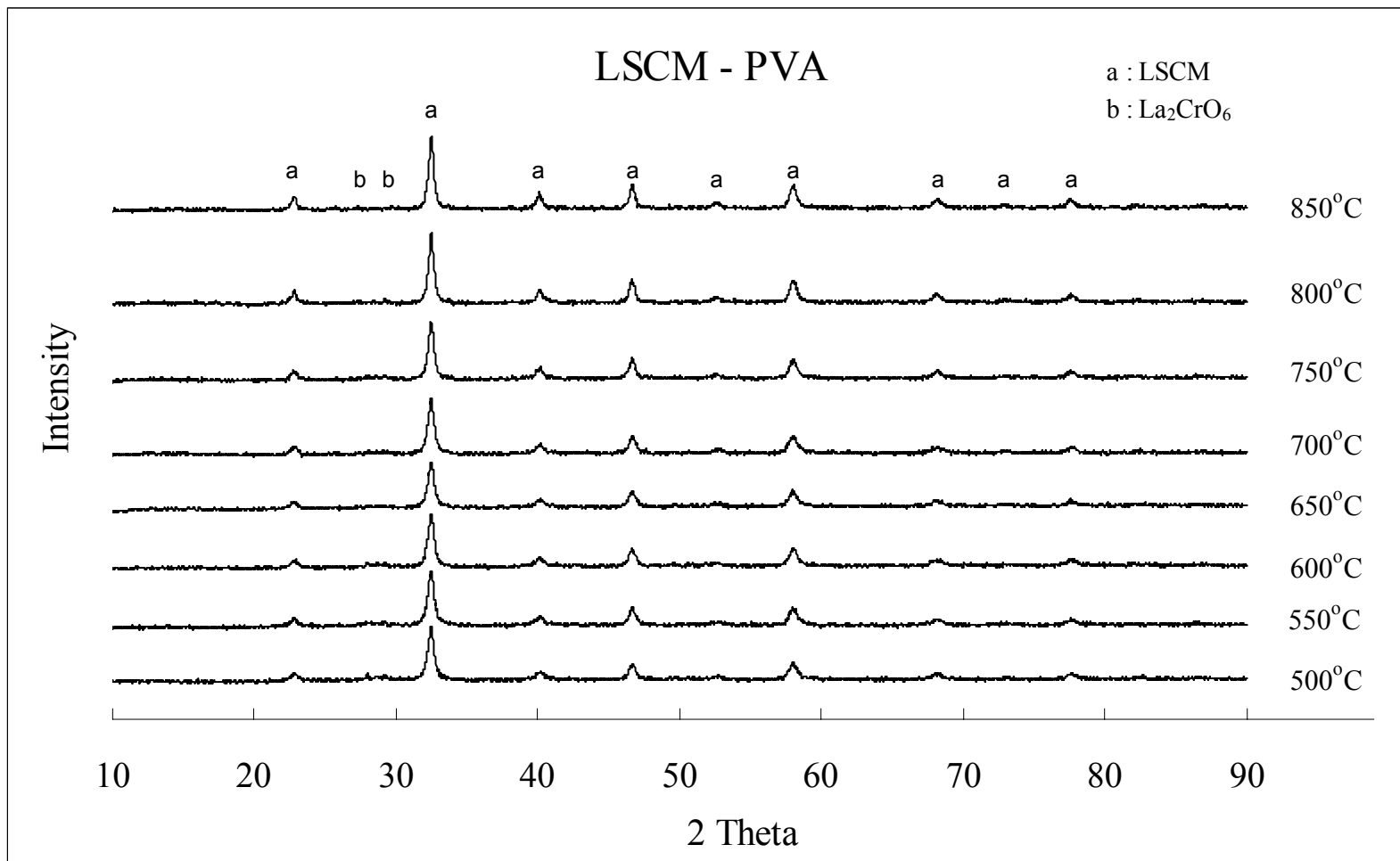


Figure G1. X-ray spectra of LSCM powders synthesized with PVA as the organic carrier material.

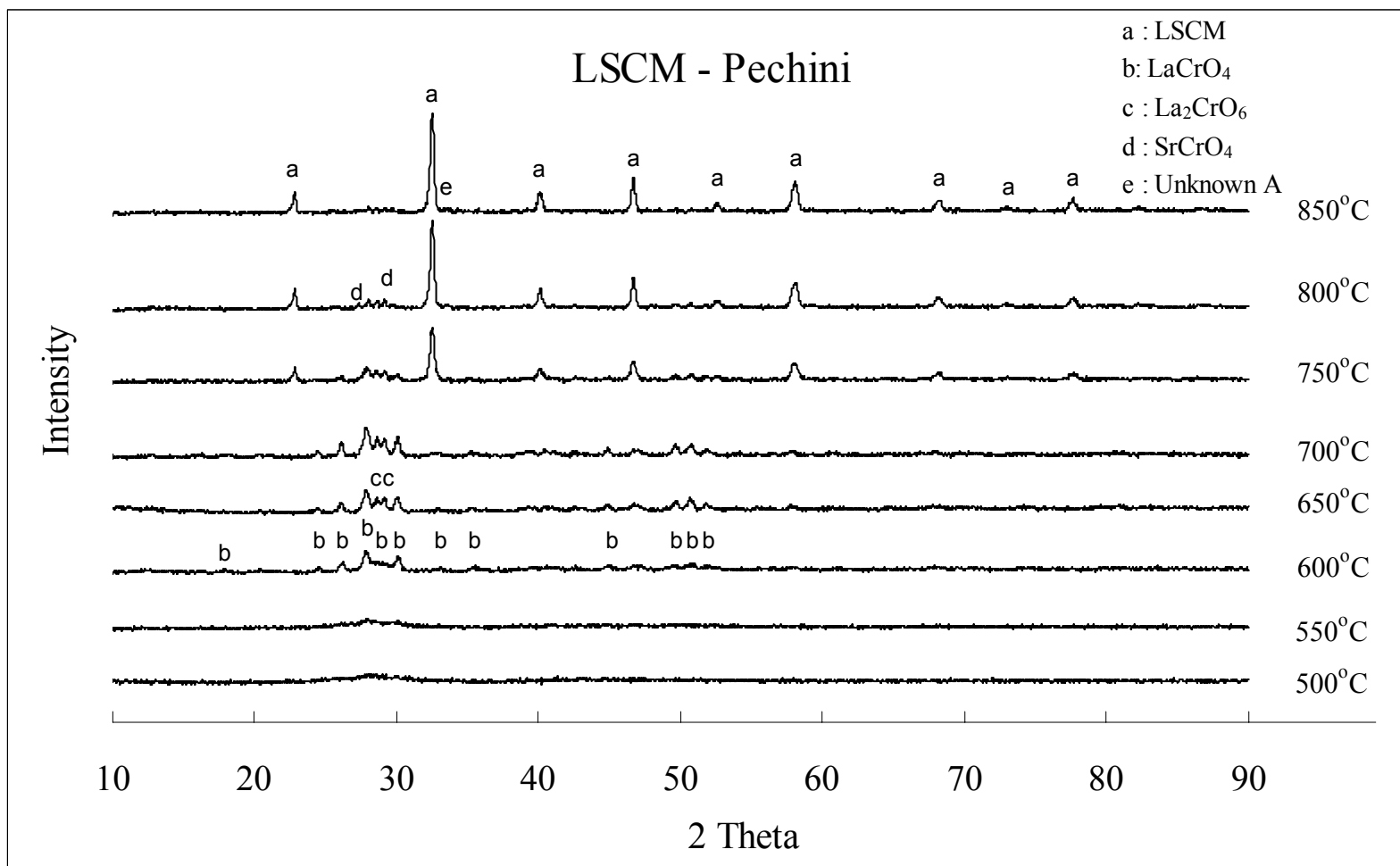


Figure G2. X-ray spectra of LSCM powders with Pechini precursor (60 wt% CA - 40 wt% EG) as the organic carrier material.

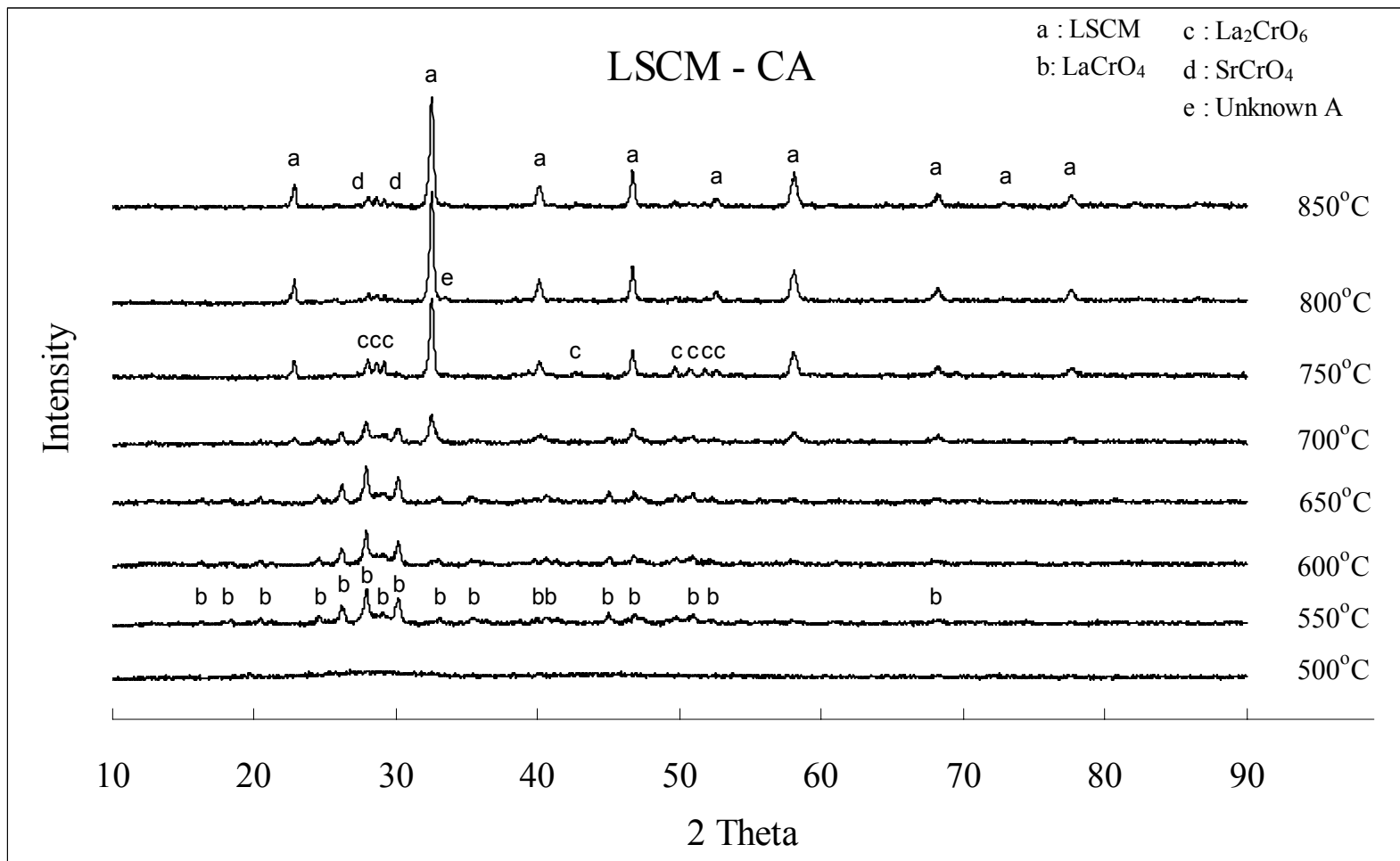


Figure G3. X-ray spectra of LSCM powders synthesized with CA as the organic carrier material.

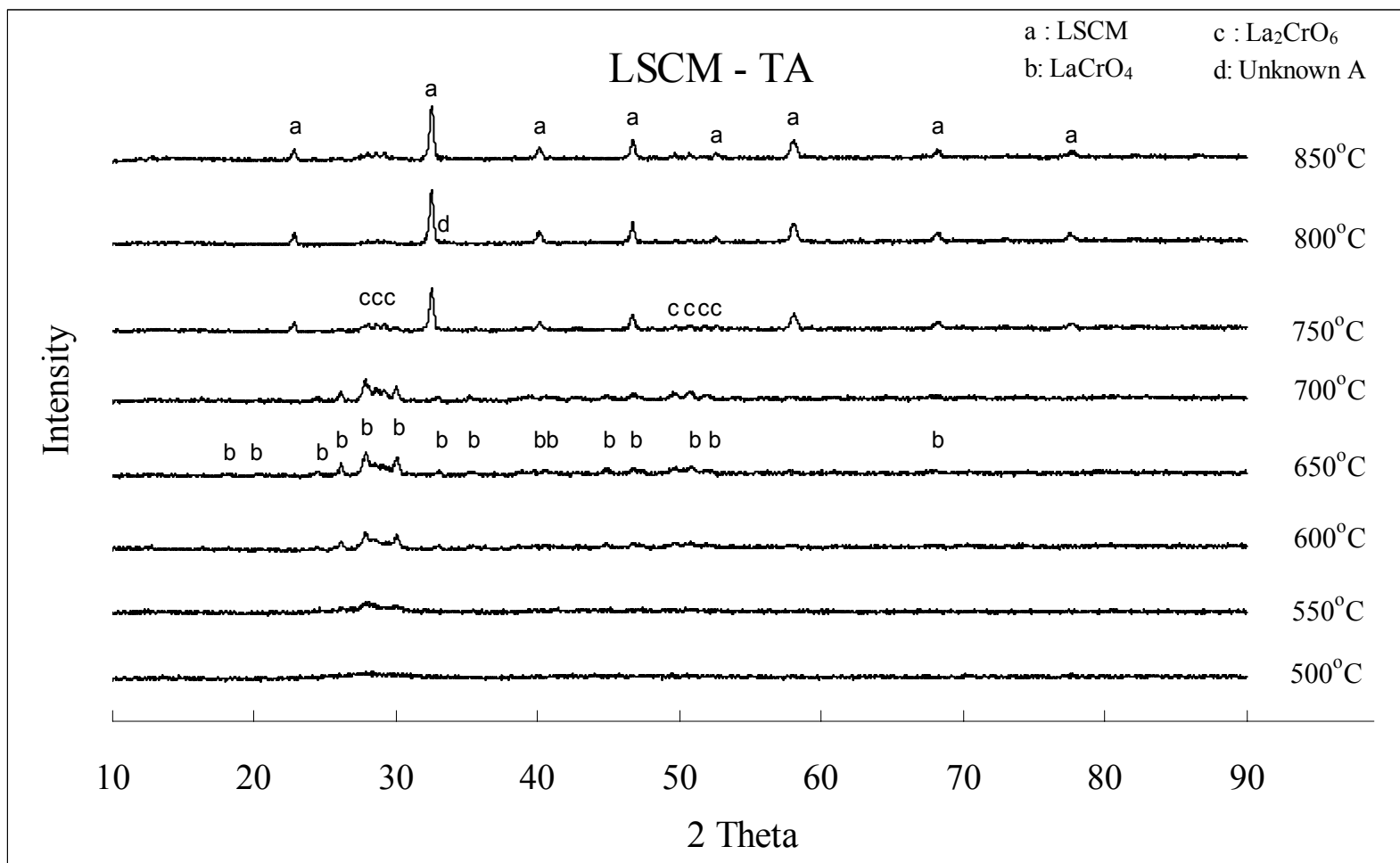


Figure G4. X-ray spectra of LSCM powders synthesized with TA as the organic carrier material.

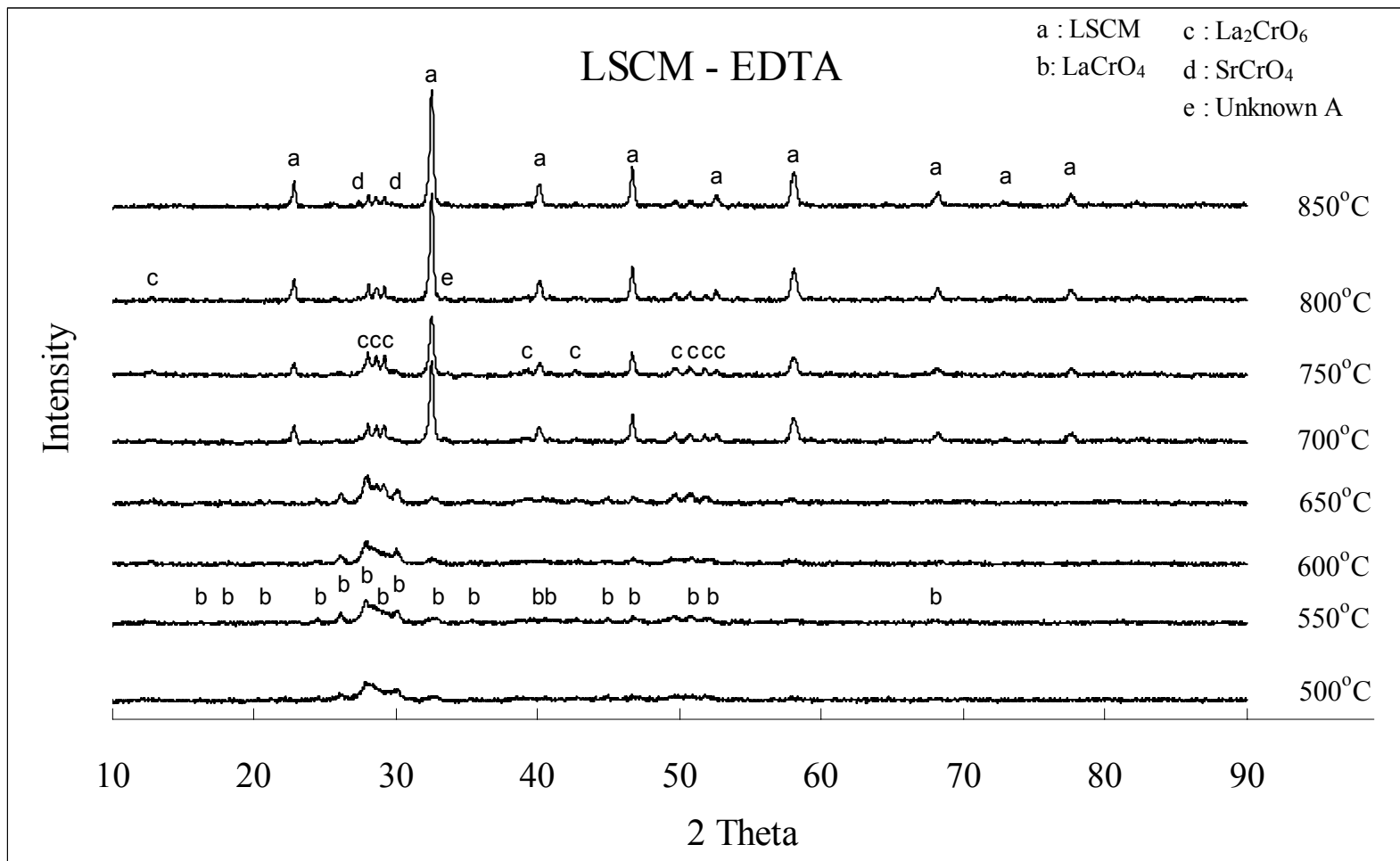


Figure G5. X-ray spectra of LSCM powders synthesized with EDTA as the organic carrier material.

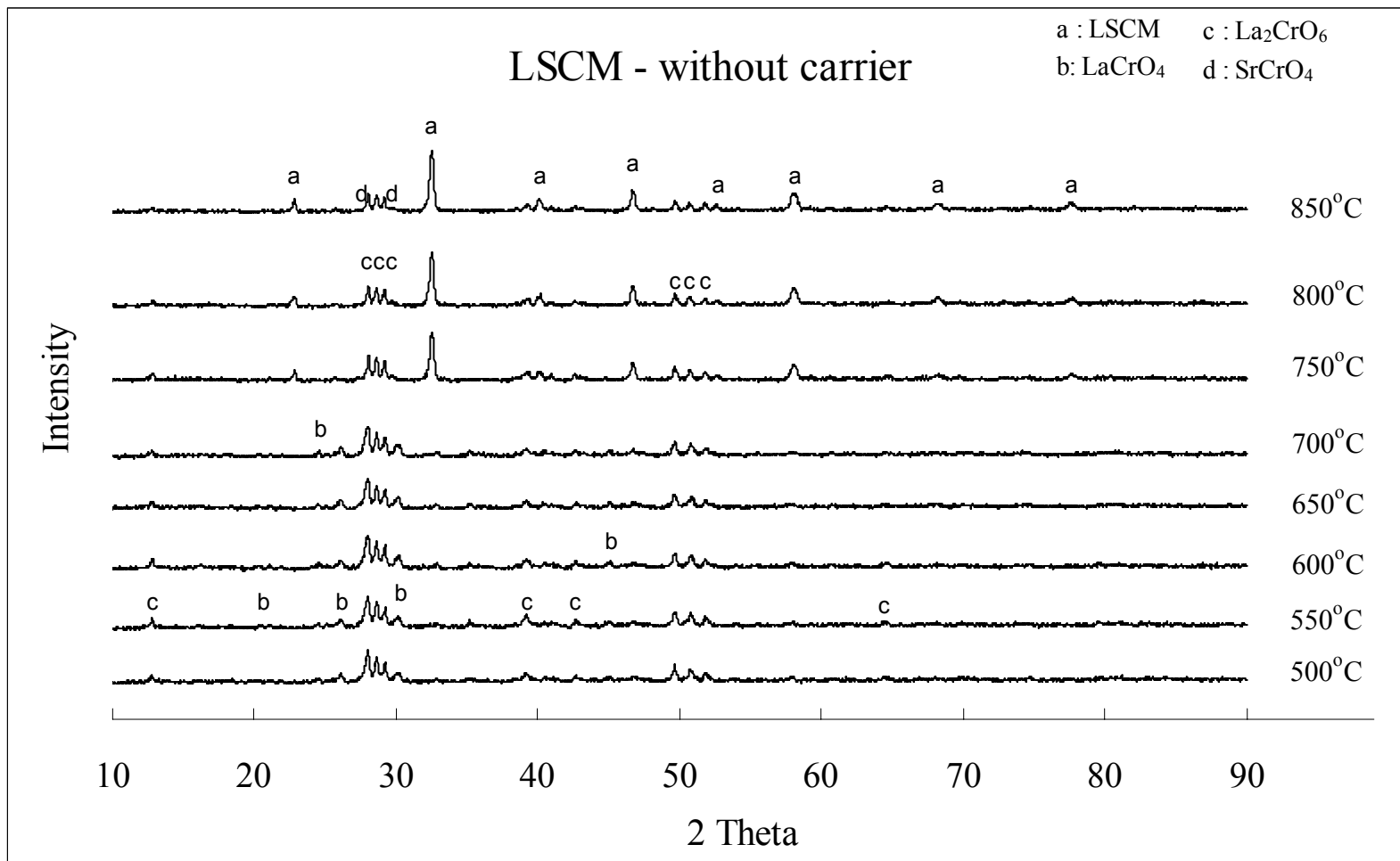


Figure G6. X-ray spectra of LSCM powders synthesized without using organic carrier material.

Appendix H.

The concentrations and amounts of each phase in the LSCM powders synthesized at different calcination temperatures and with different starting materials are tabulated. Amounts of each phase are shown in the parentheses.

Table H1. Concentrations and amounts of the phases in LSCM powders synthesized with PVA as the organic carrier material.

<i>PVA</i>	<i>LSCM</i>	<i>La₂CrO₆</i>
500°C	88.80%	11.20%
550°C	94.20%	5.80%
600°C	93.00%	7.00%
650°C	94.60%	5.40%
700°C	94.30%	5.70%
750°C	93.20%	6.80%
800°C	96.50%	3.50%
850°C	96.90%	3.10%

Table H2. Concentrations and amounts of phases in LSCM powders synthesized with Pechini precursor (60 wt% citric acid – 40 wt% ethylene glycol) as the organic carrier material.

<i>Pech</i>	<i>LSCM</i>	<i>La₂CrO₆</i>	<i>LaCrO₄</i>	<i>SrCrO₄</i>	<i>Unknown A</i>
600°C	Not Detected	Not Detected	100% (422)	Not Detected	Not Detected
650°C	Not Detected	40.2% (315)	59.8% (468)	Not Detected	Not Detected
700°C	Not Detected	42.1% (435)	57.9% (598)	Not Detected	Not Detected
750°C	66.2% (1112)	18% (303)	15.8% (265)	Not Detected	Not Detected
800°C	85.4% (1835)	8% (173)	Not Detected	2.7% (57)	3.9% (84)
850°C	90.7% (2085)	4.3% (99)	Not Detected	2% (45)	3% (70)

Appendix H. Continued

Table H3. Concentrations and amounts of the phases in LSCM powders synthesized with CA as the organic carrier material.

<i>CA</i>	<i>LSCM</i>	<i>La₂CrO₆</i>	<i>LaCrO₄</i>	<i>SrCrO₄</i>	<i>Unknown A</i>
550°C	Not Detected	Not Detected	100% (723)	Not Detected	Not Detected
600°C	Not Detected	Not Detected	100% (707)	Not Detected	Not Detected
650°C	Not Detected	Not Detected	100% (766)	Not Detected	Not Detected
700°C	57.4% (613)	Not Detected	42.6% (455)	Not Detected	Not Detected
750°C	81% (1656)	16% (339)	Not Detected	Not Detected	3% (66)
800°C	90.1% (2337)	6% (156)	Not Detected	Not Detected	3.9% (100)
850°C	87.1% (2324)	6.9% (184)	Not Detected	3% (80)	3% (80)

Table H4. Concentrations and amounts of the phases in LSCM powders synthesized with TA as the organic carrier material.

<i>TA</i>	<i>LSCM</i>	<i>La₂CrO₆</i>	<i>LaCrO₄</i>	<i>Unknown A</i>
550°C	Not Detected	Not Detected	100% (150)	Not Detected
600°C	Not Detected	41% (211)	59% (303)	Not Detected
650°C	Not Detected	37.2% (251)	62.8% (434)	Not Detected
700°C	Not Detected	41.4% (269)	58.6% (381)	Not Detected
750°C	74.2% (733)	13.3% (139)	9.6% (100)	2.9% (30)
800°C	85.7% (857)	6.1% (70)	3.8% (44)	4.4% (50)
850°C	80.9% (986)	9.8% (119)	5.7% (69)	3.6% (45)

Appendix H. Continued

Table H5. Concentrations and amounts of the phases in LSCM powders synthesized with EDTA as the organic carrier material.

<i>EDTA</i>	<i>LSCM</i>	<i>La₂CrO₆</i>	<i>LaCrO₄</i>	<i>SrCrO₄</i>	<i>Unknown A</i>
500°C	Not Detected	Not Detected	100% (373)	Not Detected	Not Detected
550°C	Not Detected	Not Detected	100% (477)	Not Detected	Not Detected
600°C	Not Detected	37.3% (275)	62.7% (463)	Not Detected	Not Detected
650°C	Not Detected	36.8% (447)	63.2% (769)	Not Detected	Not Detected
700°C	76.2% (1713)	16.7% (375)	3.6% (80)	Not Detected	3.5% (78)
750°C	66.3% (1271)	24.1% (464)	5.9% (117)	Not Detected	3.7% (70)
800°C	81.3% (2264)	11.7% (326)	2% (56)	1.6% (45)	3.4% (94)
850°C	84.9% (2479)	7.7% (225)	1.8% (52)	3.6% (106)	2% (59)

Table H6. Concentrations and amounts of the phases in LSCM powders synthesized without any organic carrier material; and with nitrate sources of the cations.

<i>Nitrate Sources</i>	<i>LSCM</i>	<i>La₂CrO₆</i>	<i>LaCrO₄</i>	<i>SrCrO₄</i>
500°C	Not Detected	59.1% (680)	40.9% (470)	Not Detected
550°C	Not Detected	54.9% (648)	45.1% (532)	Not Detected
600°C	Not Detected	55.8% (672)	44.2% (535)	Not Detected
650°C	Not Detected	49% (589)	51% (613)	Not Detected
700°C	Not Detected	49.6% (605)	50.4% (616)	Not Detected
750°C	65.6% (1006)	34.4% (528)	Not Detected	Not Detected
800°C	71.4% (1113)	26.7% (416)	Not Detected	1.9% (30)
850°C	74.3% (1281)	22.7% (392)	Not Detected	3% (52)

Appendix I.

X-ray diffraction spectra of the powders in LSGM synthesis, which held 11 days at 800⁰C for durability test, are illustrated. Present phases are shown on the XRD plots. XRD plots of the powder synthesized;

- i) with CA as the organic carrier material, and calcined at 1000⁰C compared with same powder held 11 days at 800⁰C,
- ii) with Pechini precursor (90 wt% CA – 10 wt% EG) as the organic carrier material, and calcined at 1200⁰C compared with same powder held 11 days at 800⁰C,
- iii) with TA as the organic carrier material, and calcined at 1100⁰C compared with same powder held 11 days at 800⁰C, and
- iv) with lanthanum chloride as the lanthanum source, and nitrate sources of strontium, gallium, and magnesium, and calcined at 1200⁰C compared with same powder held 11 days at 800⁰C.

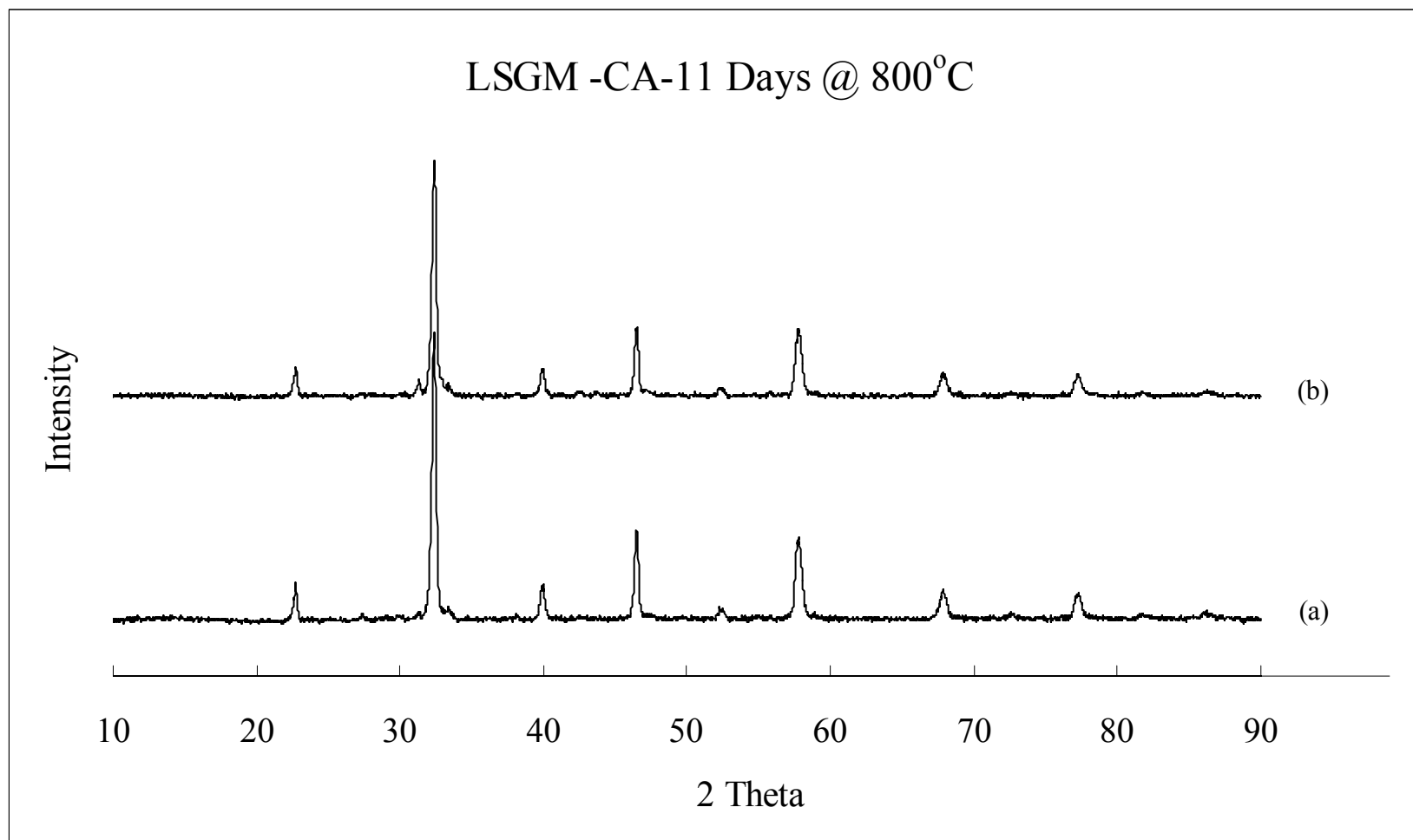


Figure I 1. X- ray spectra of LSGM powders synthesized with CA; a) calcined at 1000°C, b) calcined at 1000°C and held 11 days at 800°C.

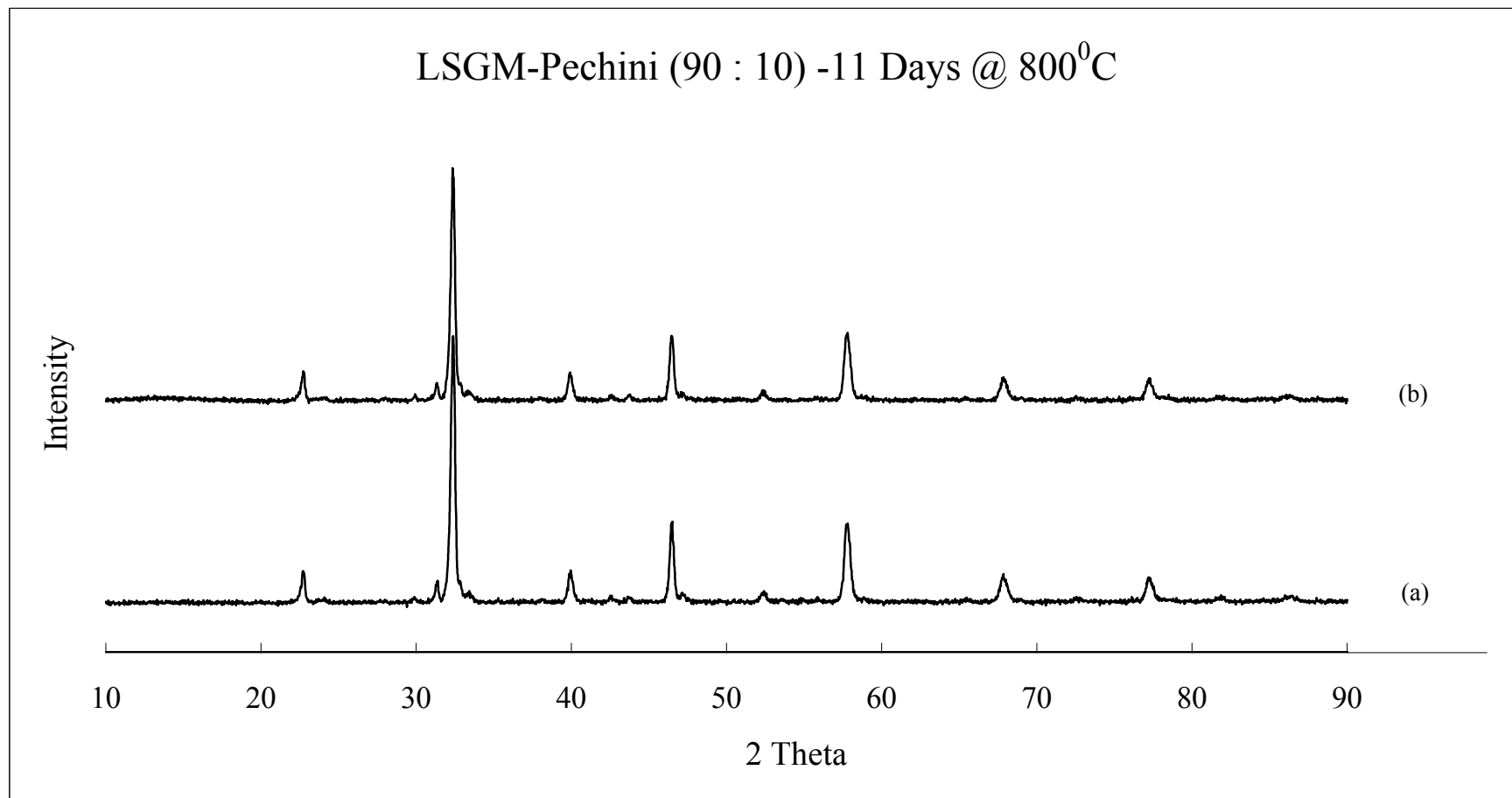


Figure I 2. X- ray spectra of LSGM powders synthesized by Pechini precursor; a) calcined at 1200°C, b) same powder held 11 days at 800°C.

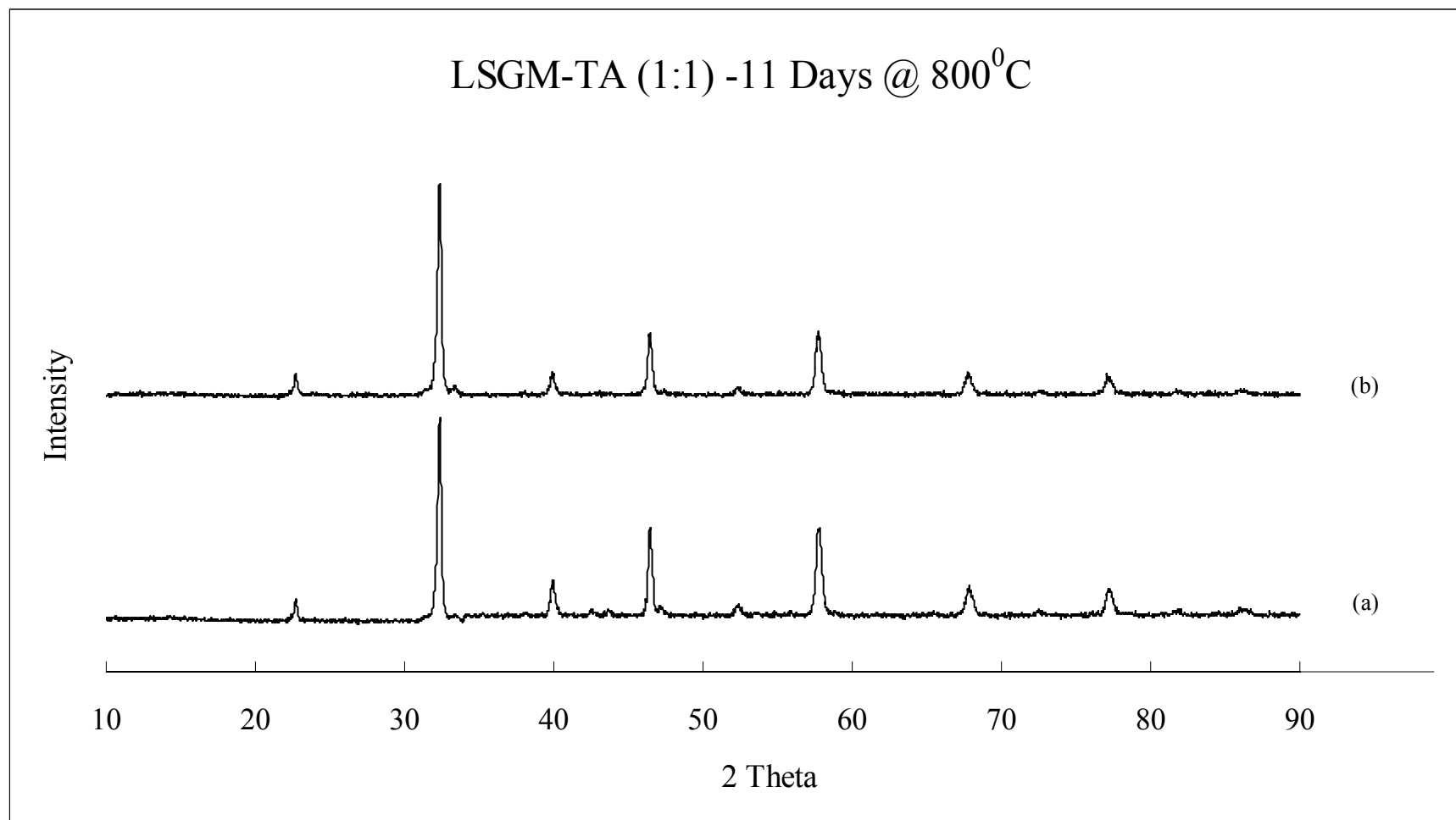


Figure I 3. X- ray spectra of LSGM powders synthesized by using TA; a) calcined at 1100°C, b) calcined at 1100°C and held 11 days at 800°C.

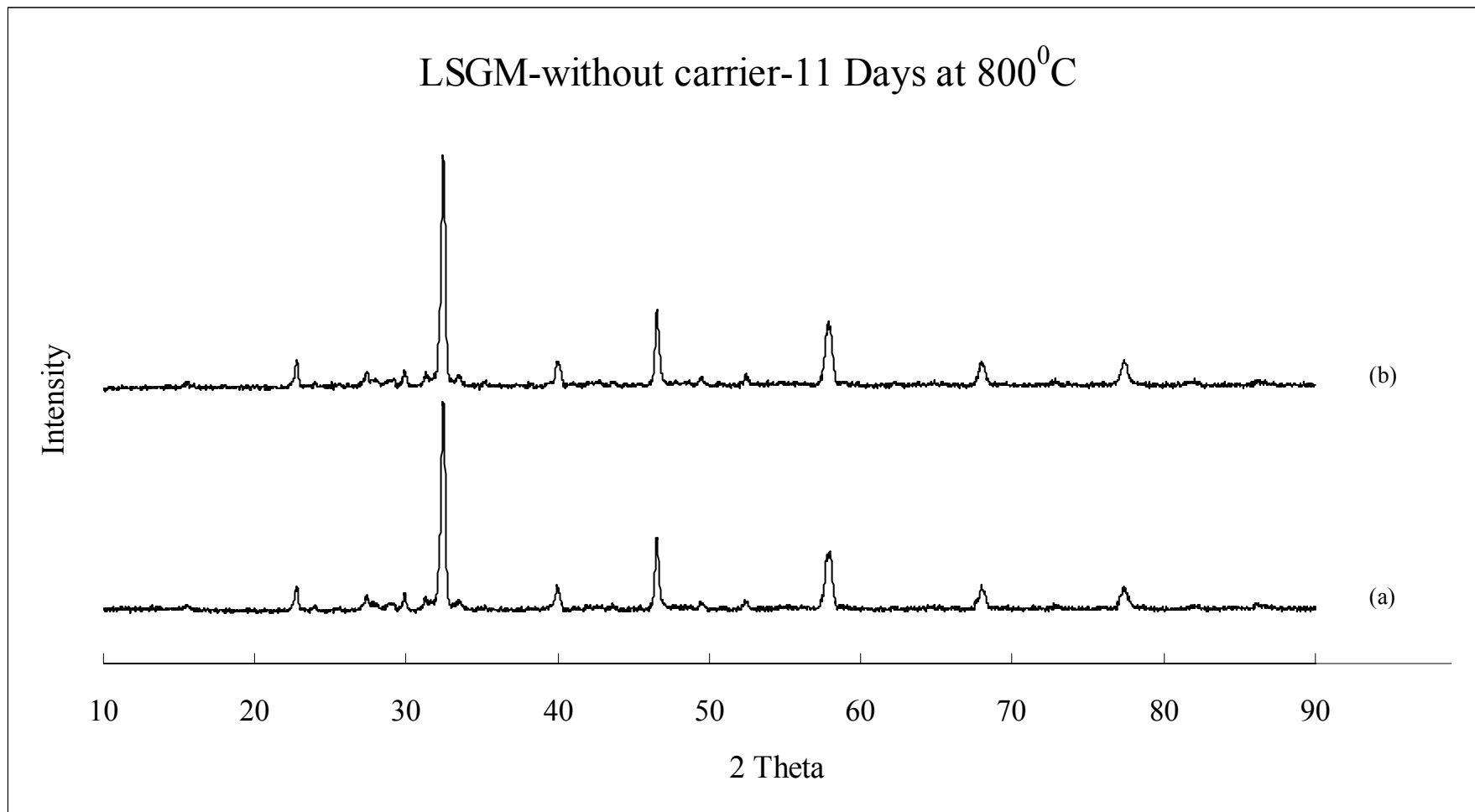


Figure I 4. X- ray spectra of LSGM powders synthesized with lanthanum chloride; a) calcined at 1200°C, b) same powder held 11 days at 800°C.

Appendix J.

X-ray diffraction spectra of the powders in LSGM synthesis, which held 7 days at their calcination temperature to see the effect of holding time at calcination temperature, are illustrated. Present phases are shown on the XRD plots. XRD plots of the powder synthesized;

- v) with PVA as the organic carrier material, and calcined at 1100°C compared with same powder held 7 hours 1100°C ,
- vi) with CA as the organic carrier material, and calcined at 900°C compared with same powder held 7 hours at 900°C ,
- vii) with CA as the organic carrier material, and calcined at 1100°C compared with same powder held 7 hours at 1100°C , and
- viii) with lanthanum chloride as the lanthanum source, and nitrate sources of strontium, gallium, and magnesium, and calcined at 1100°C compared with same powder held 7 hours at 1100°C .

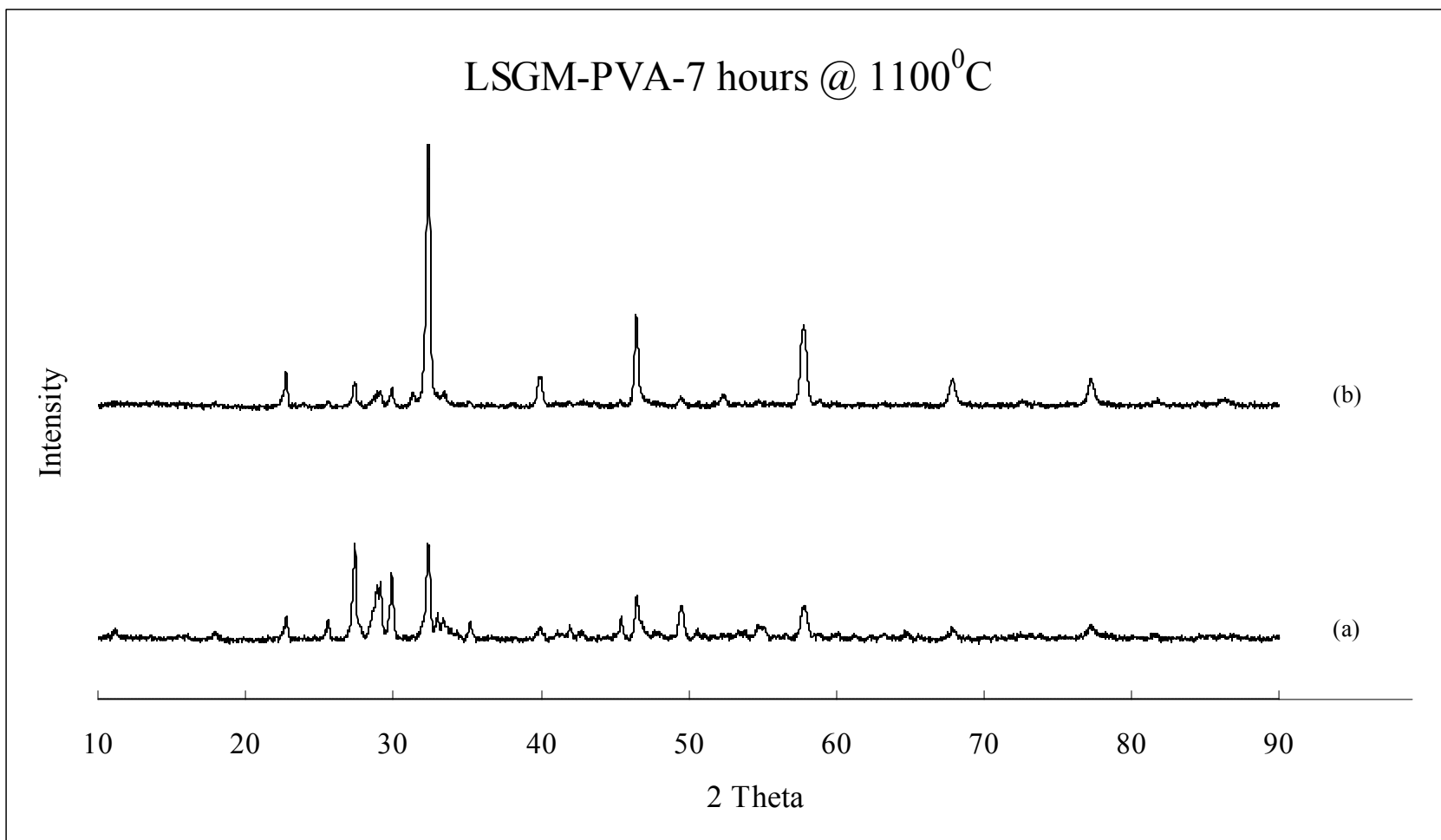


Figure J 1. X- ray spectra of LSGM powders synthesized with PVA; a) calcined at 1100°C, b) held 7 hours at 1100°C.

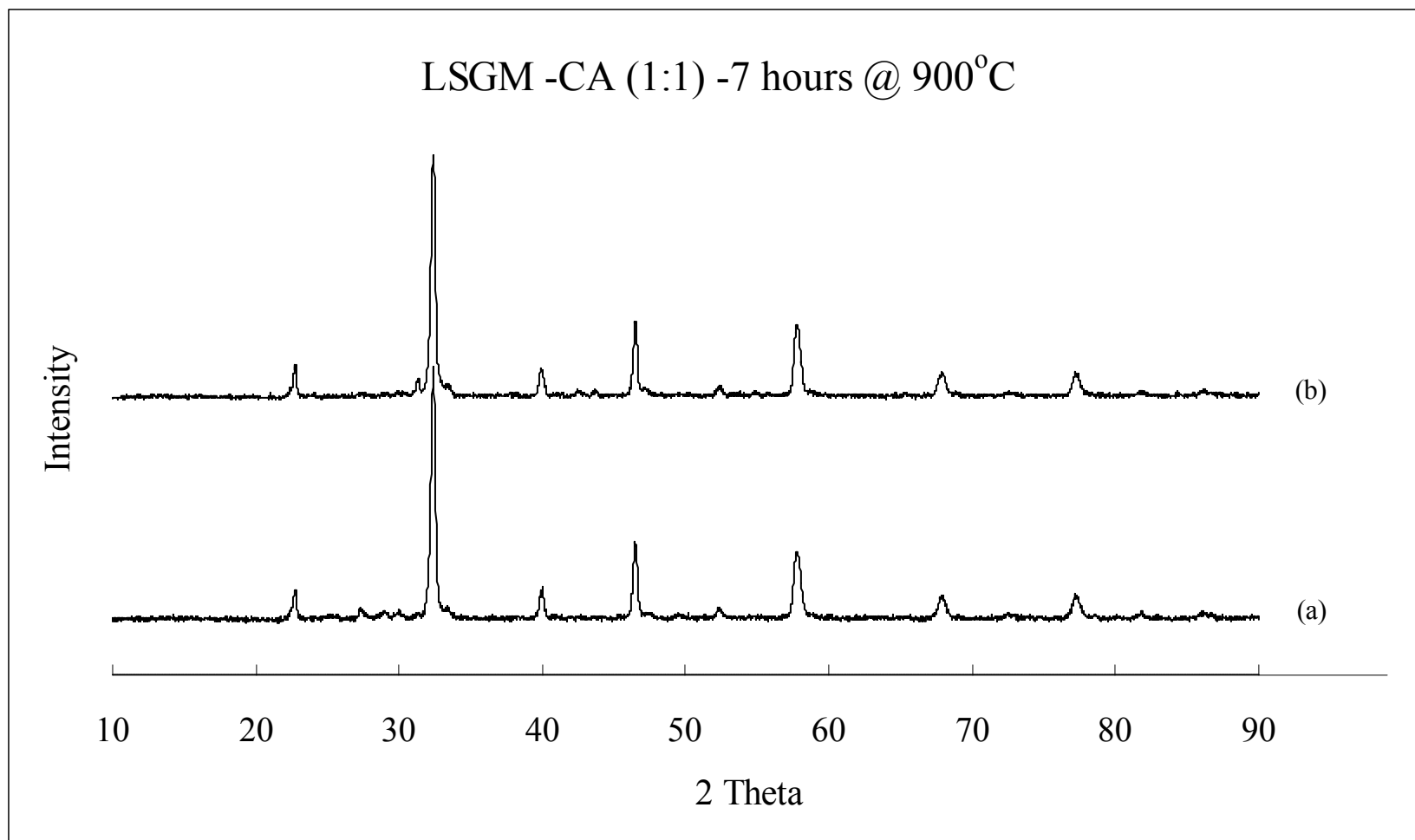


Figure J 2. X- ray spectra of LSGM powders synthesized with CA; a) calcined at 900°C, b) held 7 hours at 900°C.

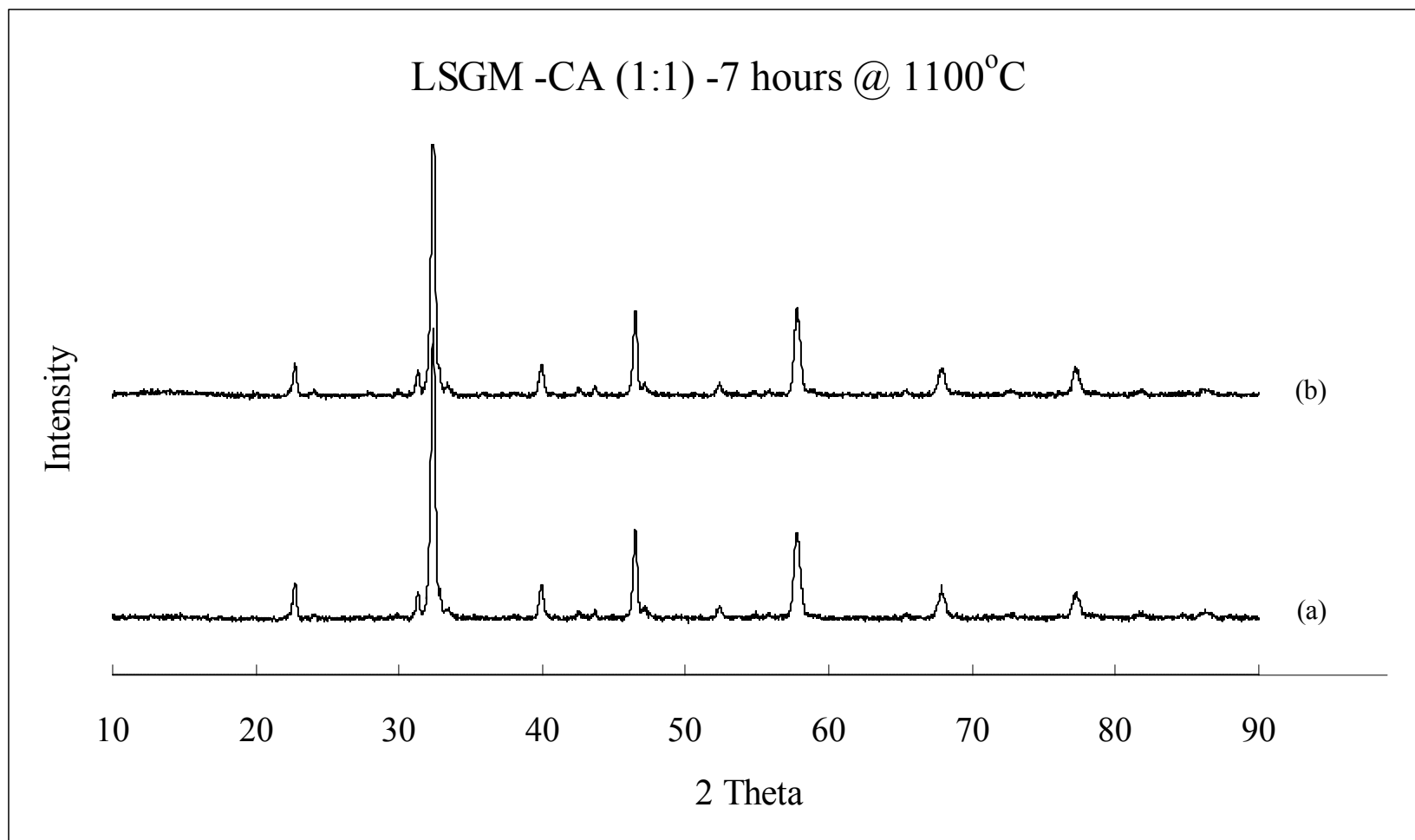


Figure J 3. X- ray spectra of LSGM powders synthesized with CA; a) calcined at 1100°C, b) held 7 hours at 1100°C.

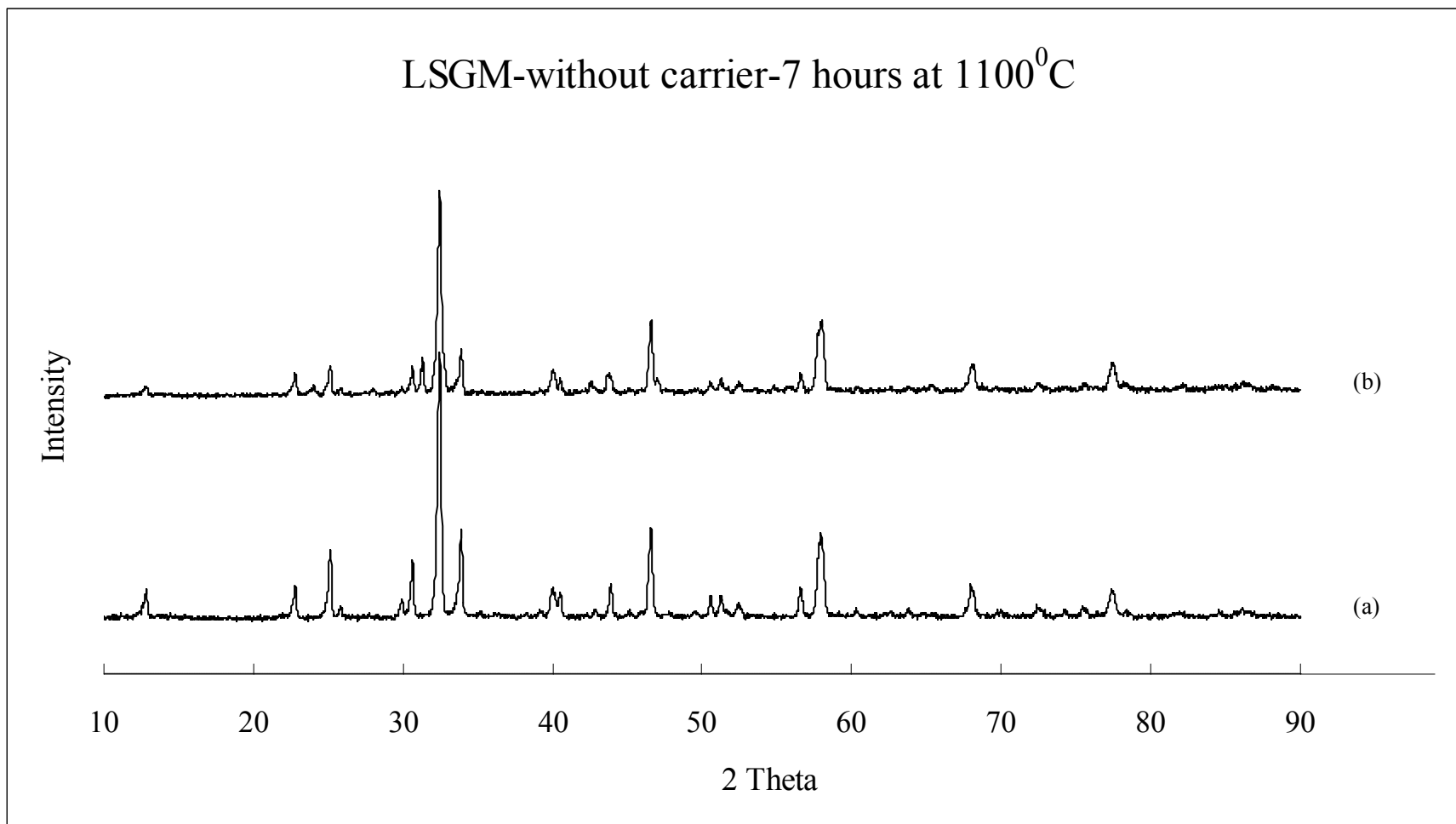


Figure J 4. X- ray spectra of LSGM powders synthesized by lanthanum chloride; a) calcined at 1100°C, b) held 7 hours at 1100°C.

REFERENCES

1. W.R. Grove, "On voltaic series and the combination of gases by platinum", *Phil. Mag.* 14, 127-130 (1839)
2. A. Boudghene Stambouli, E. Traversa, "Fuel Cells, an alternative to standard sources of energy", *Renewable and Sustainable Energy Reviews* 6, 297-306 (2002)
3. J.H. Hirschenhofer, D.B. Stauffer, R.R. Engleman, M.G. Klett, "Fuel Cell Handbook", 4th Edition, Orinda, USA, 1997
4. Seungdoo Park, Raymond J. Gorte, John M. Vohs, "Application of heterogeneous catalysis in the direct oxidation of hydrocarbons in a solid-oxide fuel cell", *Applied Catalysis A: General* 200, 55-61 (2000)
5. S. Katikaneni, C. Yuh, S. Abens, M. Farooque, "The direct carbonate fuel cell technology: advances in multi-fuel processing and internal reforming", *Catalysis Today* 77, 99-106 (2002)
6. B.C.H. Steele, *Solid State Ionics* 129, "Appraisal of $Ce_{1-y}Gd_yO_{2-y/2}$ electrolytes for IT-SOFC operation at 500⁰C", 95-110 (2000)
7. G.F.McLean, T.Niet, S.Prince-Richard, N.Djilali, "An assessment of alkaline fuel cell technology", *International Journal of Hydrogen Energy* 27, 507-526 (2002)
8. Vogel W, Lundquist JT, *J. Electrochem. Soc.* 117, 1512 (1970)
9. Al-Saleh MA, Gultekin S, Al-Zakri AS, Celiker H, "Effect of carbon dioxide on the performance of Ni =PTFE and Ag =PTFE electrodes in an alkaline fuel cell", *J. Appl. Electrochem.* 24, 575 –80 (1994)
10. Al-Saleh MA, Gultekin S, Al-Zakri AS, Celiker H, "Performance of porous nickel electrode for alkaline H₂\O₂ fuel cell", *Int. J. Hydrogen Energy* 19, 713 –8 (1994)
11. Kordesch K, Gunter S, "Fuel cells and their applications" Berlin, Germany: Wiley-VCH, 1996.

12. Gultekin S, Al-Saleh MA, Al-Zakri AS, "Effect of CO impurity in H₂ on the performance of Ni =PTFE diffusion electrodes in alkaline fuel cells", *Int. J. Hydrogen Energy* 19, 181 –5 (1994)
13. Kiros Y, "Tolerance of gases by the anode for the alkaline fuel cell", 1994 Fuel Cell Seminar, San Diego, CA, 1994
14. M. Rikukawa, K. Sanui, "Proton-conducting polymer electrolyte membranes based on hydrocarbon polymers, *Prog. Polym. Sci.* 25, 1463-1502 (2000)
15. S. Ahmed, J. Kopasz, R. Kumar, M. Krumpelt, "Water balance in a polymer electrolyte fuel cell system", *Journal of Power Sources* 112, 519-530 (2002)
16. M.H. Fronk, D.L. Wetter, D.A. Masten, A. Bosco, "PEM Fuel Cell System Solutions for Transportation", SAE Technical Paper Series, No. 2000-01-0373.
17. Viral Metha, Joyce Smith Cooper, "Review and analysis of PEM fuel cell design and manufacturing", *Journal of Power Sources* 114, 32-53 (2003)
18. T. Susai, A. Kawakami, A. Hamada, Y. Miyake, Y. Azegami, "Development of a 1 kW polymer electrolyte fuel cell power source", *Journal of Power Sources* 92, 131-138 (2001)
19. Cecilia Wallmark, Per Alvfors, "Design of stationary PEFC system configurations to meet heat and power demands", *Journal of Power Sources* 106, 83-92 (2002)
20. E. Danial Doss, R. Kumar, R.K. Ahluwalia, M. Krumpelt, "Fuel processors for automotive fuel cell systems: a parametric analysis", *Journal of Power Sources* 102, 1-15 (2001)
21. Paola Costamagna, Supramaniam Srinivasan, "Quantum jumps in the PEMFC science and technology from the 1960s to the year 2000 Part I. Fundamental scientific aspects", *Journal of Power Sources* 102, 242-252 (2001)
22. Suman Roy Choudhury, M.B. Deshmukh, R. Rengaswamy, "A two-dimensional steady-state model for phosphoric acid fuel cells (PAFC)", *Journal of Power Sources* 112, 137-152 (2002)
23. J.P. Vanhanen, P.S. Kauranen, P.D. Lund, "Operation experiences of a phosphoric acid fuel cell in a solar hydrogen energy system", *Int. J. Hydrogen Energy*, vol.22, no.7, 707-713 (1997)
24. M. Ghouse, H. Abaoud, A. Al-Boeiz, "Operational experience of a 1 kW PAFC stack", *Applied Energy* 65, 303-314 (2000)

25. B. Zhu, "Advantages of intermediate temperature solid oxide fuel cells for tractionary applications", *Journal of Power Sources* 93, 82-86 (2001)
26. Vidya S. Batra, Sanjay Bali, S. Venkatesh, "Fabrication of porous components for molten carbonate fuel cells", *Ceramics International*, Volume 29, Issue 5, 547-553 (2003)
27. José Luz Silveira, Elisangela Martins Leal, Luis F. Ragonha Jr., "Analysis of molten carbonate fuel cell: cogeneration to produce electricity and cold water", *Energy* 26, 891-904 (2001)
28. Shigenori Mitsushima, Koichi Matsuzawa, Nobuyuki Kamiya, Ken-ichiro Ota, "Improvement of MCFC cathode stability by additives", *Electrochimica Acta* 47, 3823-3830 (2002)
29. Prabhu Ganesan, Hector Colon, Bala Haran, Ralph White, Branko N. Popov, "Study of cobalt-doped lithium–nickel oxides as cathodes for MCFC", *Journal of Power Sources* 111, 109-120 (2002)
30. Choong-Gon Lee, Byoung-Sam Kang, Hai-Kyung Seo, Hee-Chun Lim, "Effect of gas-phase transport in molten carbonate fuel cell", *Journal of Electroanalytical Chemistry* 540, 169-188 (2003)
31. Changrong Xia, Meilin Liu, "Microstructures, conductivities, and electrochemical properties of $Ce_{0.9}Gd_{0.1}O_2$ and GDC – Ni anodes for low-temperature SOFCs", *Solid State Ionics* 152-153, 423-430 (2002)
32. D.V. Schur, B.P. Tasarov, S. Yu. Zaginaichenko, V.K. Pishuk, T.N. Veziroglu, Yu.M. Shul'ga, A.G. Dubovoi, N.S. Anikina, A.P. Pomytkin, A.D. Zolotareno, "The prospects for using carbon nanomaterials as hydrogen storage systems", *International Journal of Hydrogen Energy* 27, 1063-1069 (2002)
33. V. Karakoussis, N.P. Brandon, M. Leach, R. van der Vorst, "The environmental impact of manufacturing planar and tubular solid oxide fuel cells", *Journal of Power Sources* 101, 10-26 (2001)
34. A. Boudghene Stambouli, E. Traversa, "Solid oxide fuel cells (SOFCs): a review of an environmentally clean and efficient source of energy", *Renewable and Sustainable Energy Reviews* 6, 433-455 (2002)
35. S.C. Singhal, "Solid oxide fuel cells for stationary, mobile, and military applications", *Solid State Ionics* 152-153, 405-410 (2002)
36. F. Tietz, H.-P. Buchkremer, D. Stöver, "Components manufacturing for solid oxide fuel cells", *Solid State Ionics* 152-153, 373-381 (2002)

37. Keqin Huang, John B. Goodenough, "A solid oxide fuel cell based on Sr- and Mg-doped LaGaO₃ electrolyte: the role of a rare-earth oxide buffer", *Journal of Alloys and Compounds* 303-304, 454-464 (2000)
38. J. Fleig, K.D. Kreuer, J. Maier, "Handbook of Advanced Ceramics", *Materials, Applications, and Processing*, Academic Press, 1-60 (2001)
39. W.Z. Zhu, S.C. Deevi, "Development of interconnect materials for solid oxide fuel cells", *Materials Science and Engineering A*, Volume 348, Issues 1-2, 227-243 (2003)
40. J.T.S. Irvine, D.P. Fagg, J. Labrincha, F.M.B. Marques, "Development of novel anodes for solid oxide fuel cells", *Catalysis Today* 38, 467-472 (1997)
41. B. de Boer, M. Gonzales, H.J.M. Bouwmeester, H. Verweij, "The effect of the presence of fine YSZ particles on the performance of porous nickel electrodes", *Solid State Ionics* 127, 269-276 (2000)
42. Ying Li, Yusheng Xie, Jianghong Gong, Yunfa Chen, Zhongtai Zhang, "Preparation of Ni/YSZ materials for SOFC anodes by buffer-solution method", *Material Science and Engineering B86*, 119-122 (2001)
43. Mohan K. Dongare, Avinash M. Dongare, V.B. Tare, Erhard Kemnitz, "Synthesis and characterization of copper-stabilized zirconia as an anode material for SOFC", *Solid State Ionics* 152-153, 455-462 (2002)
44. Zhe Lü, Li Pei, Tian-min He, Xi-qiang Huang, Zhi-guo Liu, Yuan Ji, Xing-hai Zhao, Wen-hui Su, "Study on new copper-containing SOFC anode materials", *Journal of Alloys and Compounds* 334, 299-303 (2002)
45. Olga A. Marina, Nathan L. Canfield, Jeff W. Stevenson, "Thermal, electrical, and electrocatalytical properties of lanthanum-doped strontium titanate", *Solid State Ionics* 149, 21-28 (2002)
46. A.-L. Sauvet, J. Fouletier, "Electrochemical properties of a new type anode material La_{1-x}Sr_xCr_{1-y}Ru_yO_{3-δ} for SOFC under hydrogen and methane at intermediate temperatures", *Electrochimica Acta* 47, 987-995 (2001)
47. A.-L. Sauvet, J. Fouletier, F. Gaillard, M. Primet, "Doped lanthanum chromites as SOFC anode materials", *J. of Catalysis* 209 (1), 25-34 (2002)
48. Shizhong Wang, Yi Jiang, Yahong Zhang, Wenzhao Li, Jingwang Yan, Zigui Lu, "Electrochemical performance of mixed ionic-electronic conducting oxides as anodes for solid oxide fuel cell", *Solid State Ionics* 120, 75-84 (1999)

49. Stephanie J.A. Livermore, John W. Cotton, R. Mark Ormerod, "Fuel reforming and electrical performance studies in intermediate temperature ceria-gadolinia based SOFCs", *Journal of Power Sources* 86, 411-416 (2000)
50. B.C.H. Steele, "Materials for IT-SOFC stacks 35 years R&D: the inevitability of gradualness?", *Solid State Ionics* 134, 3-20 (2000)
51. M. Sahibzada, B.C.H. Steele, K. Zheng, R.A. Rudkin, I.S. Metcalfe, "Development of solid oxide fuel cells based on a Ce(Gd)O_{2-x} electrolyte film for intermediate temperature operation", *Catalysis Today* 38, 459-466 (1997)
52. M. Sahibzada, B.C.H. Steele, D. Barth, R.A. Rudkin, I.S. Metcalfe, "Operation of solid oxide fuel cells at reduced temperatures", *Fuel* 78, 639-643 (1999)
53. Mortaza Sahibzada, Brian C.H. Steele, Klaus Hellgardt, Dieter Barth, Astrid Effendi, Dionissos Mantzavinos, Ian S. Metcalfe, "Intermediate temperature solid oxide fuel cells operated with methanol fuels", *Chemical Engineering Science* 55, 3077-3083 (2000)
54. A. Hartley, M. Sahibzada, M. Weston, I.S. Metcalfe, D. Mantzavinos, "La_{0.6}Sr_{0.4}Co_{0.2}Fe_{0.8}O₃ as the anode and cathode for intermediate temperature solid oxide fuel cells", *Catalysis Today* 55, 197-204 (2000)
55. Kiyoshi Kuroda, Ikiko Hashimoto, Kazunori Adachi, Jun Akikusa, Yoshitaka Tamou, Norikazu Komada, Tatsumi Ishihara, Yusaku Takita, "Characterization of solid oxide fuel cell using doped lanthanum gallate", *Solid State Ionics* 132, 199-208 (2000)
56. Toru Inagaki, Kazuhiro Miura, Hiroyuki Yoshida, Radenka Maric, Satoshi Ohara, Xinge Zhang, Kazuo Mukai, Takehisa Fukui, "High-performance electrodes for reduced temperature solid oxide fuel cells with doped lanthanum gallate electrolyte II. La(Sr)CoO₃ cathode", *Journal of Power Sources* 86, 347-351 (2000)
57. Keqin Huang, John B. Goodenough, "A solid oxide fuel cell based on Sr- and Mg-doped LaGaO₃ electrolyte: the role of a rare-earth oxide buffer", *Journal of Alloys and Compounds* 303-304, 454-464 (2000)
58. J. Fleig, "On the width of the electrochemically active region in mixed conducting solid oxide fuel cell cathodes", *Journal of Power Sources* 105, 228-238 (2002)
59. T. Kenjo, Y. Kanehira, "Influence of the local variation of the polarization resistance on SOFC cathodes", *Solid State Ionics* 148, 1-14 (2002)

60. Yoshio Matsuzaki, Isamu Yasuda, "Electrochemical properties of a SOFC cathode in contact a chromium-containing alloy separator", *Solid State Ionics* 132, 271-278 (2000)
61. S. Charojrochkul, K.-L. Choy, B.C.H. Steele, "Cathode/electrolyte systems for solid oxide fuel cells fabricated using flame assisted vapour deposition technique", *Solid State Ionics* 121, 107-113 (1999)
62. E. Boehm, J.-M. Bassat, M.C. Steil, P. Dordor, F. Mauvy, J.-C. Greiner, "Oxygen transport properties of $\text{La}_2\text{Ni}_{1-x}\text{Cu}_x\text{O}_{4+\delta}$ mixed conducting oxides", *Solid State Sciences* 5, 973-981 (2003)
63. J. Van herle, R. Ihringer, R. Vasquez Cavieres, L. Constantin, O. Bucheli, "Anode supported solid oxide fuel cells with screen-printed cathodes", *Journal of the European Ceramic Society* 21, 1855-1859 (2001)
64. Selmar de Souza, Steven J. Visco, Lutgard C. De Jonghe, "Thin-film solid oxide fuel cell with high performance at low-temperature", *Solid State Ionics* 98, 57-61 (1997)
65. Tsepin Tsai, Scott A. Barnett, "Increased solid-oxide fuel cell power density using interfacial ceria layers", *Solid State Ionics* 98, 191-196 (1997)
66. L.S. Wang, S.A. Barnett, "Ag-perovskite cermets for thin film solid oxide fuel cell air-electrode applications", *Solid State Ionics* 76, 103-113 (1995)
67. H. Uchida, S. Arisaka, M. Watanabe, "High performance electrodes for medium-temperature solid oxide fuel cells: Activation of $\text{La}(\text{Sr})\text{CoO}_3$ cathode with highly dispersed Pt metal electrocatalysts", *Solid State Ionics* 135, 347-351 (2000)
68. M. Sahibzada, S.J. Benson, R.A. Rudkin, J.A. Kilner, "Pd-promoted $\text{La}_{0.6}\text{Sr}_{0.4}\text{Co}_{0.2}\text{Fe}_{0.8}\text{O}_3$ cathodes", *Solid State Ionics* 113-115, 285-290 (1998)
69. Joong-Myeon Bae, B.C.H. Steele, "Properties of $\text{La}_{0.6}\text{Sr}_{0.4}\text{Co}_{0.2}\text{Fe}_{0.8}\text{O}_{3-\delta}$ (LSCF) double layer cathodes on gadolinium-doped ceria oxide (CGO) electrolytes I. Role of SiO_2 ", *Solid State Ionics* 106, 247-253 (1998)
70. E. Maguire, B. Gharbage, F.M.B. Marques, J.A. Labrincha, "Cathode materials for intermediate temperature SOFCs", *Solid State Ionics* 127, 329-335 (2000)
71. Dionissos Mantzavinos, Anne Hartley, Ian S. Metcalfe, Mortaza Sahibzada, "Oxygen stoichiometries in $\text{La}_{1-x}\text{Sr}_x\text{Co}_{1-y}\text{Fe}_y\text{O}_{3-\delta}$ perovskites at reduced oxygen partial pressures", *Solid State Ionics* 134, 103-109 (2000)

72. Hee Sung Yoon, Seung Woo Choi, Dokyol Lee, Byong Ho Kim, "Synthesis and characterization of $Gd_{1-x}Sr_xMnO_3$ cathode for solid oxide fuel cells", *Journal of Power Sources* 93, 1-7 (2001)
73. F.M. Figueiredo, J.R. Frade, F.M.B. Marques, "Performance of composite $LaCoO_3 - La_2(Zr,Y)_2O_7$ cathodes", *Solid State Ionics* 135, 463-467 (2000)
74. N.T. Hart, N.P. Brandon, M.J. Day, N.Lapena-Rey, "Functionally graded composite cathodes for solid oxide fuel cells", *Journal of Power Sources* 106, 42-50 (2002)
75. Keqin Huang, Robin Tichy, John B. Goodenough, "Superior perovskite Oxide-ion conductor; strontium- and magnesium-doped $LaGaO_3$: III, performance tests of single ceramic fuel cells", *J. Am. Ceram. Soc.* 81 [10], 2581-2585 (1998)
76. Teruhisa Horita, Katsuhiko Yamaji, Natsuko Sakai, Harumi Yokokawa, André Weber, Ellen Ivers-Tiffée, "Oxygen reduction mechanism at porous $La_{1-x}Sr_xCoO_{3-\delta}$ cathodes/ $La_{0.8}Sr_{0.2}Ga_{0.8}Mg_{0.2}O_{2.8}$ electrolyte interface for solid oxide fuel cells", *Electrochimica Acta* 46, 1837-1845 (2001)
77. G.Ch. Kostogloudis, Ch. Ftikos, A. Ahmad-Khanlou, A. Naoumidis, D. Stöver, "Chemical compatibility of alternative perovskite oxide SOFC cathodes with doped lanthanum gallate solid electrolyte", *Solid State Ionics* 134, 127-138 (2000)
78. H. Ullmann, N. Trofimenko, F. Tietz, D. Stöver, A. Ahmad-Khanlou, "Correlation between thermal expansion and oxide ion transport in mixed conducting perovskite-type oxides for SOFC cathodes", *Solid State Ionics* 138, 79-90 (2000)
79. J.A. Kilner, "Fast oxygen transport in acceptor doped oxides", *Solid State Ionics* 129, 13-23 (2000)
80. Rajiv Doshi, Von L. Richards, J.D. Carter, Xianoping Wang, Michael Krumpelt, "Development of solid-oxide fuel cells that operate at $500^{\circ}C$ ", *Journal of The Electrochemical Society* 146(4), 1273-1278 (1999)
81. J.P.P. Huijsmans, "Ceramics in solid oxide fuel cells", *Current Opinion in Solid State and Materials Sciences* 5, 317-323 (2001)
82. Nguyen Q. Minh, "Ceramic fuel cells", *J. Am. Ceram. Soc.* 76[3], 563-588 (1993)
83. S.C. Singhal, "Advances in solid oxide fuel cell technology", *Solid State Ionics* 135, 305-313 (2000)

84. Mogens Mogensen, Nigel M. Sammes, Geoff A. Tompsett, "Physical, chemical and electrochemical properties of pure and doped ceria", *Solid State Ionics* 129, 63-94 (2000)
85. Hideaki Inaba, Hiroaki Tagawa, "Ceria-based solid electrolytes", *Solid State Ionics* 83, 1-16 (1996)
86. S.P.S. Badwal, F.T. Ciacchi, J. Drennan, "Investigation of the stability of ceria-gadolinia electrolytes in solid oxide fuel cell environments", *Solid State Ionics* 121, 253-262 (1999)
87. S.P.S. Badwal, "Stability of solid oxide fuel cell components", *Solid State Ionics* 143, 39-46 (2001)
88. Katsuhiko Yamaji, Hideyuki Negishi, Teruhisa Horita, Natsuko Sakai, Harumi Yokokawa, "Vaporization process of Ga from doped LaGaO₃ electrolytes in reducing atmospheres" *Solid State Ionics* 135, 389-396 (2000)
89. Tatsumi Ishihara, Hideaki Matsuda, Yusaku Takita, "Effects of rare earth cations doped for La site on the oxide ionic conductivity of LaGaO₃-based perovskite type oxide", *Solid State Ionics* 79, 147-151 (1995)
90. A. Ahmad-Khanlou, F. Tietz, D. Stöver, "Material properties of La_{0.8}Sr_{0.2}Ga_{0.9+x}Mg_{0.1}O_{3-δ} as a function of Ga content", *Solid State Ionics* 135, 543-547 (2000)
91. Katsuhiko Yamaji, Teruhisa Horita, Masahiko Ishikawa, Natsuko Sakai, Harumi Yokokawa, "Chemical stability of the La_{0.9}Sr_{0.1}Ga_{0.8}Mg_{0.2}O_{2.85} electrolyte in a reducing atmosphere", *Solid State Ionics* 121, 217-224 (1999)
92. Terry A. Ring, "Fundamentals of Ceramic Powder Processing and Synthesis", Academic Press, 1996
93. A. Cüneyt Taş, Peter J. Majewski, Fritz Aldinger, "Chemical preparation of pure and strontium- and/or magnesium-doped lanthanum gallate powders", *J. Am. Ceram. Soc.* 83[12], 2954-2960 (2000)
94. Mehmet A. Gülgün, My H. Nguyen, Waltraud M. Kriven, "Polymerized organic-inorganic synthesis of mixed oxides", *J. Am. Ceram. Soc.* 82[3], 556-560 (1999)
95. M.P. Pechini, U.S. Patent No.3, 330, 697, July (1967)
96. M. Marinsek, K. Zupan, J. Maeek, "Ni-YSZ cermet anodes prepared by citrate/nitrate combustion synthesis", *J. Power Sources* 106, 178-188 (2002)

97. S. Tanasescu, D. Berger, D. Neiner, N.D. Totir, "Thermodynamic characterization of some doped lanthanum chromites used as interconnects in SOFC", *Solid State Ionics*, Volume 157, Issues 1-4, 365-370 (2003)
98. F. Riza, Ch. Ftikos, F. Tietz, W. Fischer, "Preparation and characterization of $\text{Ln}_{0.8}\text{Sr}_{0.2}\text{Fe}_{0.8}\text{Co}_{0.2}\text{O}_{3-\delta}$ (Ln=La, Pr, Nd, Sm, Eu, Gd)", *Journal of the European Ceramic Society* 21, 1769-1773 (2001)
99. V. Dusastre, J.A. Kilner, "Optimisation of composite cathodes for intermediate temperature SOFC applications", *Solid State Ionics* 126, 163-174 (1999)
100. Supplement of *Journal of Bilim Teknik*, January 2002, p.22
101. Helmut Ullmann, Nikolai Trofimenko, "Composition, structure and transport properties of perovskite-type oxides", *Solid State Ionics* 119, 1-8 (1999)
102. G.J. Saunders, K. Kendall, "Reactions of hydrocarbons in small tubular SOFCs", *Journal of Power Sources* 106, 258-263 (2002)
103. Marko Hrovat, Ariane Ahmad-Khanlou, Zoran Samadzija, Janez Holc, "Interactions between lanthanum gallate based solid electrolyte and ceria", *Materials Research Bulletin*, Vol. 34, Nos. 12/13, 2027-2034 (1999)
104. K. Zupan, S. Pejovnik, J. Maeek, "Synthesis of nanometer crystalline lanthanum chromite powders by the citrate-nitrate autoignition reaction", *Acta Chim. Slov.* 48(1), 137-145 (2001)
105. *CRC Handbook of Chemistry and Physics*, 1981-1982 62nd Edition, CRC Press, Inc.
106. "Polymerized Organic-Inorganic Complex Route for Mixed-Oxide Synthesis", M.A. Gülgün, W.M. Kriven, US patent# 6,482,387
107. O. Uchiyama, M. Kakihana, M. Arima, M. Yashima, Y. Suzuki, M. Yoshimura, "Polymerized complex precursors for the synthesis of pure PbTiO_3 powders at 400-600 °C", *Advanced Materials'93, I / A: Ceramics, Powders, Corrosion and Advanced Processing*, edited by N: Mizutani et al. *Trans. Mat. Res. Soc. Jpn.*, Volume 14A
108. Xinge Zhang, Satoshi Ohara, Hajime Okawa, Radenka Maric, Takehisa Fukui, "Interactions of a $\text{La}_{0.9}\text{Sr}_{0.1}\text{Ga}_{0.8}\text{Mg}_{0.2}\text{O}_{3-\delta}$ electrolyte with Fe_2O_3 , Co_2O_3 and NiO anode materials", *Solid State Ionics* 139, 145-152 (2001)
109. Mehmet A. Gülgün, Oludele O. Popoola, Waltraud M. Kriven, "Chemical synthesis and characterization of calcium aluminate powders", *J. Am. Ceram. Soc.* 77[2], 531-539 (1994)

110. W.M. Kriven, S.J. Lee, M.A. Gülgün, M.H. Nguyen, D.K. Kim, "Synthesis of oxide powders via polymeric steric entrapment", invited paper, in Innovative Processing/Synthesis: Ceramics, Glass, Composites III, Ceramic Transactions, Vol 108, 99-110 (2000)
111. M.A. Gülgün, W.M. Kriven, "A simple solution-polymerization route for oxide powder synthesis", Technology and Commercialization of Powder Synthesis and Shape Forming Processes, in Ceramic Transactions Vol. 62. (Cincinnati, OH, April, 1995). Edited by J.J. Kingsley, C.H. Schilling, and J.H. Adair. American Ceramic Society, Westerville, Ohio, 1996
112. M. Kakihana, M. Arima, M. Yashima, M. Yoshimura, Y. Nakamura, H. Makazi, H. Yasuoka, "Polymerized complex route to the synthesis of multi-component oxides", An invited paper for "The International Symposium on Sol-Gel Science and Technology" (19-22 October, 1994. Los Angeles, USA)
113. V.P. Gorelov, D.I. Bronin, Ju. V. Sokolava, H. Nafe, F. Aldinger, "The effect of doping and processing conditions on properties of $\text{La}_{1-x}\text{Sr}_x\text{Ga}_{1-y}\text{Mg}_y\text{O}_{3-\alpha}$ ", Journal of the European Ceramic Society 21, 2311-2317 (2001)
114. W.D. Kingery, H.K. Bowen, D.R. Uhlmann, "Introduction to Ceramics", John Wiley & Sons, Inc., 1997
115. S.P. Simner, J.R. Bonnett, N.L. Canfield, K.D. Meinhardt, J.P. Shelton, V.L. Sprenkle, J.W. Stevenson, "Development of lanthanum ferrite SOFC cathodes", Journal of Power Sources 113(1), 1-10 (2003)
116. S.P. Simner, J.R. Bonnett, N.L. Canfield, K.D. Meinhardt, V.L. Sprenkle, J.W. Stevenson, "Optimized lanthanum ferrite-based cathodes for anode-supported SOFCs", Electrochemical and Solid State Letters 5(7), A173-A175 (2002)
117. Monica Popa, Johannes Frantti, Masato Kakihana, "Lanthanum ferrite LaFeO_{3+d} anopowders obtained by the polymerizable complex method", Solid State Ionics 154-155, 437-445 (2002)
118. S. Tanasescu, D. Berger, D. Neiner and N. D. Totir, "Thermodynamic characterisation of some doped lanthanum chromites used as interconnects in SOFC", Solid State Ionics 157, Issues 1-4, 365-370 (2003)
119. Hideko Hayashi, Mieko Watanabe, Miwako Ohuchida, Hideaki Inaba, Yoshiko Hiei, Tohru Yamamoto and Masashi Mori, "Thermal expansion of $\text{La}_{1-x}\text{Sr}_x\text{CrO}_{3-\delta}$ ", Solid State Ionics 144, 301-313 (2001)

120. Joseph Sfeir, "LaCrO₃-based anodes: stability considerations", *Journal of Power Sources* 118, 276-285 (2003)
121. N. Imanaka, K. Okamoto, G. Adachi, "New type of sodium ion conducting solid electrolyte based on lanthanum oxysulfate", *Electrochemical and Solid State Letters* 5(9), E51-E53 (2002)
122. N. Imanaka, K. Okamoto, G. Adachi, "Chloride ion conducting characteristics in rare earth oxychlorides", *Chemistry Letters* 2, 130-131 (2001)
123. K. Okamoto, N. Imanaka, G. Adachi, "Chloride ion conduction in rare earth oxychlorides", *Solid State Ionics* 154-155, 577-580 (2002)
124. Jae Yeon Yi, Gyeong Man Choi, "Phase characterization and electrical conductivity of LaSr(GaMg)_{1-x}Mn_xO₃ system", *Solid State Ionics* 148, 557-565 (2002)
125. V.V. Kharton, A.L. Shaula, N.P. Vyshatko, F.M.B. Marques, "Electron-hole transport in (La_{0.9}Sr_{0.1})_{0.98}Ga_{0.8}Mg_{0.2}O_{3-δ} electrolyte: effects of ceramic microstructure", *Electrochimica Acta* 48, 1817-1828 (2003)